# STUDY OF NEGATIVE MAGNETIZATION, EXCHANGE BIAS AND MAGNETIZATION SWITCHING IN RARE EARTH CHROMITES

Thesis Submitted to AcSIR For the Award of

the Degree of

DOCTOR OF PHILOSOPHY

In Physical Sciences

**AcSIR**

By

**PREETI GUPTA**

Registration Number: 10PP12A26082

Under the guidance of

**DR. PANKAJ PODDAR**

**CSIR-National Chemical Laboratory, Pune, India**

**October 2015**

\*\*\*\*\*\*\*\*\*\*\*\*\*\*\*\*\*\*\*\*\*\*\*\*\*\*\*\*\*\*\*

*Dedicated to my parents
and my better half*

\*\*\*\*\*\*\*\*\*\*\*\*\*\*\*\*\*\*\*\*\*\*\*\*\*\*\*\*\*\*\*

*A link to the past and a
bridge to the future.....*

# CERTIFICATE

This is to certify that the work presented in the thesis entitled **"Study of negative magnetization, exchange bias and magnetization switching in rare earth chromites"** by **Preeti Gupta**, submitted for the degree of **Doctor of Philosophy in Physical Sciences** was carried out under my supervision at the Physical and Materials Chemistry Division, CSIR-National Chemical Laboratory, Pune, India. All the materials obtained by other sources have been duly acknowledged in the thesis.

Date: 1st Oct. 2015

Place: NCL, Pune

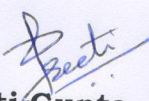**Dr. Pankaj Poddar**

(Research Guide)

# DECLARATION

I, hereby declare that the work described in this thesis entitled **"Study of negative magnetization, exchange bias and magnetization switching in rare earth chromites"** submitted for the degree of **Doctor of Philosophy in Physical Sciences** has been carried out by me at the Physical and Materials Chemistry Divisions of the CSIR-National Chemical Laboratory, Pune, India under the supervision of Dr. Pankaj Poddar. Such materials as have been obtained by other sources have been duly acknowledged in this thesis. The work is original and has not been submitted in part or full by me for award of any other degree or diploma in any other University.

Date: 1st October 2015

National Chemical Laboratory

Place: Pune

Preeti Gupta

(Research Student)

# ACKNOWLEDGEMENTS

*There are so many people, whose support, encouragement and inspiration are very much necessary to accomplish any major achievements in life, especially, if it involves the elements of fulfilling one's cherished dreams. For me, this thesis is such an important destiny and I am indeed indebted to lot of people for their wishes and blessings for completing this journey. I take this opportunity to acknowledge and extend my sincere gratitude towards all these people who have been involved, directly or indirectly, to make the research work described in this thesis possible.*

*First, I would like to express my deepest gratitude to my research supervisor Dr. Pankaj Poddar, for giving me an opportunity to pursue my Ph.D. research with him. It has been a great privilege to work under his able guidance and his dynamic laboratory environment for the past five years. I greatly appreciate the insights he provided in various studies pursued in my work. His innovative thinking and highly spirited attitude have inspired me to conduct and complete my doctoral research quite efficiently. He has not only grafted my scientific skills and knowledge but also moulded me into a better human being. His constant encouragement helped me to push beyond my limits. His guidance always challenged me intellectually and provided a perfect ambience that I needed to grow as a researcher. I am really grateful to him for his critical comments and tremendous efforts in preparing this dissertation. I thank him for their endless support filled with patience and enthusiasm during my whole tenure of Ph.D. Your advice on both research as well as on my career have been priceless.*

*I would also like to thank my doctoral advisory committee members, Dr. Chetan Gadgil, Dr. C. P. Vinod and Dr. A. K. Rath, for their constructive and innovative suggestion. I owe a great deal of appreciation and gratitude to my external expert Dr. Surjeet Singh. I warmly thank him for his precious advice, analysis, criticism and discussions on my work.*

thank my sisters Poonam and Gudiya for their constant help and support and being with me in my hard times and listening to my tantrums. I would like to thank Vijayji (Jiju) whom I troubled a lot during my PhD days. His guidance helped me a lot in achieving my goals. I thank my mother and father-in-law for their encouragement and continued support over the years and their enthusiasm as I neared my goal. I also thank Arit for encouraging me whenever I am down and listening to my PhD stories ☺ so enthusiastically. Above all, I thank them all for trusting me when I most needed it.

Finally, I specially acknowledge my hubby Nikhil for his understanding, support, love, care and for being there with me at all times. His uncanny ability to stay calm, hopeful, and patient in the midst of disaster, which has made the process of finishing a dissertation possible. You have been patient with me when I'm frustrated and annoyed☹, you celebrate with me when even the littlest things go right, and you are there whenever I need you to just listen. You are my best mentor who holded my hand and guided me to the right path. Thank you for the little things you've done like making the dinner when I worked late nights.

I would like to thank all my teachers from school till my PhD for imbibing good values and knowledge in me.

How could I forget to thank my niece, Laddoo, whose unconditional love brings smile on my face in any difficult situations.

I could not have completed my research without the support of all these wonderful people!

Last but by no means least I thank Lord Shiva for making my life so special.

Preeti Gupta………

# PREFACE

Rare earth chromites were known to be multiferroic but, the origin of ferroelectricity remain unexplored. Though, the ferroelectric in orthochromites was predicted in 1960's by Subba Rao but, still it is a topic of debate. In last decade, the research on chromites was driven towards exploring the origin of ferroelectricity by using theoretical and experimental tools. Theoretical understanding was developed in due course of time and ferroelectricity in the chromites was attributed to the local structural distortion and short range ordering. Apart from the controversies related to the ferroelectricity, the research on orthochromites was also headed towards the observed unique magnetic behavior. Few groups reported negative magnetization in some of the chromites. In 2010, our group also observed negative magnetization in $GdCrO_3$ nanoparticles which spark our interest to explore this feature in other chromites also. This thesis presents the study on rare-earth chromites.

In **chapter 1**, we will discuss about the background of the research work and also addresses the motivation behind studying the rare earth chromites (section 1). We will also talk about the stimulating features such as negative magnetization, exchange bias, magnetization switching and magnetocaloric effect which make rare earth chromites so interesting to study. Towards the end of the chapter, we will discuss the rationale behind choosing the rare earth chromites and scope of present investigation (section 2) in the thesis work.

**Chapter 2** will address the synthesis and structural properties of the rare earth chromites ($RCrO_3$, R = Dy, Sm and Yb). The detail synthetic procedures and characterization details will be presented.The characterization techniques such as X-ray diffraction, X-ray photoelectron spectroscopy and transmission electron microscopy will be used to confirm the single phase formation, stoichiometry and morphology & particle size of the compound. We will also briefly discuss about the possible role of different chelating agent and molar ratio of nitrate and citrate ions in the formation of pure phase and 2D nanoplate-like morphology.

Followed by the synthesis and structural studies, the optical properties of these rare earth chromites ($RCrO_3$, R = Dy, Sm and Yb) will be discussed in **chapter 3** by using Raman and UV-vis-NIR spectroscopy. To further elucidate the spin-phonon and magnetoelectric coupling in these rare earth chromites, we will carry out temperature dependent Raman and dielectric studies. The interest in this family of compounds has largely remain confined to

I

study the multiferroic properties. But, orthochromites are known to be p-type semiconductor rather than insulators which raised a probability of exploring its catalytic behavior. Thus, we will essentially explore the band-edge information and photocatalytic activity of these orthochromites.

Objective of **chapter 4** is to study the magnetic properties of the rare earth chromites ($RCrO_3$, R = Dy, Sm and Yb). The chapter 4 is divided into three sections. In each section we will address the unique and strange behavior such as negative magnetization (NM), exchange bias (EB) and magnetization switching in DCO, SCO and YCO polycrystallites, respectively. We will explain the possible reason behind the unique behavior in these orthochromites. We will also demonstrate the possible use of these orthochromites in thermomagnetic switches and spintronics applications.

In **chapter 5**, we present the thermal properties of rare earth chromites and explores the magnetocaloric effect by indirect measurements such as heat capacity and magnetic measurements. There is a need for discovering the new materials with large entropy change ($\Delta S_M$) and tunable operating temperature. The magnetic moment of rare earth ion is important in determining the entropy change in a magnetic system. If the magnetic moment is large then large MCE is expected. The $Dy^{3+}$ is having a large magnetic moment (10.6 $\mu_B$), hence, giant MCE is expected in DCO near the Dy ordering transition temperature. Thus, MCE will be investigated in the DCO nanoplatlets. Whereas, $Sm^{3+}$ with small magnetic moment (0.84 $\mu_B$) is not expected for giant MCE in SCO. But, the spin reorientation transition in SCO polycrystallites is anticipated to give inverse MCE leading to the enhance refrigeration efficiency. Thus, SCO will be explored to observe the coexistence of inverse and normal MCE in a single material. Lastly, YCO with $Yb^{3+}$ magnetic moment (4.5 $\mu_B$ almost half of $Dy^{3+}$) will also be explored for plausible MCE. We will also derive the adiabatic change in temperature which is one of the crucial MCE parameter from technological point of view.

Finally, **chapter 6** will describe the conclusion of the overall work presented in this thesis. The future direction of this thesis also presented in this chapter.

# <u>LIST OF ABRREVIATIONS</u>

1. Ferroelectricity      FE
2. Ferromagnetism      FM
3. Antiferromagnetic      AFM
4. Magnetoelectric      ME
5. Canted antiferromagnetic      $c$AFM
6. Paraelectric      PE
7. Dzyaloshinskii-Moriya      DM
8. Jahn-Teller      J-T
9. Virtual charge transfer      VCT
10. X-ray diffraction      XRD
11. Transmission electron microscope      TEM
12. Selected area electron diffraction      SAED
13. Ultraviolet visible spectroscopy      UV-vis
14. Methyl orange      MO
15. X-ray photoelectron spectroscopy      XPS
16. Physical Property Measurement System      PPMS
17. Vibrating sample magnetometer      VSM
18. Zero field-cooled and Field-cooled      ZFC-FC
19. AC measurement system      ACMS
20. Néel temperature      $T_N$
21. Spin reorientation temperature      $T_{SR}$
22. Compensation temperature      $T_{comp}$
23. Crossover temperature      $T_{cross}$
24. Magnetization vs. field      M-H

# CONTENTS

# Chapter 1

# Introduction

**This chapter is an introduction to the basic concepts of magnetic and electrical ordering in multiferroic materials. The rationale behind focused interest in orthochromites is also discussed in detail. The unique properties such as negative magnetization, exchange bias, and magnetization switching, are described in-depth. The current state of art of these orthochromites is discussed. Towards the end of this chapter, we have presented the outline of the thesis work.**

## Section 1. Introduction

## 1.1    Overview of multiferroics:

During the past decades, there has been an immense interest in the field of complex oxides owing to the interplay of various degrees of freedom such as spin, charge, orbital along with the lattice, leading to the new physics.[1] The coexistence of broken time reversal and spatial inversion symmetries lead to spontaneous magnetization and ferroelectric polarization in many materials.[1] The coexistence of these order parameters is limited to a few sets of materials due to the specific requirement posted by the ferroelectric polarization and magnetic order in the electronic structure of the material.[1] The interplay between these order-parameters leads to an interesting phenomenon known as 'multiferroicity'. The term "multiferroics" was coined by H. Schmid[2] in 1994, where these materials exhibit two or more order parameters in a single phase material or composites (**Figure 1**). Previously, the term multiferroics was used for the materials where, ferromagnetism (FM), ferroelectricity (FE) or ferroelasticity coexist. Recently the terms - antiferromagnetism (AFM) or ferrimagnetism have also been included as an order parameters.[1,2]
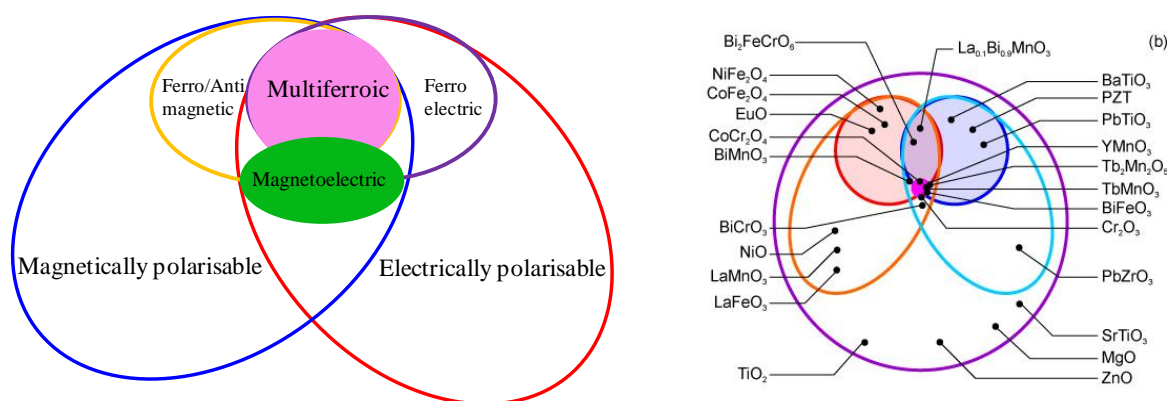


*Figure 1. Schematic of multiferroic materials and their functionalization.*[1,3]

It is well-known that most of the ferroelectrics are transition metal oxides, and have an empty $d$-orbitals where, the collective shift of cations and anions induces electric polarization, in contrast, the magnetic ordering requires partially filled $d$-orbital of

transition metal ions.[1] Consequently, these two properties were earlier thought to be mutually exclusive in a single phase material.[1] There are certain material in which these two properties coexist and are known as magnetoelectric (ME) materials. The term "magnetoelectric" was coined by P. Debye in 1926.[4] The ME coupling is described as an influence of electric (magnetic) field on the magnetization (electric polarization) and vice-versa. Thus, there is an urge to search for the new multifunctional materials where these order parameters may coexist. Due to the potential applications in various nanoscale devices, nanosize effects on the magnetic and ferroelectric properties of multiferroics materials were studied in past several decades. Till date, one of the most widely studied material in bulk single crystal, polycrystalline and thin film form is bismuth ferrite (BFO), which is a room temperature (RT) multiferroic with strong ME coupling.[5-10] The BFO has a G-type AFM ordering ($T_N \sim 643$ K) with slightly canted moments due to Dzyalonshinskii-Moriya (D-M) interaction. It shows the spontaneous polarization $\sim 90$ $\mu C/cm^2$ below its ferroelectric Curie temperature ($T_C$) $\sim 1100$ K.[7-10] The BFO shows a typical AFM behavior with zero coercivity in bulk and below the particle size of $\sim 62$ nm, it shows a sizable hysteresis and finite coercivity due to the breaking of helical ordering or incomplete rotation of the spins along the AFM axis which give rise to higher magnetization.[11,12] Beforehand, we get acquainted with the multiferroics, it is essential to understand the basic phenomena *i.e.* ferroelectricity, ferromagnetism, antiferromagnetism which is responsible for the multiferroic property in a material.

## 1.2 Ferromagnetism:

Magnetism was first observed in magnetite around 600 B.C.[13] Except diamagnetism, magnetism in a material arises due to the unpaired electrons. It is mainly observed in transition metals (unpaired *d*-electrons) and lanthanides (unpaired *f*-electrons), respectively. The random orientations of unpaired spins makes a material paramagnetic (PM) and parallel alignment leads to ferromagnetism (FM). The FM materials respond strongly to the external magnetic field and possess spontaneous magnetization. FM can be explained by two phenomenological theories *i.e.* Curie and Weiss[14] and Stoner band theory.[15] According to Curie-Weiss theory, at all

temperatures, local magnetic moments exist in a solid. Below $T_C$, the moments align in accordance with the external field to give rise to FM. Whereas, above $T_C$, they get randomized and disordered by thermal energy with no net magnetization. According to the Stoner band theory, below $T_C$, unequal population of up and down spins leads to the net magnetization whereas above $T_C$, equal population gives no net magnetization. Although, most of the known FM materials are metallic but insulating FM compounds do exist and are explained via. superexchange (SE) interaction. In magnetic insulators, exchange interaction is predominantly caused by SE, which is due to the overlap of the localized orbitals of the magnetic electrons with intermediate ligands via. oxygen in the oxide materials. The 180° SE interaction in M-O-M bond angle gives strong AFM behavior whereas, 90° leads to the FM and is much weaker. The SE interaction was elucidated by a set of empirical rules developed by Goodenough[16] and Kanamori[17] dictated by the ligand field theory. These rules were also related to the Anderson's SE theory.[18]

## 1.3    Ferroelectricity:

Ferroelectricity (FE) was discovered in Rochelle salt by J. Valasek in 1920. It is defined as the spontaneous alignment of electrical dipoles in a material with reversible polarization. All FE materials are pyroelectric and all pyroelectric materials are piezoelectric but all the pyroelectric materials are not FE. Based on the mechanism of symmetry breaking, the FE materials are classified into proper and improper ferroelectrics and are shown in **Table 1.1.**

|  | **Mechanism of symmetry breaking** | **Materials** |
|---|---|---|
| **Proper** | Covalent bonding between $3d^0$ transition metal (Ti) and oxygen | $BaTiO_3$, $PbTiO_3$ |
|  | Polarizability of $6s^2$ lone pair (Bi) | $BiFeO_3$, $BiMnO_3$ |
| **Improper** | Structural transition (R= Rare earth) | $h$-$RMnO_3$ |
|  | Charge ordering | $LuFe_2O_4$ |
|  | Magnetic ordering | $o$-$RMnO_3$, $RMn_2O_5$ |

*Table 1.1. Types of ferroelectricity on the basis of mechanism of symmetry breaking.*[19]

The FE materials can be used to store information and the best example is FE capacitors which are used in the FE random access memory (FERAMs) and radio frequency identification (RFID) cards.[20] The ferroelectricity is widely known and studied in perovskite $ABO_3$ type (A = rare earth and B = transition metal) material. The non-centrosymmetry in perovskites may arise due to various factors, which include local structural distortion, displacement of cations *etc*. The well-known example of a FE material in $ABO_3$ type is barium titanate ($BaTiO_3$) as shown in **Figure 2**.[21]
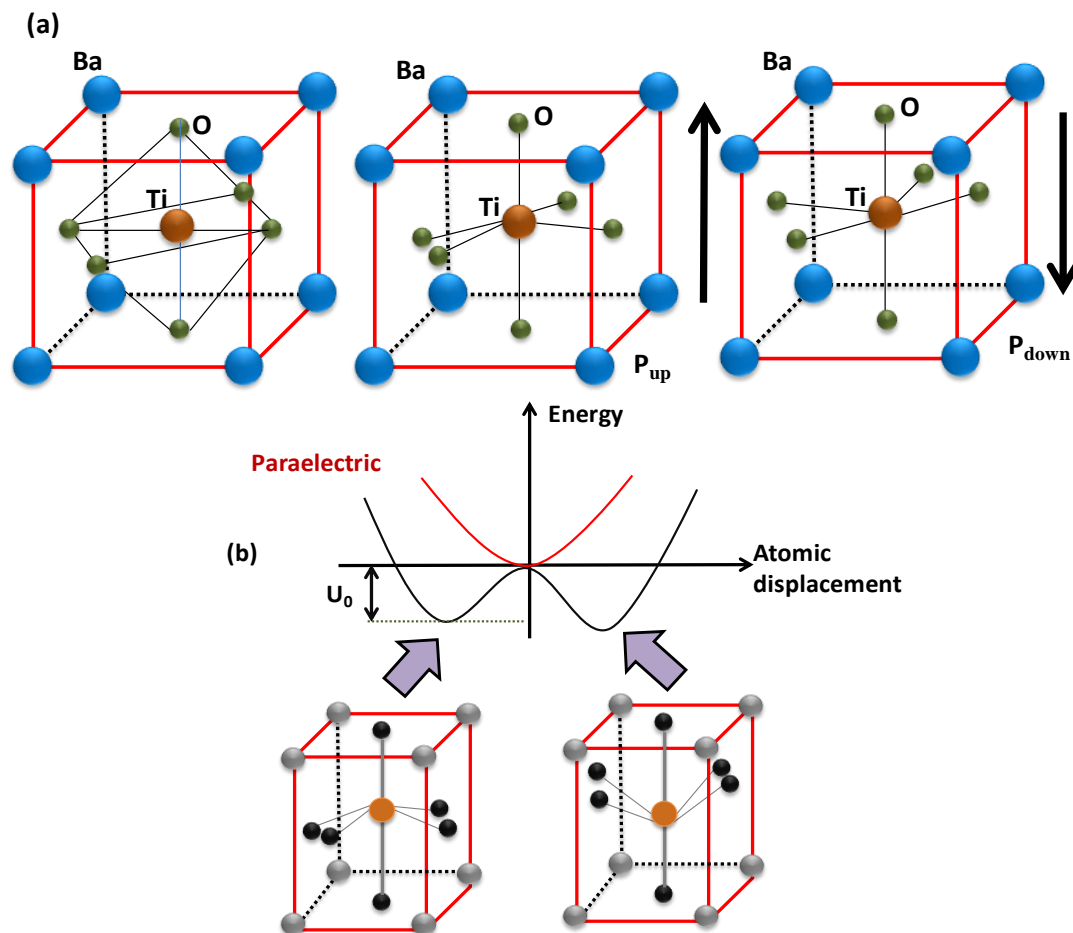


*Figure 2. (a) Crystal structure of BaTiO₃ showing up and down polarization (b) energy (U) against polarization (P).*

*http://mini.physics.sunysb.edu/~mdawber/research.htm*

Other FE materials such as lead titanate, lead zirconate titanate, lead lanthanum zirconate titanate *etc.* have been widely studied and their excellent dielectric properties make them promising candidate for electronics industry.

## 1.4    Antiferromagnetism:

Similar to ferromagnets, the antiferromagnetic (AFM) materials become PM above critical temperature (Néel temperature $T_N$). Louis Néel[22] discovered AFM ordering in magnetic systems. In perovskites, the AFM ordering is classified into three categories (**Figure 3**) based on the coupling.[23]

1) **A- type:** The intra plane coupling is FM while, inter plane is AFM.

2) **C-type:** The intra plane coupling is AFM and inter plane is FM.

3) **G-type:** Intra plane and inter plane coupling is AFM.



Ferro         A-type         C-type         G-type
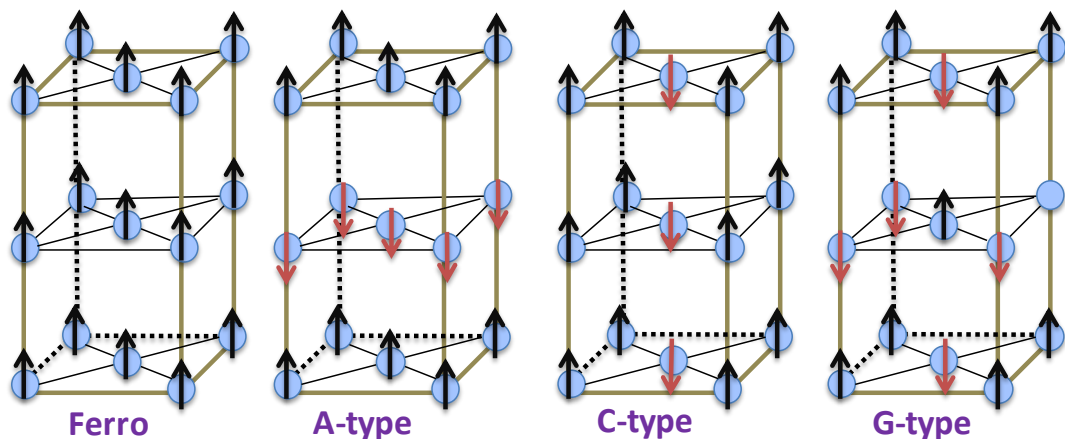
*Figure 3. Classification of AFM ordering* [23]

The AFM material can couple with FM sublattices resulting in the pinning of spins at the AFM/FM interfaces leading to an important phenomenon known as exchange bias (EB). This  unique behavior of AFM/FM sublattices can be used for promising applications such as spintronics and data storage devices.[24–26]

## 1.5    Why are there few multiferroic materials?

The coexistence of the two properties *i.e.* ferroelectricity (FE) and ferromagnetism/ antiferrormagnetism (FM/AFM) discussed above are mutually exclusive as they have an opposite requirement in terms of electronic structure. The multiferroic field was known from late 60's but the boom in multiferroic research occurred after 2000 as shown in **Figure 4**.[27]
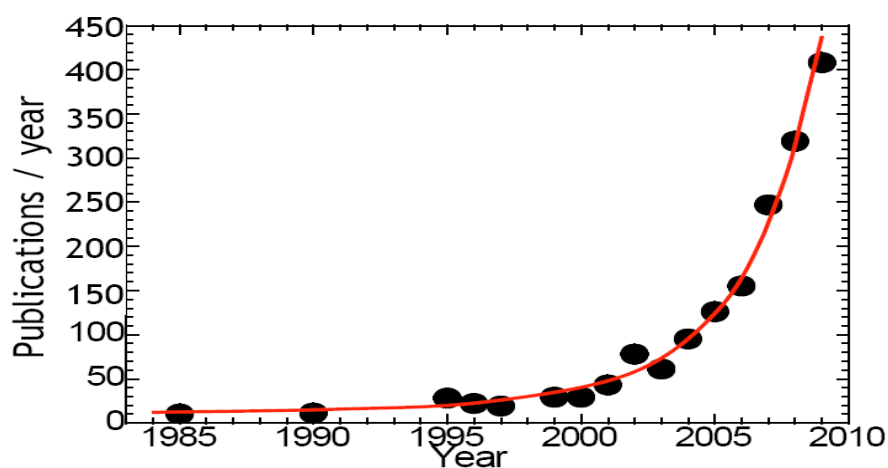


***Figure 4. Huge leap in multiferroics research after the year 2000.***[27]

The multiferroic $YMnO_3$ shows the AFM and FE ordering with transition temperature $T_N \sim 80$ K and $T_C \sim 914$ K, respectively.[28,29] Here, FE in $YMnO_3$ is mainly due to the $MnO_5$ tilting. Similarly, $BiFeO_3$, $BiMnO_3$, $BaTiO_3$-$CoFe_2O_4$ also shows multiferroic behavior.[28,30–33]In  general, there are wide classes of materials which are multiferroic such as ferrites, manganites, transition metal oxides, chromites *etc*.[8,34–37] As magnetism and ferroelectricity (**Figure 5**) exclude each other and this behavior is termed as $d^0$ vs. $d^n$ problem.[138]
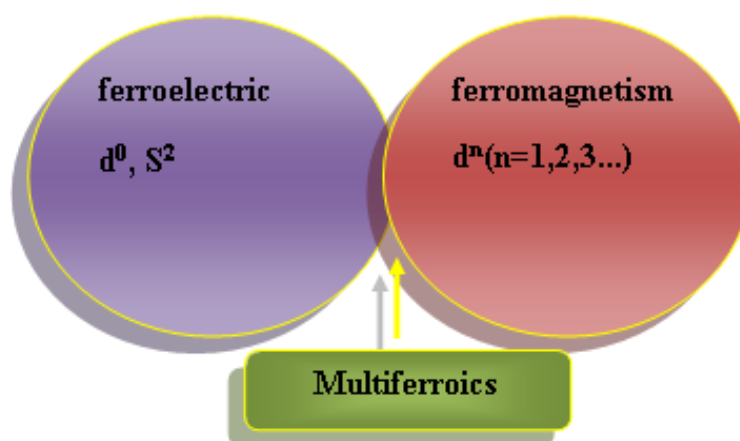
*Figure 5.   Schematic showing that ferroelectricity and ferromagnetism exclude each other.*

It has been long argued that $d^0$-ness favors lattice distortion, giving rise to the FE polarization. Besides $d^0$-ness, size of central cation also plays an important role in lattice distortion. On the other hand, magnetism observed in the FE materials is due to the intrinsic lattice defects in a crystal.    Depending on the mechanism of ferroelectricity  in the multiferroic materials, they are categorized as type I and type II multiferroics, respectively and shown in **Table 1.2**.[28] Type I multiferroics are those where magnetism and FE exist independently. In the type II multiferroics, magnetism causes FE and vice-versa along with strong coupling between them. In this context, the ME multiferroics and enhancement of ME coupling was addressed in detail by Tokura.[39]

| | Mechanism | Description | Examples |
|---|---|---|---|
| **Type I** | | | $BiFeO_3$, $BiMnO_3$ |
| | Lone-pair effects | Mixing between the (ns)2 ground state and a low-lying (ns)1 (np)1 excited state | |
| | Geometric frustration | Buckling of MnO5 pyramids & displacement of Y | $YMnO_3$ |
| | Charge ordering | Certain 'non-centrosymmetric' arrangements of ions  induce ferroelectricity in magnetic materials | $LuFe_2O_4$ |

| Type II | Magnetic ordering | Ferroelectricity is induced by magnetic long-range order in which the arrangement of magnetic dipoles lacks reflection symmetry | $TbMnO_3$, $DyMnO_3$, $TbMn_2O_4$ |
|---------|-------------------|------------------------------------------------------------------------------------------------------------------------------|-----------------------------------|

*Table 1.2. Types of multiferroics on the basis of microscopic sources of ferroelectricity in multiferroic materials.*

## 1.6    Rare earth chromites:

Rare earth chromites ($RCrO_3$; R= rare earth, Cr= chromium) are isostructural to rare earth ferrites and orthorhombic rare earth manganites.[40] $RCrO_3$ crystallizes in a distorted orthorhombic structure with the space group, *Pbnm* or *Pnma*.[37,41,42] In general, orthochromites are G-type AFM with $T_N$ varying from ∼ 110 K to ∼ 210 K.[42–44] The orthochromites are represented by G-type configuration preferably $\Gamma_1$, $\Gamma2$ and $\Gamma_4$ as shown below (**Figure 6**).[40,45]

**Γ1 (Ax, Gy, Cz)        Γ2 (Fx, Cy, Gz)        Γ4 (Gx, Ay, Fz)**
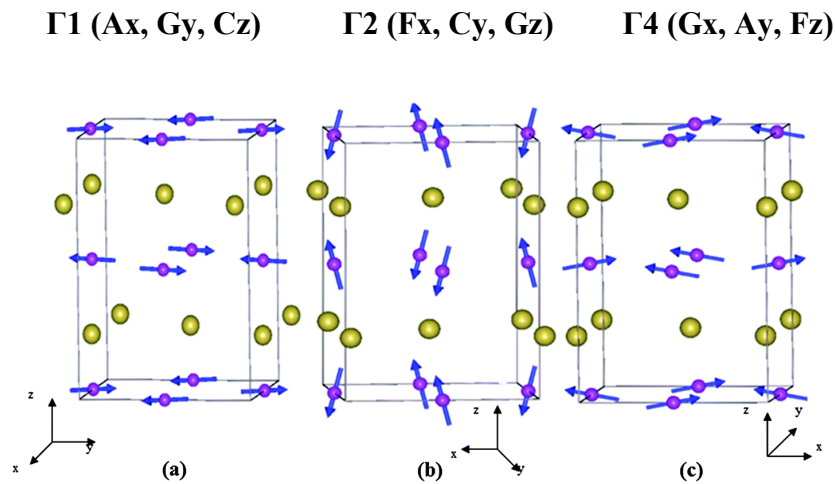


*Figure 6. G-type antiferromagnetic configuration having **Γ1, Γ2, and Γ4** spin structure with Pbnm symmetry.*[40,45]

Depending upon the magnetic character of R-site element, the magnetic structure of orthochromites can be $\Gamma_4$ or $\Gamma_2$.[40,45] However, at low temperatures, some of the $RCrO_3$ show spin reorientation (SR) transition and undergo change in spin structure from $\Gamma_2$

to $\Gamma_1$ due to the magnetic interaction between the $R^{3+}$ and canted $Cr^{3+}$ spins.[46] Also, few orthochromites such as (Er, Sm, Gd, Nd) CrO$_3$ exhibit SR transition and they can be either continuous or discontinuous.[43,44,47–49]

In addition to the multiferroic behavior, the interesting feature such as negative magnetization (NM) appears just below the $Cr^{3+}$ AFM ordering temperature along with weak FM in orthochromites.[43–45] The break in the resistivity plot with temperature hint towards the possibility of FE in RCrO$_3$ which was further confirmed by pyroelectric measurements and was first discussed by Subba Rao *et al.* in late 60's.[50] Later, Tripathi and Lal have studied the transport property of RCrO$_3$ and showed that orthochromites are p-type semiconductor rather than insulator.[51] The orthochromites are known to be centrosymmetric thus, origin of ferroelectricity is still under debate.[45] Different explanations have been put forth for the observed FE in orthochromites such as local symmetry breaking, local structural distortion, and exchange striction between rare earth and chromium moments. However, the origin and mechanism of ferroelectricity in rare earth chromites is still a topic of debate. The small polarization values of $\sim$ 2 μC/cm$^2$ and 0.35 μC/cm$^2$ are reported for YCrO$_3$ and LuCrO$_3$, respectively.[35,37]
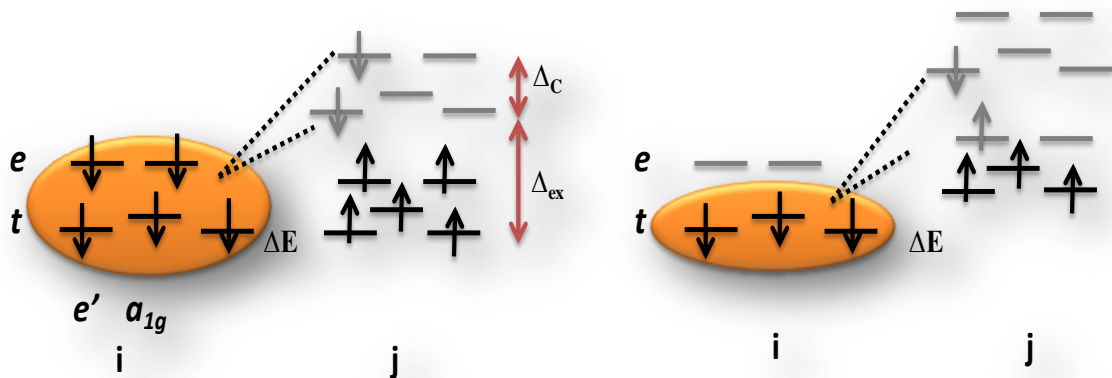


*Figure 7.   Schematic diagram of the hybridization effect on the virtual charge transfer for the superexchange interaction in perovskites RCrO₃ and RFeO₃. Here Δc stands for the crystal-field splitting, Δₑₓ is the exchange splitting, ΔE= Eₐ₁g− Eₑ* .[52]

In 2007, a new concept of local non-centrosymmetry emerged as a key feature in understanding the origin of FE in orthochromites.[45] Later in 2010, Zhou *et al.* showed that the effect of $t_{2g}$-$e_g$ hybridization due to structural distortions and virtual charge transfer (VCT) (schematic shown in **Figure 7**) similar to $RFeO_3$ are responsible for the dramatic change in $T_N$ across the $RCrO_3$ family.[52]

## 1.7    Why are rare earth chromites so interesting?

For the futuristic materials, multifunctional properties in a single phase are required. Recently, few rare earth chromites have shown interesting behavior such as NM and EB which are of technological importance in the field of spintronic and memory devices.[24,25,43,53–56] The key issue is to investigate the thermally and field assisted NM and EB in single phase $RCrO_3$ which are not explored so far. The below schematic show the key feature in rare earth chromites. (**Figure 8**)
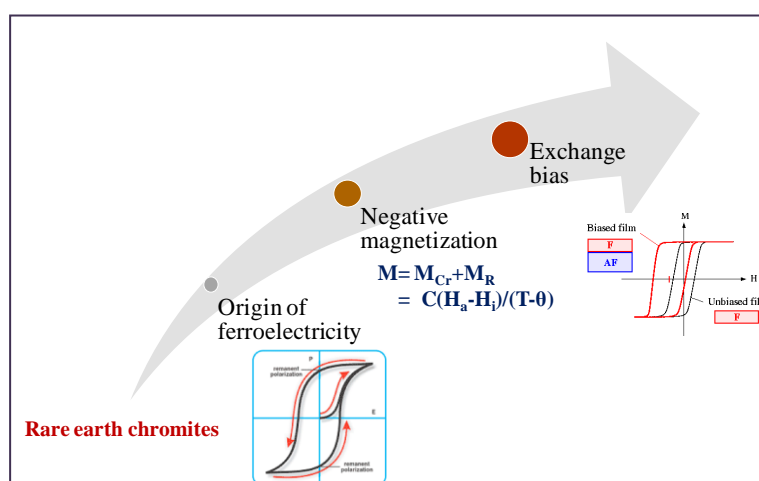


*Figure 8. Schematic showing the interesting features of rare earth chromites.*

NM can be further used to study the switching characteristic of the material. In addition, though, the study in $RCrO_3$ largely remained confined to multiferroic properties, they can be classified as semiconductors rather than insulators.[51] This has attracted further attention to study their photocatalytic and other light harvesting applications such as solar photovoltaics. These materials have an advantage over conventional photocatalytic materials such as titania as their rich optical nature

provides absorption bands in visible range also (in contrast to pure titania whose edge lies in UV range).[57] Below, we will discuss about the interesting magnetic anomalies which has been observed in some of the orthochromites and proposed to exist in others such as $DyCrO_3$, $SmCrO_3$ and $YbCrO_3$ polycrystallites. In addition, their applications in hydrogen generation using water splitting remain unexplored. The above mentioned features such as NM, magnetization switching, EB, photocatalytic activity encouraged us to study and explore the unique behavior in orthochromites.

## 1.8    Interesting behavior in orthochromites:

### 1.8.1  Negative magnetization/ magnetization reversal:

In conventional understanding, the magnetization is always assumed to be positive for PM, FM, and AFM materials and negative in case of diamagnetic contribution.[56] But there exist certain class of magnetic materials which possess negative magnetization (NM) and it is not due to the diamagnetic contribution. The NM is also referred as magnetization reversal (MR). In 1948, Louis Néel proposed a theory on NM and it was first observed in spinel ferrites.[22] The NM is observed when the system is cooled to a low temperature in presence of external applied magnetic field or in zero field cooled (ZFC) condition. Conventionally, NM is observed when the system is cooled under field (FC) but recently, ZFC NM was observed in orthochromites which is an example of a unique case.[53,56] Though, the understanding of NM is still very complex and is different for different systems, it has been widely observed and reported in literature in many magnetic materials such as perovskites, spinel ferrites, molecular magnets, garnets, intermetallic alloys and multilayers.[55,56,58–63]

There are intrinsic parameters such as magnetocrystalline anisotropy which couples and correlate the crystal structure of the material and the magnetization vector giving rise to NM in a material.[64,65] Since, it is an intrinsic property of the material, it should be a dominant factor in polycrystalline or single crystal materials. For example, the easy axis of magnetization (**Figure 9**) is different than the hard direction of magnetization and although easy directions coincide with crystallographic axes of

symmetry, it is important to note that there is no way of predicting easy directions from crystal structure alone.
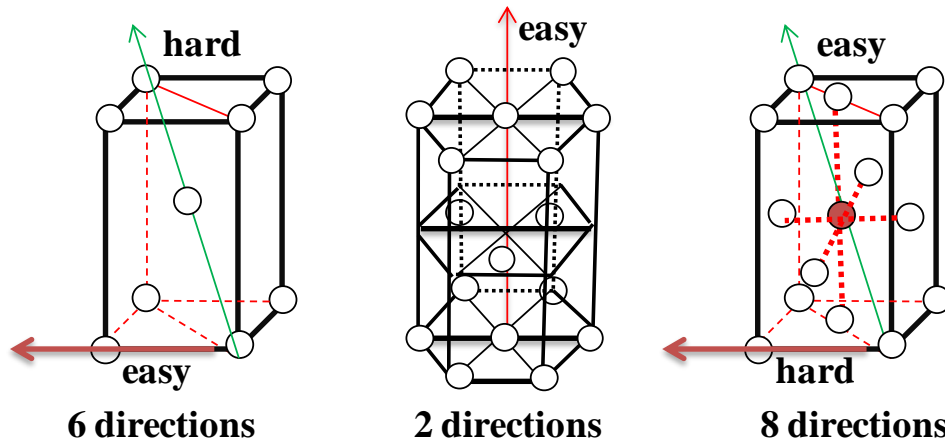


*Figure 9. Examples of easy and hard directions* [65]

This magnetocrystalline anisotropy arises due to the spin-orbit coupling and is measured in terms of energy required to magnetize a material in a particular direction rather than in other direction.[64] The NM originates in a magnetic material due to the competition between the Zeeman energy and magnetocrystalline anisotropy.[53,56,66] There are various other sources for the origin of magnetic anisotropy which includes shape anisotropy, exchange anisotropy and magnetoelastic anisotropy.[22,64,65] In nano regime, the shape anisotropy plays a key role and arises in asymmetrical particles creating one or more easy axis. In needle shaped particle, the easy axis is towards the long axis of the grain, whereas, spherical particles do not contribute to shape anisotropy.[56] Another important parameter is exchange anisotropy which was discovered by Meiklejohn and Bean in 1956.[64] It occurs in an AFM/FM material as a result of the shift in the soft magnetization curve due to the hard magnetization behavior of AFM. It is a more generalized phenomenon in the thin films and interfaces.[26] The strong exchange coupling is developed when the FM layer is cooled below $T_N$ of the AFM, resulting in the shift of the magnetization curve *i.e.* exchange bias effect.[54] In literature, the possible reasons (**Figure 10**) for the NM in magnetic material have been pinned-down into categories such as: [54,56]

- "Negative exchange coupling among FM sublattices e.g. $Co_2VO_4$, $Co_2TiO_4$

- Negative exchange coupling among canted AFM sublattices e.g. Vanadates such as $(La, Y, Sm, Nd)VO_3$ , $BiFe_{0.5}Mn_{0.5}O_3$, $(Cr_{0.7}Ti_{0.3})_5S_6$

- Negative exchange coupling among FM/canted-AFM and  PM sublattices e.g. $La_{1-x}Gd_xMnO_3$, $Nd_{0.96}Gd_{0.75}MnO_3$, $SmMnO_3$, $ErCo_{0.5}Mn_{0.5}O_3$, $GdCrO_3$

- Imbalance of spin and orbital moments e.g. $(Sm_{1-x}Gd_x)Al_2$, $Sm_2Al$, $SmNiAl$

- Interfacial exchange coupling between FM and AFM phases  e.g. $NiFeF_2$, Gd-Fe, Gd-Co, Gd-CoNi multilayers, $Fe_3O_4/Mn_3O_4$ superlattice structures"
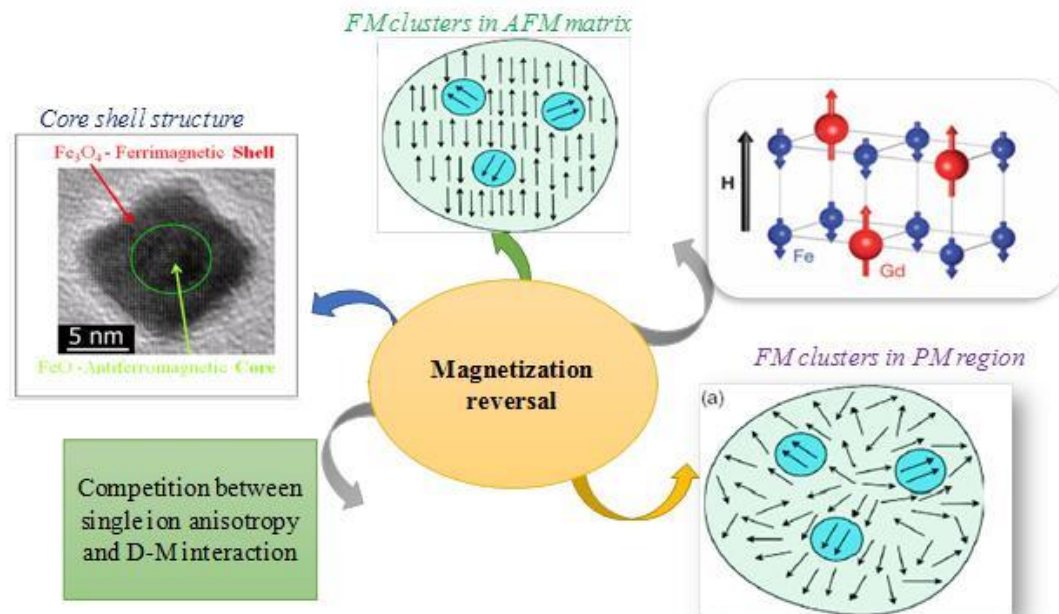


***Figure 10. Schematic representing the possible origins of magnetization reversal.***

## 1.8.2  Negative magnetization (NM) in rare earth chromites:

The NM in $RCrO_3$ is mainly due to the negative exchange coupling between the canted-AFM and FM sublattices. In orthochromites, generally, three possible magnetic interactions are dominant *i.e.* $R^{3+}$–$R^{3+}$, $R^{3+}$–$Cr^{3+}$, $Cr^{3+}$–$Cr^{3+}$. The $Cr^{3+}$ spins interact antiferromagnetically via. oxygen and being the strongest, shows up at a relatively higher temperature. Whereas, $R^{3+}$ spins starts ordering at low temperature, below 10 K. [43] There are other complex oxides which shows NM such as $La_{1-x}Gd_xMnO_3$, $Nd_{0.96}Ce_{0.04}MnO_3$, $SmMnO_3$, $GdNi_{0.3}Mn_{0.7}O_3$, $GdCo_{0.3}Mn_{0.7}O_3$ *etc*.[56,67–71] In orthochromites, NM is due to fact that, the canted AFM spins induces internal magnetic field on PM spins which is more as compared to the applied magnetic field giving NM.[43,44,56] The above explanation holds true for $GdCrO_3$.[43,44] In $GdCrO_3$, the bulk (**Figure 11**) as well as nanocrystalline sample (**Figure 12**) possess NM when system is field cooled at 100 Oe external applied magnetic field.[43,44,56,72]
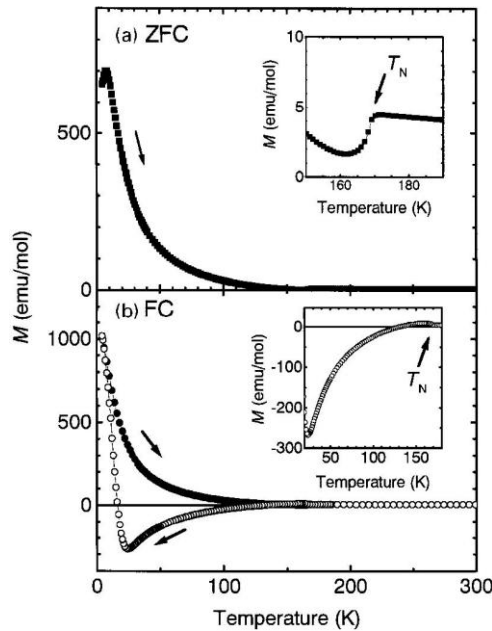


*Figure 11. (a) ZFC and (b) FC magnetization curves for GdCrO₃ with an applied field of H=100 Oe (b), filled (d) and open (s) circles stand for FC (H) and FC (C) modes, respectively.* [72]

In addition to NM, the GdCrO$_3$ nanoparticles shows T$_{comp}$ (temperature at which magnetization is zero) at two different temperatures which can be correlated with the core shell structure of the particles while in bulk, it is assumed to be due to the antisymmetric D-M interaction.[43,56]
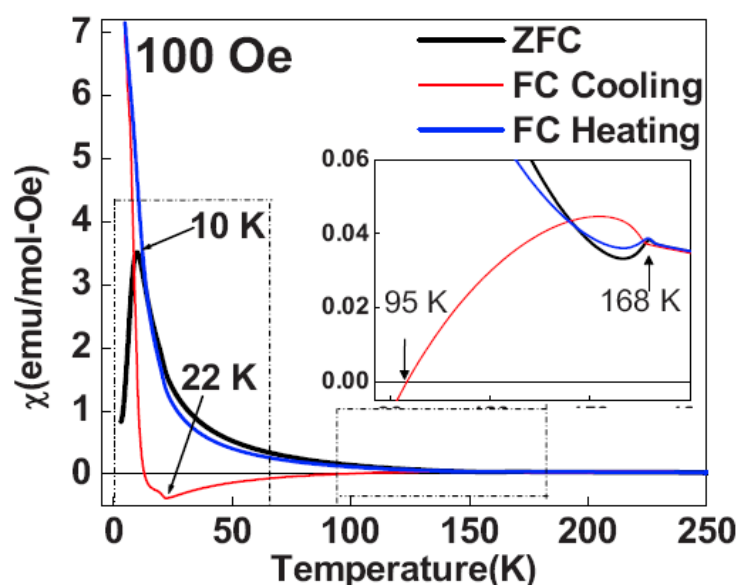


*Figure 12. Zero-field cooled and field cooled (both in cooling and heating cycle) curves at 100 Oe field. The inset shows the zoom view of the selected temperature region highlighting the negative magnetization.*[43]

Similarly, above explanation of NM holds true in the case of YbCrO$_3$,[73] HoCrO$_3$,[74,75] TmCrO$_3$[25] and SmFeO$_3$[76], respectively. The temperature dependences of the sublattices with respect to the canted AFM $Cr^{3+}$ spins in compounds such as La$_{1-x}$Pr$_x$CrO$_3$ (0.2≤$x$≤0.8),[24,56,60] La$_{0.75}$Nd$_{0.25}$CrO$_3$,[56,63] La$_{0.5}$Gd$_{0.5}$CrO$_3$,[56,77] and La$_{0.1}$Gd$_{0.9}$CrO$_3$[56,78] results in NM. "In general NM/MR occurs in a material having core shell structure; structural transitions, ferrimagnetic ordering between two sublattices, extrinsic effects like weak FM clustering, competition between single ion anisotropy and D-M interaction."[53,56,66,74,76] Based on the literatures and understanding of NM, one can expect NM in other rare earth chromites also. Recently, Lei *et al.* has studied the RCrO$_3$ (R= La, Pr, Sm, Eu, Gd, Dy, Ho, Y, Er, Tm, Yb, Lu) synthesized by hydrothermal method and noticed the NM behavior in some of the chromites.[79]

### 1.8.3  Magnetization Switching:

The temperature dependent reversal of magnetization attracted much attention due to its application in thermomagnetic switches and data storage devices.[56] NM with the change in temperature was observed in many magnetic materials which include orthochromites, orthovanadates, and orthoferrites.[25,60,72,80–84] The switching of magnetization with the change in the direction of applied external magnetic field is very well known but only few systems exist where, by merely changing the temperature and magnitude of external magnetic field, magnetization switching is possible.[25,85] For this, it is essential to have two or more compensation temperature ($T_{comp}$) in a magnetic system. In case of $TmCrO_3$, (**Figure 13**) the magnetization switching was observed where, NM can be flipped below the $T_{comp}$ by merely changing the magnitude of the applied magnetic field.[25] The magnetization switching observed in $TmCrO_3$ without flipping the direction of magnetic field offers a greater advantage over other magnetic materials to fabricate new memory devices.[25]
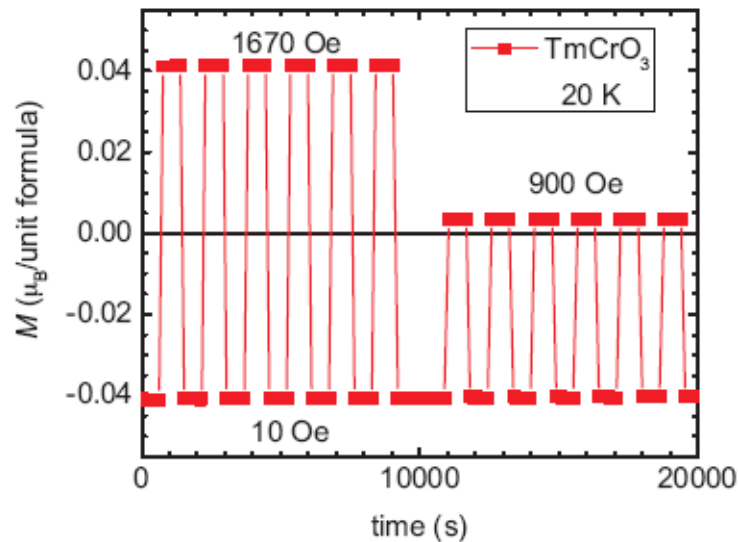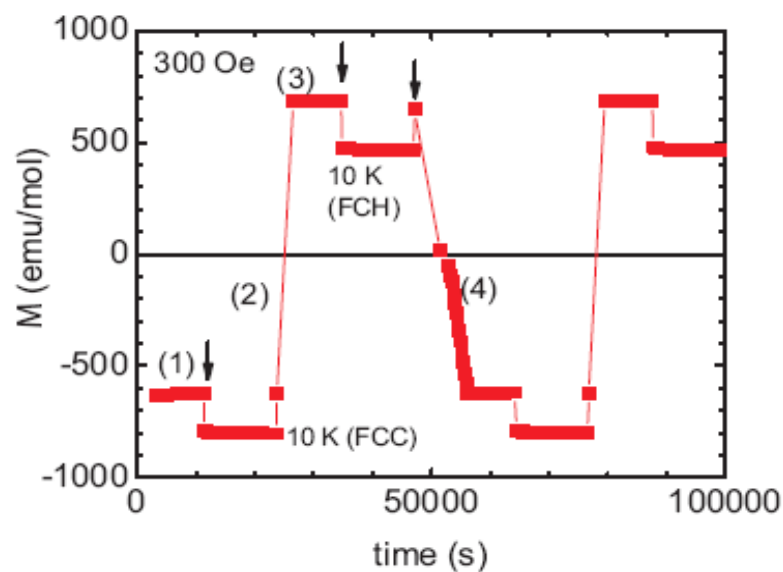
*Figure 13. External magnetic field and temperature induced magnetization switching in TmCrO₃.*[25]

Similarly, $YFe_{0.5}Cr_{0.5}O_3$ also shows magnetization switching (**Figure 14**) characteristic at 230 K under various applied magnetic field.[86]
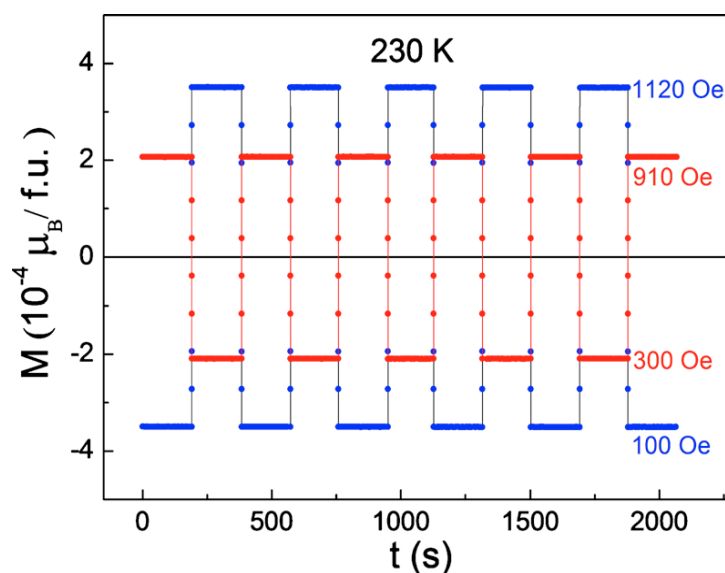


*Figure 14. Switching of magnetization between negative and positive values at 230 K under various magnetic fields for YFe₀.₅Cr₀.₅O₃.*[86]

This unique property was found in some of the chromites which may be well suited for the development of non-volatile memories.[85] As $RCrO_3$ is associated with the NM, magnetization switching is an interesting and unique characteristic property which needs to be explored and employed for various application such as thermomagnetic switches, non-volatile memories *etc*.[26,54,56]

## 1.8.4  Exchange bias:

Exchange bias (EB) is the shift of hysteresis curve away from origin, making it asymmetric as shown in **Figure 15**. EB was discovered in Co particles by Mieklejohn and Bean in 1956.[26,54,64,87] EB is associated with the anisotropy created between the AFM/FM interfaces. The exchange anisotropy can be induced externally when the system is field cooled (FC) *i.e.* conventional EB or internal factors also plays an important role. However, few systems show EB in ZFC condition also.[26,54,87] The exchange bias field ($H_{EB}$) is affected by intrinsic and extrinsic parameters which includes spin reorientation (SR), anisotropy, roughness, crystallinity, thickness of AFM layer, grain size, interface impurity layers, AFM domains *etc*.[26] The EB field vanishes above $T_N$ and becomes zero. In some case, the EB vanishes above blocking temperature $T_B$, where sometimes $T_B = T_N$. In general, EB is associated with the AFM/FM interfaces in a system but is not limited as it has expanded to AFM-ferrimagnet, FM-ferrimagnet *etc*.[26,54,88] It can occur in small particles, inhomogeneous materials, coated AFM single crystal, thin films, oxide AFM, metallic AFM, ferrimagnets *etc*.[26,54] EB was also observed in FM/FM interfaces in a sandwiches of Ni-Cu-Co and Ni-Fe-Co and were further probed using magneto-optic kerr effect (MOKE) and X-ray magnetic circular dichroism (XMCD).[89] In general, we can represent EB as shown below:
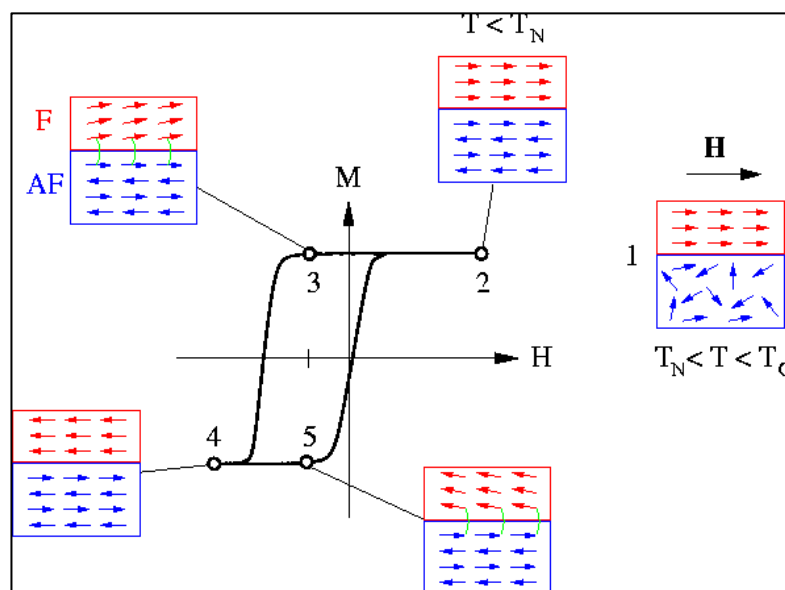
*Figure 15.  Schematic diagram of the spin configuration of an FM/AFM bilayer system showing exchange bias effect.*

*(Ref: http://magnet.atp.tuwien.ac.at/gallery/exchbias/intuitive.html)*

The qualitative information about the $H_{EB}$ can be depicted by training effect, coercivity, cooling field and perpendicular coupling.[87] The EB can be positive or negative depending on the parallel or perpendicular coupling of easy axis of FM and AFM spins, respectively.[26,90] Recently, few groups have observed EB in orthochromites.[24,25,87] It is quite interesting to note that few of the chromites show EB while others don't, which is still not understood. The widely used model for EB is core-shell model.

Giri *et al.*[90] have proposed a model for EB in $Sm_{0.5}Ca_{0.5}MnO_3$ considering core-shell structure where, core is expected to be AFM and outer uncompensated spins forms shell. The schematic for EB in core-shell structure is shown in **Figure 16**.
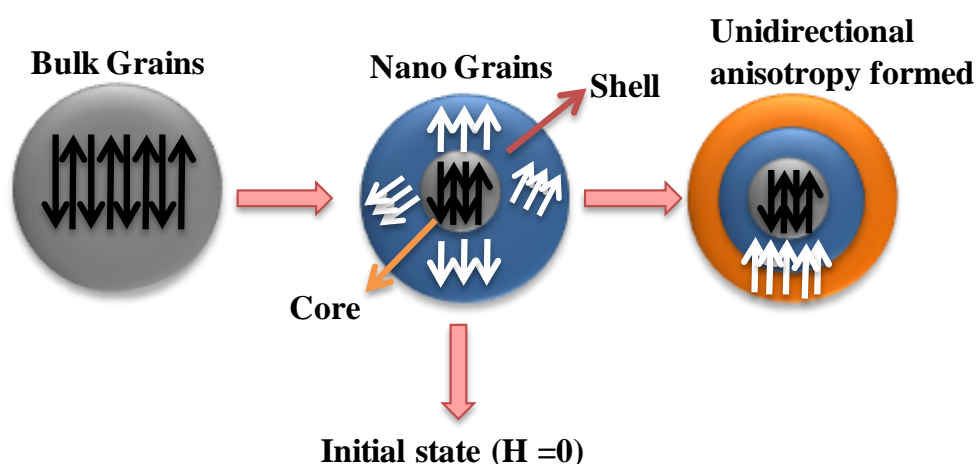
*Figure 16. The schematic representation of the phenomenological model for CO/AFM bulk manganites and the corresponding nanograins.*[90]

Few systems such as $GdCrO_3$,[43] $LaCr_{0.8}Mn_{0.2}O_3$,[53] $TmCrO_3$,[25] and $SmCr_{1-x}Fe_xO_3$[91] also shows NM as well as tunable EB. Earlier, we reported EB in $DyFeO_3$ and explained it by core-shell model.[92] However, the most widely studied material for its structural and magnetic properties in orthochromites is $LaCrO_3$.[42,93,94]

Interestingly, EB is known to be associated with NM with the relation $H_{EB}$ = - M. The conventional EB *i.e.* field cooled EB is well known but, recently, ZFC EB is observed in few magnetic systems due to the presence of multiple phases within a single material. ZFC EB was considered to be an artifact until a model came up for positive ZFC EB.[87] The ZFC EB was observed in $Ni_{80}Fe_{20}/Ni_{50}Mn_{50}$ alloys along-with a sign reversal of EB after FC.[95] The tunability of EB is very rare as most of the works address the positive/ negative EB. But, in orthochromites we can expect the tunability of EB with change in temperature and magnetization reversal, as some of the orthochromites have two $T_{comp}$.

## 1.8.5 Magnetocaloric effect:

$RCrO_3$ material are also presumed to show magnetocaloric effect (MCE) as the rare earth spins order at low temperatures making them a suitable candidate for low temperature magnetocaloric refrigeration applications. MCE of a system is broadly

defined as the adiabatic change in temperature ($\Delta T_{ad}$) or isothermal entropy change ($\Delta S_M$) upon application of magnetic field.[96] MCE was initially used to achieve sub-Kelvin temperatures by adiabatic demagnetization of PM salts.[97,98] But the research has been driven in the direction of development of ambient condition magnetocaloric refrigeration over current gas compression-expansion technology after the discovery of room temperature (RT) MCE materials such as Gd (10.2 J/kg K at 294 K ), $Gd_5Si_2$ $Ge_2$ (18.4 J/kg K at 276 K).[98,99] The goal of current research in MCE is the search of new materials having large entropy change ($\Delta S_M$) and tunable operating temperature. Thus, systems showing larger MCE at RT would be useful for ambient condition technological applications while, at low T regime down to sub-Kelvin are advantageous for applications such as space science, liquification of hydrogen in fuel industry *etc*.[98]

Apart from Gd based compounds, intermetallic materials such as $LaFe_{13-x}Si_x$, $MnAs_{1-x}Sb_x$, $MnFeAs_{1-x}P_x$ based compounds having first order magnetic transitions also shows RT MCE.[100–102] But, large magnetic hysteresis, low resistance to corrosion and oxidation poses a challenge for their use in MCE refrigeration. These issues were conquered by manganite perovskites, compensating in terms of entropy and adiabatic temperature change.[100–103] Manganites were mostly studied for its multiferroic properties in past but, recently, they are also explored for MCE related applications as they have an advantage over conventional MCE materials due to high chemical stability, high resistivity, low production cost. The large entropy change in perovskites manganites such as $RMnO_3$ crystals (R= Dy, Tb, Ho and Yb), Dy doped $TbMnO_3$ across the magnetic transition temperature suggested the possible usefulness of it to exploit in magnetocaloric refrigeration technology.[104–106] However, larger heat capacity ($C_P$) values of manganites, such as, in case of $Ce_{0.67}Sr_{0.33}MnO_3$ (550 J/kg K) resulting in low adiabatic temperature change, limits its use. As large $C_P$ value increases the thermal load therefore, additional energy is required to heat the sample itself, causing a loss of entropy. As $C_P$ is inversely proportional to the $\Delta T_{ad}$, larger $C_P$ will give smaller $\Delta T_{ad}$ and vice-versa. Thus, material with smaller $C_P$ value is desirable. Thus, for selecting the material for MCE refrigeration, large magnetic entropy ($\Delta S_M$ (T)) and adiabatic temperature change ($\Delta T_{ad}$), small specific heat ($C_P$)

& thermal hysteresis, and high chemical stability are required.[106] Similar to manganites, rare earth chromites ($RCrO_3$) were mostly studied for its rich multiferroic behavior, though, the origin of FE is still debated and research was mostly driven towards understanding its origin.[37,40,43] Recently, $RCrO_3$ family of compounds have emerged as potential MCE materials as the smaller $C_P$ values (~ 95-109 J/mol/K) observed in these materials favor larger $\Delta T_{ad}$. Recently, McDannald *et al.* studied the MCE in bulk $DyCrO_3$ (DCO) and found large change in entropy 8.1 J/Kg K at ~ 12 K and relative cooling power (RCP) ~ 196 J/Kg at 3 T applied magnetic field.[107] Similarly, for single crystals of $GdCrO_3$, the $\Delta S_m^{max}$ is reported to be 31.6 J/Kg K.[108] However, for ideal magnetocaloric refrigeration, the magnetic nanoparticles are more advantageous than their bulk counterparts.[109,110] The nanoparticles are unique in their properties such as the particle size distribution and interparticle interactions, which leads to the broadening of the change in entropy ($\Delta S_M (T)$) over a wide T range, thus, enhancing the refrigeration capacity (RC) making it expedient for commercial application.[109,111,112] In general, magnetic refrigerant operating at cryogenic temperature *i.e.* 10 to 80 K with low applied field is desirable.[107]

## Section 2. Scope of present investigation

In this section, an introduction to the various aspects of research work on rare earth chromites investigated in the thesis work is presented.

The phase diagram of these multifunctional compounds is often complex to understand.  The small changes in the parameters such as temperature, strain, pressure, or elemental ratio significantly affect the physical properties of the material.[113,114] It is therefore an utmost importance to understand and develop new methods of engineering these phenomena. The research was mainly focused on the development of multifunctional devices  that combines logic, storage, and communications which may also improve energy efficiency.[115,116] The potential of spins and manipulation of spins namely termed as spintronics, has long been identified as a backbone of electronics industry.
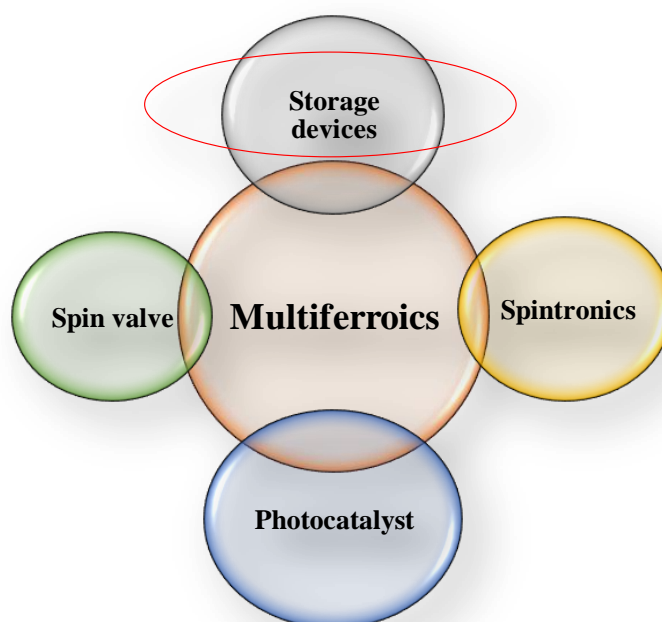


*Figure 17. Applications of multiferroic rare earth chromites.*

The memories are broadly classified into two categories. First one is volatile and other is non-volatile memories. Both have their pros and cons which is presented in *Figure 18.*
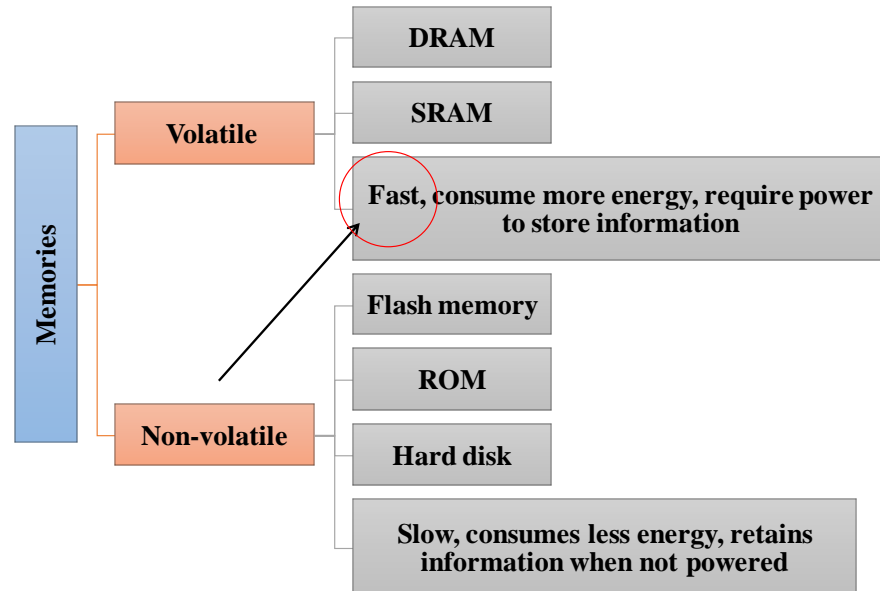


*Figure 18. Brief classification of memories and its advantages.*

Till now, charge based devices have been exploited for storage applications such as capacitor based RAM but movement of charges and power dissipation still remains a challenge. Although, "spin polarized charge currents have been exploited in storage applications such as magnetic RAM".[116] As it involves the charge movement, the power dissipation still remains an issue. However, recently pure spin currents based devices, where only the electron spin is transported and charge being stationary, have been identified as an efficient energy alternative to the spin polarized charge current based devices. However, the energy efficiency still remains a challenge.[115–117] The advances in discovering and investigating the new magnetic materials may lead towards the realization of these devices.

Moreover, a lot of work has been done on non-volatile memories making it energy efficient and are classified into two generation as presented in **Figure 19**. First generation non-volatile RAM includes MRAM and FERAM whereas, second

generation includes thermal assisted switching and spin valves. For thermal assisted switching devices, the material should possess important features such as NM, two or more compensation temperature and EB, whereas, spin valve devices rely on EB.
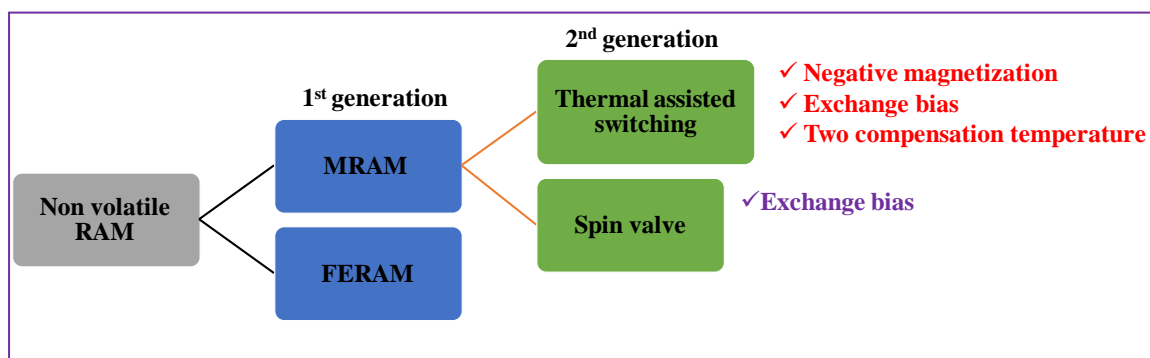


*Figure 19. First and second generation non-volatile random access memory.*

In an attempt to search for second generation non-volatile MRAM, research is driven towards exploring the candidates possessing these characteristic features such as NM, EB, and two or more compensation temperatures which can be realized in real time device applications. However, spin-based electronics devices *i.e.* MRAM and heat assisted magnetic recording (HAMR) is already in realization and in development stage.[116–118] To provide the path towards the realization of these devices, lot of work is being carried out in the development of new magnetic materials. To date, spin-based electronics have largely involved materials such as FM metallic alloys and semiconductors. However, oxide materials have also been incorporated into many prototypical spin-based electronic devices but the materials challenges still remain.[116,119]

Our group previously studied the structural, magnetic and electrical properties of $GdCrO_3$ nanoparticles.[43,120] We observed unusual NM which sparked the interest in this family of multiferroic materials. Here, we aim to study the rare earth chromites and explore the materials with characteristic features required for second generation non-volatile MRAM making it useful for probable spintronics and data storage device applications. Apart from spintronics application, the orthochromites

can also be useful for magnetocaloric refrigeration technology at cryogenic temperature. Moreover, there is an open question, why chromites exhibit NM unlike orthoferrites and manganites which still needs to be addressed.

In this thesis, we aim to address the unique and strange behavior such as negative magnetization, exchange bias and magnetization switching in rare earth orthochromites. The schematic is shown below in **Figure 20**.
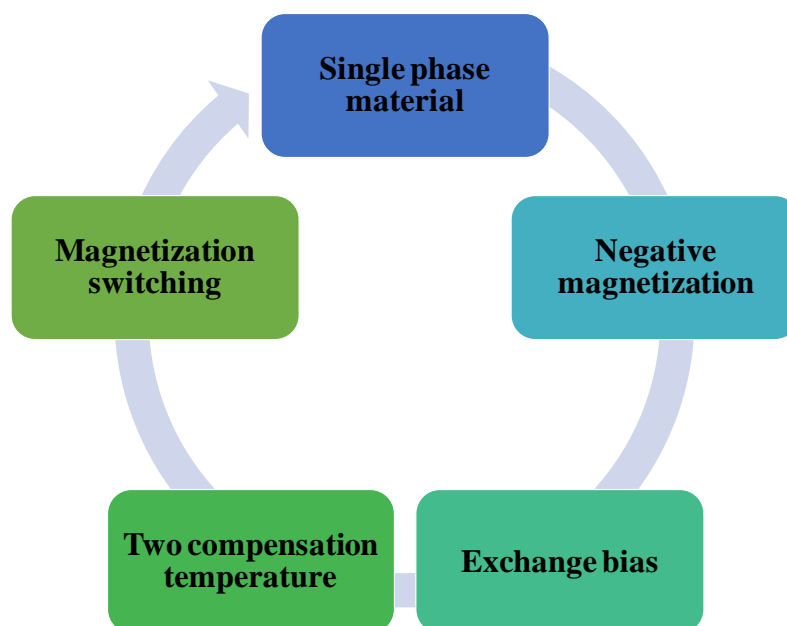


*Figure 20. Schematic showing the aim of the proposed thesis work.*

As NM has a practical implication such as EB, we also developed an understanding about the phenomenon and proposed the model for EB in rare earth orthochromite polycrystallites unlike conventional core-shell model for nanoparticles. In view of this, there has been an increased trend in the research for exploring new multifunctional materials to deal with the technological and environmental requirements. In the broad area of magnetism, the search for new giant magnetocaloric materials covering a wide working temperature range is of an immense interest since last several decades. The materials, with MCE at cryogenic temperature ($< 30$ K) are advantageous for applications such as space science,

liquefaction of hydrogen in fuel industry *etc.* In addition to unique magnetic behavior such as NM and EB, magnetocaloric effect in these orthochromites is also essential to study. Thus, we studied dysprosium chromite, samarium chromite and ytterbium chromite prepared by hydrolytic sol-gel method to explore and understand these properties in detail.

## 2.1    Thesis Outline:

The thesis mainly describes a detailed work on rare earth chromites ($RCrO_3$; R= Dy, Sm and Yb). The second chapter describes the basic aspects of synthesis methods and structural properties of $RCrO_3$ in more detail. The third chapter describes the optical properties of $RCrO_3$ nanoparticles investigated by Raman spectroscopy and UV-vis-NIR studies. The information gained by the optical studies further helped us to study the photocatalytic activity of $RCrO_3$, where, $DyCrO_3$ was used as a representative material. The fourth chapter gives the details of interesting magnetic features such as negative magnetization, exchange bias and magnetization switching in $RCrO_3$ polycrystallites. The fact that these unique and strange features make orthochromites, a plausible candidates for spintronics applications, is also discussed in this chapter. The thermal properties such as heat capacity and magnetocaloric effect of orthochromites are described in the fifth chapter. This chapter also presents the work on the use of $RCrO_3$ nanoparticles as a possible candidate for magnetocaloric refrigeration at cryogenic temperature. Also, results on our efforts towards the exploring the orthochromites covering wider range of working temperature in magnetocaloric refrigeration are presented in the same chapter.   The concluding chapter six presents the brief summary of the results achieved during the thesis work. It also describes the future scope for the present research work.

## 2.2 References:

[1] R. Ramesh, Curr. Sci. **105**, 1107 (2013).

[2] H. Schmid, Ferroelectrics **162**, 371 (1994).

[3] M. Opel, J. Phys. D. Appl. Phys. **45**, 033001 (2011).

[4] P. Debye, J. Phys. **36**, 300 (1926).

[5] G. Catalan and J.F. Scott, Adv. Mater. **21**, 2463 (2009).

[6] M.K. Singh, R.S. Katiyar, and J.F. Scott, J. Phys. Condens. Matter **20**, 252203 (2008).

[7] M.K. Singh, W. Prellier, M.P. Singh, R.S. Katiyar, and J.F. Scott, Phys. Rev. B - Condens. Matter Mater. Phys. **77**, 1 (2008).

[8] J. Wang, J.B. Neaton, H. Zheng, V. Nagarajan, S.B. Ogale, B. Liu, D. Viehland, V. Vaithyanathan, D.G. Schlom, U. V Waghmare, N. a Spaldin, K.M. Rabe, M. Wuttig, and R. Ramesh, Science **299**, 1719 (2003).

[9] T. Zhao, a Scholl, F. Zavaliche, K. Lee, M. Barry, a Doran, M.P. Cruz, Y.H. Chu, C. Ederer, N. a Spaldin, R.R. Das, D.M. Kim, S.H. Baek, C.B. Eom, and R. Ramesh, Nat. Mater. **5**, 823 (2006).

[10] Y.H. Chu, L.W. Martin, M.B. Holcomb, and R. Ramesh, Mater. Today **10**, 16 (2007).

[11] A. Jaiswal, R. Das, K. Vivekanand, P.M. Abraham, S. Adyanthaya, P. Poddar, and P. Mary Abraham, J. Phys. Chem. C **114**, 2108 (2010).

[12] T.J. Park, G.C. Papaefthymiou, A.J. Viescas, A.R. Moodenbaugh, and S.S. Wong, Nano Lett. **7**, 766 (2007).

[13] M.A.. H, *The Physical Principles of Magnetism* (Wiley, Newyork, 1965).

[14] P. Weiss, J. Phys. **6**, 661 (1907).

[15] E.C. Stoner, Philos. Mag. **15**, 1018 (1933).

[16] J.B. Goodenough, Phys. Rev. **100**, 564 (1955).

[17] J. Kanamori, J. Phys. Chem. Solids **10**, 87 (1959).

[18] P.W. Anderson, Phys. Rev. **115**, 2 (1959).

[19] S.-W. Cheong and M. Mostovoy, Nat. Mater. **6**, 13 (2007).

[20] J.F. Scott, Phys. World **8**, 46 (1995).

[21] M.K. Lee, T.K. Nath, C.B. Eom, M.C. Smoak, and F. Tsui, MRS Proc. **587**, 3547 (1999).

[22] L. Néel, *Propriétées Magnétiques Des Ferrites; Férrimagnétisme et Antiferromagnétisme* (Annales de Physique (Paris), 1948).

[23] E.O. Wollan and W.C. Koehler, Phys. Rev. **100**, 545 (1955).

[24] K. Yoshii, Appl. Phys. Lett. **99**, 142501 (2011).

[25] K. Yoshii, Mater. Res. Bull. **47**, 3243 (2012).

[26] J. Nogués and I.K. Schuller, J. Magn. Magn. Mater. **192**, 203 (1999).

[27] N.A. Hill, J.Phys.Chem.B **104**, 6694 (2000).

[28] D. Khomskii, Physics (College. Park. Md). **2**, (2009).

[29] M. Fiebig, T. Lottermoser, D. Fröhlich, a V Goltsev, and R. V Pisarev, Nature **419**, 818 (2002).

[30] J.R. Teague, R. Gerson, and W.J. James, Solid State Commun **8**, 1073 (1970).

[31] R. Seshadri and N. a. Hill, Chem. Mater. **13**, 2892 (2001).

[32] a. Moreira Dos Santos, S. Parashar, a. R. Raju, Y.S. Zhao, a. K. Cheetham, and C.N.R. Rao, Solid State Commun. **122**, 49 (2002).

[33] W. Eerenstein, N.D. Mathur, and J.F. Scott, Nature **442**, 759 (2006).

[34] M. Staruch, (2013).

[35] C.R. Serrao, A.K. Kundu, S.B. Krupanidhi, U. V. Waghmare, and C.N.R. Rao, Phys. Rev. B - Condens. Matter Mater. Phys. **72**, 2 (2005).

[36] Subba Rao Gv and Rao Cnr, Appl. Spectrosc. **24**, 436 (1970).

[37] J.R. Sahu, C.R. Serrao, N. Ray, U. V. Waghmare, and C.N.R. Rao, J. Mater. Chem. **17**, 42 (2007).

[38] D.I. Khomskii, J. Magn. Magn. Mater. **306**, 1 (2006).

[39] Y. Tokura, J. Magn. Magn. Mater. **310**, 1145 (2007).

[40] R. Saha, a. Sundaresan, and C.N.R. Rao, Mater. Horizons **1**, 20 (2014).

[41] I.B. Krynetskii and V.M. Matveev, Phys. Solid State **39**, 584 (1997).

[42] K. Sardar, M.R. Lees, R.J. Kashtiban, J. Sloan, and R.I. Walton, Chem. Mater. **23**, 48 (2011).

[43] A. Jaiswal, R. Das, K. Vivekanand, T. Maity, P.M. Abraham, S. Adyanthaya, and P. Poddar, J. Appl. Phys. **107**, 013912 (2010).

[44] a H. Cooke, D.M. Martin, and M.R. Wells, J. Phys. C Solid State Phys. **7**, 3133 (1974).

[45] B. Rajeswaran, D.I. Khomskii, a. K. Zvezdin, C.N.R. Rao, and a. Sundaresan, Phys. Rev. B - Condens. Matter Mater. Phys. **86**, 1 (2012).

[46] T. Yamaguchi and K. Tsushima, Phys. Rev. B **8**, 5187 (1973).

[47] G. Gorodetsky, R.M. Hornreich, S. Shaft, B. Sharon, a. Shaulov, and B.M. Wanklyn, Phys. Rev. B **16**, 515 (1977).

[48] X. Qian, L. Chen, S. Cao, and J. Zhang, Solid State Commun. **195**, 21 (2014).

[49] R.M. Hornreich, Y. Komet, R. Nolan, B.M. Wanklyn, and I. Yaeger, Phys. Rev. B **12**, 5094 (1975).

[50] G.V.S. Rao, B.M. Wanklyn, and C.N.R. Rao, J. Phys. Chem. Solids **32**, 345 (1971).

[51] a. K. Tripathi and H.B. Lal, Mater. Res. Bull. **15**, 233 (1980).

[52] J.S. Zhou, J. a. Alonso, V. Pomjakushin, J.B. Goodenough, Y. Ren, J.Q. Yan, and J.G. Cheng, Phys. Rev. B - Condens. Matter Mater. Phys. **81**, 1 (2010).

[53] T. Bora and S. Ravi, J. Magn. Magn. Mater. **358-359**, 208 (2014).

[54] P.K. Manna and S.M. Yusuf, Phys. Rep. **535**, 61 (2014).

[55] S.M. Yusuf, A. Kumar, and J. V. Yakhmi, Appl. Phys. Lett. **95**, 182506 (2009).

[56] A. Kumar and S.M. Yusuf, Phys. Rep. **556**, 1 (2015).

[57] S. Sadhu, A. Jaiswal, S. Adyanthaya, and P. Poddar, RSC Adv. **3**, 1933 (2013).

[58] A. a. Belik, Inorg. Chem. **52**, 8529 (2013).

[59] L.G. Antoshina, a. N. Goryaga, and V. V. San'kov, Phys. Solid State **42**, 1488 (2000).

[60] K. Yoshii and a. Nakamura, J. Solid State Chem. **155**, 447 (2000).

[61] A. Kumar, S.M. Yusuf, L. Keller, and J. V. Yakhmi, Phys. Rev. Lett. **101**, 1 (2008).

[62] Y.K. Jeong, J.H. Lee, S.J. Ahn, and H.M. Jang, Solid State Commun. **152**, 1112 (2012).

[63] V. a. Khomchenko, I.O. Troyanchuk, R. Szymczak, and H. Szymczak, J. Mater. Sci. **43**, 5662 (2008).

[64] W. H. Meiklejohn and C. P. Bean, Phys. Rev. Lett. **105**, 904 (1957).

[65] B.D.Cu. AndC.D.Graham, *Introduction to Magnetic Materials* (Wiley, n.d.).

[66] T. Bora and S. Ravi, J. Appl. Phys. **114**, 033906 (2013).

[67] J. Hemberger, S. Lobina, H. a. Krug Von Nidda, N. Tristan, V.Y. Ivanov, a. a. Mukhin, a. M. Balbashov, and a. Loidl, Phys. Rev. B - Condens. Matter Mater. Phys. **70**, 1 (2004).

[68] S. Zhang, L. Luan, S. Tan, and Y. Zhang, Appl. Phys. Lett. **84**, 3100 (2004).

[69] J.S. Jung, A. Iyama, H. Nakamura, M. Mizumaki, N. Kawamura, Y. Wakabayashi, and T. Kimura, Phys. Rev. B - Condens. Matter Mater. Phys. **82**, 3 (2010).

[70] O. Peña, C. Moure, P. Barahona, M. Baibich, and G. Martinez, Phys. B Condens. Matter **384**, 57 (2006).

[71] O. Peña, K. Ghanimi, C. Moure, D. Gutiérrez, and P. Durán, **709**, 706 (2004).

[72] K. Yoshii, J. Solid State Chem. **159**, 204 (2001).

[73] Y. Su, J. Zhang, Z. Feng, L. Li, B. Li, Y. Zhou, Z. Chen, and S. Cao, J. Appl. Phys. **108**, 013905 (2010).

[74] Y.L. Su, J.C. Zhang, L. Li, Z.J. Feng, B.Z. Li, Y. Zhou, and S.X. Cao, Ferroelectrics **410**, 102 (2010).

[75] B. Tiwari, M.K. Surendra, and M.S.R. Rao, **25**, (2013).

[76] S. Cao, H. Zhao, B. Kang, J. Zhang, and W. Ren, Sci. Rep. **4**, 5960 (2014).

[77] N. Sharma, B.K. Srivastava, A. Krishnamurthy, and a. K. Nigam, Solid State Sci. **12**, 1464 (2010).

[78] N. Sharma, B.K. Srivastava, A. Krishnamurthy, and a. K. Nigam, J. Alloys Compd. **545**, 50 (2012).

[79] S. Lei, L. Liu, C. Wang, C. Wang, D. Guo, S. Zeng, B. Cheng, Y. Xiao, and L. Zhou, J. Mater. Chem. A **1**, 11982 (2013).

[80] Y. Cao, S. Cao, W. Ren, Z. Feng, S. Yuan, B. Kang, B. Lu, and J. Zhang, Appl. Phys. Lett. **104**, 14 (2014).

[81] S.J. Yuan, W. Ren, F. Hong, Y.B. Wang, J.C. Zhang, L. Bellaiche, S.X. Cao, and G. Cao, Phys. Rev. B - Condens. Matter Mater. Phys. **87**, 1 (2013).

[82] H. Shen, Z. Cheng, F. Hong, J. Xu, S. Yuan, S. Cao, and X. Wang, Appl. Phys. Lett. **103**, 192404 (2013).

[83] Y. Ren, T.T.M. Palstra, D.I. Khomskii, E. Pellegrin, a. a. Nugroho, a. a. Menovsky, and G. a. Sawatzky, Nature **396**, 441 (1998).

[84] R.M. Hornreich, J. Magn. Magn. Mater. **7**, 280 (1978).

[85] P. Mandal, a. Sundaresan, C. Rao, a. Iyo, P. Shirage, Y. Tanaka, C. Simon, V. Pralong, O. Lebedev, V. Caignaert, and B. Raveau, Phys. Rev. B **82**, 1 (2010).

[86] J. Mao, Y. Sui, X. Zhang, Y. Su, X. Wang, Z. Liu, Y. Wang, R. Zhu, Y. Wang, W. Liu, and J. Tang, Appl. Phys. Lett. **98**, 3 (2011).

[87] J. Krishna Murthy and a. Venimadhav, Appl. Phys. Lett. **103**, 0 (2013).

[88] T.M. Hong, Phys. Rev. B **58**, 10 (1998).

[89] C. Won, Y.Z. Wu, E. Arenholz, J. Choi, J. Wu, and Z.Q. Qiu, Phys. Rev. Lett. **99**, 1 (2007).

[90] S.K. Giri, a. Poddar, and T.K. Nath, AIP Adv. **1**, 032110 (2011).

[91] L.H. Yin, Y. Liu, S.G. Tan, B.C. Zhao, J.M. Dai, W.H. Song, and Y.P. Sun, Mater. Res. Bull. **48**, 4016 (2013).

[92] A. Jaiswal, R. Das, S. Adyanthaya, and P. Poddar, J. Phys. Chem. C **115**, 2954 (2011).

[93] R. Schmidt, J. Romero, A. David, U. Amador, and E. Mora, (2013).

[94] G. a. Tompsett and N.M. Sammes, J. Power Sources **130**, 1 (2004).

[95] J. Saha and R.H. Victora, Phys. Rev. B - Condens. Matter Mater. Phys. **76**, 1 (2007).

[96] K. Das, T. Paramanik, and I. Das, J. Magn. Magn. Mater. **374**, 707 (2015).

[97] N. Pavan Kumar and P. Venugopal Reddy, Mater. Lett. **132**, 82 (2014).

[98] K. a GschneidnerJr, V.K. Pecharsky, and a O. Tsokol, Reports Prog. Phys. **68**, 1479 (2005).

[99] V.K. Pecharsky and K. a Gschneidner, Phys. Rev. Lett. **78**, 3 (1997).

[100] M. Balli, P. Fournier, S. Jandl, and M.M. Gospodinov, J. Appl. Phys. **115**, 173904 (2014).

[101] H. Wada, T. Takahara, K. Katagiri, T. Ohnishi, K. Soejima, and K. Yamashita, J. Appl. Phys. **117**, 172606 (2015).

[102] O. Tegus, E. Brück, K.H.J. Buschow, and F.R. de Boer, Nature **415**, 150 (2002).

[103] M. Balli, S. Jandl, P. Fournier, S. Mansouri, a. Mukhin, Y.V. Ivanov, and a. M. Balbashov, J. Magn. Magn. Mater. **374**, 252 (2015).

[104] a. Midya, S.N. Das, P. Mandal, S. Pandya, and V. Ganesan, Phys. Rev. B - Condens. Matter Mater. Phys. **84**, 1 (2011).

[105] M. Shao, S. Cao, S. Yuan, J. Shang, B. Kang, B. Lu, and J. Zhang, Appl. Phys. Lett. **100**, 222404 (2012).

[106] M.H. Phan and S.C. Yu, J. Magn. Magn. Mater. **308**, 325 (2007).

[107] a. McDannald, L. Kuna, and M. Jain, J. Appl. Phys. **114**, 0 (2013).

[108] L.H. Yin, J. Yang, X.C. Kan, W.H. Song, J.M. Dai, and Y.P. Sun, J. Appl. Phys. **117**, 133901 (2015).

[109] P. Poddar, J. Gass, D.J. Rebar, S. Srinath, H. Srikanth, S. a. Morrison, and E.E. Carpenter, J. Magn. Magn. Mater. **307**, 227 (2006).

[110] P. Poddar, S. Srinath, J. Gass, B.L. V Prasad, and H. Srikanth, J. Phys. Chem. C **111**, 14060 (2007).

[111] S. Srinath, P. Poddar, R. Das, D. Sidhaye, B.L.V. Prasad, J. Gass, and H. Srikanth, ChemPhysChem **15**, 1619 (2014).

[112] V. Franco, a. Conde, D. Sidhaye, B.L. V Prasad, P. Poddar, S. Srinath, M.H. Phan, and H. Srikanth, J. Appl. Phys. **107**, 1 (2010).

[113] J.F. Mitchell, D.N. Argyriou, C.D. Potter, D.G. Hinks, J.D. Jorgensen, and S.D. Bader, Phys. Rev. B **54**, 6172 (1996).

[114] J. Puustinen, J. Lappalainen, J. Hiltunen, and V. Lantto, Ferroelectrics **370**, 46 (2008).

[115] Z. Wang, Y. Yang, R. Viswan, J. Li, and D. Viehland, Appl. Phys. Lett. **99**, 043110 (2011).

[116] Y. Suzuki, APL Mater. **3**, 062402 (2015).

[117] I.L. Prejbeanu, M. Kerekes, R.C. Sousa, H. Sibuet, O. Redon, B. Dieny, and J.P. Nozières, J. Phys. Condens. Matter **19**, 165218 (2007).

[118] R.L. Stamps, S. Breitkreutz, J. Åkerman, A. V Chumak, Y. Otani, G.E.W. Bauer, J.-U. Thiele, M. Bowen, S. a Majetich, M. Kläui, I.L. Prejbeanu, B. Dieny, N.M. Dempsey, and B. Hillebrands, J. Phys. D. Appl. Phys. **47**, 333001 (2014).

[119] M. Bibes and A. Barthélémy, IEEE Trans. Electron Devices **54**, 1003 (2007).

[120] A. Jaiswal, R. Das, S. Adyanthaya, and P. Poddar, J. Nanoparticle Res. **13**, 1019 (2011).

# Chapter 2

# Synthesis and structural properties of rare earth chromites

**This chapter presents the synthesis of rare earth chromites by hydrolytic sol-gel method. It explores the role of different chelating agents in the single phase formation. The structural and microscopic analysis using X-ray diffraction and transmission electron microscopy are discussed in detail in this chapter. In order to further confirm the stoichiometric and oxidation states, X-ray photoelectron spectroscopy studies were done.**

## 2.1    Introduction

There is a renewed interest among physicists and chemists in developing new routes to synthesize complex oxides such as rare earth ferrites, manganites, and chromites due to their potential use in magnetoelectric (ME) and optoelectronic devices as well as in catalysts (as discussed in the previous chapter).[1–9] These class of compounds show multifunctional properties where, ferroelectric, ferroelastic, and magnetic ordering might coexist in a single phase materials (multiferroicity) apart from the interesting optoelectronic properties. The theoretical prediction of ME coupling in orthochromites fuel the interest in these materials.[10,11] Among the single phase multiferroic compounds such as rare earth ferrites, manganites and chromites, rare earth chromites ($RCrO_3$; R= rare earth) have been primarily studied in single crystal and thin film forms.[12,13] $RCrO_3$ typically crystallizes in orthorhombic distorted perovskite structure with Pbnm or Pnma space group. More recently, wet-chemical synthesis of few of these compounds has also been reported with the investigation of their structural, optical, magnetic and electrical properties.[10,14–17] The orthochromites have been primarily studied for their multiferroic properties and were considered to be insulators. But, they are known to be p-type semiconductor and found to be useful for sensing application along with the catalytic properties.[18,19] Due to high electrical conductivity ($10^{-4}$ to $10^{-1}$ ohm$^{-1}$cm$^{-1}$) of $RCrO_3$, it was found to be promising for interconnect material in fuel cells.[19–21]

In contrast to the conventional nanoscale materials such as transition metals and their oxides, the synthesis of rare earth ferrites, chromites and manganites in nanoscale is still full of challenges as it is quite difficult to stabilize single-phase materials at an ambient pressure. Due to the challenges associated with the nanoscale synthesis of these materials, the particle size dependent physical properties are relatively less reported despite of their potential applications. However, for the nanoscale synthesis, few attempts have been made but remain confined to hydrothermal method which employs high pressure.[3,5,6,18,22] Nanoscale tuneability of the ferroelectric and magnetic properties in oxides was demonstrated recently in related compounds such as $BaTiO_3$,[23] $Fe_3O_4$,[24,25] $BiFeO_3$,[7,9,26] $DyFeO_3$[22] and $GdCrO_3$[3] *etc*. The widely used synthesis method for $RCrO_3$ includes self-propagating high

temperature synthesis, citrate sol-gel route, hydrazine method, spray pyrolysis, solvothermal, metathesis of metal chlorides and polyol mediated synthesis.[27–32] Almost, all the mentioned synthesis methods are known to reduce the crystallization time but calcination of the material at higher temperature is a must. Even though, a lot of work is done to eliminate the requirement of high calcination temperature, still, solid state reaction method is preferred for synthesis of orthochromites such as HoCrO$_3$, YCrO$_3$, *etc*. The conventional solid state synthesis method depends on the ionic diffusion through the reactants and, in order to obtain uniform homogeneous products, it requires repeated grinding with subsequent long firing cycles at high temperatures. This ceramic route provides poor control of the morphology and a broad dispersion in the particle size leading to undesirable features, such as phase and stoichiometry inhomogeneities and the concomitant dispersion of properties in the final products. Thus, to avoid multiple steps during synthesis, one step solution methods attracted immense interest. One step solution method was employed for similar perovskites *i.e.* BaTiO$_3$, PbZr$_{1-x}$Ti$_x$O$_3$ and some manganites Ln$_{1-x}$A$_x$MnO$_3$ (Ln = La, Pr, Nd, *etc*. and A=Ca, Sr, Ba) as this method would provide better control over morphologies, crystallinity *etc*.[33–37]

In orthochromites, Lanthanum chromite (LaCrO$_3$) is well studied material and hydrothermal method was employed to synthesize LaCrO$_3$ at 400 °C but, the requirement of high temperature in this method ruled out its common use for other orthochromites.[38] To reduce the synthesis temperature potassium hydroxide (KOH) was involved during the synthesis and the temperature reduced considerably to 350 °C for Ca-doped LaCrO$_3$[39] and 250 °C for LaCrO$_3$.[40] As, hydrothermal method at times require higher calcination temperature and solid state method involves multiple steps to obtain the desired phase, we used hydrolytic sol-gel method to synthesize the rare earth chromites (RCrO$_3$, R=Dy, Sm and Yb).

After the material is synthesized, it is desirable to validate the single phase formation and investigate it's microstructure by diffraction studies such as X-ray diffraction and transmission electron microscopy. High Resolution Transmission Electron Microscopy (HRTEM) can be used to confirm the crystal structure in real space, determined previously by X-ray diffraction (XRD). Such comprehensive

analysis allows correlating the physical properties such as, magnetization behavior to the crystal structure. In most of the inorganic synthesis research, the main aim is to establish the relationships between the synthesis procedure, the crystal structure and physical properties.[41] Moreover, the orthochromites are p-type semiconductor rather than insulator due to the presence of $Cr^{3+}$ and $Cr^{4+}$ centers and hopping conduction. Thus, it is also essential to investigate the oxidation states of the as-synthesized orthochromites by X-ray photoelectron spectroscopy.[42,43] It can be seen from above discussion that, only work on hydrothermal synthesis of orthochromites so far has been focused on $LaCrO_3$ and its doped analogues. In the light of potential applications of the orthochromites in memory devices, data storage and spintronics, simple synthetic approaches is desirable to form single phase material.

In this chapter, we present simple synthesis route to form $DyCrO_3$, $SmCrO_3$ and $YbCrO_3$ polycrystallites with platelet morphology and demonstrate the effect of chelating agent and decomposition temperature on phase formation and morphology. This chapter further elaborate a detailed X-ray diffraction, transmission electron microscopy, X-ray photoelectron spectroscopic (XPS) study of $DyCrO_3$ nanoparticles synthesized by using two different chelates *i.e.* citric acid and oxalic acid. We used these co-ordination ligands as they make more stable chelates and serve as excellent combustive fuel in the reaction. Further, in this chapter, the structural and morphological studies of $SmCrO_3$ and $YbCrO_3$ polycrystallites were studied using the experimental tools mentioned above as a part of thesis work and presented in different sections.

## 2.2    Characterization techniques:

### 2.2.1  X-ray diffraction (XRD):

X-ray diffraction (XRD) technique is used to realize structural properties of materials and get information like crystal structure/phase, lattice parameters, crystallite size, orientation of single crystals, preferred orientation of polycrystals, defects, strains and so on. Powder X-ray diffraction (XRD) patterns were collected using PANalytical X'PERT PRO instrument using iron filtered Cu - Kα radiation ($\lambda$ = 1.5406 Å) in the $2\theta$ range of 20–80 °  with a step size of 0.02°.

### 2.2.2  Transmission electron microscopy (TEM):

In the present work, TEM measurements were performed using FEI Tecnai F30 high resolution transmission electron microscope (HRTEM) operated at 300 keV accelerating voltage equipped with a super-twin lens operated at 300 keV accelerating voltage with Schottky field emitter source with maximum beam current (> 100 nA) and small energy spread (0.8 eV or less). The point resolution is 0.2 nm with a $C_S$ = 1.2 mm and $C_C$ 1.4 mm, respectively. Prior to TEM measurements, the as-synthesized powder were dispersed in ethanol and then, drop-casted on carbon coated copper TEM grid with 200 mesh. The TEM grids drop-casted with the sample was allowed to vacuum dry overnight and TEM & selected area electron diffraction (SAED) measurements were performed. The size, morphology, lattice fringes of the prepared particles were obtained by using this tool.

### 2.2.3  X-ray photoelectron spectroscopy (XPS):

X-ray photoelectron spectroscopy (XPS) data of as-synthesized sample was collected using VG Microtech, model ESCA 3000 equipped with ion-gun (EX-05) for cleaning the surface.  The binding energy resolution was 0.1 eV, however the overall resolution was limited to the bandwidth of X-ray source (~ 1 eV). Here, we used Shirley algorithm for background correction and chemically distinct species were resolved using a non-linear least square fitting procedure.

# Section 2.3

# Effect of surface chemistry on structural properties of DyCrO$_3$ nanoplatelets

_____

This section essentially addresses the role of chelating agent in the phase formation of DyCrO$_3$ nanoplatelets. It also discusses the effect of surface chemistry on the structural and morphological properties of DyCrO$_3$ nanoplatelets. From our study, we inferred that the crystalline phase of DyCrO$_3$ was attained at the decomposition temperature of 800 °C for citric acid and oxalic acid, respectively. The structural analysis further indicate a distorted orthorhombic perovskite structure of the DyCrO$_3$ nanoplatelets. Further, the formation of plate-like morphology of DyCrO$_3$ has been studied in detail. Finally, the stoichiometric analysis was done using X-ray photoelectron spectroscopy as, it can directly influence the magnetic and optical properties.

_____

## 2.3.1  Experimental Details

### 2.3.1.1       Synthesis of DyCrO₃ nanoparticles:

A hydrolytic sol-gel method was used to synthesize dysprosium chromite ($DyCrO_3$) (DCO) nanoparticles using two different chelating agents *i.e.* oxalic acid ($H_2C_2O_4.2H_2O$, Merck, 99.5%) and citric acid ($C_6H_8O_7$, Merck, 99.5 %) and to study the effect of chelating agent on the morphology and crystallinity of the particles. In addition to the chelating agents, dysprosium (III) nitrate hydrate ($Dy(NO_3)_3 \cdot xH_2O$, Aldrich, 99.9 % metal basis), chromium tri oxide ($CrO_3$, Thomas baker, 99.9%) were used without any further purification. Stoichiometric amount of $Dy(NO_3)_3 \cdot xH_2O$, $CrO_3$ and $C_2H_2O_4.2H_2O$ (molar ratio, 1:1) were dissolved in the de-ionized water. The solution was continuously stirred for 3 h to obtain a homogeneous solution. The pH was raised to ~ 9 by drop-wise addition of liquid ammonia followed by stirring at room temperature for 3 h resulting into sol formation. This sol was heated at 80 °C and dried gel was obtained, which was further calcined at different decomposition temperature of 500, 600, 700 and 800 °C for 6 h. In another reaction, $C_6H_8O_7$ *i.e.* citric acid was used as chelating agent and the whole reaction was carried out as discussed above. The resulting material was used for further characterization. DCO particles obtained by using oxalic acid and citric acid was named as DCO (O) and DCO (C), respectively.

## 2.3.2  X- ray diffraction:

**Figures 1 and 2** show the XRD patterns of DCO (C) and DCO (O) powders obtained after the calcinations of gel at various decomposition temperatures (500, 600, 700 and 800 ºC). In both the cases, we found that the gel when thermally decomposed at 800 ºC, showed the formation of single phase orthorhombic DCO. [**JCPDS file no. 251050**]
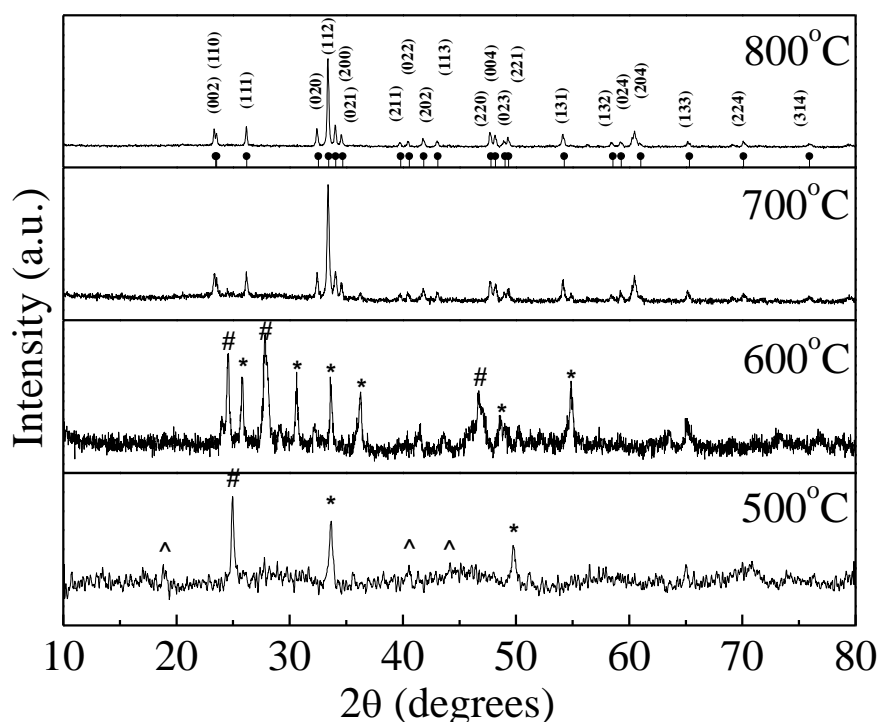


*Figure 1. Powder x-ray diffraction patterns of DCO (C) at different temperatures. [Peaks with symbols ^, *, # represent Dy-citrate, DyONO$_3$, Dy-Cr-O complexes respectively].*

From **Figure 1**, it has been observed that the XRD pattern corresponding to the samples calcined at 700 and 800 $^o$C showed the formation of DCO (C) phase. In contrast, for sample calcined at 500 and 600 ºC, which were formed using different chelates *i.e.* citric acid and oxalic acid, we did not find the indication of phase formation (**Figure 1 and 2**). Instead, the peaks corresponding to intermediate phases

such as DyONO$_3$, dysprosium oxalate (Dy$_2$ (C$_2$O$_4$)$_3$) [**JCPDS file no. 190435**] and chromium oxalate (CrC$_2$O$_4$) [**JCPDS file no. 40896**] were found to be present. From **Figure 2**, it is clear that DCO (O) forms at 800 °C with an extra peak marked with arrow at 24.4° which can be attributed to the DyCrO$_4$ phase [**JCPDS file no. 741249**].
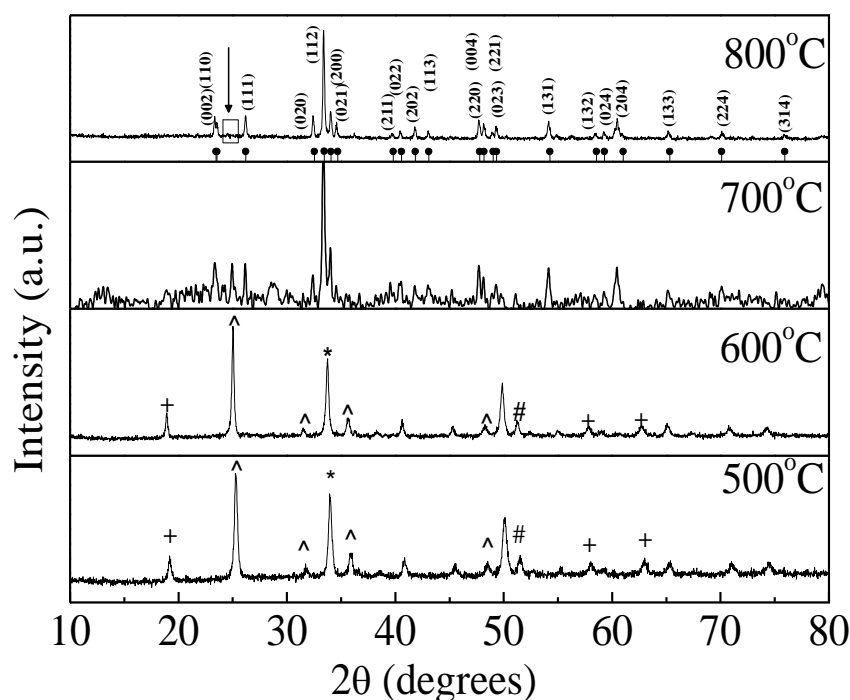


*Figure 2. Powder x-ray diffraction patterns of DCO (O) at different temperatures. [The peaks with symbols ^, *, #, + represent Dy-oxalate, DyONO$_3$, Dy-Cr-O complex, and Cr-oxalate respectively]. DCO (O) at 800 $^\bullet$C show a small peak labeled with arrow represents DyCrO$_4$ phase.*

As seen from the **Figure 2**, the intensity ratio of the most intense peak of DyCrO$_3$ (DCO (O)) and DyCrO$_4$ peak in DCO(O) is found to be ~ 6. It is well known that DyCrO$_4$ remains stable below 700 °C and decomposes to DyCrO$_3$ at higher calcinations temperature.[44] It should be noted that in DCO (C) we didn't find any peak corresponding to DyCrO$_4$ phase whereas, in DCO (O), the impurity of DyCrO$_4$ exists even though the as-synthesized sample was calcined at 800 °C. Our study highlights an important role played by the chelating agents in forming the pure phase.

The Debye–Scherrer equation gave the average crystallite size around ~ 70 nm for DCO (C) and ~ 40 nm for DCO (O). The lattice parameters as calculated from the powder XRD data for DCO (C) and DCO (O) are tabulated in **Table 2.1**.

| Lattice parameters (Å)→ Decomposition Temperature (ºC) ↓ | DCO(C) | | | DCO(O) | | |
|---|---|---|---|---|---|---|
| | $a$ | $b$ | $c$ | $a$ | $b$ | $c$ |
| **700** | 5.27 | 5.52 | 7.57 | 5.33 | 5.57 | 7.47 |
| **800** | 5.17 | 5.48 | 7.54 | 5.19 | 5.50 | 7.54 |

***Table 2.1.  Lattice parameters of DyCrO₃ nanoparticles synthesized using citric acid and oxalic acid as chelating agents.***

For both the chelating agents, we observed rise in the value of lattice parameter $a$ with the increase in decomposition temperature. However, not much change was found for other two lattice parameters $b$ and $c$.  Lattice parameters of the particles obtained at 800 ºC with citrate chelate were found to be $a$ = 5.17, $b$ = 5.48 Å and $c$ = 7.54 Å and for oxalate chelate, it was obtained as $a$ = 5.19, $b$ = 5.5 and $c$ = 7.54 Å, respectively. The change in crystallite size and lattice parameters at different decomposition temperatures can be related to the effect of chelating agents used during the synthesis process. We found it interesting that, even at 700 ºC,  pure and highly crystalline phase was formed for citric acid, whereas, for oxalic acid, we observed remnants of intermediate phase ($DyCrO_4$) along with well crystalline $DyCrO_3$ (which was present as a dominant phase). Such phenomenon can be ascribed to the bidentate and tridentate nature of oxalic ($C_2H_2O_4$) and citric acid ($C_6H_8O_7$), respectively. Due to the change in number of carboxylate (–COOH) and hydroxyl (–OH⁻) functional groups in the citric and oxalic acid, they have different behavior. Oxalic acid offers 2 sites to bind with metal ions whereas, citric acid can provide three ionic sites to the metal ion. The formation of chelate ring in the case of citric acid is much stronger than the oxalic

acid and thus, citrates are more stable than oxalates. Normally, in chelation – COO-, =O moieties do not participate. It is only –O⁻ moiety that participates. Thus, number of ionizable groups present in the citric and oxalic acid usually influences the combustion process. In addition, the energy released from the exothermic reaction between various fuels is different thereby, affecting the phase formation. As observed, for citrate gel precursor route, the single phase forms even at 700 ºC owing to stable complex formation due to its tridentate nature.[45,46] Thus, citric acid was found to be a better chelating agent than oxalic acid as oxalic acid gives some remnant phase of $DyCrO_4$ in a single phase DCO (O).

## 2.3.3  Transmission electron microscopy:

**Figure 3(a)** shows the TEM micrograph of DCO (C) nanoplatelets.
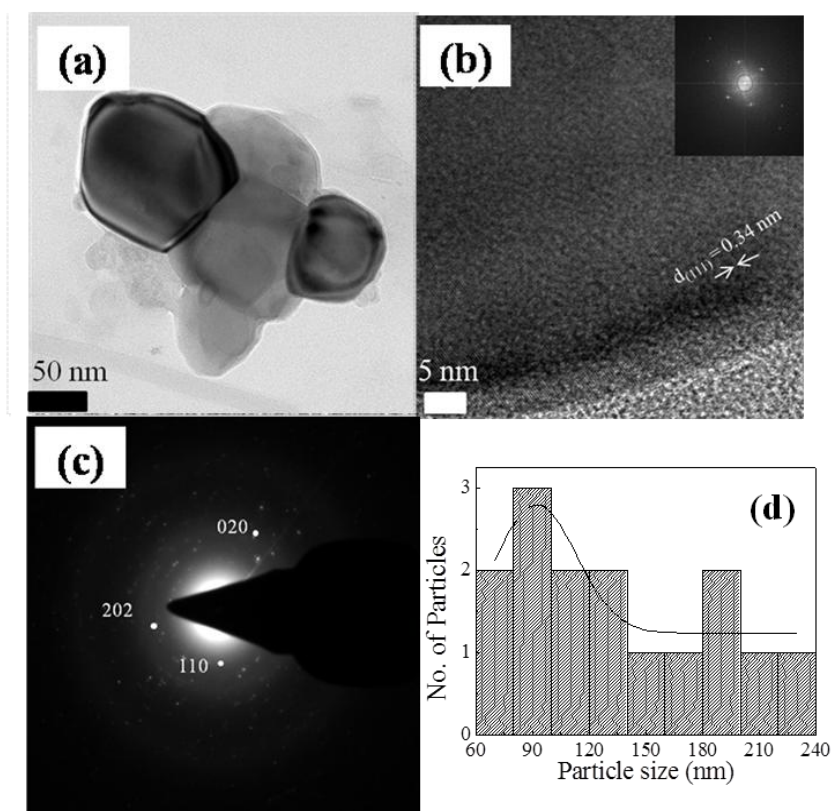


*Figure 3. (a) TEM image showing plate-like morphology (b) HRTEM image (inset shows FFT pattern) (c) SAED pattern and (d) particle size distribution of DCO (C) nanoparticles.*

As seen from the **Figure**, the particles are having 2D platelet structure with an average particle size around ~ 90 nm. **Figure 3(b)** shows the HRTEM image of these DCO (C) nanoplatelets. It displays the clear lattice fringes with interplaner spacing of 0.34 nm which represents the (111) plane of DCO. **Figure 3(c)** shows the selected area electron diffraction (SAED) of DCO (C) where, dot pattern confirms the crystallinity of the platelets. The spots corresponding to (202), (020) and (110) planes are clearly visible. The average particle size distribution for DCO (C) is calculated and shown in **Figure 3** (d). Similarly, **Figure 4(a)** shows the bright field TEM micrographs of DCO (O) nanoplatelets.
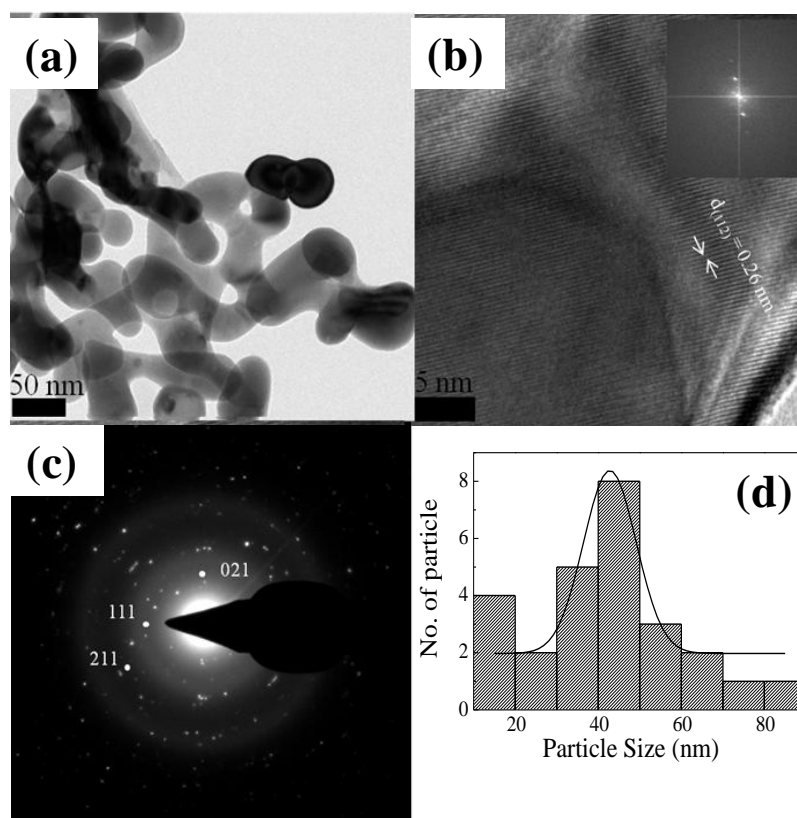


*Figure 4. (a) TEM image showing plate-like morphology (b) HRTEM image (inset shows FFT pattern)  (c) SAED pattern and (d) particle size distribution of DCO (O) nanoparticles.*

As seen from the **Figure**, DCO (O) nanoplatelets possess slightly different morphology than the particles synthesized by the citrate route. The average particle size of DCO (O) was found to be ~ 50 nm which is smaller than the DCO (C). Here, we observe that two or more nanoplatelets are fused together. This change in the morphology with the chelating agent might be due to the effects such as varied level of stability constants, combustion energy of different ligands present in the chelates which can affect the nucleation process during the reaction.[36,37] The HRTEM image (**Figure 4(b)**) of DCO (O) nanoparticles shows the lattice-fringes with the *d*-spacing of 0.26 nm corresponding to the (112) plane.

Even in our previous studies on the synthesis of $GdCrO_3$, $BiFeO_3$ and $DyFeO_3$ nanoparticles, we had reported the formation of similar plate-like morphologies.[3,47,48] We believe that the role of nitrate and citrate/oxalate ions is exceptionally important in the formation of nanoplatelets. Other factors such as different types of defects also play an important role in determining the morphologies of nanoparticles. On the other hand, during wet chemical synthesis, preferential binding of ionic ligands and surfactants used, strongly affect the affinity of one facet over other which however, allows the growth of particular facet only while restricting the other facets (based on their surface energy). **Figure 4(c)** represents the selected area electron diffraction (SAED) pattern showing the diffraction spots and rings corresponding to (021), (111), (211) planes for DCO (O). The average particle size distribution for DCO (O) is calculated and shown in **Figure 4(d)**. Thus, TEM analysis clearly demonstrates the effect of chelating agent on the particle morphology and its size.

### 2.3.4   X- ray photoelectron spectroscopy:

In order to reveal the chemical composition and state of surface atoms, X-ray photoelectron spectroscopy (XPS) measurements were done. The core level binding energy (BE) was aligned with the carbon BE of ~ 285 eV.
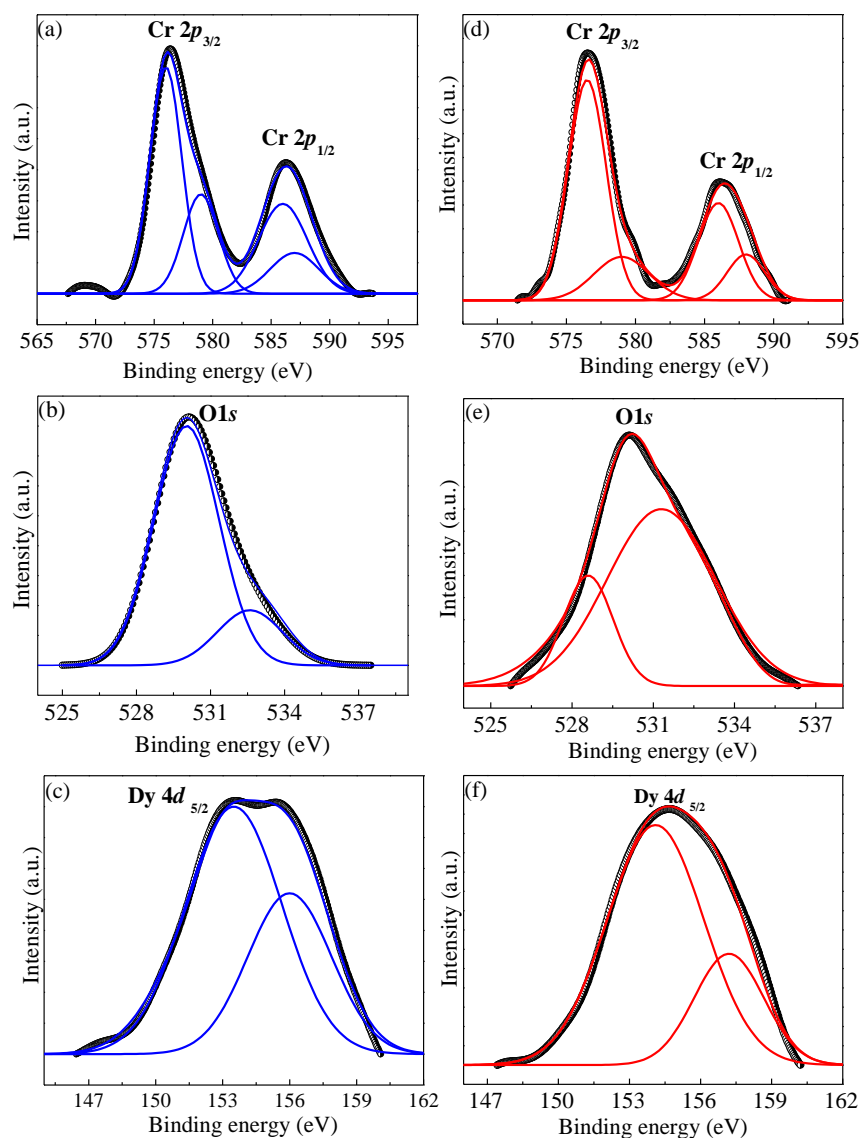
*Figure 5. Core level XPS spectra of Cr 2p, O 1s, Dy 4d in (a-c) DCO (C) and (d-f) DCO (O).*

**Figure 5(a)** shows the DCO (C) core level BE spectra of Cr (*2p*) which contains two peaks at ~ 576.3 and ~ 586.2 eV due to the characteristic spin–orbit splitting in the *2p* level (*$2p_{3/2}$* and *$2p_{1/2}$*). The Cr (*2p*) peaks were further resolved into four peaks situated at ~ 576, ~ 579, ~ 586 and ~ 587 eV. The peak at BE ~ 576 and ~ 579 eV can be correlated to the presence of $Cr^{3+}$ and $Cr^{6+}$ states, respectively. Our group has previously identified and reported the peaks at ~ 576.5 and ~ 588.8 associated with

the $Cr^{3+}$ $2p_{3/2}$ and $Cr^{3+}$ $2p_{1/2}$ levels, respectively.[3,49] The peak at ~ 586 eV corresponds to $Cr^{3+}$ $2p_{1/2}$ and a small shake-up contribution at ~ 587 eV was also observed.[49] It is known that chromium (VI) has only paired electrons in its valence band and contributes to only one photoelectron peak to the Cr $2p_{3/2}$ spectrum. The particle size of DCO is around 50-90 nm and XPS is a surface sensitive technique which can probe only few monolayers of unit cell. The presence of minute amount of +6 state of chromium derived from the deconvolution of Cr XPS peak in DCO (C) and DCO (O) is mainly due to the surface ions and not from precursors. It is likely that the oxidation state of the surface chromium states could change from the bulk chromium.

**Figure 5(b)** shows the O $1s$ XPS spectrum of DCO (C) which was resolved into two peaks at ~ 530 and ~ 532 eV. Peak at ~ 530 eV usually denotes the presence of structural oxide ($O^{2-}$) as in case of DCO (C). However, oxygen in adsorbed water ($H_2O$) at surface was seen as a peak at ~ 532 eV.[50] **Figure 5(c)** shows the Dy $4d$ core level photoemission spectra of DCO (C) which contain a doublet at ~ 153.5 and ~ 156.6 eV. These are similar to those evidenced in pure dysprosium and were attributed to Dy (III) $4d_{5/2}$ .[51–53] The peak near ~ 153.5 and ~ 156.6 eV are due to different bonds *i.e* Dy-Cr and Dy-O present in the compound.[45] Burzo *et al.* also deconvulated the Dy $4d$ spectra in four peaks located at ~ 152.3, ~ 153.6, ~ 155.0, and ~ 157.0 eV for $DyNi_{5-x}Al_x$.[54] Similarly, one can also say that in DCO (C) the two nearby peaks present in the Dy $4d$ XPS spectrum may result from the Dy-Cr and Dy-O bonds.

In order to see the change in surface with the chelating agent, XPS of DCO (O) was also recorded, shown in **Figure 5(d - f)**. XPS spectra of Cr $2p$ core level BE of DCO (O) contain two peaks at ~ 576.4 and ~ 586.2 eV corresponding to Cr $2p_{3/2}$ and Cr $2p_{1/2}$, respectively. The peaks were deconvulated into subpeaks situated at ~ 576.4, ~ 579, ~ 586.2 and ~ 587.6 eV. Peaks at BE ~ 576.4 and ~ 586.2 eV are associated with the $Cr^{3+}$ $2p_{3/2}$ and $Cr^{3+}$ $2p_{1/2}$ states of chromium. The peak at ~ 579 eV can be correlated with the $Cr^{6+}$ states of chromium. From **Figure 5(a)** and **5 (d),** one can notice that the ratio of $Cr^{3+}/Cr^{6+}$ changes.

In the case of DCO (O), the percentage of $Cr^{6+}$ was found to be low as compared to DCO (C). This change in percentage of fully oxidized chromium ($Cr^{6+}$)

at the surface of the sample shows the segregation of the oxidized chromium species is larger in DCO (C).[55] The satellite peak of Cr $2p_{3/2}$ was observed near ~ 587 and ~ 587.6 eV for DCO (C) and DCO (O) nanoplatelets, respectively. From XRD we have seen that, in case of DCO (O) a small peak of $DyCrO_4$ phase is present so it is likely that $Cr^{5+}$ state will be present in XPS spectra of Cr in DCO (O). It is well known that the BE of $Cr^{6+}$ and $Cr^{5+}$ are nearly same thus, it is difficult to distinguish them. Thus, it clearly shows the effect of chelating agents on the oxidation state of chromium in DCO (O).[56]

**Figure 5(e)** shows the XPS spectra of O *1s* in DCO (O) showing the characteristic peak at ~ 530.1 eV. After deconvulation, two subpeaks were obtained, the major one at BE ~ 530 eV related to the oxide and the other at ~ 531 eV related to the surface adsorbed oxygen species in the form of hydroxide ($OH^-$).[50] In comparison with DCO (C), instead of adsorbed water, a hydroxide related peak was found in DCO (O). This change in O *1s* state can be attributed to the change in chemical environment due to the presence of hydroxyl ion in citric acid rather than in oxalic acid. This hydroxyl group of citric acid may react with the adsorbed hydroxide species to form adsorbed water as confirmed by the XPS spectra of O *1s* at ~ 531 eV BE. Thus, XPS of oxygen clearly indicates the role of carboxyl and hydroxyl groups of chelating agents.

XPS of dysprosium for DCO (O) is shown in **Figure 5(f)**. The Dy $4d_{5/2}$ spectra obtained was deconvulated into two peaks situated at ~ 154.1 and ~ 157.1 eV, respectively. These two nearby peaks are due to Dy-Cr and Dy-O bonds present in the compound. There is a minute change in Dy *4d* XPS spectra when compared with DCO (C) which may arise due to the change in the bonding environment near $Dy^{3+}$.[53] Thus, XPS shows a clear change in chemical environment near all the constituent elements.

## 2.3.5 Conclusions

In this section, the effect of chelating agents on the crystallization temperature and phase formation has been studied for DCO nanoparticles. We have shown that DCO (C) and DCO (O) was successfully synthesized using hydrolytic sol-gel method. Our

studies further revealed that citric acid is better chelating agent than oxalic acid in single phase formation. XRD studies clearly demonstrate the formation of orthorhombic single phase $DyCrO_3$ nanoparticles by both the chelating agent at 800 °C. Our X-ray diffraction studies showed that oxalic acid can stabilize $DyCrO_4$ even at 800 °C thus, giving remnant $DyCrO_4$ phase in $DyCrO_3$ nanoparticle. Our morphological studies shows the formation of plate-like structure with an average particle size of ~ 90 and ~ 50 nm for DCO (C) and DCO (O) respectively. XPS study of $DyCrO_3$ nanoplatelets revealed that the presence of $Cr^{6+}/Cr^{5+}$ states in $DyCrO_3$ nanoparticle (DCO (O)) is mainly due to contribution from $DyCrO_4$ phase.

# Section 2.4

# Samarium chromite (SmCrO₃) polycrystallites

_____

This section essentially addresses the synthesis and structural properties of $SmCrO_3$ nanoplatelets. The structural analysis further indicated a distorted orthorhombic perovskite structure of the $SmCrO_3$ nanoplatelets. Further, the formation of plate-like morphology of $SmCrO_3$ has been studied in detail. The stoichiometry of the compound can directly influence the magnetic and optical properties. Thus, X-ray photoelectron spectroscopy analysis was done.

_____

### 2.4.1 Experimental Details

### 2.4.1.1        Synthesis of SmCrO$_3$ nanoparticles:

Following the synthesis protocol of DyCrO$_3$ nanoplatelets,[57] samarium chromite was synthesized using hydrolytic sol-gel method. The starting material samarium (III) nitrate hydrate (Sm(NO$_3$)$_3$· x H$_2$O, Aldrich, 99.9% metal basis), chromium nitrate (Cr(NO$_3$)$_3$, Thomas Baker, 99.9 %) and citric acid were used without any further purification. Stoichiometric amount of Sm (NO$_3$)$_3$·xH$_2$O, Cr(NO$_3$)$_3$ and C$_6$H$_8$O$_7$ (molar ratio, 1:1) were dissolved in the deionized water and solution was continuously stirred for 3 h to obtain a homogeneous solution. The pH of the solution was raised to ~ 9 by adding liquid ammonia drop-wise followed by stirring at room temperature for again 3 h resulting in sol formation due to the formation of metal-citrate complex. The obtained sol was heated at 80 °C and dried gel obtained was calcined at 800 °C and used for further characterization.

## 2.4.2  X-ray diffraction:

**Figure 1** shows the powder XRD diffraction pattern of $SmCrO_3$ (SCO). The pattern could be indexed with an orthorhombic perovskite structure having *Pbnm* space group according to **JCPDS file no.00-039-0262**. The XRD ruled-out any secondary phase in SCO. Lattice parameters of SCO particles were found to be $a = 5.35 \pm 0.01$, $b = 5.48 \pm 0.014$, $c = 7.64 \pm 0.01$ Å which agreed well with the JCPDS data.
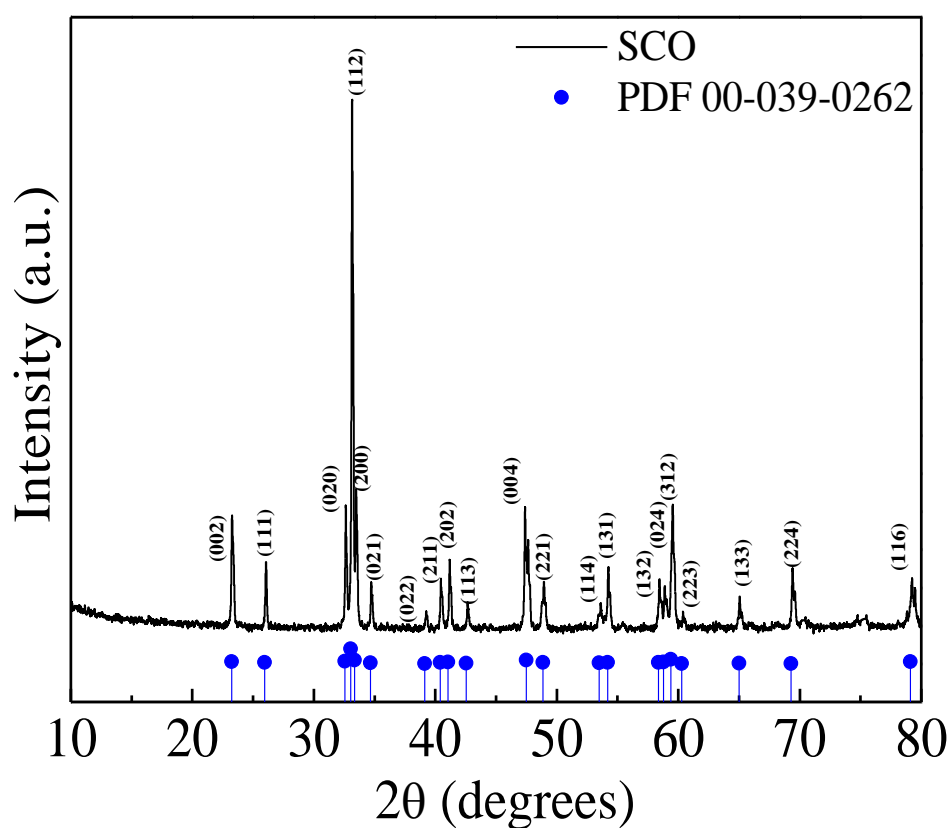


*Figure 1. Powder X-ray diffraction pattern of SmCrO₃ polycrystallites compared with reference data (shown in blue).*

## 2.4.3  Transmission electron microscopy:

**Figure 2(a)** shows the representative TEM image of SCO sample. As seen from the figure, the particles have plate-like structure similar to $GdCrO_3$[3], $DyCrO_3$[57], $DyFeO_3$[48], $BiFeO_3$[6] and Ca-doped $LaCrO_3$.[39] **Figure 2(b)** shows HRTEM image of

SCO nanoplatelets with interplaner spacing d ~ 0.27 nm, corresponds to (112) plane of SCO lattice which is also the most intense peak in the XRD pattern [**Figure 1**]. **Figure 2(c)** represents the selected area electron diffraction (SAED) pattern showing the diffraction spots and rings corresponding to (004), (022), (311) planes for SCO.
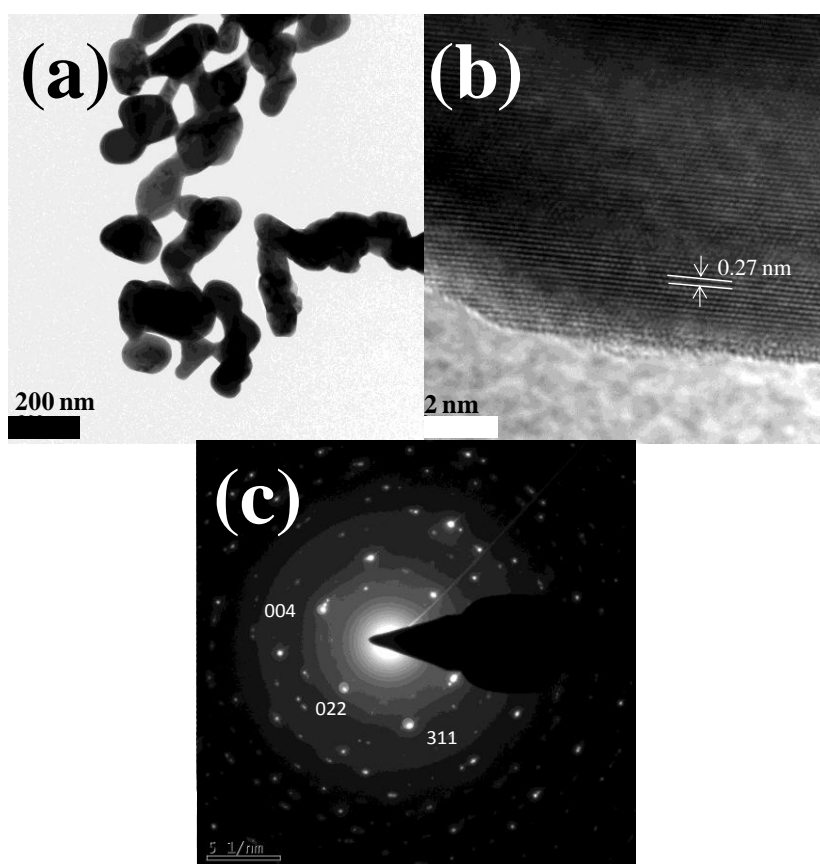


*Figure 2. (a) TEM image, (b) HRTEM image and (c) SAED pattern of SmCrO$_3$ polycrystallites showing plate-like morphology.*

## 2.4.4  X-ray photoelectron spectroscopy:

XPS was carried out to identify the chemical composition and valence state of the elements in the SmCrO$_3$ polycrystallites. **Figure 3(a-c)** shows the XPS spectra of SmCrO$_3$ polycrystallites.
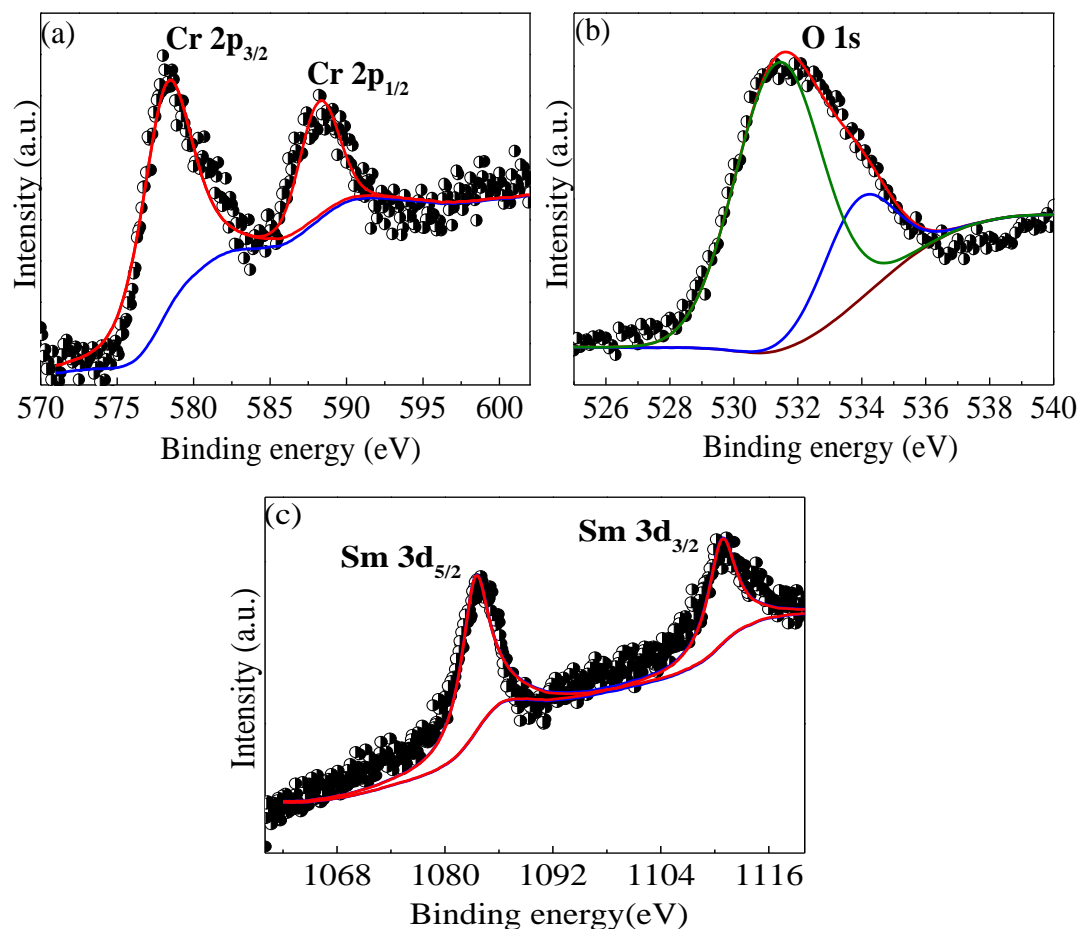
*Figure 3. Core level binding energy spectra of Cr 2p, O 1s and Sm 3d in SmCrO₃ polycrystallites.*

**Figure 3(a)** shows the SCO core level BE spectra of Cr (*2p*) which contains two peaks at ~ 577.9 and ~ 588.5 eV due to the characteristic spin–orbit splitting in the *2p* level (*2p₃/₂* and *2p₁/₂*).[3,55,57] **Figure 3(b)** shows the O *1s* XPS spectrum of SCO which was resolved into two peaks at ~ 531.5 and ~ 534 eV. Peak at ~ 531.5 eV usually denotes the presence of structural oxide ($O^{2-}$) and can be assigned to $Sm^{3+}$ - O group as in case of $Sm_2O_3$.[58] The weak peak at ~ 534 eV can be attributed to the oxygen of $OH^-$ group at the surface.[59] This further indicates that the BE of O 1*s* in SCO can vary depending on the oxidation state of samarium.[58] **Figure 3(c)** shows the Sm *3d* core level photoemission spectra of SCO. The samarium *3d* states split due to spin-orbit interaction (Sm *3d₅/₂* - Sm *3d₃/₂* ) with energy $\Delta$ ~ 27 eV. [58] The core level Sm *3d₅/₂*

and Sm $3d_{3/2}$ peaks are observed at BE of ~ 1083.3 and ~ 1110.9 eV, respectively, similar to what observed in pure samarium[58,60] The BE (~ 1083.3 eV) of Sm $3d_{5/2}$ in SCO nanoplatelets  is slightly less than that of $Sm_2O_3$ (~ 1087.5 eV) and can be attributed to the difference in chemical and coordination environments of Sm in SCO nanoplatelets. However, the peak situated at  ~ 1083.3 and ~ 1110.9 eV are related to the $Sm^{3+}$ component. Thus, Sm is mainly present in 3+ oxidation state.

## 2.4.5  Conclusions

In this section, we have presented the synthesis and structural studies on SCO nanoplatelets. The SCO nanoplatelets were successfully synthesized using sol-gel method and our XRD studies clearly demonstrate the formation of orthorhombic single phase and rule out the presence of any impurity phase. Our morphological studies shows the formation of platelet like structure with an average particle size of ~ 90 nm for SCO nanoplatelets.  XPS study of SCO nanoplatelets revealed the core level BE of Sm $3d$ is slightly less than that of $Sm_2O_3$ and can be  attributed to the difference in chemical and coordination environments of Sm. Our studies also confirmed that, Sm in SCO is mainly present in +3 oxidation state.

# Section 2.5

# Ytterbium chromite (YbCrO$_3$) polycrystallites

_____

This section discuss the hydrolytic sol-gel synthesis of YbCrO$_3$ polycrystallites. The formation of single phase YbCrO$_3$ polycrystallites were confirmed by X-ray diffraction technique. The structural analysis further suggest a distorted orthorhombic perovskite structure of the YbCrO$_3$ nanoplatelets. Further, the morphology of YbCrO$_3$ polycrystallies were studied by transmission electron microscopy. The possible reason behind the formation of plate-like morphology of YbCrO$_3$ has been discussed in detail and presented schematically. Finally, X-ray photoelectron spectroscopy analysis of YbCrO$_3$ polycrystallites were done.

_____

## 2.5.1 Experimental Details

### 2.5.1.1    Synthesis of YbCrO₃ nanoparticles:

The YbCrO$_3$ (YCO) particles were synthesized by the hydrolytic sol-gel method from ytterbium (III) nitrate hydrate (Yb(NO$_3$)$_3 \cdot$ xH$_2$O, Aldrich, 99.9% metal basis), chromium nitrate (Cr(NO$_3$)$_3$, Thomas baker, 99.9%) and citric acid without any further purification.[57,61] Stoichiometric amount of Yb(NO$_3$)$_3 \cdot$ xH$_2$O, Cr(NO$_3$)$_3$ and C$_6$H$_8$O$_7$ (molar ratio, 1:1) were dissolved in the deionized water and solution was continuously stirred for 3 h to obtain a homogeneous solution. The pH of the solution was raised to ~ 9 by drop-wise adding the liquid ammonia followed by stirring at room temperature for again 3 h resulting into sol formation. The obtained sol was heated at 80 °C and dried gel obtained was calcined at 800 °C and used for further characterization.

## 2.5.2  X-ray diffraction:

**Figure 1** shows the powder XRD diffraction pattern of $YbCrO_3$ (YCO).
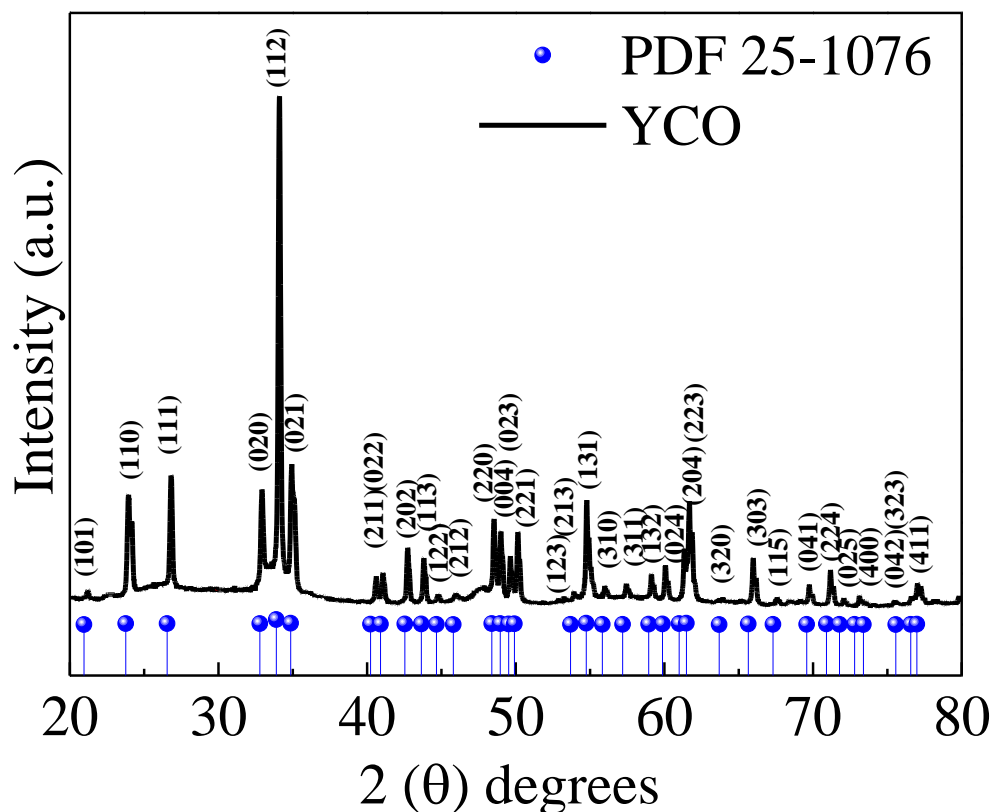


*Figure 1. Powder XRD pattern of YbCrO₃ nanocrystallites with reference data (shown in blue).*

The XRD peaks of YCO were indexed with an orthorhombic perovskite structure having *Pbnm* space group according to JCPDS file no. 25-1076. Lattice parameters of YCO particles were found to be *a*=5.18, *b*=5.49, *c*=7.47 Å, which agreed well with the previously reported values.[14] These results clearly demonstrate the formation of pure phase of YCO, with no observed impurity peak. The average crystallite size of YCO nanocrystallites was calculated using Debye-Scherer method and was found to be ~ 70 nm. The lattice parameters calculated from the present XRD data with the *Pbnm* space group found to be close to the previously reported results.

### 2.5.3  Transmission electron microscopy:
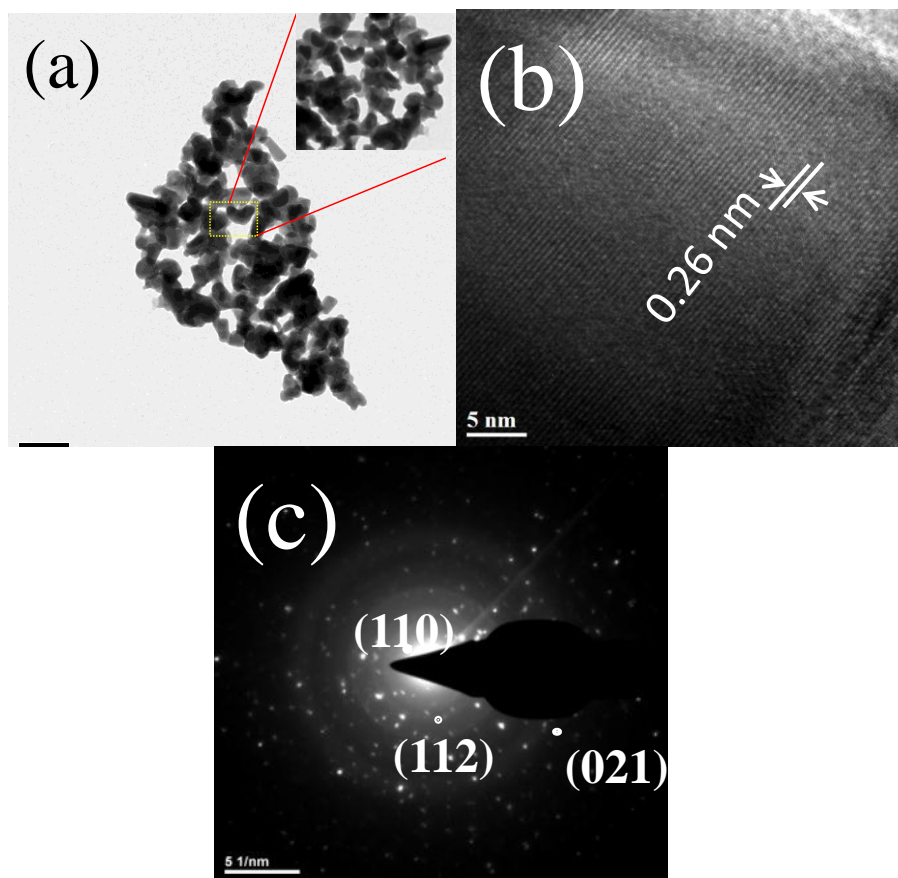


*Figure 2. (a) The bright field TEM image show plate-like morphology with average particle size around 80 nm. The inset shows zoomed view of the dotted region. (b) The HRTEM image shows lattice fringes corresponding to (112) plane of the YCO crystal and (c) The SAED pattern of YCO crystallites shows dot pattern originating from several YCO nanocrystals in the selected area.*

**Figure 2(a)** shows the representative TEM image of YCO nanocrystallites, indicating plate-like structure. Inset shows the zoomed view of the dotted region as shown in **Figure 2(A)**. The average particle size of YCO was found to be ~ 80 nm. The HRTEM image in the **Figure 2(b)** shows the good crystallinity with interplaner spacing d ~ 0.26 nm corresponding to (112) plane of YCO lattice, which is also the most intense peak in XRD pattern. **Figure 2(c)** represents the selected area electron

diffraction (SAED) pattern with diffraction spots and rings corresponding to planes (021), (112) and (110) for YCO, respectively, indicating the crystalline nature of YCO however, the contribution is from several crystallites in the selected area.

In TEM images, we also observe that two or more nanoplatelets are fused together. In addition, the formation of plate-like structure can be understood by considering the role of nitrate and citrate ions[3,57] It is well-known that, faceted growth of crystal is affected and altered by the intrinsic crystal structure and other parameters such as reaction conditions *i.e.* the kinetic energy barrier, temperature, time and capping molecules.[62–64] In general, ligands or surfactants preferentially bind to the facets having higher density of surface atoms and gets blocked, restricting the growth along this facet.[63,64] Apart from the role of nitrate and citrate in governing the morphology of the particle, there are various other factors such as twinning, stacking faults, preferential binding of ligands on particular facets facilitate the plate-like morphology.[3,57] The citric acid used here acts as a chelating agent and it also governs the morphology of the particle. From our previous studies, we observed that the chelating agent *i.e.* citric acid and oxalic acid plays an important role in the phase formation of $DyCrO_3$ nanoparticle. We found that the formation of a chelate ring is much stronger in the citric acid assisted synthesis and form more stable complexes than oxalates.[57] Also, the number of ionizable groups present in the citric and oxalic acid usually influences the combustion process and the energy released from the exothermic reaction is different, thereby affecting the phase formation.[57] Thus, the tridentate nature of citric acid forms more stable metal complex and molar ratio of citrate to nitrate plays a significant role in determining the shape and size of the particles. Here, the molar ratio of nitrate to citrate also determines the plate-like morphology of YCO. It can be concluded that citrate has a function to inhibit the longitudinal growth of crystals along <001> with the enhancement in the sideways growth giving 2D plate-like structure, similar to what observed when sodium citrate, citric acid or phosphate ions are used.[3,62,65,66] Similarly, as YCO crystallizes in orthorhombic structure, the citrate ion preferentially bind on <001> facets having higher density of atoms and thus, restrict its growth longitudinally and results in plate-like morphology. Below we present the Schematic for platelet formation (**Scheme 1**).
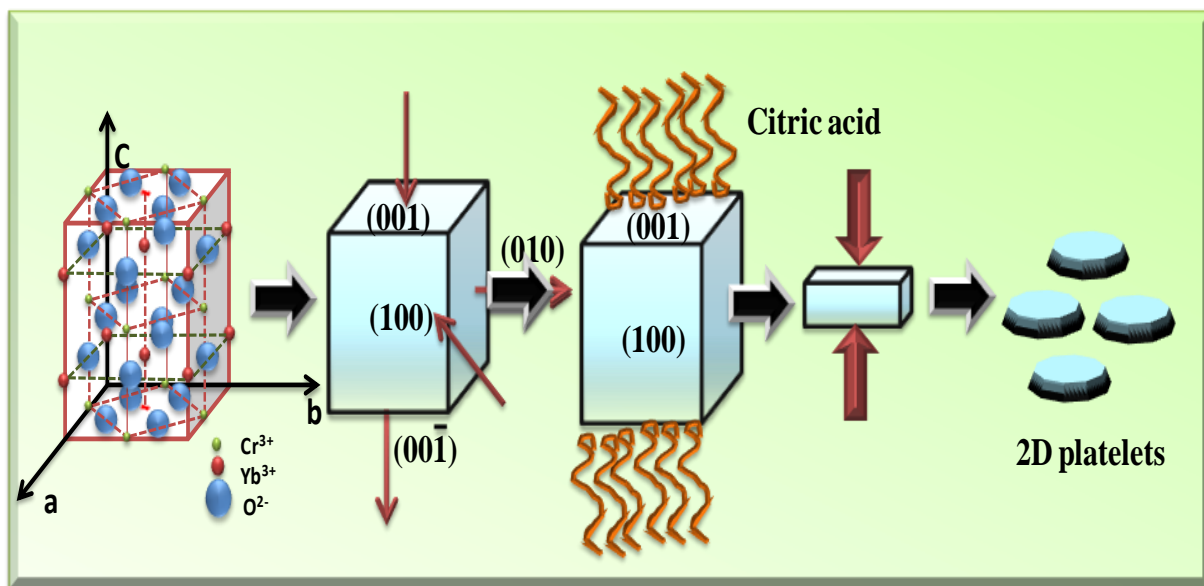
*Scheme 1. Schematic showing the formation of plate-like morphology of orthorhombic perovskite YCO nanocrystals.*

However, the increase in the citrate and nitrate molar ratio will in turn leads to suppression of the growth sideways by the adsorption of more citrate ions resulting in the reduction of thickness of the crystals. Thus, molar ratio 1: 1 and role of citric acid was found to be favorable for the YCO nanoplatelets formation.[63]

## 2.5.4 X-ray photoelectron spectroscopy:

To further reveal the chemical composition and oxidation states of YCO, X-ray photoelectron spectroscopy (XPS) measurements were done. The core level BE was aligned with the BE (285 eV) of carbon. **Figure 3(a-c)** shows the Cr 2*p*, O 1*s* and Yb 4*d* core level BE spectra of YCO.
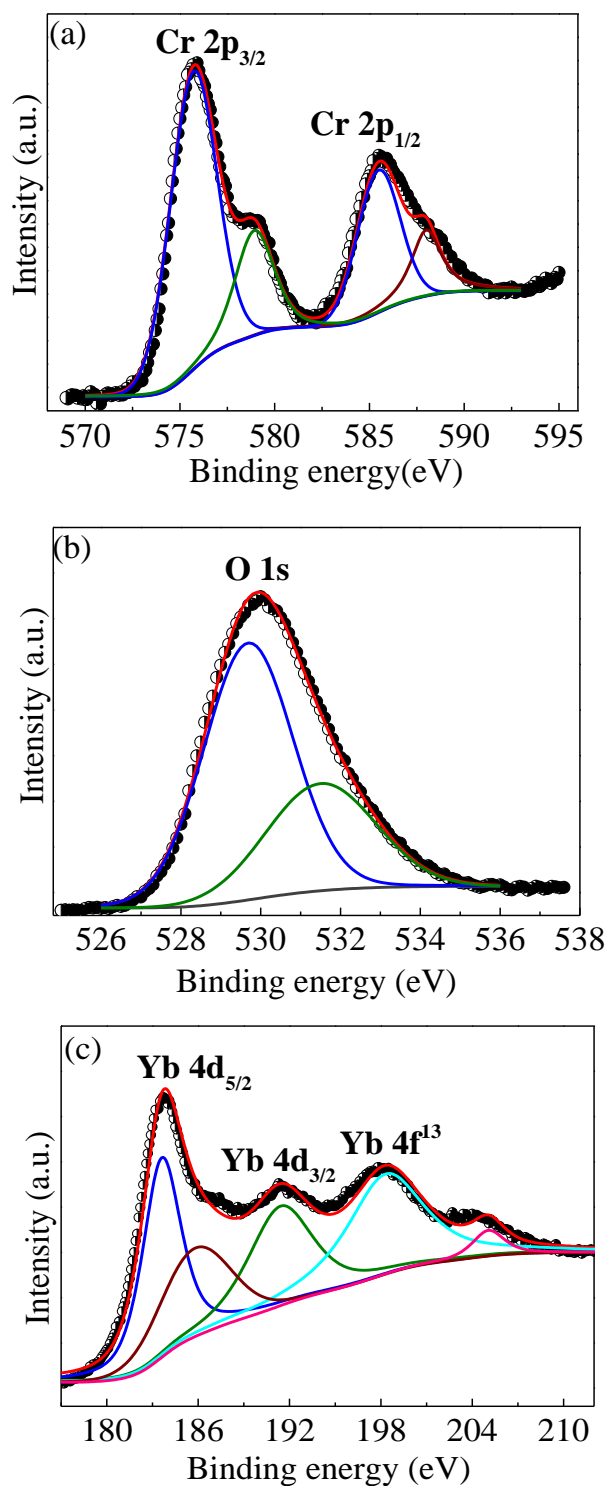
*Figure 3. Core level XPS spectra of (a) Cr 2p, (b) O 1s and (c) Yb 4d in YbCrO₃ nanocrystallites.*

**Figure 3(a)** represents the Cr ($2p$) core level BE spectra with two peaks situated at ~ 575.7 and ~ 585.5 eV due to the characteristic spin-orbit splitting in the

$2p$ level ($2p_{3/2}$ and $2p_{1/2}$). The Cr ($2p$) peaks for YCO were further resolved into peaks situated at ~ 575.7, ~ 578.9, ~ 585.6 and ~ 587.9 eV, respectively. The peak at ~ 575.7 and ~ 578.9 eV can be correlated to the presence of the $Cr^{3+}$ and $Cr^{6+}$ states, respectively.[3,57,67] The presence of the $Cr^{6+}$ state is an usual feature of such chromium perovskite samples. The peak at ~ 585.6 eV corresponds to $Cr^{3+}$ $2p_{1/2}$ and a small shake-up contribution at ~ 587.9 eV was also observed.[49,57]

**Figure 3(b)** shows the O 1$s$ XPS spectra, which were resolved into two peaks at ~ 529.7 and ~ 531.6 eV for YCO, respectively. The presence of structural oxide was seen as a peak situated at ~ 529.7 eV. However, a peak at ~ 531.6 eV for YCO corresponds to oxygen in adsorbed water ($H_2O$) at the surface. [50,57]

**Figure 3(c)** shows the Yb 4$d$ core level photoemission spectra, containing prominent peak situated at ~ 183.7 eV. The Yb$^{3+}$ ions show very complex pattern. We observed the peak situated at ~ 191.3 eV with a lower intensity and a feature at ~ 197.9 eV. The peak at ~ 183.7 eV and ~ 191.3 eV can be attributed to the spin-orbit splitting of 4$d$ levels $i.e.$ $4d_{5/2}$ and $4d_{3/2}$, respectively. The spin orbit splitting was found to be ~ 7.6 eV. The peak corresponding to $4d_{5/2}$ and $4d_{3/2}$ levels was found to be slightly shifted at higher BE when compared with the Yb metal and agrees well with $Yb_2O_3$.[68,69] The peak at ~ 186.2 eV can be attributed to the Yb-O bond of YCO which is similar to the observed Dy-O in DCO.[57] The XPS spectrum of Yb is known to be very complex and despite its complexity, the Yb oxidation state is 3+ dominated corresponding to $Yb_2O_3$.[68] The additional feature at ~ 197.9 eV is attributed to the Yb $4f^{13}$ configuration and a shoulder at ~ 204.9 eV corresponds to the intra-atomic hybridization.[70] There has been different explanation given for the observed complex spectrum of $Yb^{3+}$ ion such as possibility of Auger electrons, chemical decomposition or quantized energy losses during the inelastic collisions of photoelectron[42] which has been ruled out by Signorelli and Hayes.[70] The electrostatic coupling between the 4$d$ levels and unfilled 4$f$ levels strongly affect the 4$d$ levels of $Yb^{3+}$ ion and according to Russell- Saunders coupling, the final states of $4d^9 4f^{13}$ are mixed and proved to be more closer to j-j states rather than L-S states.[69,71] Theoretically, it has been concluded that the spread in energy and intensity distribution was quite similar to the experimental observation by calculating the intensities by considering $d^9$

configuration and expanding final states by elementary method. Hence the complex spectrum of $Yb^{3+}$ was explained using electrostatic interaction between $4d$-$4f$.[44]


## 2.5.5  Conclusions

In this section, YCO was successfully synthesized using hydrolytic sol-gel method. XRD pattern clearly demonstrate the formation of orthorhombic single phase YCO nanocrystallites. TEM images shows the formation of platelet like structure with an average particle size of YCO ~ 80 nm. The formation of plate-like morphology has been studied in detail with a discussion on role of nitrate and citrates. Here, we also proposed the mechanism of plate-like morphology by considering the role of ligands, nitrates, citrates, molar ratio, preferential binding of ligands *etc*. Our XPS studies further revealed the additional feature at ~ 197.9 eV which is attributed to the Yb $4f^{13}$ configuration and a shoulder at  ~ 204.9 eV corresponds to the intra-atomic hybridization. The XPS spectrum of Yb is known to be very complex and despite its complexity, the Yb oxidation state is 3+ dominated corresponding to $Yb_2O_3$.

## 2.5.6   References:

[1] R. Das, A. Jaiswal, S. Adyanthaya, and P. Poddar, 12104 (2010).

[2] R. Das, A. Jaiswal, S. Adyanthaya, and P. Poddar, J. Appl. Phys. **109**, (2011).

[3] A. Jaiswal, R. Das, S. Adyanthaya, and P. Poddar, J. Nanoparticle Res. **13**, 1019 (2011).

[4] A. Jaiswal, R. Das, T. Maity, K. Vivekanand, S. Adyanthaya, and P. Poddar, J. Phys. Chem. C **114**, 12432 (2010).

[5] A. Jaiswal, R. Das, K. Vivekanand, T. Maity, P.M. Abraham, S. Adyanthaya, and P. Poddar, J. Appl. Phys. **107**, 013912 (2010).

[6] A. Jaiswal, R. Das, K. Vivekanand, P.M. Abraham, S. Adyanthaya, P. Poddar, and P. Mary Abraham, J. Phys. Chem. C **114**, 2108 (2010).

[7] W. Eerenstein, N.D. Mathur, and J.F. Scott, Nature **442**, 759 (2006).

[8] C. Binek and B. Doudin, J. Phys. Condens. Matter **17**, L39 (2005).

[9] S.-W. Cheong and M. Mostovoy, Nat. Mater. **6**, 13 (2007).

[10] J.R. Sahu, C.R. Serrao, N. Ray, U. V. Waghmare, and C.N.R. Rao, J. Mater. Chem. **17**, 42 (2007).

[11] a K. Zvezdin and a a Mukhin, Jetp Lett. **88**, 505 (2008).

[12] P.N. Kotru, A.K. Řazdan, and B.M. Wanklyn, J. Mater. Sci. **24**, 2401 (1989).

[13] C.R. Serrao, A.K. Kundu, S.B. Krupanidhi, U. V. Waghmare, and C.N.R. Rao, Phys. Rev. B - Condens. Matter Mater. Phys. **72**, 2 (2005).

[14] Y. Su, J. Zhang, Z. Feng, L. Li, B. Li, Y. Zhou, Z. Chen, and S. Cao, J. Appl. Phys. **108**, 013905 (2010).

[15] R. Saha, a. Sundaresan, and C.N.R. Rao, Mater. Horizons **1**, 20 (2014).

[16] J. Prado-Gonjal, R. Schmidt, J.J. Romero, D. Ávila, U. Amador, and E. Morán, Inorg. Chem. **52**, 313 (2013).

[17] V.S. Bhadram, D. Swain, R. Dhanya, a Sundaresan, and C. Narayana, Mater. Res. Express **3**, 13 (2013).

[18] K. Sardar, M.R. Lees, R.J. Kashtiban, J. Sloan, and R.I. Walton, Chem. Mater. **23**, 48 (2011).

[19] J. Beckers and G. Rothenberg, ChemPhysChem **6**, 223 (2005).

[20] G. a. Tompsett and N.M. Sammes, J. Power Sources **130**, 1 (2004).

[21] G.V.S. Rao, B.M. Wanklyn, and C.N.R. Rao, J. Phys. Chem. Solids **32**, 345 (1971).

[22] A. Jaiswal, R. Das, T. Maity, and P. Poddar, J. Appl. Phys. **110**, 124301 (2011).

[23] V. Bansal, P. Poddar, A. Ahmad, and M. Sastry, J. Am. Chem. Soc. **128**, 11958 (2006).

[24] P. Poddar, T. Fried, and G. Markovich, Phys. Rev. B **65**, 3 (2002).

[25] P. Poddar, T. Telem-Shafir, T. Fried, and G. Markovich, Phys. Rev. B **66**, 1 (2002).

[26] N.A. Hill, J.Phys.Chem.B **104**, 6694 (2000).

[27] M. Kuznetsov and I. Parkin, (1998).

[28] I.P. Parkin, a. V. Komarov, and Q. Fang, Polyhedron **15**, 3117 (1996).

[29] T. Kikkawa, M. Yoshinaka, K. Hirota, O. Yamaguchi, and K. Tanabe, J. Mater. Sci. Lett. **14**, 1071 (1995).

[30] P.S. Devi, J. Mater. Chem. **3**, 373 (1993).

[31] M. Inagaki, O. Yamamoto, and M. Hirohara, J. Ceram. Soc. Japan **98**, 675 (1990).

[32] P. Vernoux, E. Djurado, and M. Guillodo, J. Am. Ceram. Soc. **95**, 2289 (2001).

[33] D.R. Modeshia and R.I. Walton, Chem. Soc. Rev. **39**, 4303 (2010).

[34] P.K. Dutta and J.R. Gregg, Chem. Mater. **4**, 843 (1992).

[35] J. Eckert Jr, C. Hung-Houston, B. Gersten, M. Lencka, and R. Riman, J. Am. Ceram. Soc. **79**, 2929 (1996).

[36] K. Fukai, K. Hidaka, M. Aoki, and K. Abe, Ceram. Int. **16**, 285 (1990).

[37] R.I. Walton, F. Millange, R.I. Smith, T.C. Hansen, and D. O'Hare, J. Am. Chem. Soc. **123**, 12547 (2001).

[38] S.T. Song, H.Y. Pan, Z. Wang, and B. Yang, Ceram. Int. **10**, 143 (1984).

[39] L.P. Rivas-Vázquez, J.C. Rendón-Angeles, J.L. Rodríguez-Galicia, C. a. Gutiérrez-Chavarria, K.J. Zhu, and K. Yanagisawa, J. Eur. Ceram. Soc. **26**, 81 (2006).

[40] W. Zheng, W. Pang, G. meng And, and D. Peng, J. Mater. Chem. **9**, 2833 (1999).

[41] R. Schmidt and U. Amador, 819 (2014).

[42] Subba Rao Gv and Rao Cnr, Appl. Spectrosc. **24**, 436 (1970).

[43] a. K. Tripathi and H.B. Lal, Mater. Res. Bull. **15**, 233 (1980).

[44] Y. Long, Q. Liu, Y. Lv, R. Yu, and C. Jin, Phys. Rev. B - Condens. Matter Mater. Phys. **83**, 4 (2011).

[45] J. Glusker, Acc. Chem. Res. **572**, 345 (1980).

[46] J. Chandradass, M. Balasubramanian, and K.H. Kim, Mater. Manuf. Process. **25**, 1449 (2010).

[47] A. Jaiswal, R. Das, K. Vivekanand, P. Mary Abraham, S. Adyanthaya, and P. Poddar, J. Phys. Chem. C **114**, 2108 (2010).

[48] A. Jaiswal, R. Das, S. Adyanthaya, and P. Poddar, J. Phys. Chem. C **115**, 2954 (2011).

[49] I. Grohmann, E. Kemnitz, a Lippitz, and W.E.S. Unger, Surf. Interface Anal. **23**, 887 (1995).

[50] D. Briggs and G. Beamson, Anal. Chem. **65**, 1517 (1993).

[51] P. Wu and C. Cai, Electroanalysis **17**, 1583 (2005).

[52] D. Barreca, A. Gasparotto, A. Milanov, E. Tondello, A. Devi, and R. a. Fischer, Surf. Sci. Spectra **14**, 52 (2007).

[53] Y.T. Tsai, T.C. Chang, W.L. Huang, C.W. Huang, Y.E. Syu, S.C. Chen, S.M. Sze, M.J. Tsai, and T.Y. Tseng, Appl. Phys. Lett. **99**, 92106 (2011).

[54] E. Burzo, S.G. Chiuzbăian, M. Neumann, M. Valeanu, L. Chioncel, and I. Creanga, J. Appl. Phys. **92**, 7362 (2002).

[55] K. Rida, a. Benabbas, F. Bouremmad, M. a. Peña, E. Sastre, and a. Martínez-Arias, Appl. Catal. A Gen. **327**, 173 (2007).

[56] K. Jagannathan and A. Srinivasan, **427**, 418 (1981).

[57] P. Gupta, R. Bhargava, R. Das, and P. Poddar, RSC Adv. **3**, 26427 (2013).

[58] T. Nguyen, D. Mrabet, and T. Do, 15226 (2008).

[59] T. He, D. Chen, X. Jiao, Y. Wang, and Y. Duan, Chem. Mater. **17**, 4023 (2005).

[60] Y. Mori, S. Tanemura, S. Koide, Y. Senzaki, P. Jin, K. Kaneko, a. Terai, and N. Nabotova-Gabin, Appl. Surf. Sci. **212-213**, 38 (2003).

[61] P. Gupta, R. Bhargava, and P. Poddar, J. Phys. D. Appl. Phys. **48**, 025004 (2015).

[62] P. Padhye and P. Poddar, J. Mater. Chem. A **2**, 19189 (2014).

[63] H. Lu, S. Wang, L. Zhao, B. Dong, Z. Xu, and J. Li, RSC Adv. **2**, 3374 (2012).

[64] R. Das and P. Poddar, J. Phys. Chem. C **118**, 13268 (2014).

[65] Z.R. Tian, J. a. Voigt, J. Liu, B. Mckenzie, and M.J. Mcdermott, J. Am. Chem. Soc. **124**, 12954 (2002).

[66] H. Imai, S. Iwai, and S. Yamabi, Chem. Lett. **33**, 768 (2004).

[67] R. Merryfield, M. McDaniel, and G. Parks, J. Catal. **77**, 348 (1982).

[68] S.B.M. Hagström, P.O. Hedén, and H. Löfgren, Solid State Commun. **8**, 1245 (1970).

[69] R.J. Iwanowski and J.W. Sobczak, **91**, 809 (1997).

[70] S.B.M. Hagström, G. Brodén, P.O. Héden, and H. Löfgren, Le J. Phys. Colloq. **32**, C4 (1971).

[71] A. J. Signorelli and R.G. Hayes, Phys. Rev. B **8**, 81 (1973).

# Chapter 3

## Optical properties of rare earth chromites

In this chapter, we have assigned phonon-modes for $DyCrO_3$, $SmCrO_3$ and $YbCrO_3$ nanoplatelets by Raman spectroscopy. To further study the spin-phonon coupling, we have performed temperature dependent Raman studies on $DyCrO_3$ as a representative. The band edge information obtained by UV-vis absorption spectroscopy for $DyCrO_3$, $SmCrO_3$ and $YbCrO_3$ indicated towards its promising application in photocatalytic activity, which has been studied for $DyCrO_3$ as a model system.

## 3.1    Introduction

In last one decade, researchers have shown renewed interest in the search for the multiferroic materials with magnetoelectric coupling due to their simultaneous ordering of electrical dipoles and spins. The coexistence of ferro/ferri/antiferromagnetic, ferroelectric, and ferroelastic properties in these materials make them suitable for different applications such as high density data-storage devices, spintronics, magnetoelectric sensors, and lead-free piezoelectrics.[1–4] Few of these materials show weak magnetoelectric (ME) coupling at much lower temperature than room temperature (RT), in which, the magnetization is controlled by applied electric field or the electric-polarization is controlled by the magnetic field. In solids, at microscopic level, spin-phonon coupling leads to the modulation of magnetic exchange due to any structural changes associated with phonon.[5] The spin-phonon coupling is a measure of phonon frequency dependence on the magnetic order of the system. This can be determined by measuring the change in the phonon frequencies by varying the temperature through the magnetic transition of the material.[6] "It is relevant to numerous phenomena exhibited by solids such as superconductivity, magnetic semiconductors, charge transport and ME effect in multiferroics."[5] Also, to develop new functionality in a material, the spin-phonon coupling can be useful as in case of $LaMnO_3$, where the desired magnetic order was stabilized with epitaxial strain. The spin-phonon coupling is essentially interesting and it has been studied extensively in oxides, particularly in multiferroics. For quantitative understanding of spin-phonon coupling, first principle density functional theoretical (DFT) calculation is known to be very effective.[6,7] The identification and quantification of phonon modes that couples strongly with the spin and the mechanism associated with the spin-phonon coupling can be inferred from DFT calculation.[8]

The spin-lattice coupling in the multiferroic materials contributes significantly to the interplay between the electric-polarization and magnetic ordering. In order to study these features in such materials, it is essential to study the lattice dynamics. In recent years, the Raman spectroscopy has emerged as a powerful non-destructive technique to study molecular and crystal lattice vibrations. It probes the zone-centre

phonons, and it is found to be very versatile technique as it can detect even subtle structural distortion in a oxide material.[9] There are several reports, which deal with the Raman studies of multiferroic materials. Recently, Weber *et al.* studied the phonon-spectra of $RCrO_3$ series to get a better understanding of its structure.[10] Feng *et al.* studied the pressure-dependent changes in the phase transition temperature of Dy-doped $HoMnO_3$ via. Raman spectroscopy.[11] In perovskites such as $RMnO_3$, $RFeO_3$, $RNiO_3$, $RCrO_3$ etc., the octahedral tilt angle or the distortion can be tuned by the ionic size of rare earth ion.[12] Among such materials, rare-earth chromites have attracted greater attention in the past owing to their ME properties, in addition to its rich and complex magnetic phases at very low temperature.[12–16] In orthochromites, the interplay between the magnetic and electric order can be understood by considering the spin-lattice coupling phenomenon. Recently, the room-temperature Raman-spectra of $LnCrO_3$ (Ln = Y, La, Pr, Sm, Gd, Nd, Dy, Ho, Yb, Er and Lu) have been reported and analyzed based on the symmetry associated with the structural distortion.[14,17–21] Though, manganites and ferrites have been studied extensively in the past, but, very few Raman studies are reported for chromites. [10,12,18]

In addition to the Raman measurements, the dielectric properties of the rare earth chromites have been studied but they are limited to few $RCrO_3$ (R= Gd, Sm).[12,22] Recently, Prado-Gonjal *et al*. have studied the dielectric properties of submicron-sized $RCrO_3$ particles.[23] However, most of the studies are reported at RT and above, while the magnetic transitions in orthochromites appear at much lower temperatures.[15,23] Therefore, the coupling between dielectric properties and magnetic anomalies is still not investigated in detail for the nanosized DCO as this subtle coupling appears at much lower temperature (much below the Nèel transition). Thus, there is a need to study the temperature and frequency dependence of the dielectric properties of DCO nanocrystallites and correlate with the interesting magnetic transitions at low temperature.

Though, the interest in this family of compounds (not limited to rare earth chromites) has largely remained confined to the study of the multiferroic properties. However, recent studies have revealed that the multiferroic materials can be classified as semiconductors rather than insulators.[24] This has attracted further attention to study

their photocatalytical and other light-harvesting properties such as solar photovoltaics and water-splitting. Among several multiferroic materials, bismuth ferrite (BFO) has gained a considerable interest in studying the photocatalytic activity due to its favorable band-gap of ~ 2.7 eV. The BFO nanoparticles showed enhanced photocatalytic properties under UV-visible light irradiation.[25] The rare earth chromites are known to be p-type semiconductors which shows electronic sensitivity toward humidity and various gases such as $H_2$, CO, NO, $N_2O$, and so forth, which is useful for sensor applications.[26,27] Apart from sensing application, doped-$LaCrO_3$ were found to be good candidates as a interconnect materials in solid oxide fuel cells.[28,29] For some doped chromites, catalysis properties towards hydrocarbon oxidation have also been investigated.[30] The rare earth chromites have an advantage over conventional photocatalytic materials such as titania as their rich optical nature provides absorption bands in visible range also (in contrast to pure titania).[31]

Thus, it is essential to explore the optical properties of rare earth chromites. In this chapter, we have summarized the optical properties of $RCrO_3$ (R= Dy, Sm and Yb) studied by Raman and UV-vis spectroscopy. We have investigated temperature-dependent Raman spectroscopy studies of DCO nanoplatelets in an effort to elucidate the origin of local structural distortion, and spin-phonon coupling in the orthochromites. These chromites are known to be ferroelectric and to investigate the possible magnetoelectric coupling, dielectric-spectroscopy has been carried out for DCO nanoplatelets. As a representative, we have chosen DCO for temperature dependent Raman, dielectric and photocatalytic studies.

## 3.2    Experimental and Characterization Details

The DCO, SCO and YCO nanoplatelets were prepared using the sol-gel technique. The details of the sample preparation and characterization are discussed in chapter 2. The same samples were used to carry out further studies.

### 3.2.1  Raman Spectroscopy:

Raman spectra were recorded on a HR-800 Raman spectrophotometer (Jobin Yvon-Horiba, France) using monochromatic radiation (achromatic Czerny-Turner type monochromator with silver treated mirrors) emitted by a He–Ne laser (633 nm), operating at 20 mW and with Raman-shift detection accuracy of $\pm$ 1 cm$^{-1}$ between 450 nm and 850 nm, equipped with thermoelectrically cooled (with Peltier junctions), multi-channel, spectroscopic-grade CCD detector (1024×256 pixels of 26 microns) with dark current lower than 0.002 electrons pixel$^{-1}$ s$^{-1}$ using a 100 X objective. In order to record the temperature dependent Raman spectra using cooling-heating stage, the samples (pressed into pellet) were mounted on a LINKAM THMS 600 heating/freezing stage to which a temperature programmer TP 94 was connected with a temperature controller and the temperature varied in the range of 93–300 K with a heating rate of 10 K/min. To maintain the stage at low temperature, liquid nitrogen was used. Temperature dependent Raman spectra of as-synthesized DCO nanoplatelets were recorded in a temperature range 93-300 K.

### 3.2.2  Dielectric spectroscopy:

For the dielectric measurements, the DCO polycrystallites were pressed into 13 mm circular pellet. To probe the dielectric response in the proximity of magnetic transitions, impedance spectroscopy was carried out in a temperature range 20-300 K using a Novacontrol Beta NB Impedance Analyser with a home-built sample holder coupled with a Janis make helium close-cycle cryostat based on expansion-compression cycles. The data were recorded in a frequency range 1 to $10^6$ Hz at 1 V (rms).

### 3.2.3  UV-vis-NIR spectroscopy:

UV-vis-NIR spectroscopy measurements were performed on a Jasco UV-vis-NIR (Model V570) dual beam spectrometer operated at a resolution of ~ 2 nm.

### 3.2.4  Photocatalytic activity:

The photocatalytic activity of the DCO nanoplatelets was studied by monitoring the degradation of methyl orange in aqueous medium under UV light using a 400 W mercury lamp. The reaction was carried out at room temperature by circulating cooling water in order to prevent thermal catalytic effect. Prior to the UV illumination, the suspensions were stirred continuously in dark to reach the equilibrium between catalyst and methyl orange (MO) dye. The aqueous suspensions of MO with the concentration of 15 mg/L and the DCO powder (1.57 g/L) were placed in a round bottom flask followed by continuous stirring. The degradation of MO was evaluated by centrifuging the retrieved samples and recording the intensity of absorption peak of methyl orange (~ 462 nm) relative to its initial intensity ($C/C_0$) using a spectrophotometer.

# Section 3.3

# Study of spin-phonon and magnetoelectric coupling in DyCrO₃ nanoplatelets using Raman and dielectric spectroscopy

_____

In this section, we report the phonon-mode assignment of $DyCrO_3$ nanoplatelets by Raman spectroscopy. The temperature dependent Raman studies were carried out to study the spin-phonon coupling in $DyCrO_3$. The impedance spectroscopy reveals anomalies in dielectric constant vs. temperature curve in the proximity to the magnetic transitions, thereby, hinting towards the possible weak magnetoelectric coupling in $DyCrO_3$ nanoplatelets. The UV-vis absorption spectroscopy and photocatalytic activity of $DyCrO_3$ nanoplatelets have been studied in detail.

_____

### 3.3.1 Raman spectroscopy:

Raman scattering is a powerful technique to measure the structural anomalies as it is sensitive to the crystal symmetry. The perovskite DCO has an orthorhombic structure belonging to *Pbnm* space group with four formula units in the primitive cell. The irreducible representation $\Gamma$ for the *Pbnm* space group of the Raman-active modes at the zone centre can be decomposed [32] and represented as:

$$\Gamma(Raman) = 7A_{1g}+7B_{1g}+5B_{2g}+5B_{3g} \dots\dots\dots\dots\dots\dots\dots\dots\dots\dots\dots\dots\dots\dots\dots\dots(1)$$

These 24 modes are Raman active modes and can be classified as two symmetric ($A_g + B_{1g}$), four antisymmetric octahedral stretching modes ($2B_{2g} + 2B_{3g}$), four bending modes ($A_g + 2B_{2g} + B_{3g}$), and six rotation or tilt modes of the octahedra ($2A_g + B_{1g} + 2B_{2g} + B_{3g}$). The other eight modes are usually associated with the dysprosium cation movement ($3A_g + 3B_{1g} + B_{2g} + B_{3g}$).[32] However, this space group also consists of other 25 optical modes which include 8 optical modes with symmetry $A_u$, and three acoustic modes. These 36 modes are not Raman active. The irreducible representation for these modes can be done as [32,33]

$$\Gamma(IR) = 9B_{1u}+7B_{2u}+9B_{2u}. \qquad \dots\dots\dots\dots\dots\dots\dots\dots\dots\dots\dots\dots\dots\dots(2)$$

$$\Gamma(acoustic) = B_{1u}+B_{2u}+B_{2u} \qquad \dots\dots\dots\dots\dots\dots\dots\dots\dots\dots\dots\dots\dots(3)$$

$$\Gamma(silent) = 8A_u \qquad \dots\dots\dots\dots\dots\dots\dots\dots\dots\dots\dots\dots\dots(4)$$

Weber *et al.* assigned these modes by following various previous reports on Raman spectroscopy on RCrO$_3$ family of compounds.[10] The structural distortion from the parent cubic perovskite structure may result from (i) the rotation of CrO$_6$ octahedra along [010] and [101] axes, (ii) displacement of $Dy^{3+}$ along certain direction, and (iii) the Jahn-Teller (J-T) distortion.[34] The $Cr^{3+}$ion is a Jahn-Teller (JT) in-active cation and no dispersion in the Cr-O bonds are expected.
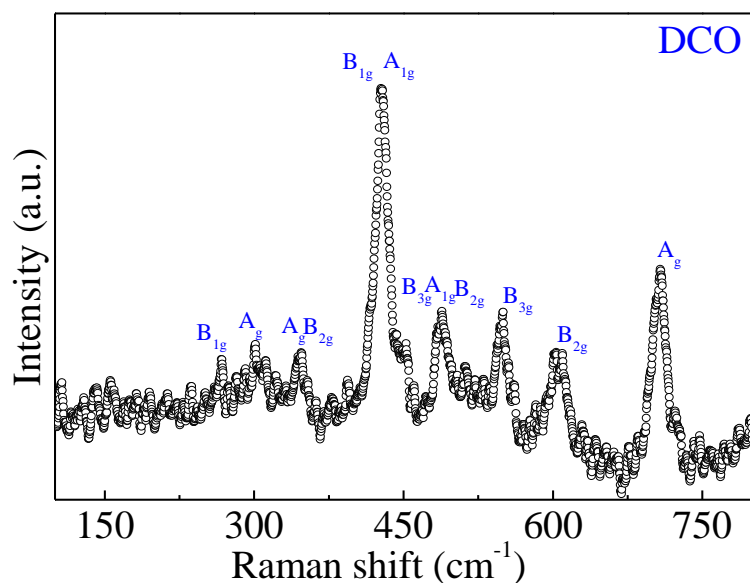
*Figure 1. Room temperature Raman spectrum of DCO nanoplatelets.*

Such distortion (tilt, octahedra distortion and *A*-cation displacement) breaks the cubic symmetry in the perovskite which cannot be detected by simple diffraction techniques, but it is possible to study by Raman spectroscopy.

In the present study, we tried to assign symmetry to the phonon modes based on orthorhombic structure with space group of *Pbnm* using RT Raman spectroscopy study.[18,19] The **Figure 1** represents the RT- Raman spectrum of DCO nanoplatelets in the spectral range $100 - 800$ cm$^{-1}$ showing prominent Raman modes near $\sim$ 295, 346, 427, 488, 547, 602, and 707 cm$^{-1}$. The modes involving $Dy^{3+}$ atomic vibration show-up at lower wavenumber, below 200 cm$^{-1}$.[10] In the region above 200 cm$^{-1}$, phonon modes at 265 and 300 cm$^{-1}$ corresponds to the in-phase and out-of-phase octahedral rotation around y-axis. The doublets observed around $\sim$ 346 cm$^{-1}$ ($A_g$ and $B_{2g}$) are related to the R-O vibration. The phonon modes, $A_g$ and $B_{1g}$, at $\sim$ 429 cm$^{-1}$ are associated with the in-phase and out-of-phase octahedral rotation around x axis. It was surprising to see an intense mode at $\sim$ 429 cm$^{-1}$ as compared to other Raman modes. The Raman mode at $\sim$ 488 cm$^{-1}$ consists of a very complex region involving overlapping and crossing of several bands.[10] The presence of this mode at $\sim$ 488 cm$^{-1}$ is observed for most of the distorted $RCrO_3$ compounds and can be assigned to $B_{3g}$,

$A_{1g}$ and $B_{2g}$ symmetry, respectively. This symmetry allows the crossing of modes resulting into single mode with same frequency at ~ 488 cm$^{-1}$ as observed for the DCO nanoplatelets. The sharp peak around ~ 550 cm$^{-1}$ mainly involves the stretching vibration ($B_{3g}$) of CrO$_6$ octahedra. The phonon-mode at ~ 610 cm$^{-1}$ involves the in-phase O$_2$ stretching ($B_{2g}$). It is interesting to note that in our study, we also found a peak in high frequency region *i.e.* near 707 cm$^{-1}$ which can be assigned to the defects caused in the CrO$_6$ octahedra by *Dy$^{3+}$*cations. Raman spectrum (**Figure 1**) for the present DCO sample looks analogous to the spectrum reported for bulk DCO. [35]

### 3.3.2  Temperature dependent Raman Spectroscopy:

In a magnetic material, the effect of temperature on Raman modes of frequency ω is generally given as :[36]

$$\omega\ (T) = \omega(0) + \Delta\omega_{qh}(T) + \Delta\omega_{anh}(T) + \Delta_{\omega sp\text{-}lat}(T) + \Delta_{\omega el\text{-}ph}(T) \quad ....................(5)$$

where, ω(0): frequency at zero K.

$\Delta\omega_{qh}(T)$:   change in frequency due to quasi anharmonic effect.

$\Delta\omega_{anh}(T)$: change in frequency due to intrinsic anharmonic contribution i.e. the anharmonic ferquency shift at constant volume

$\Delta_{\omega sp\text{-}lat}(T)$: change in frequency due to spin-lattice coupling caused by modulation of exchange integral by lattice vibrations

$\Delta_{\omega el\text{-}ph}(T)$: change in frequency due to electron-phonon coupling

The last term $\Delta_{\omega el\text{-}ph}(T)$ can be neglected if the carrier concentration is low.

Due to the complexity of the orthochromites, the ferroelectric behavior is described by considering both order-disorder and displacive type aspects. The order-disorder and displacive behavior are characterized by pseudo-spins and lattice distortions, respectively.[37,38] In general, the magnetic and ferroelectric subsystem in multiferroic materials are expressed in terms of the spin-operator 'S' and pseudo-spin operators 'B'. Thus, the magnetoelectric coupling (H$_{mf}$) is the direct influence of magnetic order

parameter on the polar order parameter. Thus, both the subsystems are simultaneously influenced by lattice distortions and spin-phonon interactions.[39] The spin-phonon interactions has to be discussed within pseudo spin approach and for multiferroic materials, the pseudo spin-phonon coupling is expressed as $H_{fph}$ (ferroelectric order and phonon coupling) and $H_{mph}$ (magnetic order and phonon coupling), respectively.[39]

In orthochromites, one observes interaction between antiferromagnetic and ferroelectric subsystem. In order to see the origin of Raman active modes and to better understand the signature of magnetic transition, Raman spectra of the DCO nanoplatelets were investigated in a temperature range of 93-273 K (**Figure 2(a)**). As seen from the **Figure 2(b)**, following changes can be noticed in the spectra: (1) an increase in the intensity of all the major peaks was observed after cooling from 300 K to 153 K and decreases with the temperature down to 93 K. (**Figure 2(b) inset**) (2) higher wave-number peaks become broader close to Néel temperature ($T_N \sim$ 143 K).
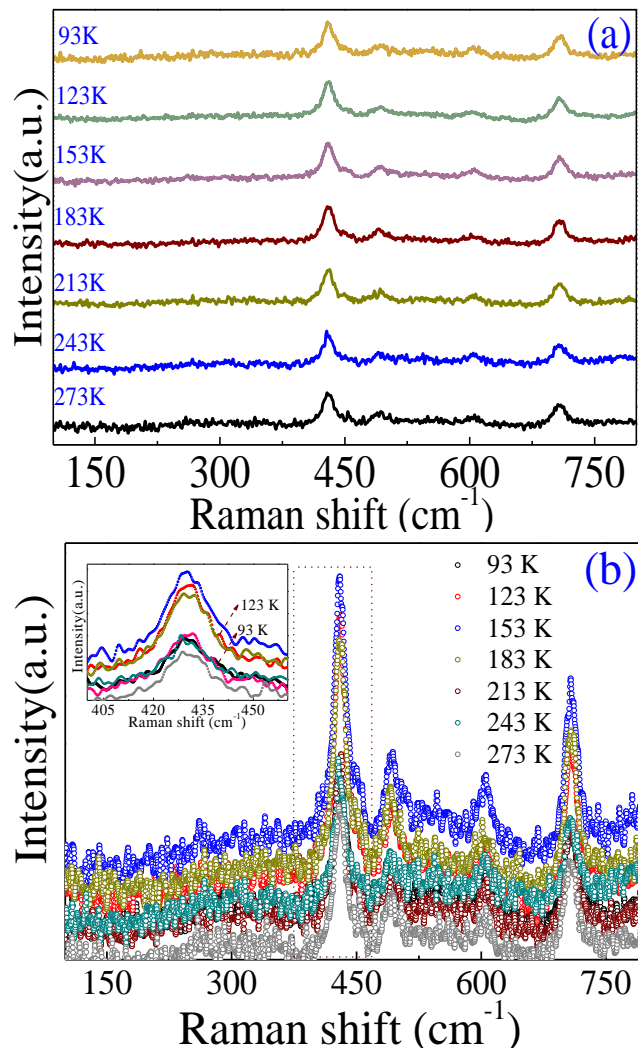
*Figure 2. (a, b)Temperature dependent Raman Spectra of DCO nanoplatelets in a temperature range 93 K - 273 K. Inset of 2(b) showing the change in the peak intensity with respect to the temperature.*

Raman line-width are closely associated with the phonon lifetime, which can provide the information on spin-phonon coupling in the system. To observe the spin-phonon coupling, it is better to study the temperature dependency of line-width rather than phonon frequencies as it will not be affected by parameters such as reduction in unit cell volume e*tc*. The temperature dependence of the line-width of (a) in-phase and (b) out-of-phase octahedral rotation (265 cm$^{-1}$ and 300 cm$^{-1}$) in the temperature range 93- 273 K is plotted in **Figure 3**.
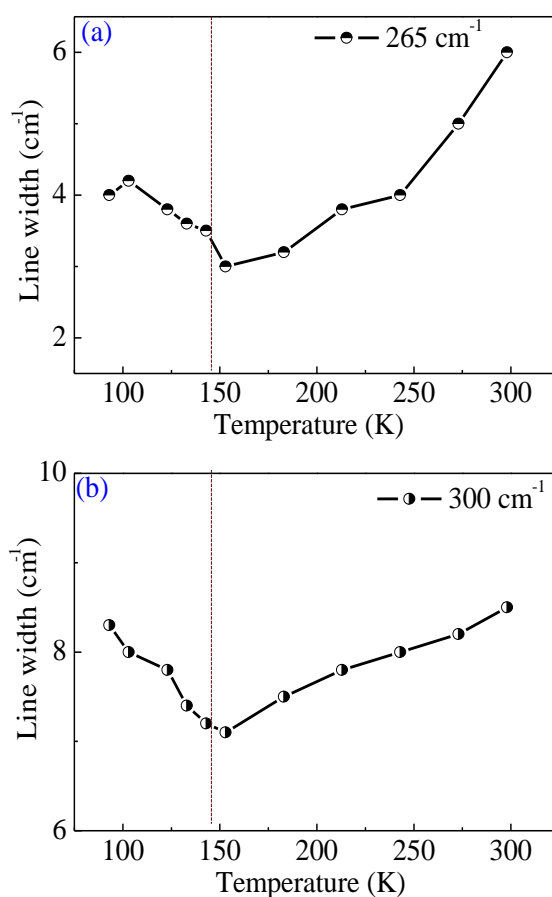


*Figure 3. The temperature dependence on phonon line width of (a) B$_{1g}$ and (b) A$_g$ mode (265 and 300 cm$^{-1}$), representing the in-phase and out of phase octahedral rotation in DCO nanoplatelets.*

We observe an anomaly near ~ $T_N$ (143 K) for both in-phase and out-of-phase octahedra  rotation of the $CrO_6$ octahedral which reflects the tilting of octahedra and its deviation from 180° which is affected by the magnetic interaction of $Dy^{3+}$ and $Cr^{3+}$ spins. We observe that the line-width decreases with the temperature till ~ $T_N$ and increases below ~ $T_N$. The Raman line-width tends to decrease with temperature due to anharmonicity but, here, we observe an increase below ~ $T_N$ signifying the contribution from change in phonon lifetime. This change in phonon lifetime is greatly affected by the processes such as spin-phonon coupling and electron-phonon coupling.[36] Since phonon line-width decreases with decreasing temperature due to reduced anharmonicity, the increase in the phonon line-widths below $T_N$ cannot be explained without taking the intricate coupling between the phonons and spin degrees of freedom into account which become prominent below the magnetic transition temperature $T_N$. The sharp increase in the phonon line-width below $T_N$ clearly suggest the strong coupling between these two degrees of freedom; the spin-phonon coupling will also affect the phonon decay rate below the $T_N$ where, the optical phonon may decay into another phonon and magnon/or two magnons.

The temperature dependence of phonon frequencies also provides an insight into the spin-phonon interaction in a magnetic system. The spin-phonon interaction constant (R) is positive or negative leading to the hardening or softening of the phonon mode, respectively.[39] For a closer inspection, phonon frequencies (429 cm$^{-1}$, 485 cm$^{-1}$ and 550 cm$^{-1}$) (**Figure**s **4(a-c)**) and their corresponding line-widths (**Figure 4(d-f)**) were plotted in a temperature range ~ 93-300 K, respectively. **Figure 4(a)** reveals the change in Raman spectra in the vicinity of the Nèel temperature ($T_N$ ~ 143 K). The mode at 429 cm$^{-1}$ gradually hardens (phonon frequency increases) with increasing temperature and shows an anomaly near the $T_N$. The hardening of the Raman mode is attributed to the thermal contraction while, softening (phonon frequency decreases) of the mode occurs below the $T_N$; which may be related to different magnetic interaction between $Dy^{3+}$ and $Cr^{3+}$ spins.
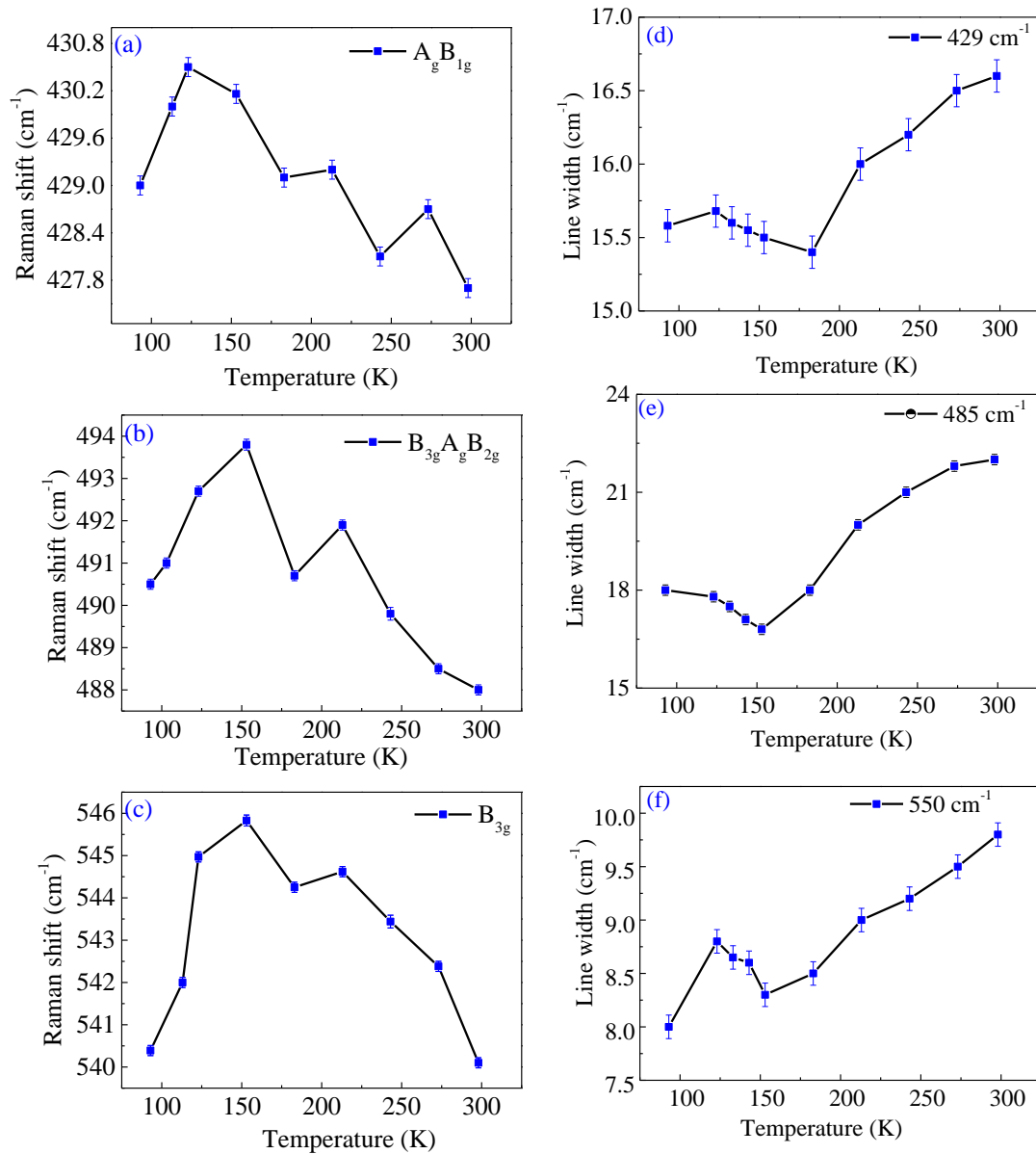
*Figure 4. The temperature dependence of phonon frequency and the corresponding line-width of phonon modes at (a, d) 429 cm⁻¹, (b, e) 485 cm⁻¹, (c, f) 550 cm⁻¹, respectively. The $A_{1g}$ mode (485 cm⁻¹) representing Cr-O vibration in $CrO_6$ octahedral of DCO nanoplatelets.*

The anomalous behavior of $A_g$ and $B_{1g}$ modes (429 cm⁻¹) in the DCO may be due to the combined effect of thermal contraction and spin-phonon coupling. To get a deeper insight into the origin of anomalous behavior of 429 cm⁻¹ mode, the

corresponding line-width with respect to the temperature was plotted (**Figure 4(d)**). The change in Raman line-width was found to be non-monotonous in the DCO nanocrystallites. An anomalous increase in line-width below $\sim T_N$ is mainly due to the change in the phonon lifetime contributing from the spin-phonon coupling.[36] The line-width plot shows a dip near the $T_N$ and a sudden increase below the $T_N$, suggesting the contribution from the various processes such as spin-phonon coupling and electron-phonon coupling.[36]

The temperature dependence of Raman mode ($B_{3g}$, $A_g$, $B_{2g}$) at 488 cm$^{-1}$ and their corresponding line-width are shown in **Figure 4(b, e)**. As analyzed, the phonon frequency shows an anomaly at around $T_N$ and a sudden increase in phonon frequency below $T_N$ suggests the change in the phonon lifetime. Moreover, the decrease in line-width till $T_N$ with decrease in temperature can be accounted for the reduction of anharmonic phonon decay in the DCO nanoplatelets and increase in line width below $T_N$ suggesting the presence of spin-phonon coupling.[36,40]

To verify, whether the phonon mode, $B_{3g}$ (550 cm$^{-1}$) is associated with the stretching vibrational mode of CrO$_6$ octahedra, we analyzed the temperature dependent behavior of phonon frequency and corresponding line width as shown in **Figure 4(c, f)**. Similar to the other modes as explained above, we have observed an anomaly around the $T_N$. The decrease in the phonon frequency below $T_N$ suggesting the softening of phonon mode which also demonstrates the Dy-ion displacement due to the weak ferromagnetism originated from the Cr-ordering.[36] The displacement of Dy-ion and stretching of CrO$_6$ octahedra give rise to the ferroelectricity in this class of materials. The observed decrease in line-width with decrease in temperature is associated with the reduction of anharmonic phonon decay in the DCO nanoplatelets.[36] The broadening of line-width below $T_N$ in $B_{3g}$ mode also suggest the presence of spin-phonon coupling as full width at half maximum (FWHM) is due to the change in the phonon lifetime.

From temperature dependent Raman studies (**Figure 2(b)**), we can infer that, in DCO nanoplatelets, the Raman intensity was found to increase till $T_N$ which drops

at ~ 123 K and decreases further at ~ 93 K. This behavior can be understood by considering the fact that the increased $CrO_6$ octahedra distortion and the shortened bond results into the enhanced Raman intensity and hardening of Raman frequencies. Also, the anomalous behavior of line-width with the change in temperature can be accounted to the spin-phonon coupling in the DCO nanocrystallites.

### 3.3.3  Dielectric spectroscopy:

In order to understand the dielectric response of the DCO polycrystallites, frequency and temperature dependent plots of real and imaginary parts of complex permittivity of the DCO nanoplatelets in a temperature range of 20-300 K are shown in **Figure 5**. As seen from **Figure 5(a)** and **5(b)**, the ε′ and ε ″ values decrease with the increase in frequency. However, at low frequency ($\omega \ll 1/\tau$), dipoles follow the field and the increased value of ε′ and ε′′ is observed. In addition to the interfacial, dipolar, atomic, ionic, and  electronic contribution in dielectric constant, the dielectric behavior in nanostructures is also influenced by interparticle interfaces and defects that can cause a change of space charge distribution.  These space charge oscillate when an ac-electric field is applied and get trapped by these defects leading to the additional space charge polarization . At higher frequency, dipoles no longer follow the field and lag behind. At low frequency, larger values of ε′ are mainly due to contribution from the interfacial, dipolar, atomic, ionic and electronic polarization and can be explained by the Maxwell-Wagner effect.[41] The higher value of dielectric constant can be accounted to the conduction in the grain and grain boundary of the material as they are separated by the insulating intergrain barriers.[42] Moreover, with the increase in the temperature from 20 K to 300 K, the dipoles overcome the thermal barrier and orients themselves in the field direction giving larger value of dielectric constant as shown in **Figure 5(a) & 5(b)**.[43]
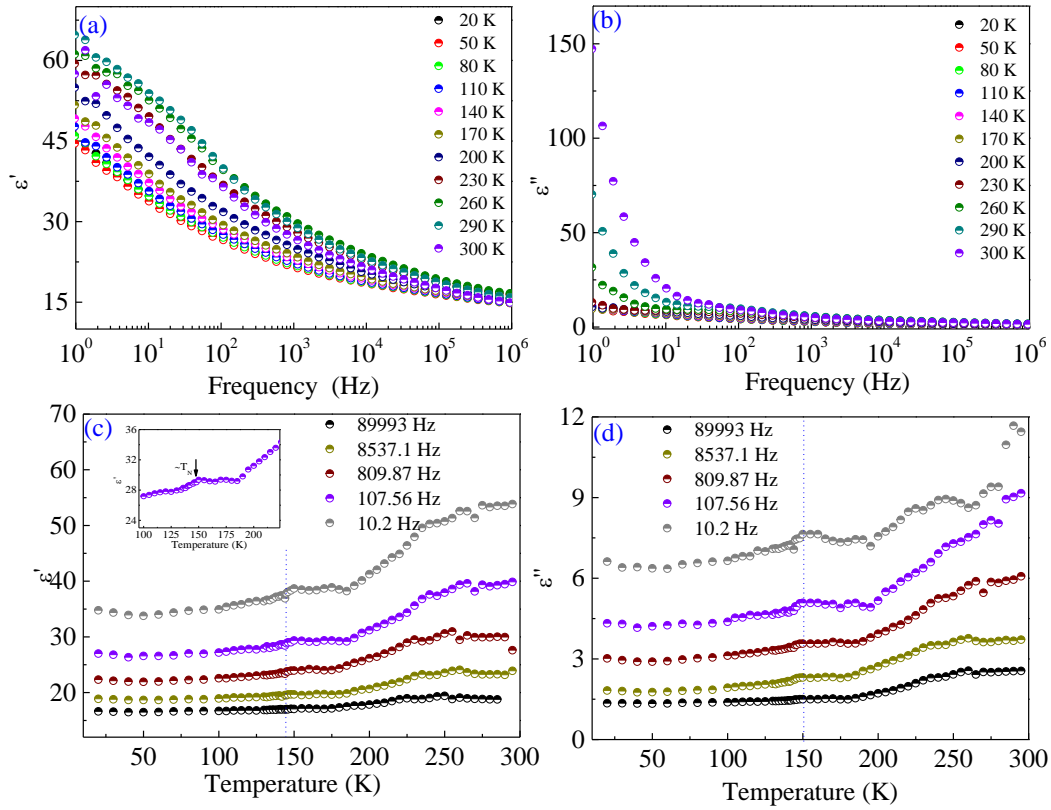
*Figure 5. The frequency and temperature dependence of (a, c) real part (b, d) imaginary part of permittivity values in the temperature range of 20- 300 K for DCO nanoplatelets.*

The temperature dependence of $\varepsilon'$ and $\varepsilon''$ at different frequencies also show the increasing trend in the dielectric constant value with the increase in temperature till 300 K as shown in **Figure 5(c) & 5(d)**. However, below 100 K, the $\varepsilon'$ and $\varepsilon''$ values show a plateau (inset of **Figure**s. 5(c)) above which the gradual increase is observed with an anomaly at $\sim$ 144 K ($T_N$) suggesting a weak coupling between the magnetic and electric ordering. Above $\sim$ 150 K, the dielectric permittivity values increased further. The $\varepsilon'$ and $\varepsilon''$ values strongly depend on the frequency and increases with decrease in the frequency. Similar behavior was observed in the (**Figure 5(a) & 5(b)**) frequency spectrum also.

The variation of dielectric loss (tan $\delta$) with frequency at different temperatures is shown in **Figure 6(a)**.
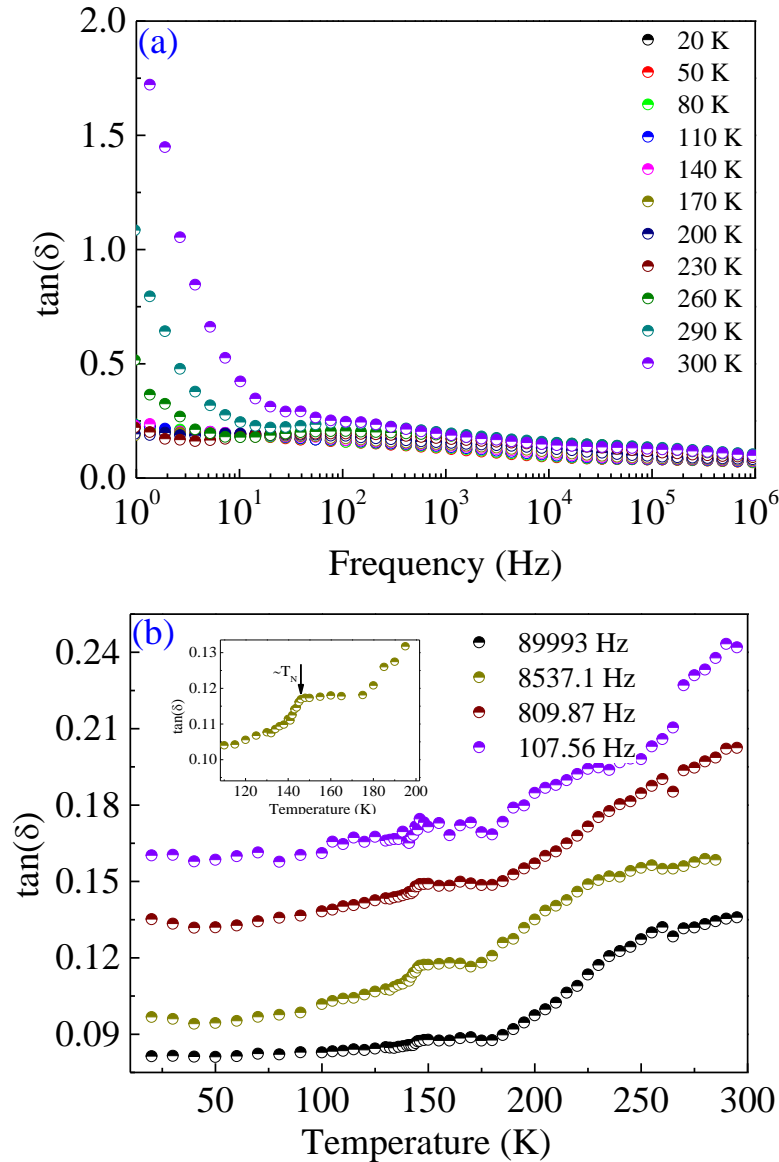
*Figure 6. (a) Frequency dependent dielectric loss (tan δ) value in a temperature range 20-300 K. (b) Temperature dependent dielectric loss at varying frequency showing an anomaly at $T_N$ ~144 K for DCO nanoplatelets. Inset shows the zoomed view at ~$T_N$.*

The dielectric loss value increases at lower frequency and vice-versa giving flatness at higher frequency. The tan δ value increases after certain temperature, as dipoles no longer follow the field direction. The increase in tan δ can be due to the increase in number of charge carriers in DCO by thermal activation. It can be seen from the **Figure** that there is a knee above ~ $10^4$ Hz followed by an increase in loss value. We

see a clear peak in the plot (**Figure 6(b)**) of temperature dependent dielectric loss at ~ 144 K in close proximity with the magnetic transition ($T_N$) (inset of **Figure 6(b)**) suggesting the weak coupling between electric and magnetic order parameter.

### 3.3.4  UV-visible spectroscopy:

As the UV-vis absorption edge is relevant to the band energy, it is essential to study the optical absorption of the DCO nanoplatelets. In rare earth chromites, the energy states consist of $R^{3+}$: 4f levels, filled $O^{2-}$: 2p band , partially filled $Cr^{3+}$: 3d, empty $Cr^{3+}$:4s band and $R^{2+}$:4f $^{n+1}$ levels or extremely narrow bands.[44]  In a similar fashion, $Dy^{3+}$ ions have half-filled $4f^7$ electronic configuration and can have $4f$-$4f$, $4f$-5d transition. It can also be associated with charge transfer transitions. **Figure 7(a)** shows the UV-visible absorption spectrum of the DCO nanoplatelets. The transitions involving $4f$-$5d$ and charge transfer cannot be detected due to the limitation of our instrument as it appears at much higher energies. The absorption spectrum of DCO showed two peaks at ~ 455 nm and ~ 603 nm which can be attributed to the $^4A_2$ to $^4T_2$ and $^4T_1$ transitions, respectively. The observed transition can be explained by considering octahedral crystal field splitting.[44–46] The $4f$ level splits into singlet ground state ($^4A_2$) and triplet excited state ($^4T_2$ and $^4T_1$).[44,45,47] The presence of $Cr^{3+}$centers in DCO gives the light green color to the material.[44,48] The bands at ~ 455 nm and ~ 603 nm, are associated with the vibrational transitions of $Cr^{3+}$ ion.[46,49] The observed bands can also be assigned due to the Zeeman splitting of an excited electron due to the local field of $Dy^{3+}$ ion.
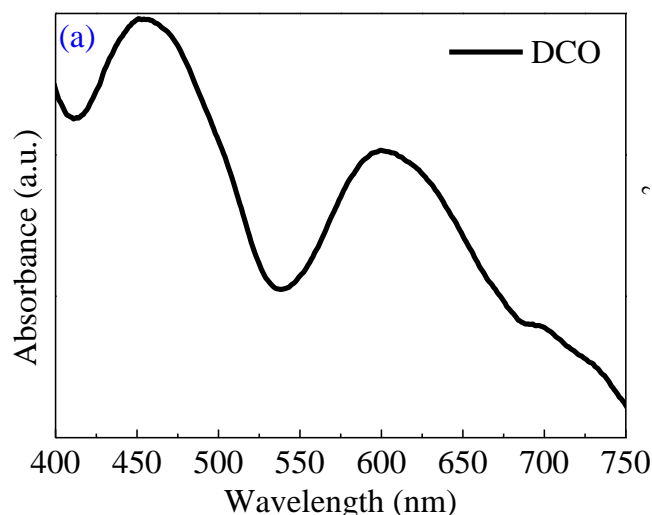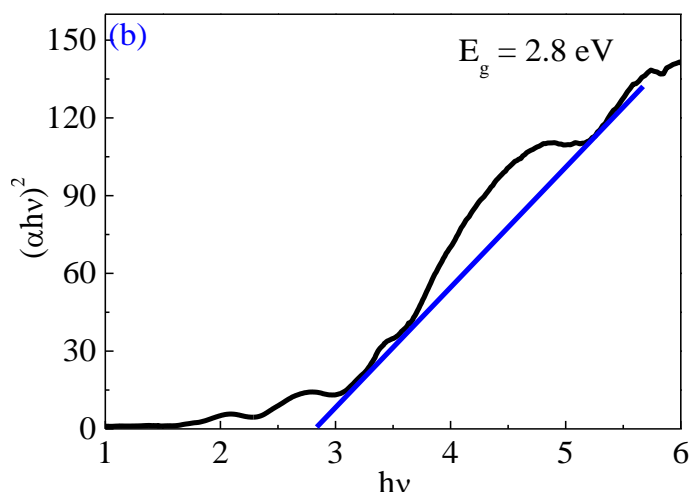
*Figure 7. (a) UV-Vis absorption spectrum and (b) band edge energy of DCO nanoplatelets.*

The bandgap of the DCO nanoplatelets is calculated from the tangent line in the plot of $(\alpha h\upsilon)^2$ against $h\upsilon$ (where $\alpha$ is absorption coefficient and $h\upsilon$ is photon energy) and found to be ~ 2.8 eV as shown in **Figure 7(b)**. Thus, the band gap obtained for the DCO nanoplatelets indicates towards the possibility of utilizing UV-vis light for photocatalysis. However, perovskites such as bismuth ferrite (BFO) have been studied a lot for their photocatalytic activity as the band gap of BFO could be tuned from ~ 1.82 to ~ 2.27 eV for different morphologies.[50]

## 3.3.5  Photocatalytic activity:

The band edge information on DCO nanoplatelets suggested it as a possible candidate for photocatalysis. The photocatalytic activity of the DCO nanoplatelets was evaluated by the degradation of the methyl orange (MO) under UV illumination. The sequential evolution of the spectral changes taking place during the photodegradation of MO with DCO nanoplatelets is displayed in **Figure 8(a)** and time-dependent photodegradation is illustrated in **Figure 8(b)**.
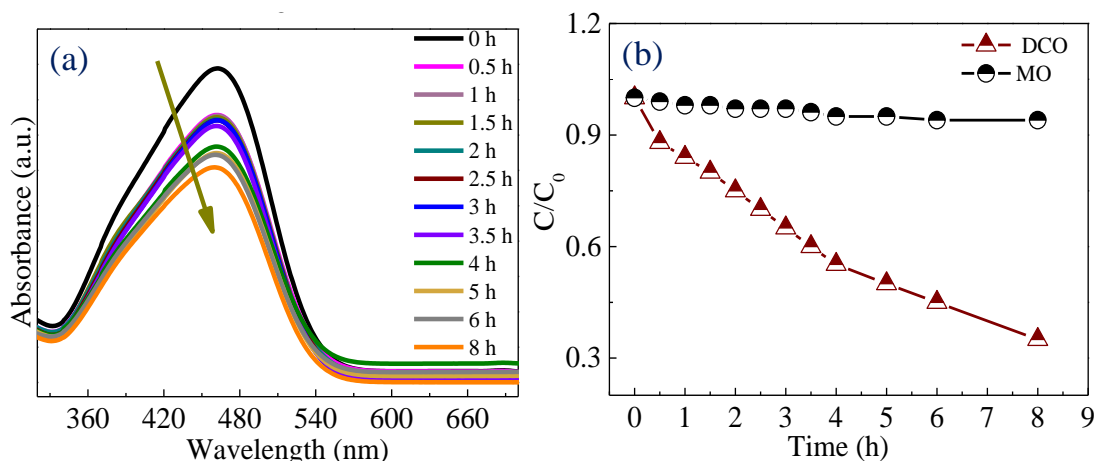
*Figure 8. (a) UV-Vis absorption spectra and (b) photodegradation efficiency of MO as a function of irradiation time under UV light by DCO nanoplatelets.*

The sample suspensions were magnetically stirred and kept in dark for ~ 4 h to achieve the adsorption-desorption equilibrium between photocatalyst and MO. The reaction kinetics was plotted as $(C/C_0)$ against time (t), where $C_0$ is the initial concentration and C is the final concentration of dye. The characteristic absorbance peak of MO was found at $\lambda$ = ~ 463 nm. The degradation of MO without photocatalyst under UV light is extremely slow and only 4 % MO was degraded after 8 h of illumination. However, in presence of DCO as a photocatalyst, the rate of MO degradation increased to 55 % after 6 h UV irradiation. After 8 h UV-vis irradiation with DCO, the MO degradation rate was saturated to about 65 %. The possible explanation for the efficient degradation of MO using DCO as a catalyst can be understood by considering DCO as a semiconductor rather than insulator.[25] The rare earth chromites are known as p-type semiconductor due to the conduction of holes from $Cr^{4+}$ to $Cr^{3+}$ centers. Owing to the native defects in $RCrO_3$, there exist a $Cr^{4+}$ centers and presence of these defects results in the enhance conduction of electrons, which in due course increases the formation of $OH^-$ radical responsible for MO degradation efficiently. [44] From these studies, we can infer that DCO can be used as a potential photocatalyst.

### 3.3.6  Conclusions

In conclusion, Raman spectroscopy has provided significant information on the lattice-distortion and their variation with the temperature. The temperature dependent Raman spectra of the DCO nanoplatelets and the associated phonon-modes provide a better understanding of structural investigation in the DCO nanoplatelets. The observed anomalies around Nèel temperature for all the modes illustrate the possible spin-phonon coupling in the DCO nanoplatelets. A weak magnetoelectric coupling is observed for the DCO nanoplatelets by impedance spectroscopic studies, showing a signature in the vicinity of the Nèel transition. The band-edge information of the DCO nanoplatelets raised a probability of using it as a photocatalyst. The DCO nanoplatelets were found to be an efficient photocatalyst in degrading the MO to 65 % after 8 h UV illumination. Moreover, in context to above, other rare earth chromites can also be used as a promising candidate for photocatalysis, which is addressed in next section.

# Section 3.4

# Optical properties of SmCrO₃ polycrystallites

_____

In this section, we report the phonon-mode assignment of $SmCrO_3$ nanoplatelets by Raman spectroscopy. The UV-vis absorption spectroscopy of $SmCrO_3$ nanoplatelets have been studied in detail.

_____

### 3.4.1 Raman spectroscopy:

**Figure 1** shows the Raman spectrum of $SmCrO_3$ (SCO) in the spectral range of 100-650 $cm^{-1}$. SCO has an orthorhombic structure (*Pbnm*) and irreducible representation for *Pbnm* space group of Raman active modes that can be represented as: [32]

$$\Gamma(Raman) = 7A_{1g}+7B_{1g}+5B_{2g}+5B_{3g}. \quad ...........................................................(6)$$
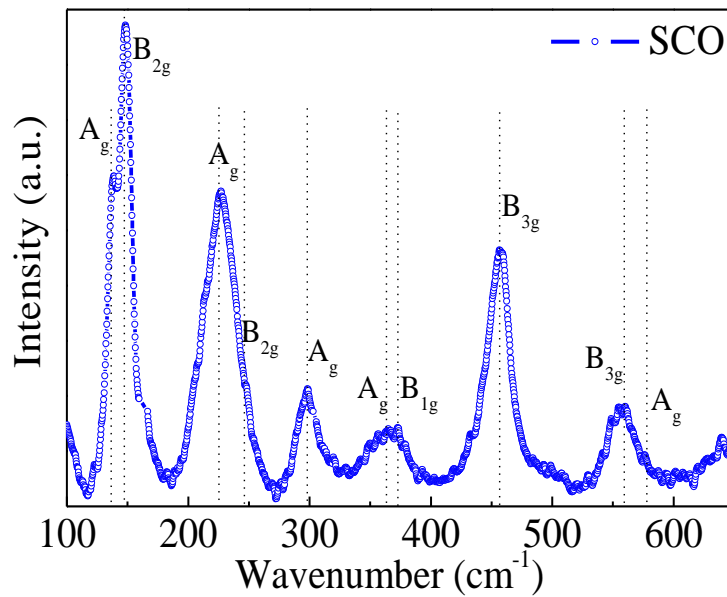


*Figure 1. Room temperature Raman spectrum of SCO polycrystallites. The vertical dotted lines depict the peak positions corresponding to various modes.*

The SCO polycrystallites, at room temperature, show prominent Stokes-shift peaks at ~137, 147, 226, 247, 304, 364, 456, and 557 $cm^{-1}$. The bonds containing the heavier atoms is likely to vibrate at lower wave number and two sharp $A_g$ and $B_{2g}$ modes at 137 and 147 $cm^{-1}$can be assigned to Sm-atomic vibrations. The region below 300 $cm^{-1}$, where two $A_g$ and $B_{2g}$ modes of same symmetry are likely to interact and mix, resulting into the transfer of their vibrational character.[51] The higher $B_{2g}$ mode is more likely due to the R cationic shift and lower one ($B_{2g}$) is mainly due to the $CrO_6$ octahedral rotation.[10] The singlet at 304 $cm^{-1}$ is related to the Sm-O vibration. The $A_g$,

$B_{1g}$ and $B_{3g}$ modes at 364, 375 and 456 $cm^{-1}$ correspond to the bending modes of O-Cr-O within the octahedra.[52] The Raman modes at 557 $cm^{-1}$ and 577 $cm^{-1}$ can be attributed to the   bending ($B_{3g}$) and antistretching vibration modes ($A_g$) of $CrO_6$ octahedral.[36]

## 3.4.2  UV-visible spectroscopy:

It is essential to study the optical absorption and the absorption edge which are equally important, especially in connection with the theory of electronic structure of materials. Here, we study the optical absorption of the SCO nanoplatelets. Moreover, determination of band gap is an important feature to study as they determine their wide application in optoelectronics.[53] **Figure 2(a)** shows the UV-visible absorption spectrum of the SCO nanoplatelets. In rare earth chromites, the energy states consist of $R^{3+}$: 4f levels, filled $O^{2-}$: 2p band , partially filled $Cr^{3+}$: 3d,  empty $Cr^{3+}$:4s band and $R^{2+}$:4f $^{n+1}$ levels or extremely narrow bands.[44]  The $Sm^{3+}$ ion shows absorption bands in the near infrared region which cannot be detected due to the limitation of our instrument as it appears at much higher energies. Presence of two prominent peaks at around 455 nm and 608 nm is attributed to the transition of O 2p –Cr 3d $_{t2g}$ and Cr 3d $_{t2g}$ –Cr 3d $_{eg}$ in SCO, respectively. The observed transition can be explained by considering the octahedral crystal field splitting.[44–46] The 4f  level splits into singlet ground state ($^4A_2$) and triplet excited state ($^4T_2$ and $^4T_1$).[44,45,47] The presence of $Cr^{3+}$centers in SCO gives the light green color to the material.[44,48] The bands at ~ 455 nm and ~ 608 nm, are associated with the vibrational transitions of $Cr^{3+}$ ion and can also be assigned due to the Zeeman splitting of an excited electron due to the local field of $Sm^{3+}$ ion.[46,49]

The bandgap of the SCO nanoplatelets is calculated from the tangent line in the plot of $(\alpha h\upsilon)^2$ against $h\upsilon$ (where $\alpha$ is absorption coefficient and $h\upsilon$ is photon energy) and found to be ~ 3.1 eV as shown in **Figure 2(b)**. Thus, the band gap obtained for the SCO nanoplatelets indicates towards the possibility of utilizing UV-vis light for photocatalysis.
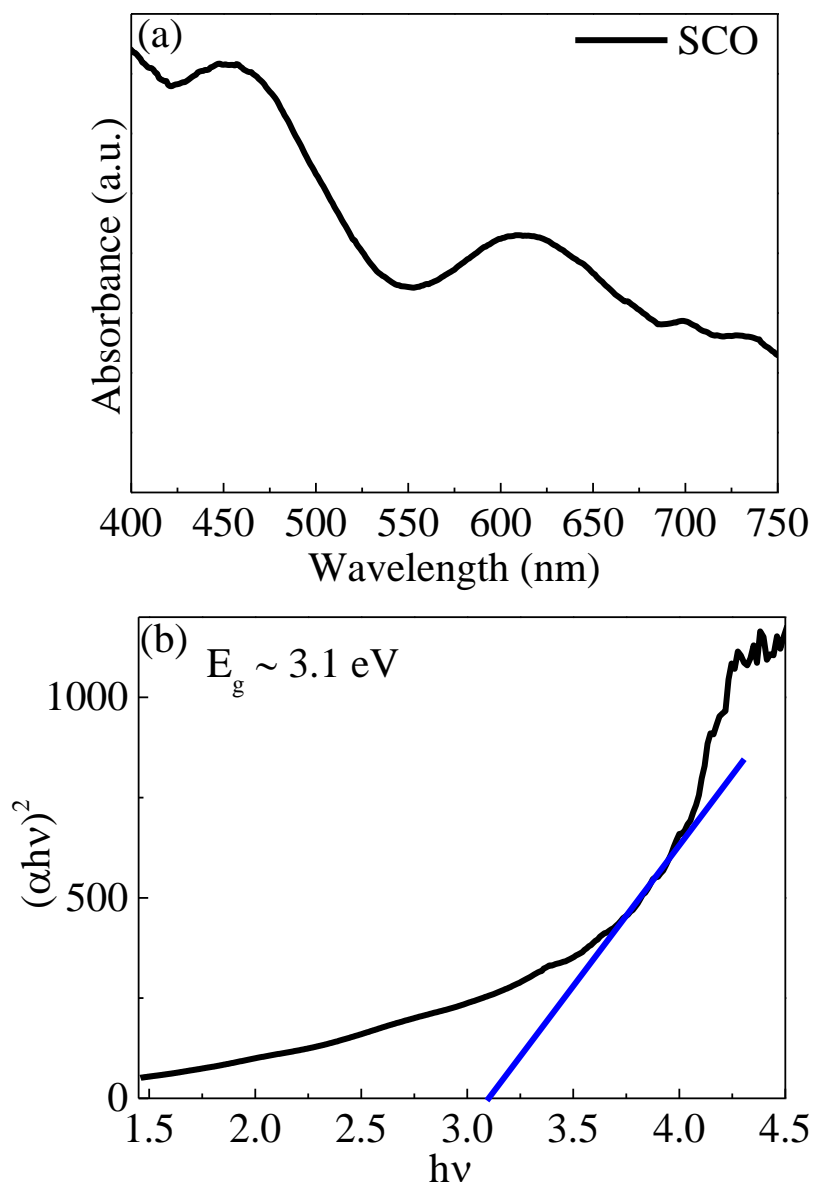
*Figure 2. (a) UV-Vis absorption spectrum and (b) band edge energy of SCO nanoplatelets.*

### 3.4.3  Conclusions

The as-synthesized SCO polycrystallites were studied for its optical properties in detail using Raman and UV-vis spectroscopy. Room temperature Raman studies of SCO revealed the information on the modes related to Sm-O, Cr-O vibration and rotation. Further, we observed modes at lower wavenumber corresponding to the Sm atomic vibrations and below 300 cm$^{-1}$, mode mixing due to the same symmetry is also

observed. The band gap obtained for the SCO nanoplatelets indicates towards the possibility of utilizing it for photocatalytic studies or other light harvesting application.

# Section 3.5

# Optical properties of YbCrO$_3$ nanoplatelets

_____

In this section, we report the phonon-mode assignment of YbCrO$_3$ nanoplatelets by Raman spectroscopy. The UV-vis absorption spectroscopy of YbCrO$_3$ nanoplatelets have been studied in detail.

_____

*Reproduced from Inorg. Chem., 10.1021/acs.inorgchem.5b01448 with permission from the American Chemical Society*

### 3.5.1  Raman spectroscopy:

Raman spectroscopy is an expedient tool to study the effect of magnetic ordering and anomalies in YCO where, the $Yb^{3+}$ and $Cr^{3+}$ spins and competing interaction between them play an important role in determining their optical and magnetic properties. YCO crystallizes in distorted orthorhombic perovskite structure with Pbnm (Pnma) space group. As $Cr^{3+}$ is a Jahn-Teller (JT) in-active cation, it will lead to almost no dispersion in the Cr-O bonds.[10] In general, in orthochromites, the tilting of octahedra induces distortion and the three distortions *i.e.* A-cation displacement, tilting and octahedra distortion, breaks the cubic symmetry, thus, activates zone centre Raman modes. The orthorhombic Pbnm structure with four formula-units per unit cell gives rise to 24 Raman-active modes:[18,54]

$$\Gamma \text{ (Raman)} = 7A(1)g + 7B(1)g + 5B(2)g + 5B(3)g \qquad \text{...............................(7)}$$

**Figure 1** shows the room-temperature (RT) Raman spectrum of YCO in the spectral range of 100-600 cm$^{-1}$.
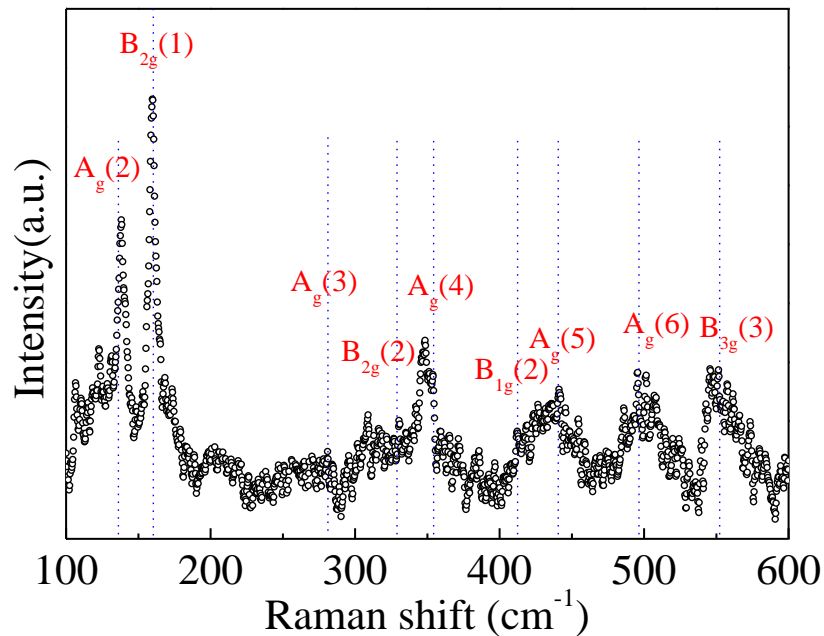


*Figure 1.  Room temperature Raman spectrum of YCO nanocrystallites.*

The vertical dotted lines depict the peak positions corresponding to the various modes as tabulated in Table 1. The Raman results were compared with the previous reported values by Weber *et al*., where the modes were assigned based on single crystal work on chromites (La, Gd, Y and Ho) $CrO_3$[10], tabulated in **Table 1**.

| Raman modes | Our study | Bulk YCO Weber et al[10] | Activating distortion |
|---|---|---|---|
| $A_g(2)$ | 138 cm$^{-1}$ | 138.5 cm$^{-1}$ | rot[101] |
| $B_{2g}(1)$ | 160 cm$^{-1}$ | 161.4 cm$^{-1}$ | rot[101] |
| $A_g(3)$ | 278.4 cm$^{-1}$ | 278 cm$^{-1}$ | rot[010] |
| $B_{2g}(2)$ | 332 cm$^{-1}$ | 333.4 cm$^{-1}$ | A shift |
| $A_g(5)$ | 440 cm$^{-1}$ | 441.7 cm$^{-1}$ | rot[101] |
| $B_{1g}(2)$ | 412 cm$^{-1}$ | 408.8 cm$^{-1}$ | A shift |
| $A_g(6)$ | 501 cm$^{-1}$ | 501.9 cm$^{-1}$ | rot[101] |
| $B_{3g}(3)$ | 551 cm$^{-1}$ | 563.8 cm$^{-1}$ | rot[101] |

*Table 1. A comparison of the Raman mode positions between YbCrO$_3$ nanocrystallites calculated from the current work on YbCrO$_3$ reported by Weber et al.*[10]

Below 400 cm$^{-1}$, it is the $Yb^{3+}$ ions that play a dominant role in determining the phonon frequencies of YCO, and above 450 cm$^{-1}$, the $Cr^{3+}$ ions play an important role. As seen from the **Figure 4**, the YCO nanocrystallites, with Pbnm space group, showed prominent modes situated at ~ 138, 160, 278, 332, 348, 412, 440, 501 and 551 cm$^{-1}$. Two sharp Ag (2) and B2g (1) modes situated at ~ 138 and ~ 160 cm$^{-1}$ were assigned to Yb- cation vibrations as the heaviest atom is expected to vibrate at lower wavenumber by considering harmonic oscillator approximation.[10,36]

$$\omega = (k/\mu)\ 1/2 \qquad\qquad .............................................................(8)$$

where, k is the force constant and $\mu$ is reduced mass.

The rotational modes observed between 250 to 350 cm$^{-1}$ were related to Yb-O vibrations and B2g (2) modes was related to Yb cationic shift.[10] The Ag (3) modes at 278 cm$^{-1}$ corresponds to the in-phase rotation of $CrO_6$ octahedra. The Ag (5) and B1g (2) modes belong to the same symmetry and involve mode-mixing and crossing. The Ag (5) mode corresponds to the rotation of $CrO_6$ octahedra depending upon the octahedral tilting. At higher frequency, the modes involve the Cr-O bending and anti-stretching vibration modes inside the octahedra.[10,36] Thus, it is concluded that all the prominent Raman modes of YCO are present.

## 3.5.2  UV-visible spectroscopy:

As the UV-vis absorption edge is relevant to the band energy and rare earth chromites are known to be p type semiconductor, similar to DCO and SCO, we were also interested to study the optical absorption of the YCO nanoplatelets. **Figure 2(a)** shows the UV-visible absorption spectrum of the YCO nanoplatelets.
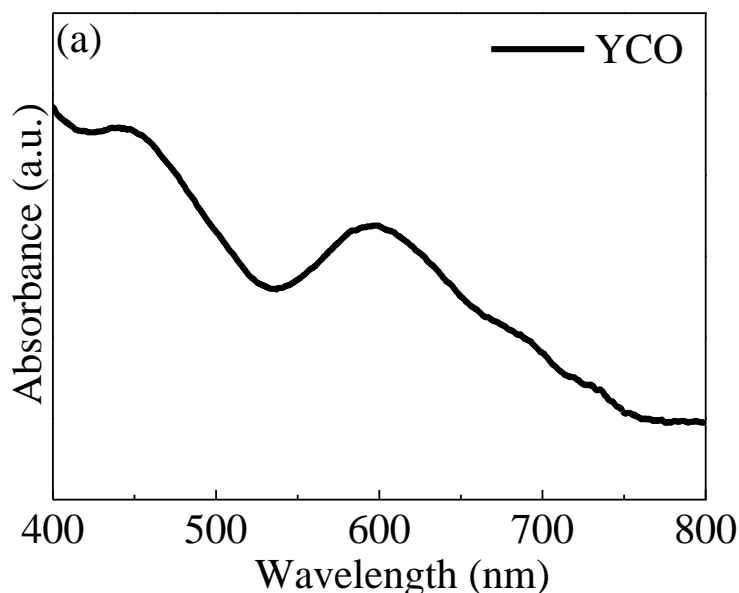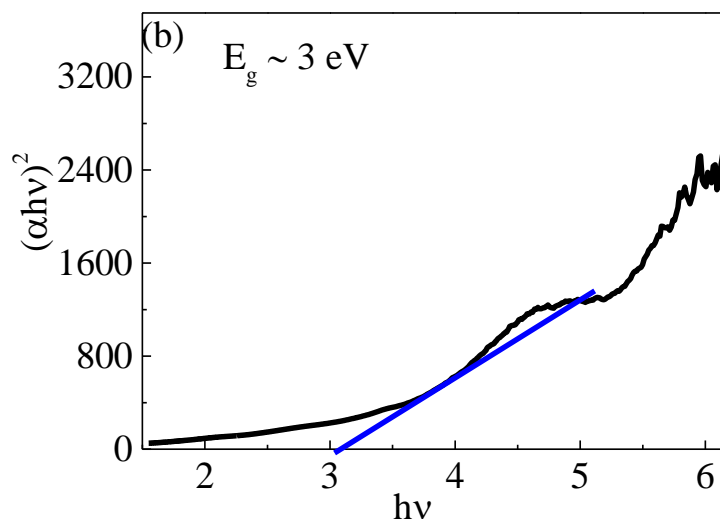
*Figure 2. (a) UV-Vis absorption spectrum and (b) band edge energy of YCO nanoplatelets.*

As discussed in earlier section, in rare earth chromites, the energy states consist of $R^{3+}$: 4f levels, filled $O^{2-}$: 2p band , partially filled $Cr^{3+}$: 3d, empty $Cr^{3+}$:4s band and $R^{2+}$:4f $^{n+1}$ levels or extremely narrow bands.[44] The transitions involving 4f-5d and charge transfer in $Yb^{3+}$ ions cannot be detected due to the limitation of our instrument as it appears at much higher energies.[55] The absorption spectrum of YCO show two peaks at ~ 455 nm and ~ 602 nm are associated with vibrational transitions of $Cr^{3+}$ ion. The two adsorption peaks is attributed to the $^{4}A_2$ to $^{4}T_2$ and $^{4}T_1$ transitions, respectively and can be explained by considering octahedral crystal field splitting.[44–46,49] The presence of $Cr^{3+}$ centers in YCO and other orthochromites,renders light green color to these materials.[44,48]

The bandgap of the YCO nanoplatelets is calculated from the tangent line in the plot of $(\alpha \upsilon)^2$ against $h\upsilon$ (where $\alpha$ is absorption coefficient and $h\upsilon$ is photon energy) and found to be ~ 3 eV as shown in **Figure 2(b)**. Thus, the band gap obtained for the YCO nanoplatelets indicates towards the possibility of utilizing UV-visible light for photocatalysis.

### 3.5.3 Conclusions

Our Raman studies inferred that below 400 cm$^{-1}$, $Yb^{3+}$ ions play a dominant role in determining the phonon frequencies of YCO, and above 450 cm$^{-1}$, the $Cr^{3+}$ ions. The rotational modes between 200 - 350 cm$^{-1}$ were related to Yb-O vibrations and the B2g (2)  modes was related to the Yb cationic shift. Also, we observed modes corresponding to the in-phase rotation of CrO$_6$ octahedra. The known semiconducting behavior of the rare earth chromites and band gap of YCO provides the possibility towards exploring its photocatalytic property.

### 3.5.4   References:

[1] D. Khomskii, Physics (College. Park. Md). **2**, (2009).

[2] C.N.R. Rao and C.R. Serrao, J. Mater. Chem. **17**, 4931 (2007).

[3] W. Eerenstein, N.D. Mathur, and J.F. Scott, Nature **442**, 759 (2006).

[4] T. Arima, a. Tokunaga, T. Goto, H. Kimura, Y. Noda, and Y. Tokura, Phys. Rev. Lett. **96**, 1 (2006).

[5] N. Ray and U. V. Waghmare, Phys. Rev. B - Condens. Matter Mater. Phys. **77**, 1 (2008).

[6] Y. Zhou and K. Rabe, arXiv Prepr. arXiv1305.6943 **094416**, 1 (2013).

[7] J.H. Lee, K.T. Delaney, E. Bousquet, N. a. Spaldin, and K.M. Rabe, Phys. Rev. B - Condens. Matter Mater. Phys. **88**, 1 (2013).

[8] H. Das, U. V. Waghmare, T. Saha-Dasgupta, and D.D. Sarma, Phys. Rev. Lett. **100**, 1 (2008).

[9] O. Chaix-Pluchery and J. Kreisel, J. Phys. Condens. Matter **21**, 175901 (2009).

[10] M.C. Weber, J. Kreisel, P. a. Thomas, M. Newton, K. Sardar, and R.I. Walton, Phys. Rev. B - Condens. Matter Mater. Phys. **85**, 1 (2012).

[11] S.M. Feng, L.J. Wang, J.L. Zhu, F.Y. Li, R.C. Yu, C.Q. Jin, X.H. Wang, and L.T. Li, J. Appl. Phys. **103**, 026102 (2008).

[12] A. Jaiswal, R. Das, K. Vivekanand, T. Maity, P.M. Abraham, S. Adyanthaya, and P. Poddar, J. Appl. Phys. **107**, 013912 (2010).

[13] K. Tsushima, K. Aoyagi, and S. Sugano, J. Appl. Phys. **41**, 1238 (1970).

[14] K. Sardar, M.R. Lees, R.J. Kashtiban, J. Sloan, and R.I. Walton, Chem. Mater. **23**, 48 (2011).

[15] J.R. Sahu, C.R. Serrao, N. Ray, U. V. Waghmare, and C.N.R. Rao, J. Mater. Chem. **17**, 42 (2007).

[16] C.R. Serrao, A.K. Kundu, S.B. Krupanidhi, U. V. Waghmare, and C.N.R. Rao, Phys. Rev. B - Condens. Matter Mater. Phys. **72**, 2 (2005).

[17] N.D. Todorov, M. V. Abrashev, V.G. Ivanov, G.G. Tsutsumanova, V. Marinova, Y.Q. Wang, and M.N. Iliev, Phys. Rev. B - Condens. Matter Mater. Phys. **83**, 5 (2011).

[18] M.N. Iliev, M. V. Abrashev, J. Laverdière, S. Jandl, M.M. Gospodinov, Y.Q. Wang, and Y.Y. Sun, Phys. Rev. B - Condens. Matter Mater. Phys. **73**, 3 (2006).

[19] M. Udagawa, K. Kohn, N. Koshizuka, T. Tsushima, and K. Tsushima, Solid State Commun. **16**, 779 (1975).

[20] W. Kaczmarek and I. Mörke, J. Magn. Magn. Mater. **58**, 91 (1986).

[21] Y. Du, Z.X. Cheng, X.-L. Wang, and S.X. Dou, J. Appl. Phys. **108**, 093914 (2010).

[22] B. Rajeswaran, D.I. Khomskii, a. K. Zvezdin, C.N.R. Rao, and a. Sundaresan, Phys. Rev. B - Condens. Matter Mater. Phys. **86**, 1 (2012).

[23] J. Prado-Gonjal, R. Schmidt, J.J. Romero, D. Ávila, U. Amador, and E. Morán, Inorg. Chem. **52**, 313 (2013).

[24] G.V.S. Rao, B.M. Wanklyn, and C.N.R. Rao, J. Phys. Chem. Solids **32**, 345 (1971).

[25] F. Gao, X. Chen, K. Yin, S. Dong, Z. Ren, F. Yuan, T. Yu, Z. Zou, and J.M. Liu, Adv. Mater. **19**, 2889 (2007).

[26] M. Siemons and U. Simon, Sensors Actuators, B Chem. **126**, 181 (2007).

[27] N. Russo, D. Mescia, D. Fino, G. Saracco, and V. Specchia, Ind. Eng. Chem. Res. **46**, 4226 (2007).

[28] G. a. Tompsett and N.M. Sammes, J. Power Sources **130**, 1 (2004).

[29] L.P. Rivas-Vázquez, J.C. Rendón-Angeles, J.L. Rodríguez-Galicia, C. a. Gutiérrez-Chavarria, K.J. Zhu, and K. Yanagisawa, J. Eur. Ceram. Soc. **26**, 81 (2006).

[30] J. Beckers and G. Rothenberg, ChemPhysChem **6**, 223 (2005).

[31] A.L. Linsebigler, A.L. Linsebigler, J.T. Yates Jr, G. Lu, G. Lu, and J.T. Yates, Chem. Rev. **95**, 735 (1995).

[32] N. Iliev, M.. Abrashev, H.-G. Lee, V.. Popov, Y.. Sun, C. Thomsen, R.. Meng, and C.. Chu, J. Phys. Chem. Solids **59**, 1982 (1998).

[33] M. Abrashev, J. Bäckström, L. Börjesson, V. Popov, R. Chakalov, N. Kolev, R.-L. Meng, and M. Iliev, Phys. Rev. B **65**, 1 (2002).

[34] M. Fiebig, J. Phys. D. Appl. Phys. **38**, R123 (2005).

[35] a. McDannald, L. Kuna, and M. Jain, J. Appl. Phys. **114**, 0 (2013).

[36] V. Srinu Bhadram, B. Rajeswaran, a. Sundaresan, and C. Narayana, EPL (Europhysics Lett. **101**, 17008 (2013).

[37] R. Blinc and B. Žekš, Adv. Phys. **21**, 693 (1972).

[38] C. Jia and J. Berakdar, 1 (2009).

[39] S.G. Bahoosh, J.M. Wesselinowa, and S. Trimper, Eur. Phys. J. B **86**, (2013).

[40] R. Gupta, G.V. Pai, a. K. Sood, T. V Ramakrishnan, and C.N.R. Rao, Europhys. Lett. **58**, 778 (2007).

[41] U. Intatha, S. Eitssayeam, J. Wang, and T. Tunkasiri, Curr. Appl. Phys. **10**, 21 (2010).

[42] A. Jaiswal, R. Das, T. Maity, K. Vivekanand, S. Adyanthaya, and P. Poddar, J. Phys. Chem. C **114**, 12432 (2010).

[43] A. Jaiswal, R. Das, T. Maity, and P. Poddar, J. Appl. Phys. **110**, 124301 (2011).

[44] a. K. Tripathi and H.B. Lal, Mater. Res. Bull. **15**, 233 (1980).

[45] R. Bhatt, S. Kar, K.S. Bartwal, and V.K. Wadhawan, Solid State Commun. **127**, 457 (2003).

[46] A. Jaiswal, R. Das, S. Adyanthaya, and P. Poddar, J. Nanoparticle Res. **13**, 1019 (2011).

[47] G. a. Torchia, J. a. Muñoz, F. Cussó, F. Jaque, and J.O. Tocho, J. Lumin. **92**, 317 (2001).

[48] Subba Rao Gv and Rao Cnr, Appl. Spectrosc. **24**, 436 (1970).

[49] H. Xu, T. Lou, and Y. Li, Inorg. Chem. Commun. **7**, 666 (2004).

[50] S. Li, Y.H. Lin, B.P. Zhang, Y. Wang, and C.W. Nan, J. Phys. Chem. C **114**, 2903 (2010).

[51] M.N. Iliev, a. P. Litvinchuk, V.G. Hadjiev, Y.Q. Wang, J. Cmaidalka, R.L. Meng, Y.Y. Sun, N. Kolev, and M. V. Abrashev, Phys. Rev. B - Condens. Matter Mater. Phys. **74**, 1 (2006).

[52] M. El Amrani, M. Zaghrioui, V. Ta Phuoc, F. Gervais, and N.E. Massa, J. Magn. Magn. Mater. **361**, 1 (2014).

[53] A. Nashim and K.M. Parida, Chem. Eng. J. **215-216**, 608 (2013).

[54] P. Gupta and P. Poddar, RSC Adv. **5**, 10094 (2015).

[55] M.S. Centre and O.F. Unit, **27**, 367 (2004).

# Chapter 4

## Magnetic properties of rare earth chromites

**This chapter briefly describes the novel, unique and strange behavior of rare earth chromites. It describes the distinctive magnetic behavior which includes negative magnetization, exchange bias and magnetization switching in orthochromites. This unique behavior makes orthochromites a possible candidate for spintronics and memory based device applications.**

## 4.1    Introduction

Functional oxides exhibit a wide set of physical phenomena across the whole spectrum of electrical, magnetic, and optical properties ranging from insulating to superconducting.[1–6] This class of materials has enormous potential and could revolutionize the field of electronics and energy. In recent years, the future of many technologies has become reliant on complex oxides. Several of these oxides show multifunctional properties where ferroelectric, ferroelastic, and magnetic ordering might coexist in a single phase material (multiferroicity) apart from interesting optoelectronic properties. Some of these multiferroic compounds are discovered to exhibit magnetoelectric effect.[7–9] One of the oxides which has emerged as an important class of materials for spintronics based devices is rare earth chromites. Over the years, chromites have been investigated using neutron diffraction,[10,11] specific heat capacity,[11] Mossbauer,[12] magnetic,[11,13] and   optical measurements.[14] In the year 1960's, based on the resistivity and combined with dielectric measurements by Rao *et al.* some of the orthochromites ($DyCrO_3$, $HoCrO_3$, $YbCrO_3$ and $LuCrO_3$) were predicted to show ferroelectricity.[15] However, there is still a lack of understanding on the origin of ferroelectricity in orthochromites and is still a complex issue.

According to Bertaut notation, in $RCrO_3$ (*Pbnm*) (R= rare earth chromites), three G-type antiferromagnetic (AFM) configurations are observed: $\Gamma_1$(Ax,Gy,Cz), $\Gamma_2$(Fx,Cy,Gz) and $\Gamma_4$(Gx,Ay,Fz).[16] Depending upon magnetic character of the R site element, the magnetic structure can be $\Gamma_4$ or $\Gamma_2$. However, at low temperatures, some of the $RCrO_3$ show SR transition and undergo change in spin structure from $\Gamma_2$ to $\Gamma_1$.[16] It has been reported that SR is found to be discontinuous for $ErCrO_3$,[14] $NdCrO_3$,[17] and continuous for $GdCrO_3$,[18,19] and $SmCrO_3$.[20] Sardar *et al.* have also observed the $Cr^{3+}$ AFM transition at ~ 192 K and SR transition at ~ 33 K for submicron $SmCrO_3$ particles (SCO).[21] In $RCrO_3$, below $T_N$, canted $Cr^{3+}$ spins induces a magnetic field on $R^{3+}$ (R= Gd, Dy) site which leads to the alignment of $R^{3+}$ spins towards the induced field which is large as compared to $H_{ext}$. Some of these less understood features include — external field ($H_{ext}$) and temperature dependent negative magnetization (NM), exchange bias (EB) *etc.*[4,22–24] The NM and EB effects continue to draw attention due to their potential applications in magnetic read heads, magnetic random

access memories and other spintronics devices.[25–28] The complex nature of spin-ordering at low temperature and their modifications in finite particle size also brings new science resulting from the modified surface spin structure which overall influences the magnetic behavior.[4,22–24] NM was observed in $Li_{0.5}(FeCr)_{2.5}O_4$ spinel and was explained using Nèel model.[29,30] This phenomenon was also discovered in orthovanadates,[31] $La_{1-x}Gd_xMnO_3$,[32] $YFe_{0.5}Cr_{0.5}O_3$,[33] $GdCrO_3$,[4] $La0.75Nd_{0.25}CrO_3$,[34] and some other perovskites. Few systems such as $GdCrO_3$,[4] $LaCr_{0.8}Mn_{0.2}O_3$,[35] $TmCrO_3$,[36] and $CeCrO_3$[37] also shows NM and tunable EB. It is interesting to note that some of the $RCrO_3$ compounds also show EB effect while others do not. It is well known that the EB occurs in ferromagnetic (FM) and AFM interfacial systems and vanishes at Nèel temperature.[25] EB was also observed in FM-only system where, some of the FM spins remain fixed while other responds to the external magnetic field.[38,39] The EB can be observed in various systems such as FM/AFM, FM/ferrimagnet, FM/spin glass, core-shell structures, heterostructures, superlattices *etc.*[25,38–41] However, EB can be referred as negative or positive depending upon the parallel or perpendicular easy axes of FM and AFM spins.[41]

Conventionally, EB is generally observed during field-cooled (FC) process but, recently zero field-cooled (ZFC) EB has gained attention as it rules out the requirement of $H_{ext}$ to shift the hysteresis loop and create unidirectional anisotropy in a crystal.[42] The presence of multiple phases in a single material resulted in the observed ZFC EB which was considered as an artifact until a model came up for positive zero-field cooled EB.[42] The ZFC EB was observed in $Ni_{80}Fe_{20}/Ni_{50}Mn_{50}$ alloys along-with a sign reversal of EB after FC.[43] Most of the previous reports, either showed positive or negative EB but the $H_{ext}$ and T tunability of EB is not reported so frequently. However, the polarity of EB can be changed by FC at higher applied magnetic field.[44] In few materials, the tunability of EB can be achieved with the change in temperature and magnetization reversal.[37,42] In past, we have also studied EB in $DyFeO_3$ orthoferrites fine particles and proposed core-shell model for the observed EB.[5] The origin of NM and EB in orthochromites can be correlated, where the sign of exchange bias field ($H_{EB}$) can be related to the magnetization reversal.

As some of the $RCrO_3$ are associated with the magnetization reversal, it would be useful to explore the possible existence of EB in this class of compounds. Recent studies of NM and EB are leading towards exploring $RCrO_3$ for applications such as spintronics and memory devices.[36,37] The materials possessing NM are useful in applications such as non-volatile memories,[45] where, below the compensation temperature ($T_{comp}$), (the characteristic temperature where the material exhibits a net zero magnetization) the polarity of magnetization can be flipped by changing the polarity of external magnetic field ($H_{ext}$).[36,37] However, instead of $H_{ext}$, the polarity of magnetization can also be flipped by varying the T which is seen as an attractive option in thermomagnetic switches.[46] Similar to thermally-assisted NM, the sign reversal of EB, with the change in T, is found to be useful in designing thermally-assisted magnetic random access memory (MRAM).[26,47] However, the interesting temperature for observing such an effect is relatively low in $RCrO_3$, well below room temperature, limiting the material from practical use. Therefore, seeking materials with enhanced effect and operating temperatures is needed.

Similar to several other chromites, $DyCrO_3$, $SmCrO_3$ and $YbCrO_3$ crystallizes in an orthorhombic structure with *Pbnm* space group.[15,48] The single crystals of $DyCrO_3$ exhibits weak ferromagnetism where $Cr^{3+}$ ions ordered just below Nèel temperature at ~ 142 K[49] and $Dy^{3+}$ ions ordered below Nèel temperature at $1.5 < T_{N2} < 4.2$ K in an antiferromagnetic structure. From single crystal studies of $SmCrO_3$, the AFM ordering temperature of $Cr^{3+}$ spins at ~ 190 K and spontaneous change in magnetic structure at ~ 33 K was observed.[20] This spontaneous reorientation is due to the strong AFM coupling of $Sm^{3+}$ spins and canted antiferromagnetic (CAFM) $Cr^{3+}$ spins moment at low temperature.[20] Moreover, reversal of magnetization can also be achieved due to strong single ion magnetic anisotropy which becomes significant at low temperatures and NM appears at low applied magnetic field.[34] The AFM ordering temperature of $Cr^{3+}$ spins at ~119 K and crossover temperature ($T_{cross}$) ~ 19.6 K with $T_{comp}$ ~ 18.5 K was found from studies of YCO.[50] The strong anisotropic superexchange interaction between the $Cr^{3+}$ and $Yb^{3+}$ spins in YCO can induce interesting magnetic anomalies at low temperature. The YCO is known to be

ferroelectric at room temperature with an ordering temperature ~ 793 K and it shows frequency dependent loss tangent and dielectric constant.[65]

In the present work, we studied the magnetic properties of sol-gel derived $DyCrO_3$, $SmCrO_3$ and $YbCrO_3$ nanoparticles with platelet morphology. With the help of detailed static and dynamic magnetization measurements, we have explained temperature and external magnetic field dependent behavior of NM, EB effects and SR transitions in these orthochromites. The coercivity and EB dependence on temperature has also been studied in detail. Temperature and field cooled dependence of EB is also discussed in detail. To further confirm the intrinsic nature of EB, training cycle experiment was done. The temperature as well as field-dependent sign reversal of NM and EB in orthochromites, makes it a model system for various applications such as spintronics devices, non-volatile memories *etc.*

## 4.2    Experimental and Characterization Details

After studying the structural and optical properties of $DyCrO_3$, $SmCrO_3$ and $YbCrO_3$ as discussed in **chapter 2** and **3**, we moved towards understanding the rich interplay among the spins in these systems.

Static and dynamic magnetic property measurements of DCO, SCO and YCO nanoparticles were performed using a Physical Property Measurement System (PPMS) from Quantum Design Inc., San Diego, California equipped with a 9 Tesla superconducting magnet. We performed dc-magnetization vs. temperature (M -T) and magnetization vs. magnetic field (M–H) measurements using a vibrating sample magnetometer (VSM) attachment and ac-susceptibility measurements were performed using an ACMS attachment. For dc-magnetic measurements, the DCO, SCO and YCO nanoparticles were precisely weighed and packed inside a plastic sample holder which fits into a brass sample holder provided by Quantum Design Inc. with negligible contribution in overall magnetic signal. We collected M–H loops at a rate of 75 Oe/s in a field sweep from - 90 to 90 kOe at the vibrating frequency of 40 Hz at varied temperature to scan the behavior around the phase transitions observed in bulk phase. Before each measurement, the sample was heated above its reported Néel temperature to completely demagnetize the sample. Also, the M-T measurements were carried out in temperature range from 3–300 K at varying field. The cooling and heating rates were kept constant at 2 K/min for all the measurements. Firstly, at 300 K, the desired field was applied and data were recorded while cooling down to 3 K and heating back from 3 to 300 K. These curves obtained were designated as field cooled (FC) cooling and field-cooled heating respectively. For zero field-cooled (ZFC) magnetic measurements, the sample was first cooled from 300 to 3 K in zero magnetic field and data was collected in heating mode once the field was applied at 3 K. The de-gauss procedure was followed carefully in order to nullify the trapped field in the superconducting magnet. The ac-magnetic measurements were carried out at frequency range 101 to 9999 Hz at 10 Oe applied dc-magnetic field.

# Section 4.3

# Static and dynamic magnetic properties of DyCrO$_3$ nanoplatelets
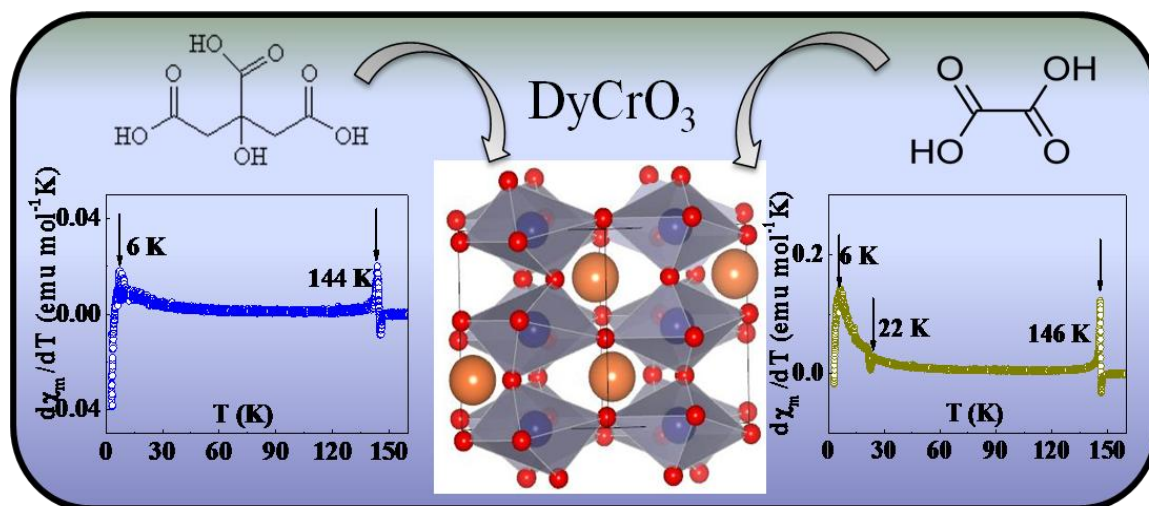


In this section, we present a detail study of static and dynamic magnetic behavior of DyCrO$_3$ nanoplatelets synthesized using citric acid (DCO (C)) and oxalic acid (DCO (O)) with an average particle size of ~ 90 and ~ 50 nm, respectively. We also studied negative magnetization and exchange bias behavior in DCO nanoplatlets which may be useful for spintronics application. The particle size effect on coercivity is also discussed. To further prove the negative magnetization in DCO, switching behavior was also studied.

*Reproduced from RSC Adv. 3 (48), 26427-26432 with permission from the Royal Society of Chemistry*

## 4.3.1    Negative magnetization:

**Figure 1(a)** compares M-T curves (~ 100 Oe) of DCO (C) and DCO (O) nanoplatelets, respectively. Above 150 K, both the samples showed paramagnetic behavior. Below ~ 150 K, we observed a strong bifurcation of ZFC–FC magnetization curves due to the onset of antiferromagnetic (AFM) ordering of $Cr^{3+}$-$Cr^{3+}$ spins mediated by superexchange (SE) interactions. This AFM ordering temperature (Néel temperature $T_N$) of $Cr^{3+}$ spins was found to be situated at ~ 144 and ~ 146 K for DCO (C) and DCO (O), respectively. **Figure 1(b)** shows the expanded view of ZFC-FC magnetization curves near the transition temperatures clearly showing the small change in Nèel temperature, $T_{N1}$ = 144 K and 146 K for DCO (C) and DCO (O), respectively. This change in $T_N$ can be associated with the crystalline quality of DCO nanoplatelets.
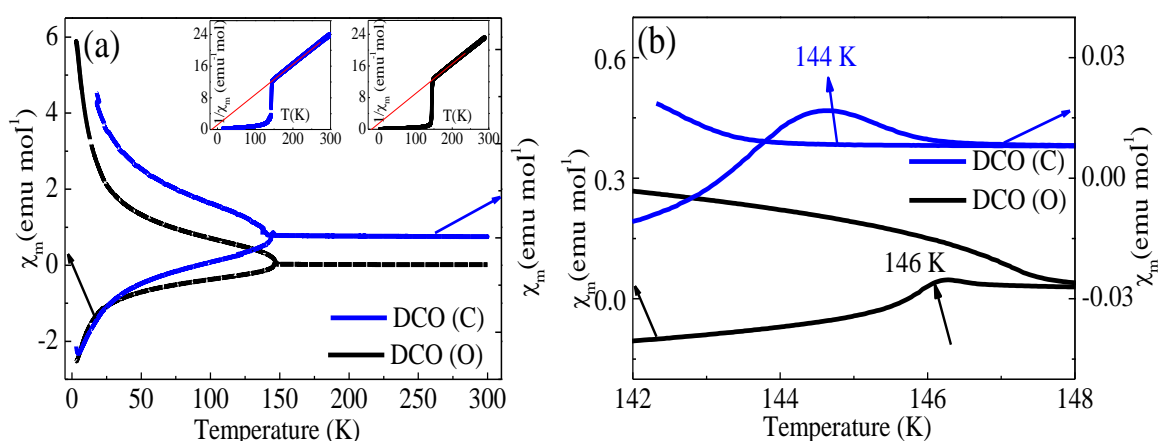


*Figure 1. (a) The comparison of ZFC-FC magnetization curves for both the samples at 100 Oe. The curves in insets show 1/ $\chi_m$ vs. T plots for both the samples. Panels (b) show zoom view of ZFC-FC of DCO (C) and DCO (O) nanoplatelets respectively.*

It can be seen from **Table 1**, the AFM ordering of $Cr^{3+}$ spins in DCO (C) is in close proximity to the $T_{N1}$ = 144 K observed in single crystal $DyCrO_3$.[51] In case of DCO (O) the $T_{N1}$ = 146 K observed agrees well with the reported values of bulk

polycrystalline and sub-micron size $DyCrO_3$ particle.[21,52] This indicates that DCO (C), when compared with DCO (O), approaches more close to single crystal $T_{N1}$ value.(**Table 1**)

| Transition temperature | DCO (C) (Our study) | DCO(O) (Our study) | $DyCrO_3$ single crystal[51] | $DyCrO_3$[52] Bulk | $DyCrO_3$ particle[21] Sub micron |
|---|---|---|---|---|---|
| $T_{N1}$ **(K)** | 144 | 146 | 142 | 146 | 145 |
| $T_{N2}$ **(K)** | - | - | 2 | 2.2 | - |
| $T_N$ **($DyCrO_4$)** **(K)** | - | 22 | - | - | - |

*Table 1. Magnetic transition temperatures obtained from the DC-magnetic measurements of the $DyCrO_3$ nanoplatelets in comparison with the earlier reported data.*

In **Figure 1(c),** a small peak was observed in ZFC magnetization curve at ~ 22 K for DCO (O) which was found to be absent in DCO (C). This peak can be assigned to AFM transition of $DyCrO_4$[53] at Nèel temperature (~ 23 K) which exists as an impurity in DCO (O) as discussed in **chapter 2**.

**Figure 1(d)** shows the temperature dependence on derivative of magnetic susceptibility. From the $d\chi_{FC}/dT$ vs. T curve, we observe a prominent peak at ~ 22 K and ~ 6 K which appeared as a weak transition in ZFC-FC magnetization curve of DCO (O). However, we could not map the possible low temperature transition ($T_{N2}$ = 2.2 K) due to the limitation of our instrument. Among three possible magnetic interactions between cation ($Dy^{3+}$-$Dy^{3+}$, $Dy^{3+}$-$Cr^{3+}$, $Cr^{3+}$-$Cr^{3+}$), $Cr^{3+}$-$Cr^{3+}$ interaction is the strongest and it shows up at relatively higher temperature.
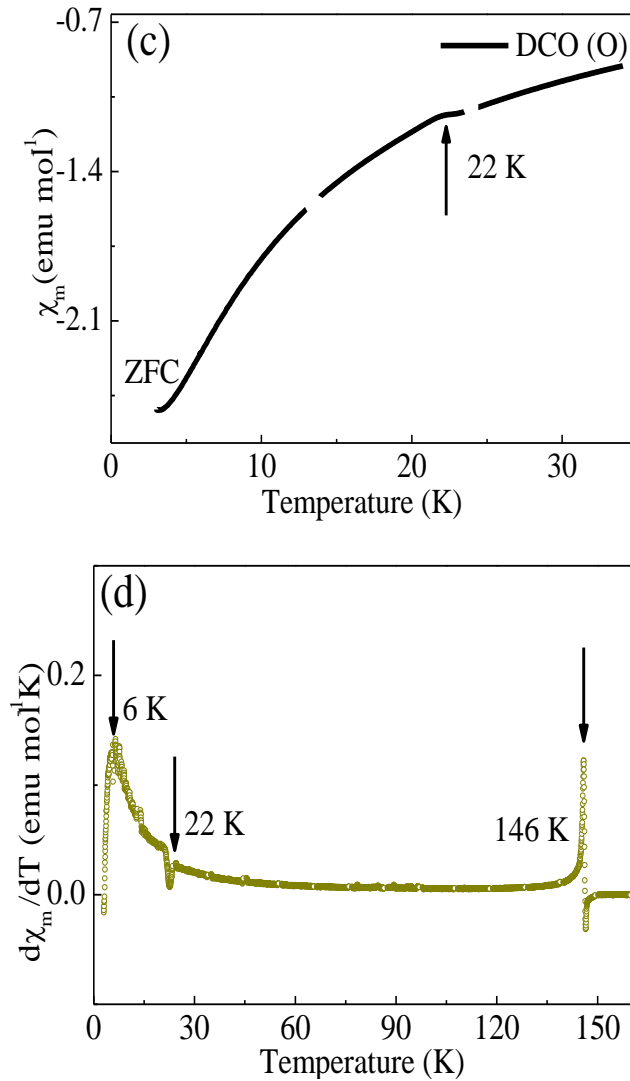
***Figure 1. Panel (c) shows the small hump in ZFC of DCO (O) at 22 K. Panel (d) shows the temperature dependent dχ_FC/dT susceptibility plot of DCO (O).***

The magnetic moment of $Dy^{3+}$ is due to the $4f$ electrons which are shielded by $5s$ and $5p$ orbitals. In this case, $f$ electrons of $Dy^{3+}$ hybridize with $p$ electrons of oxygen and also with the $t_{2g}$-$e_g$ orbital's of $Cr^{3+}$ ions. In addition, NM due to the presence of different magnetic entities with AFM and ferromagnetic (FM) interaction has been observed in ZFC magnetization curve. Similar behavior was observed by our group earlier in GdCrO$_3$ nanoparticles.[4] To explain the NM observed in ZFC-FC magnetization curve in GdCrO$_3$ and DyCrO$_3$, a possible elucidation can be given by exploring the temperature dependent interaction between $R^{3+}$ and $Cr^{3+}$ spins. In

GdCrO$_3$ and DyCrO$_3$ at temperature below 130 K and 140 K, respectively, $Cr^{3+}$ spins get canted and induces a magnetic field on $R^{3+}$ (R= Gd, Dy) site which leads to the alignment of $R^{3+}$ spins toward the field which is opposite to the canted $Cr^{3+}$ spins.[4] This is due to the antisymmetric exchange interaction between $R^{3+}$ and $Cr^{3+}$spins. This produces effective magnetic field at $Gd^{3+}$ (4$f^7$, $\mu_{\text{eff}}$ = 7.94 $\mu_B$) and $Dy^{3+}$ (4$f^9$, $\mu_{\text{eff}}$ = 10.6 $\mu_B$), respectively. This can be understood by the opening of hysteresis loop at this temperature. The overall moment ($\mu_{av}$) at any temperature is given by,

$$\mu_{av} = \mu_{Cr} + \mu_R \qquad\qquad ................................................................(1)$$

Here, if we assume that $R^{3+}$ spins follow a Curie-Weiss law, then

$$\mu_{av} = \mu_{Cr} + \frac{C(H_a - H_i)}{T - \theta}, \qquad ................................................................(2)$$

Where, $\mu_{Cr}$ and $\mu_R$ are magnetic moment of $Cr^{3+}$ and $R^{3+}$ ion (R = Rare earth), respectively, and C, H$_a$, H$_i$ and θ are the Curie constant, applied field, induced field and Weiss constant, respectively. If at a given temperature, the induced field is larger than the applied field, the second term in the above equation becomes greater (negative sign) and hence, net magnetization goes to the negative value. As we increase the applied magnetic field, the first term becomes larger and hence, net magnetic moment becomes positive which contributes to positive magnetization value. It can be seen that, onset of $Dy^{3+}$-$Dy^{3+}$ AFM ordering becomes prominent below 6 K. Inset of **Figure 1(a)** shows graph between 1/χ$_m$ vs. T in the temperature range 3-300 K for DCO (C) and DCO (O). In both the cases, above T$_N$, data was nicely fitted using Curie-Weiss equation. A decrease in Curie constant from -15 to -20 K was observed as we changed the chelating agent from citric acid to oxalic acid. A small decrease in Curie constant shows the increase in AFM ordering in DCO (O). The Weiss constant was also found to decrease from 15.2 to 13.8 which is close to the reported value for hydrothermally synthesized DCO.[21]

## 4.3.2  Temperature dependent coercivity in DCO(C) and DCO(O):

To further study the influence of various level of interaction between $Dy^{3+}$ and $Cr^{3+}$ spins, we measured the M-H loops for DCO (C) and DCO (O) nanoparticles. **Figure 2(a)** and **(b)** show the M-H curves at 10, 100, 125, 150, and 300 K of DCO (C) and DCO (O), respectively, whereas, inset of **Figure 2(a)** and **2(b)** shows the  zoom view of same set of curves.
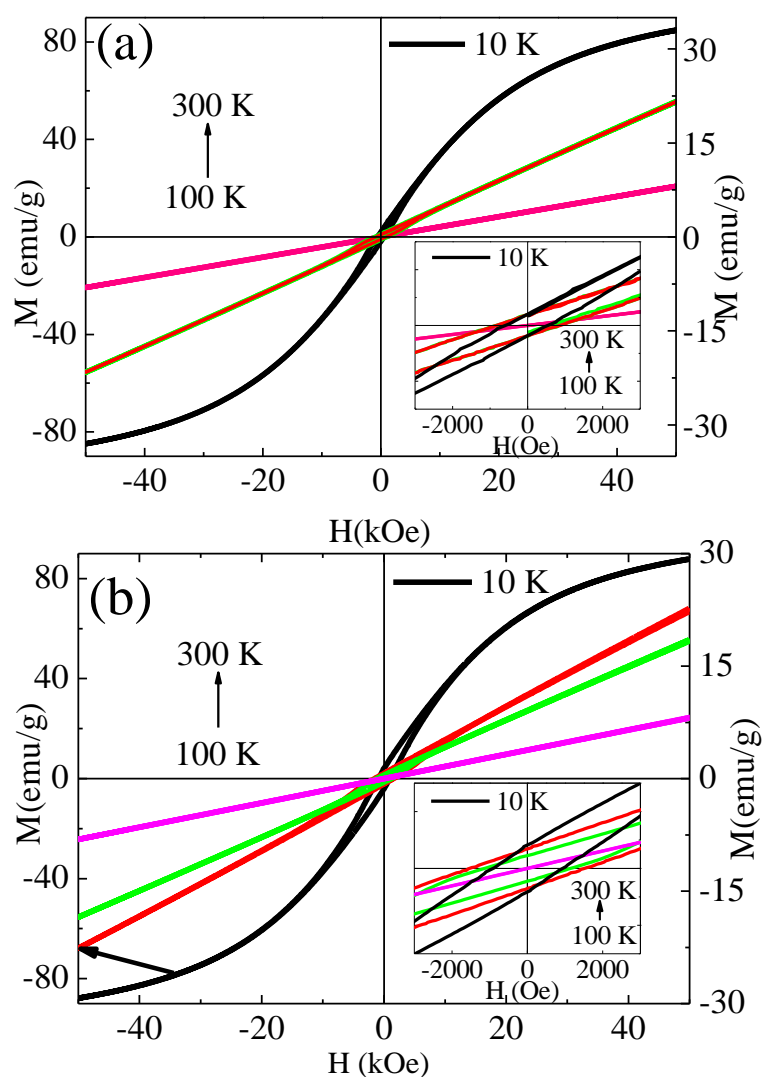


*Figure 2. A comparison of M - H hysteresis loop of (a) DCO (C) (b) DCO (O) nanoplatelets. Inset represents the zoom view of same set of hysteresis which shows the increase in coercivity of DCO (O) by a factor of 2 (approx.) as compared to DCO (C)*

From **Figure 2(a),** we observed that for T > $T_N$, M-H curves show linear behavior indicating paramagnetic nature. For T= 125 K and 100 K, we observed almost similar coercivity in the range of 830 - 840 Oe, but no saturation was observed for field up to 50 kOe. At this temperature *i.e. $Cr^{3+}$- $Cr^{3+}$* interactions are taking part in total magnetization. However, at 10 K, a clear FM loop with decrease in coercivity of about ~ 565 Oe was observed. A similar trend in the coercivity was observed for DCO (O) as shown in **Figure 2(b)**, but the coercivity was found to be increased by a factor of 2 (approx.) as compared to DCO (C). In DCO (O) a coercivity of about ~ 1140 Oe was observed at T=125 K, which increased to ~ 1520 Oe at 100 K. Here, at these two temperatures, no saturation was observed for a field up to 50 kOe. In addition, coercivity was found to decrease at 10 K and reaches to 930 Oe. This further indicates that at such a low temperature $Dy^{3+}$ moments strongly interact AFM with another $Dy^{3+}$ moments, which results in the closing of hysteresis loop.

This change in coercivity with temperature for DCO (C) and DCO (O) is tabulated in **Table 2** and shown in **Figure 3**. The change in $H_C$ can be attributed to the varying particle size of DCO (C) (90 nm) and DCO (O) (50 nm) nanoplatelets, respectively.

| Temperature (K) | Hc (Oe) DCO(C) | Hc (Oe) DCO(O) |
|:---:|:---:|:---:|
| 125 | 830 | 1140 |
| 100 | 840 | 1520 |
| 50 | 882 | 1323 |
| 10 | 565 | 930 |

*Table 2. Coercivity ($H_C$) versus temperature for DCO (C) and DCO (O) nanoplatelets.*

Similar change in coercivity with the temperature was also observed by Jaiswal *et al.* for $DyFeO_3$.[5]
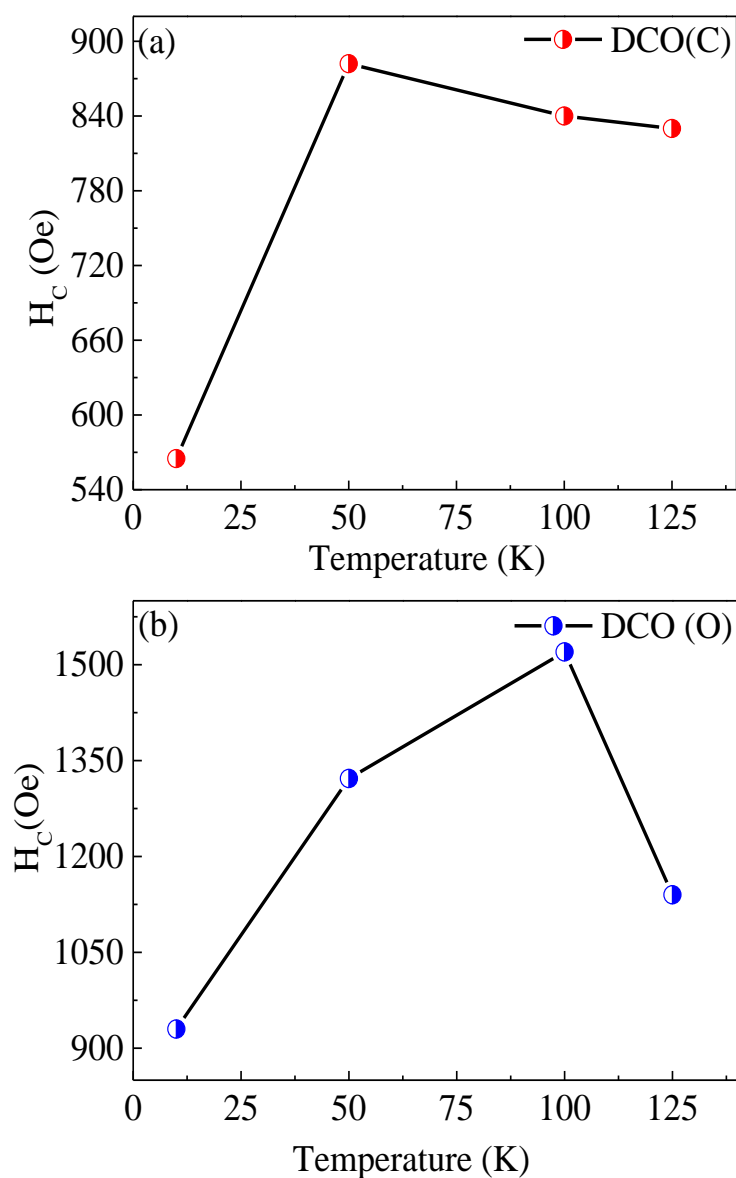
*Figure 3. Temperature variation of coercive field $H_C$ (a) DCO(C) and (b) DCO(O) of DCO nanocrystallites in ZFC condition.*

## 4.3.3 Temperature dependent exchange bias in DCO(C) and DCO(O):

**Figure 4(a, b)** shows the temperature dependent EB in DCO (C) and DCO (O) nanoplatlets, respectively. We can see from the **Figure** that exchange bias field ($H_{EB}$) strongly depends on the temperature as the complex magnetic interaction in chromites

are temperature dependent. The EB is known to be associated with the NM, therefore, the observation of NM below ~ $T_N$ prompted us to explore the possibility of EB behavior in DCO(C) and DCO(O) nanocrystallites. The M-H loops were measured in a broad temperature range (5–130 K) in ZFC condition and shown in **Figure 2**.
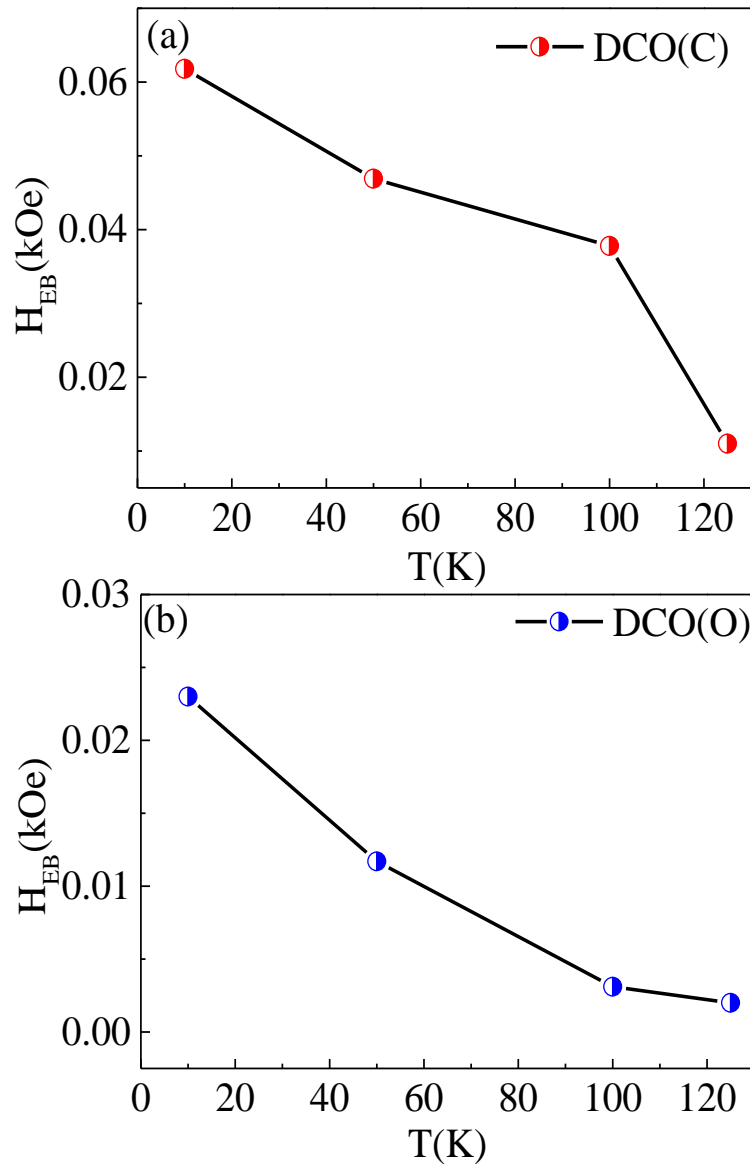


*Figure 4. Temperature variation of exchange bias field $H_{EB}$ (a) DCO( C) and (b) DCO (O) of DCO nanocrystallites in ZFC condition.*

The $H_{EB}$ was found to increase with decreasing temperature for DCO(C) and DCO(O), respectively. We observed that the EB becomes prominent as $Dy^{3+}$–$Dy^{3+}$ spin interaction starts dominating at lower temperatures. As we go down from 130 K to 10 K, $H_{EB}$ increased from ~ 90 Oe to ~ 4709 Oe for DCO (C) and DCO(O). The increase in $H_{EB}$ can be attributed to the weak FM arising due to small canting of $Cr^{3+}$ spins from AFM axis and strong AFM coupling with $Dy^{3+}$ spins.

### 4.3.4    AC-magnetization studies of DyCrO₃ nanoplatelets:

In order to observe the spin dynamics in DyCrO₃ nanoplatelets, ac-magnetic measurements were performed. Here, for the first time ac-magnetic measurements on DyCrO₃ nanoplatelets is reported. To probe the magnetic transitions in the orthochromites, the ac-magnetic measurements of the DyCrO₃ nanoplatelets at a lower excitation field (H=10 Oe) was measured in the temperature range 3−160 K and frequency range 101−9999 Hz. **Figure 5** represents the real and imaginary part of ac-magnetization curves of DCO (O) and DCO(C) nanoplatelets.

In **Figure 5(a)** we observe that the real component of the moment (M') exhibits maxima at ~ 21 and ~ 145 K. It is interesting to know that the maxima observed in real part (M') at ~ 21 K was also seen in dc-magnetic measurements as a weak transition in ZFC of DCO (O) as shown in **Figure 1(c)**. The sharp peak at ~145 K corresponds to the $T_N$ of DCO (O). The imaginary part of moment (M″) exhibits peak at ~ 22 K and ~ 145 K as shown in **Figure 5(b)**. The transition observed at ~ 146 K in dc-magnetic measurement corresponding to the $T_N$ of DCO(O) nanoplatelets was found to be prominent in ac-magnetic measurement which also showed up transition around ~ 22 K. The transition at ~ 22 K was understood as a contribution from very small amount of DyCrO₄ present in DCO (O) which has its $T_N$ at ~ 23 K.[53] However, we did not observe any anomaly in real part (M') at 22 K in DCO (C) as shown in **figure 5(c).** The sharp peak at ~143 K corresponds to the $T_N$ of DCO (C) in imaginary part M' as shown in **figure 5(d)**.
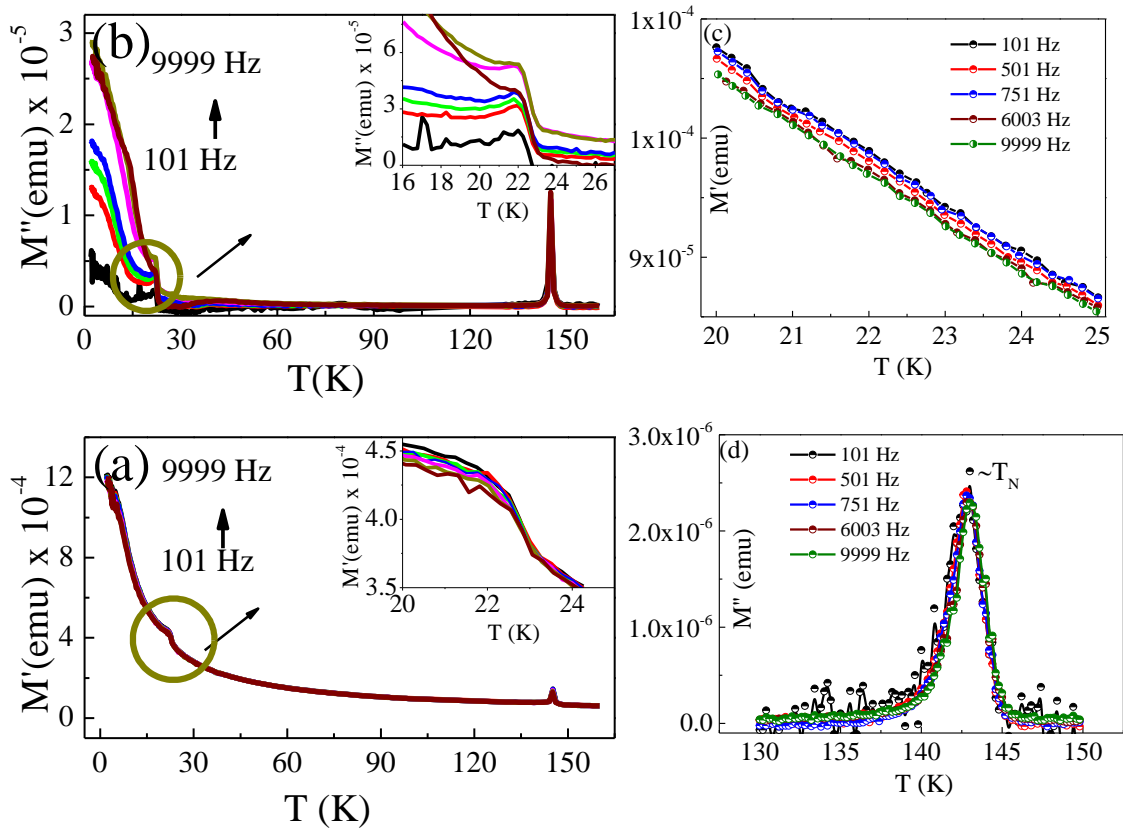
*Figure 5. Temperature dependence of the a) real and b) imaginary part of the ac magnetization measured in 10 Oe magnetic field and varying frequencies for DyCrO$_3$ (DCO(O)) nanoplatelets. Inset of (a) and (b) representing zoom view of imaginary component of ac magnetization at 22 K. The panel (c) and (d) representing the real and imaginary part of ac magnetization for DCO(C) in a temperature range 20-25 K and 130-150 K, respectively.*

However, any frequency dependence of the transition temperature of DyCrO$_3$ was not observed.

## 4.3.5  Field assisted memory-switching application:

Negative magnetization has a practical implication and magnetization switching is one of them.[46] The minimum NM in DCO(C) was found to be at 60 K, thus, we choose to show NM at 60 K. We observed that NM is field dependent and with the

increase in magnetic field, the NM behavior disappears. Thus, by applying 1000 Oe external magnetic field ($H_{ext}$), NM observed at 100 Oe in ZFC magnetization curve can be flipped to positive. Similar to conventional magnetic materials, DCO(C) shows the characteristic magnetization flipping from negative to positive by varying the magnitude of $H_{ext}$ as shown in **Figure 6**. The change in the polarity of magnetization by varying $H_{ext}$, cycled several times showed good reproducibility and no noticeable decay in magnetization was observed. Thus, the magnetization can be tuned in a predictable way and this behavior is favorable for a subtle application in non-volatile magnetic memories.[33] Similar feature was also observed in other chromites exhibiting NM such as $YFe_{0.5}Cr_{0.5}O_3$,[33] $SmCr_{1-x}Fe_xO_3$[54] and $TmCrO_3$[36]. Thus, by simply changing the magnitude of the $H_{ext}$, the polarity of the magnetization can be switched between negative and positive.
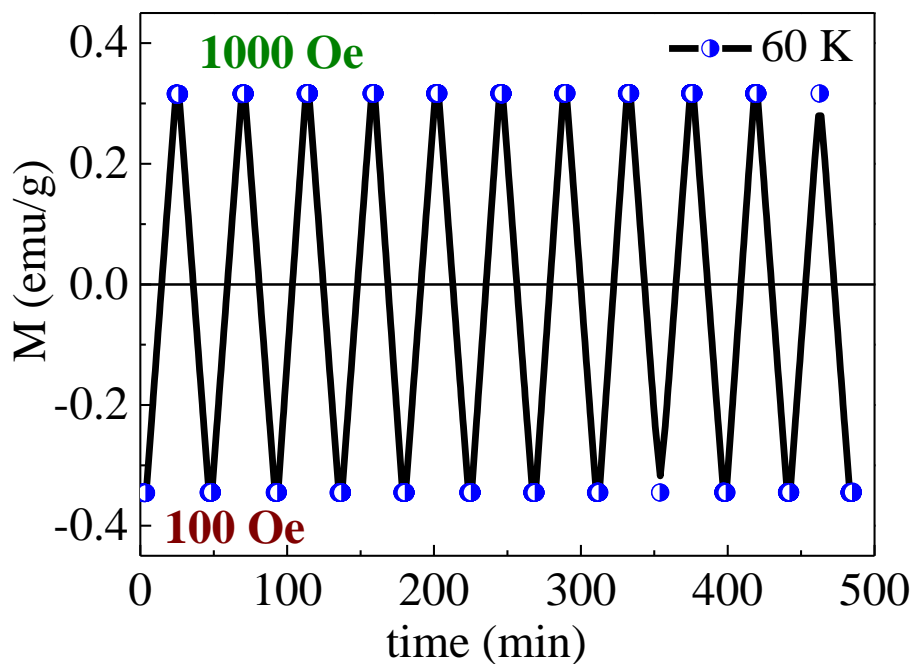


*Figure 6. Magnetic field assisted magnetization switching in DCO(C) nanoplatlets at 60 K. The polarity of magnetization is flipped by varying external magnetic field from 100 Oe to 1000 Oe.*

## 4.3.6 Conclusions:

In this work, we have studied static and dynamic magnetization behavior of DCO(C) and DCO(O), respectively. DC magnetic measurement showed the Néel transition temperature near ~ 144 and ~ 146 K for DCO (C) and DCO (O). We also observed that M-H curve for both DCO (C) and DCO (O) shows linear behavior which persists till 150 K. But when the temperature is lowered than $T_{N1}$, the loop starts showing some opening due to weak FM interaction between $Cr^{3+}$-$Dy^{3+}$ ion. Moreover, at 10 K the closing of loop can be attributed to the $Dy^{3+}$-$Dy^{3+}$ AFM interaction. We also found that $H_C$ and $H_{EB}$ of DCO (C) and DCO (O) strongly depend on the temperature. However, an ac-magnetic measurement of DCO (O) does not show any frequency dependence. The real (M′) and imaginary component (M″) of magnetization show the maxima at ~145 K which agrees well with dc-magnetic measurement, clearly indicating the $T_N$ of DCO (O). The peak at ~ 22 K can be assigned to the AFM ordering temperature of $DyCrO_4$ which was found to be present as an impurity peak in DCO (O). We observe ZFC NM rather than conventional FC NM in DCO (C) and DCO (O), respectively, which was later employed to study the characteristic magnetization switching behavior in the system.

## Section 4.4

## Colossal increase in negative magnetization, exchange bias and coercivity in samarium chromite due to a strong coupling between $Sm^{3+}$-$Cr^{3+}$ spins sublattices
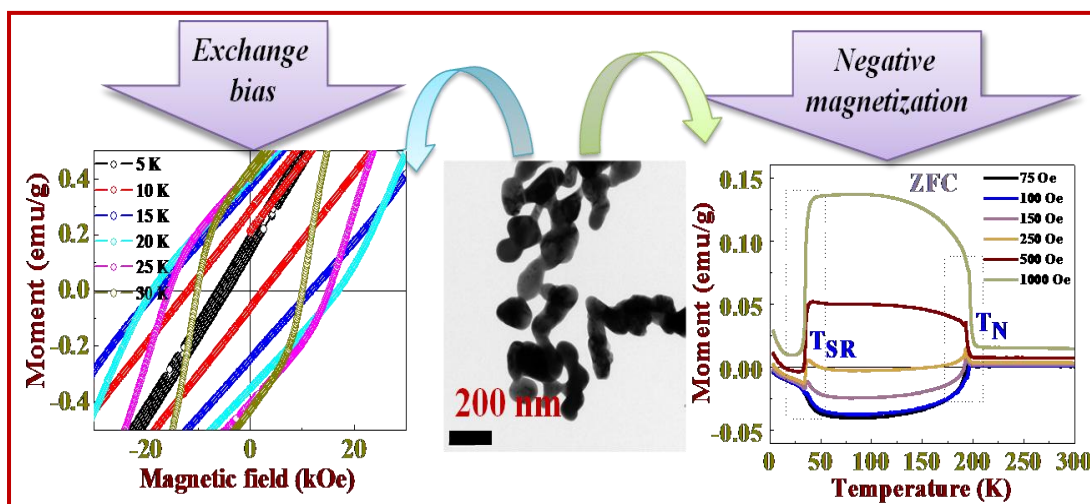


Our aim is to find the material having negative magnetization, exchange bias and two or more compensation temperature in a single system. In this section, we studied giant temperature dependent negative magnetization (magnetization reversal) along with a large exchange bias and large coercivity in $SmCrO_3$ by systemic investigation. The temperature dependent exchange bias shows non-monotonic behavior and at 35 K, we found that, exchange bias ceases to exist due to the orientation of $Sm^{3+}$ moments with respect to canted $Cr^{3+}$ moments. To further confirm the exchange bias in $SmCrO_3$, training effect measurements were employed. The static and dynamic magnetization measurements were found to be consistent with each other. The magnetization switching characteristic was also discussed in detail.

## 4.4.1 Negative magnetization and spin reorientation:

**Figure 1** shows the temperature dependent ZFC ($M_{ZFC}$ – T) and FC ($M_{FC}$ – T) magnetization curves for $SmCrO_3$ (SCO) at different applied magnetic field.
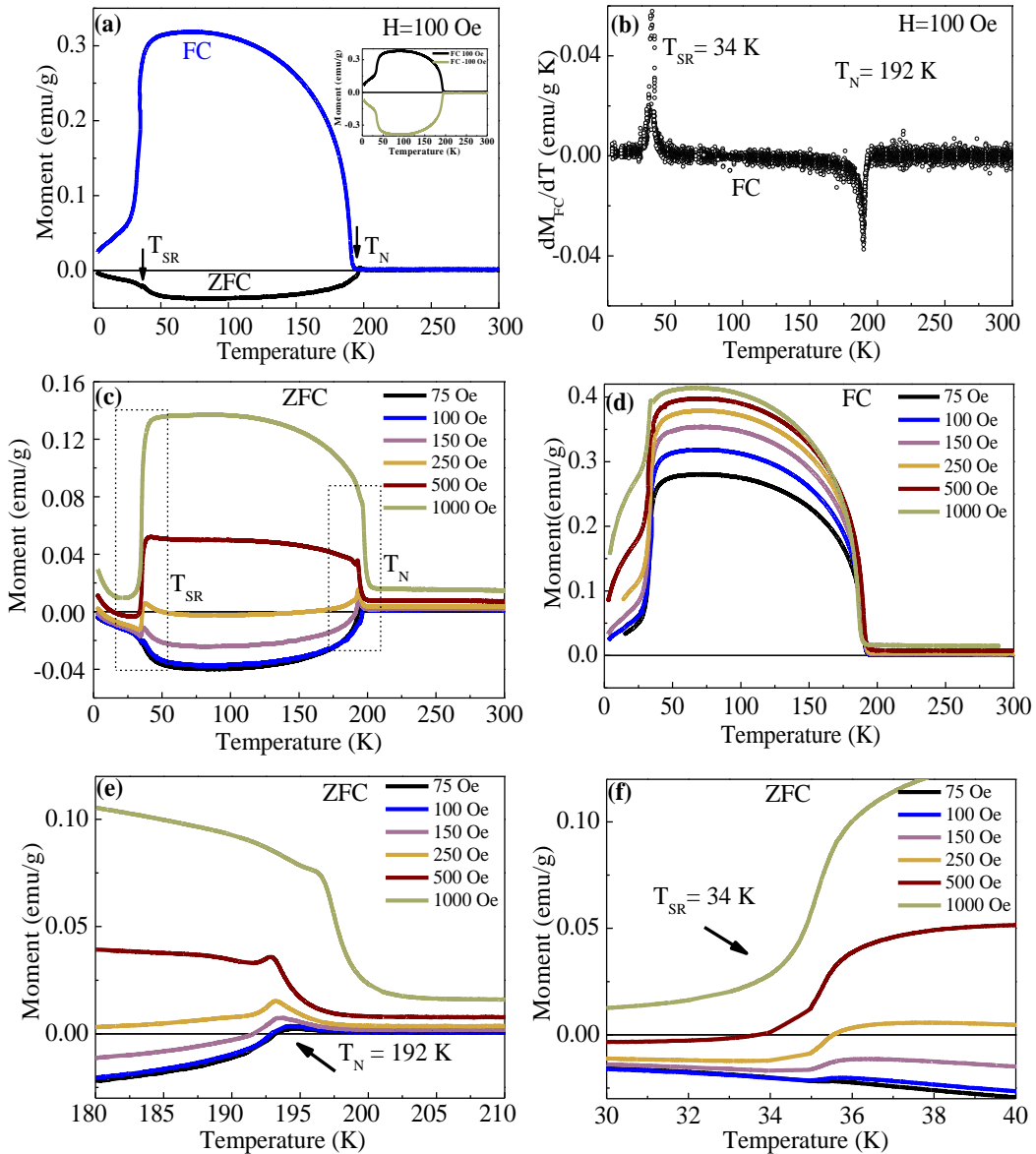


*Figure 1. (a) ZFC-FC magnetization curves of SCO at 100 Oe (b) temperature dependent $dM_{FC}/dT$ plot of SCO polycrystallites at 100 Oe. Inset of (a) shows a comparison of $M_{FC}$ vs T curves at ±100 Oe. (c)An external field dependent*

*comparison of $M_{ZFC}$ vs. T curves clearly showing a change from positive to negative magnetization at lower external magnetic field. (d) An external field dependent comparison of $M_{FC}$ vs. T curves show positive magnetization at all the applied field values. (e) zoomed view of $M_{ZFC}$ vs. T curves around Néel temperature $T_N$ and (f) around spin reorientation transition $T_{SR}$ as indicated by dotted boxes in figure 3(c).*

The $M_{ZFC}$ – T curve at 100 Oe exhibits an increase in $M_{ZFC}$ which reaches a maximum at ~ 192 K, then $M_{ZFC}$ drops down and cross $M_{ZFC} = 0$ at ~ 191 K and shows $M_{ZFC}(min)$ of ~ - 0.037 emu/g at ~ 70 K. After further decrease in T, the $M_{ZFC}$ again increases to ~ - 0.003 emu/g at ~ 3 K (**Figure 1(a)**). This NM behavior indicates that the direction of net $M_{ZFC}$ is opposite to the external applied magnetic field ($H_{ext}$). [4,22] It can be seen from **Figure 1(a)** that the $M_{FC}$ –T curve show an increase in $M_{FC}$ ~ 0.318 emu/g at 70 K which can be attributed to the superposition of the $Sm^{3+}$ and $Cr^{3+}$ spins contributing to net magnetization.[50] Below ~ 70 K, the $M_{FC}$ – T curves shows the change in slope with a decrease in $M_{FC}$ down to ~ 3 K. The decrease in $M_{FC}$ below 40 K is due to spin reorientation (SR) caused by $Cr^{3+}$- $Sm^{3+}$ interactions. Inset of **Figure 1(a)** represents the $M_{FC}$ vs. T curves at ±100 Oe which shows almost mirror-like magnetization curves indicating NM in SCO. Similar behavior was also observed in $SmCr_{1-x}Fe_xO_3$ system.[54] **Figure 1(b)** shows the derivative of $M_{FC}$ as a function of T at 100 Oe which clearly indicates strong magnetic anomalies at ~ 192 and ~ 34 K, corresponding to the onset of AFM ordering of $Cr^{3+}$ spins and reorientation of $Sm^{3+}$ moments with respect to canted $Cr^{3+}$ moments, respectively. NM observed in SCO is quite interesting phenomenon and possible explanation could be given by considering the temperature and field dependent interplay between $Sm^{3+}$– $Cr^{3+}$ spins. NM in SCO is mainly due to the antiparallel coupling between $Sm^{3+}$– $Cr^{3+}$ spins sublattices.[55,56]

**Figure 1(c)** shows the $M_{ZFC}$ – T curves at varying $H_{ext}$ in a T-range from 3 to 300 K. The NM is observed in $M_{ZFC}$ – T curves for $H_{ext} \leq 250$ Oe where, the AFM coupling between $Sm^{3+}$ and the canted $Cr^{3+}$ moments dominates over the $H_{ext}$ leading to the antiparallel alignment of $Sm^{3+}$ spins with respect to the $Cr^{3+}$ spins. Similar model have successfully explained the NM behavior in $GdCrO_3$,[4] $DyCrO_3$,[22] $DyFeO_3$[5] and $La_{1-x}Pr_xCrO_3$[57] perovskites. For $H_{ext} \geq 250$ Oe, the NM is suppressed, as the internal induced field becomes smaller than the $H_{ext}$ which prevents the opposite alignment of

$Sm^{3+}$ with respect to weak FM $Cr^{3+}$ moments giving net positive magnetization. However, the SR transition can still be achieved at ~ 34 K even at 1000 Oe as $H_{ext}$ is not strong enough to overcome the induced field on $Sm^{3+}$ spins.

**Figure 1(d)** illustrates the $H_{ext}$-dependence of $M_{FC}$–T curves in T range 3-300 K. Below 200 K, at $H_{ext} \geq 75$ Oe, the $M_{FC}$ increases and reaches to a maximum value at ~ 70 K and thereafter, it drops down sharply in the vicinity of SR transition (~ 34 K). At ~ 34 K, the $Cr^{3+}- Sm^{3+}$ spin interaction becomes prominent and SR transition takes place resulting into a sudden drop in the $M_{FC}$ which is due to the onset of AFM ordering of $Sm^{3+}$ spins at low T.[50] To further explore the existence of magnetic transitions in SCO polycrystallites, we have shown a zoom view of $M_{ZFC}$ − T curves around $T_N$ and $T_{SR}$ in **Figure 1(e)** and **(f)**, respectively. The compensation temperature ($T_{cross}$: temperature at which magnetization cross from positive to negative) in $M_{ZFC}$ - T curves is strongly dependent on $H_{ext}$. From 100 Oe to 150 Oe, there is not much change in $T_{cross}$ which is at ~ 191 K for 100 Oe and ~190 K for 150 Oe. But at 250 Oe, $T_{cross}$ further decreases to ~ 153 K. At higher magnetic fields, the applied field is much larger and enough to dominate the induced field on $Sm^{3+}$ spins and thus, $M_{ZFC}$ − T curve shows positive $M_{ZFC}$ at 1000 Oe. However, no change in SR transition ($T_{SR}$ ~ 34 K) with $H_{ext}$ was observed.

## 4.4.2  Exchange bias:

As discussed earlier in **section 4.3**, the EB is known to be associated with the NM, which encouraged us to explore the EB effect in SCO polycrystallites. The M-H curves are clubbed in three different temperature-ranges taken in a field range from − 90 to +90 kOe in ZFC mode (**Figure 2(a), (b)** and **(c)** showing M-H plots at 5-30 K, 40-65 K and 85-180 K, respectively). As observed from **Figure 2**, the curves at T < $T_N$, show a clear opening of hysteresis loop due to weak FM and magnetization does not saturate even up to 90 kOe, indicating strong predominant AFM exchange interaction. The weak FM is mainly attributed to the canting of $Cr^{3+}$ spins followed by tilting of $CrO_6$ octahedral.[55]

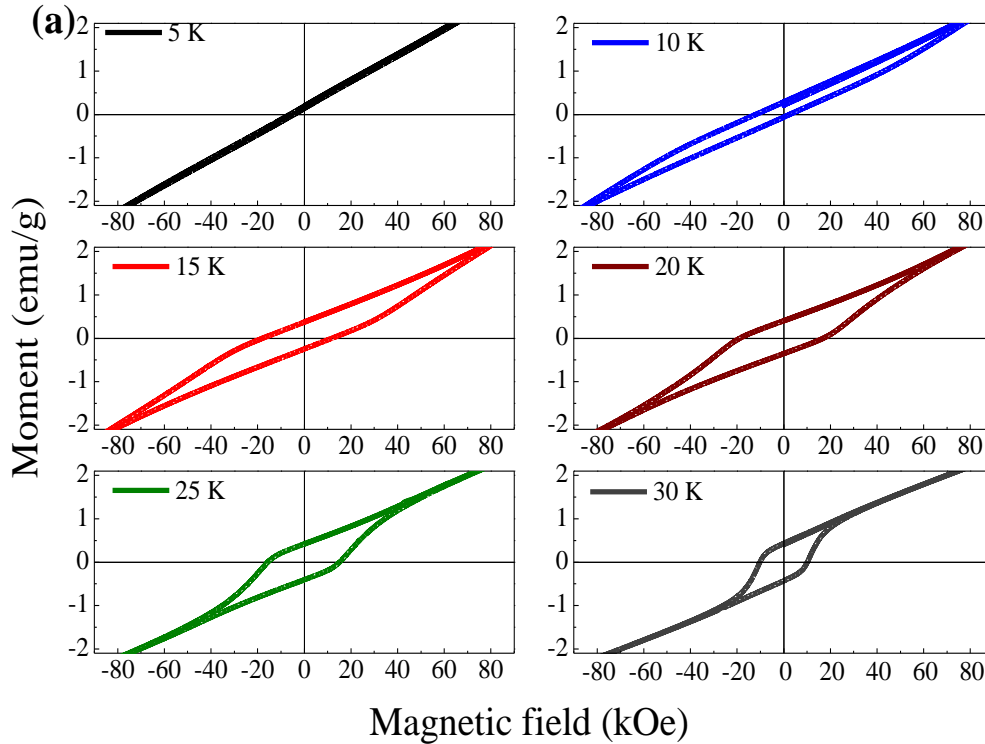Fig. 2 (a) shows the comparison of M-H curves in 5–30 K range.



*Figure 2. M-H hysteresis loops of SCO polycrystallites in ZFC mode in a temperature range (a) 5-30 K. These curves show temperature dependent changes in the coercivity, remanent magnetization and exchange bias field.*

We observed that the negative EB becomes prominent as $Sm^{3+} - Sm^{3+}$ spin interaction starts dominating at lower temperatures. As we go down from 30 K to 5 K, exchange bias field ($H_{EB}$) increased from ~ 90 Oe to ~ 4709 Oe which can be attributed to the weak FM arising due to small canting from AFM axis of $Cr^{3+}$ spins to strong AFM coupling of $Sm^{3+}$ spins. On the other hand, it can be seen that coercivity ($H_C$) suddenly increased from ~ 10096 Oe to ~ 15324 Oe, as we go from 30 K to 25 K and reaches maximum of ~ 17890 Oe at 20 K. This sudden increase can be understood as a change of structure of $Cr^{3+}$ spins for T < $T_{SR}$ (~ 35 K) and development of exchange anisotropy resulting into enhanced $H_C$.[25] However, at 10 K, $H_{EB}$ was found to be maximum and $H_C$ decreased to ~ 7215 Oe. Whereas, at 5 K, the hysteresis curve completely shifts towards the negative side of the origin with

decrease in coercivity, suggesting strong AFM contribution from $Sm^{3+}$ spins dominating at low temperature.

In **Figure 2(b)**, with the decrease in temperature from 60 - 40 K, $H_C$ decreases from ~ 13,244 Oe to ~ 7403 Oe and remanent asymmetry ($M_{EB}$) increases from 0 till 60 K to ~ 0.005 emu/g at 45 K. But, below 45 K, $M_{EB}$ (~ 0.003 emu/g) decreases at 40 K and disappear at 35 K ($T_{SR}$). At 35 K, the $H_C$ also becomes relatively small ($H_C$ ~ 4501 Oe) and EB nearly vanishes and loop becomes symmetric at this temperature ($T_{SR}$).
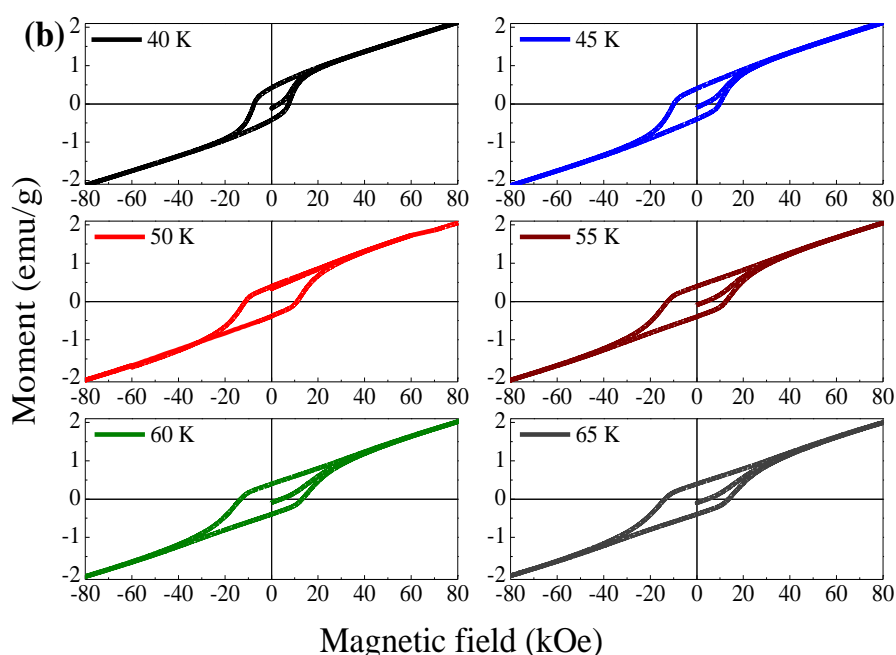


**Figure 2.** *(b) M-H hysteresis loops of SCO polycrystallites in ZFC mode in a temperature range 40 - 65 K . These curves show temperature dependent changes in the coercivity, remanent magnetization and exchange bias field.*

In **Figure 2(c)**, we have discussed the last important temperature range *i.e.* 85 − 180 K.
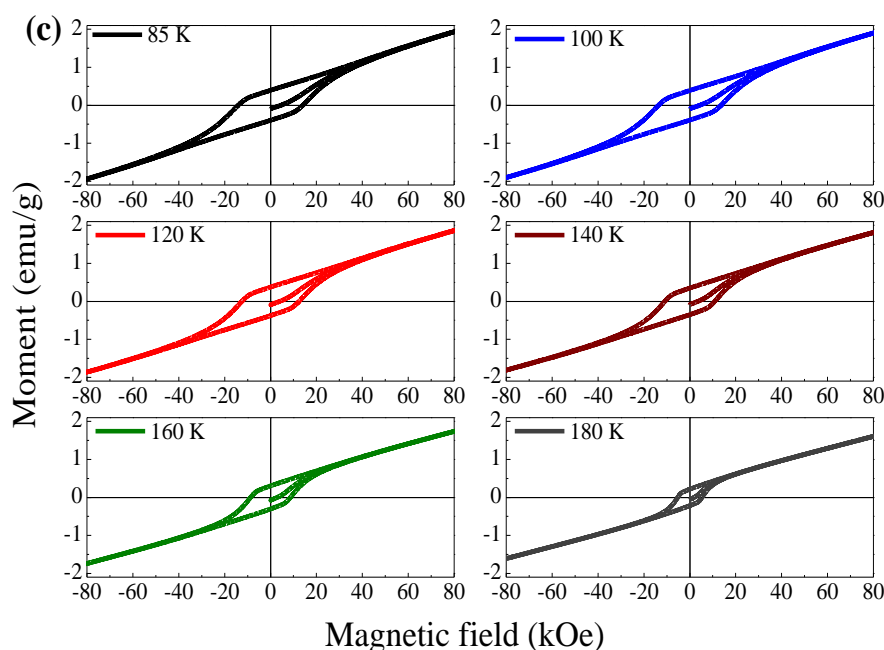
*Figure 2. (c) M-H hysteresis loops of SCO polycrystallites in ZFC mode in a temperature range 85 - 180 K . These curves show temperature dependent changes in the coercivity, remanent magnetization and exchange bias field.*

As can be seen from **Figure**, $H_C$ increased from ~ 5274 Oe to ~ 14,112 Oe with a decrease in T from 180 K to 85 K, but the trend in $H_{EB}$ was found to be abrupt which is however difficult to explain and quantify due to competing and complex magnetic interactions in this class of system. Also, $M_{EB}$ was zero in this temperature range. It is surprising to observe the change in sign of $H_{EB}$ to positive (32 Oe) along with the decrease in $H_C$ down to 13,710 Oe at 65 K. Below 65 K, $H_{EB}$ again becomes negative till 40 K and vanishes at 35 K as discussed earlier.

**Figure 2(d)** clearly shows the M - H curve at 35 K, where, EB disappears and at 200 K, linearity indicates the paramagnetic behavior of SCO.
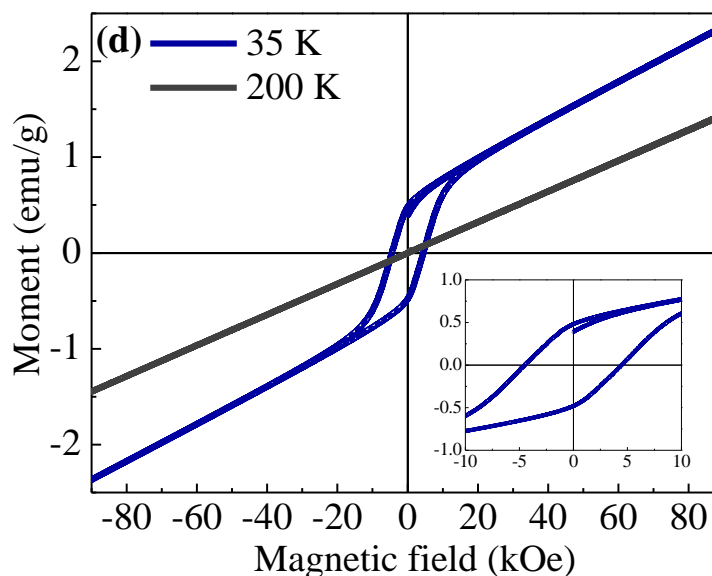
*Figure 2. (d) M-H hysteresis loops of SCO polycrystallites in ZFC mode in a temperature range 35 & 200 K. The inset of panel (d) shows the zoom view of the curves in the main panel.*

### 4.4.3 Temperature dependence of coercivity and exchange bias:

In order to get an insight into the temperature effects on EB, the temperature dependent parameters, $H_C$ (T) and $H_{EB}$ (T), $M_{EB}$ (T) are plotted in **Figure 3(a)** and **(b)**, respectively and tabulated in **Table 3**.

| Temperature | Exchange Bias field | Coercivity | Remanent asymmetry |
|:---:|:---:|:---:|:---:|
| T(K) | $H_{EB}$ (Oe) | $H_C$ (Oe ) | $M_{EB}$ (emu/g) |
| 10 | -4709 | 7215 | 0.115 |
| 15 | -3092 | 14880 | 0.032 |
| 20 | -1015 | 17890 | 0.026 |
| 25 | -250 | 15324 | 0.0085 |
| 30 | -90 | 10096 | 0.003 |
| **35** | **0** | **4501** | **0** |
| 40 | -34 | 7403 | 0.003 |

| 45 | -76 | 9798 | 0.005 |
|---|---|---|---|
| 50 | -143 | 11138 | 0.0045 |
| 55 | -102 | 12476 | 0.0015 |
| 60 | -81 | 13244 | 0 |
| **65** | **32** | **13710** | **0** |
| 85 | -55 | 14112 | 0 |
| 100 | -38 | 13636 | 0 |
| 120 | -25 | 12493 | 0 |
| 140 | -56 | 10857 | 0 |
| 180 | 9 | 5274 | 0 |

*Table 3. Exchange bias parameters and coercivity of the M-H curves for SmCrO$_3$ at various temperatures.*

Below $T_{SR}$, $H_C$ (T) increases and exhibits a peak at 20 K with $H_C$ ~17890 Oe, as seen from **Figure 3(a)**.
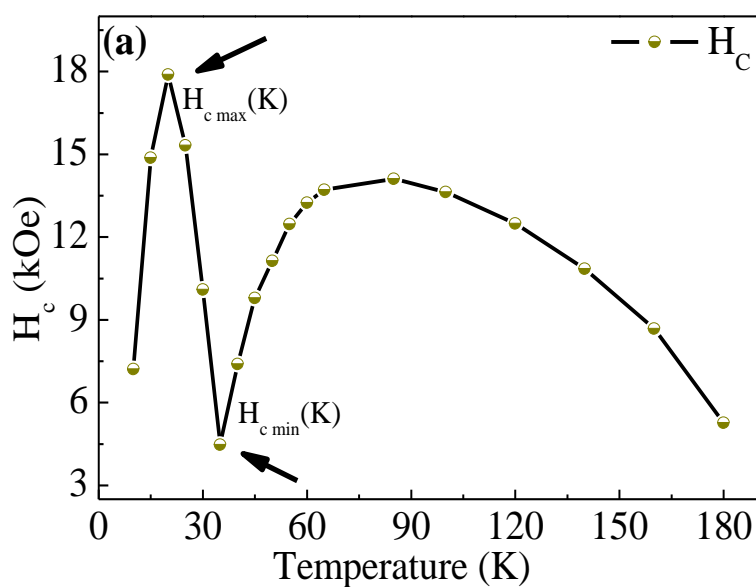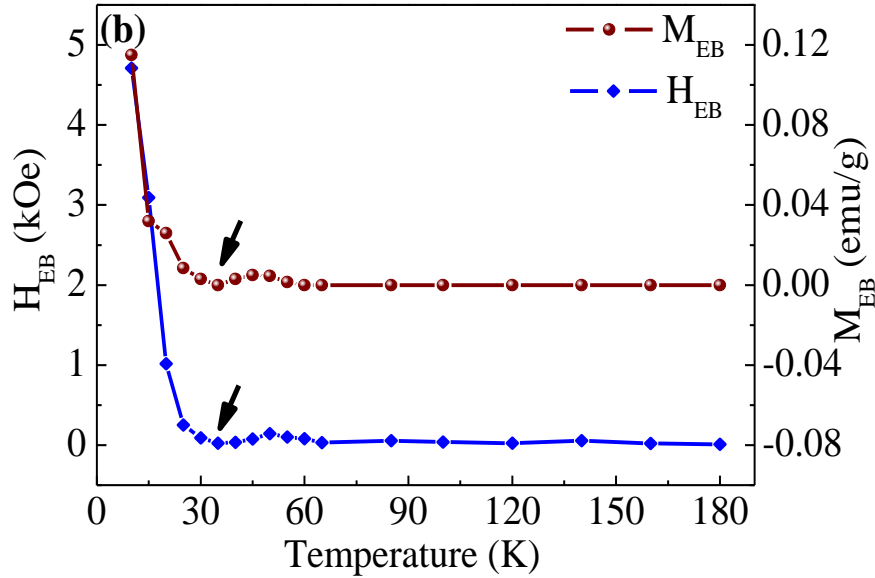
*Figure 3. Temperature dependence of (a) coercivity ($H_C$) (b) exchange bias field ($H_{EB}$) and remanent asymmetry ($M_{EB}$) of SCO polycrystallites with the measuring field between +9 and -9 T.*

The $H_C$ (T) above $T_{SR}$ again shoots up till 85 K and decreases in the vicinity of $T_N$. **Figure 3(b)** shows that $H_{EB}$ (T) and $M_{EB}$ (T) decreases monotonically with increasing T and vanishes at 35 K, which can be related to the increase in weak FM moments that can be easily aligned to the $H_{ext}$. The observed decrease in $M_{EB}$ (T) with an increase in T indicates that the AFM phase was suppressed due to weakening of FM/AFM coupling and above $T_{SR}$; FM interaction dominates over the AFM interaction. Above 35 K, $M_{EB}$ (T) was found to decrease till 50 K and the presence of $M_{EB}$ below 60 K suggests the existence of net uncompensated spin which do not rotate with applied magnetic field resulting in remanent magnetization shift ($M_{shift}$).[25] This uncompensated spins can be related to the large coercive field required to reverse the weak FM spins and thus, the hysteresis loop shift to negative field giving rise to negative EB.[15] However, $M_{EB}$ disappears above 60 K and remains same till 180 K.

### 4.4.4  Effect of field cooling on exchange bias:

To further confirm the intrinsic nature of EB, effect of field cooling (FC) and number of hysteresis cycle (n) were studied to probe the spin dynamics at the locally formed FM/AFM interface.[25,58] **Figure 4(a)** shows the M-H curves at 25 K with the applied $H_{FC} \pm 20$ kOe.
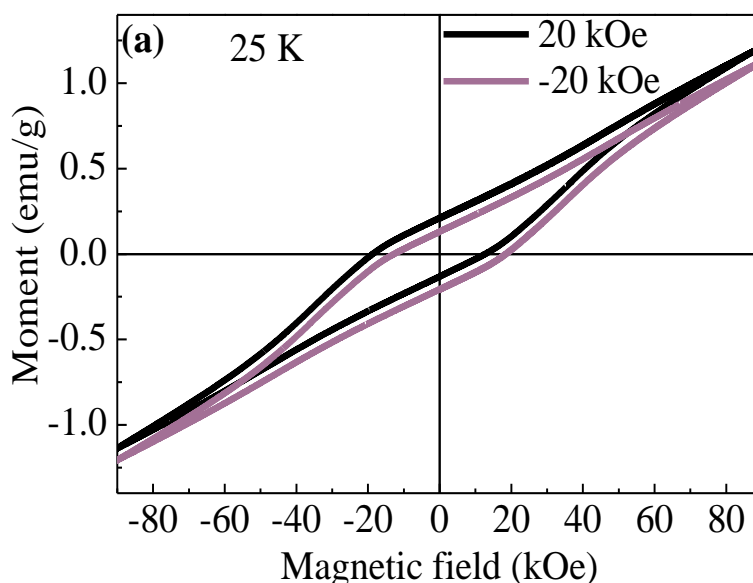


*Figure 4.(a) A comparison of M-H hysteresis loops at 25 K with the field cooling at ±20 k Oe.*

The $H_{EB}$ (~ 3085 Oe) was found to be the same while cooling in ± 20 kOe magnetic field. The applied $H_{FC}$ was comparatively more than the observed $H_C$ at 25 K. Thus, by changing the polarity of $H_{FC}$, $H_{EB}$ changes accordingly. This symmetric shift with $\pm H_{FC}$ further confirmed, that the observed EB was due to the uncompensated spins at the locally formed FM/AFM interface instead of unsaturated minor loop.[25,58]

### 4.4.5  Training effect on exchange bias:

By studying the training effect on SCO for 5 consecutive repeating cycles, the EB was reconfirmed. The $H_{EB}$ was found to decrease monotonically with the increase in the number of cycles (n) as seen from **Figure 4(b)**.
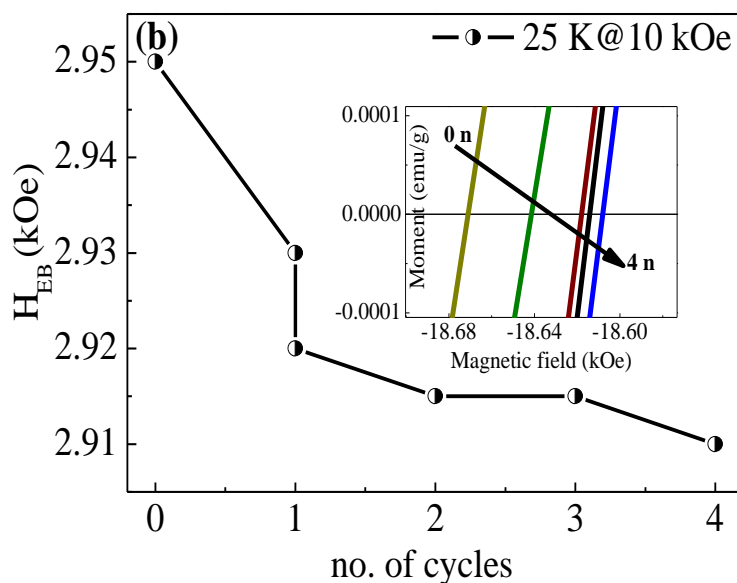
*Figure 4.(b) The effect of training cycles on $H_{EB}$ with an increase in number of cycles (n). Inset showing the zoomed view of M-H hysteresis loop from 0 n to 4 n.*

This further indicated that the spin configuration is quite stable at the locally formed FM/AFM interface even against the $H_{FC}$ and after each cycle, the AFM spins tries to find an energetically favorable condition.[25,58,59]

## 4.4.6 AC-magnetization studies:

The dynamic magnetic measurement is an extremely sensitive technique to detect magnetic anomalies such as SR transition as it depends on the strength of the anisotropies, Nèel transition, reversible rotation of magnetic moments or small impurities in a single phase multiferroic compound.[56]

To detect these transitions, ac-magnetic measurements at excitation field ($H_{ac}$= 10 Oe),without any applied dc-bias, were done at a frequency range 501-9999 Hz.
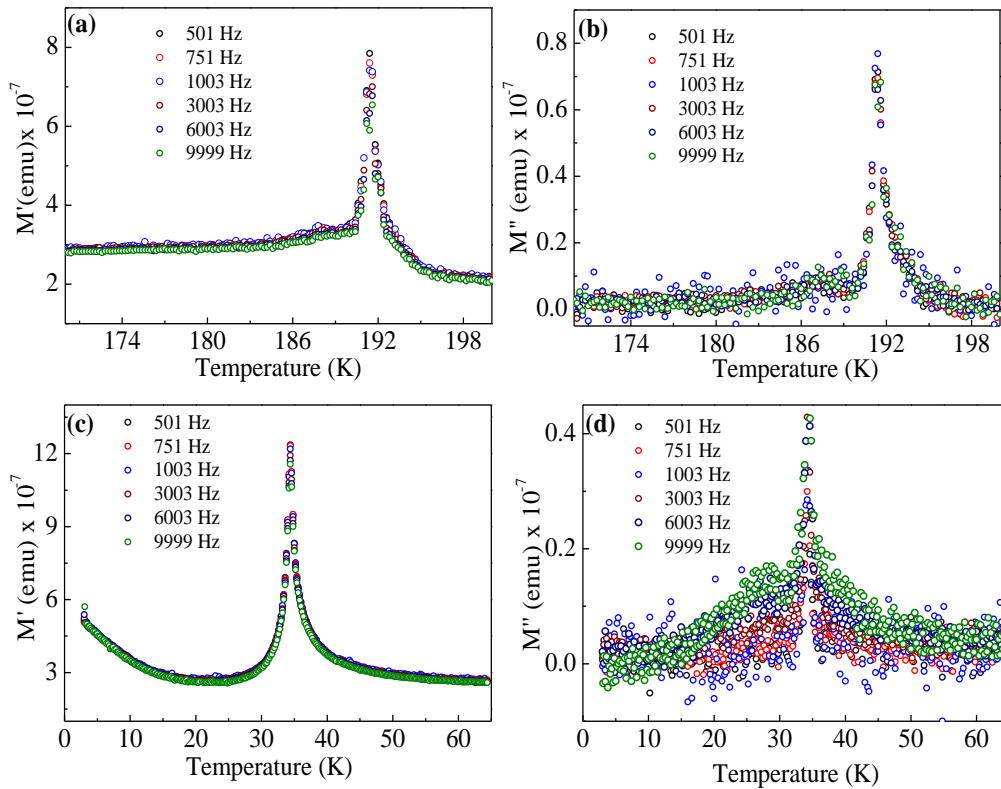
*Figure 5. Temperature dependence of the (a, c) real and (b, d) imaginary part of the ac-magnetization around $T_N$ and $T_{SR}$ at 10 Oe ac amplitudes ($H_{ac}$) and varying frequencies (501-999 Hz) for SCO polycrystallites.*

In **Figure 5(a, c)** and **(b, d)**, the real M′ (T) and imaginary parts M″(T) are shown. All the curves show characteristic maxima around $T_N$ (~ 192 K), commonly ascribed to the $Cr^{3+}$AFM ordering and an anomaly at $T_{SR}$ ~ 34 K corresponds to the SR transition. No change in the peak intensity and position was observed with respect to the frequency.

## 4.4.7 Field assisted memory-switching application:

The characteristic feature of magnetization flipping from negative to positive by simply changing the $H_{ext}$ in SCO nanocrystallites (**Figure 6**) is similar to the conventional magnetic materials where, $H_{ext}$ is required to change the polarity.
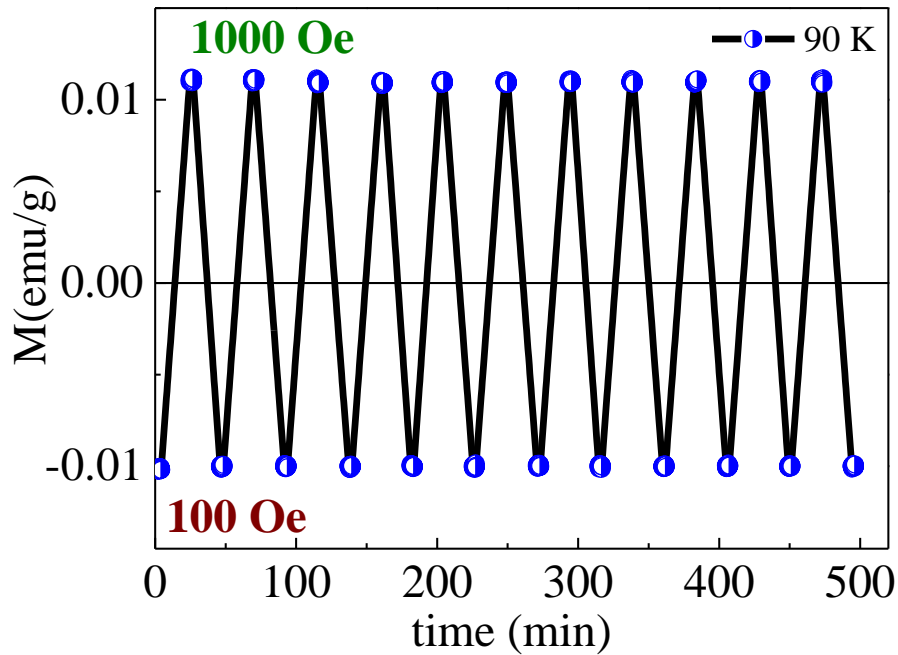
*Figure 6. Field induced magnetization switching in SCO at 90 K.*

The change in the polarity of magnetization by varying $H_{ext}$, cycled several times showed good reproducibility and no noticeable decay in magnetization was observed. Thus, the magnetization can be tuned in a predictable way and this behavior is favorable application such as in non-volatile magnetic memories.[33] Similar feature was also observed in other chromites exhibiting NM such as $YFe_{0.5}Cr_{0.5}O_3$[33] $SmCr_{1-x}Fe_xO_3$[54] and $TmCrO_3$[36]. Thus, by simply changing the magnitude of the $H_{ext}$, the polarity of the magnetization can be switched between negative and positive in SCO. The magnetization switching characteristic in SCO is similar to DCO. We believe that, ZFC NM plays a vital factor in orthochromites for determining the switching behavior.

## 4.4.8 Conclusions

In this contribution, structural and magnetic properties of SCO polycrystallites have been investigated. NM in SCO was found to be strongly dependent on the $H_{ext}$. Systematic isothermal M-H measurements below SR-transition temperature confirmed the EB effect in SCO. The training effect on SCO further confirmed that the EB observed was mainly due to the stable spin configuration at the locally formed

FM/AFM interface rather than unsaturated minor loop. The real and imaginary parts of ac-magnetization peaks at $T_N$ and $T_{SR}$ were found to be frequency independent.

# Section 4.5

# Temperature and magnetic-field assisted switching of magnetization and observation of exchange bias in YbCrO₃ nanocrystals



_____
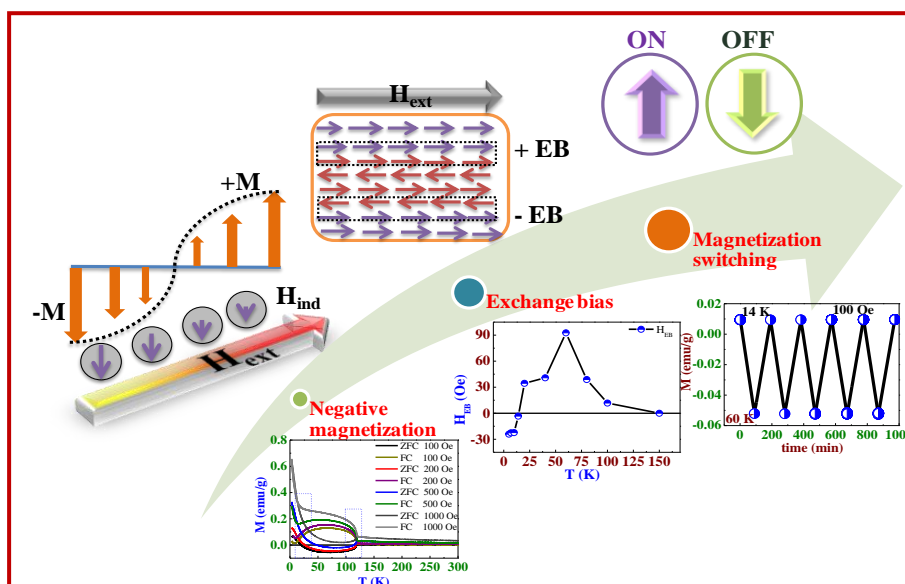
In this section, we demonstrate an interesting feature in YbCrO$_3$ (YCO) nanocrystals in which the material shows temperature and external magnetic field assisted switching (a complete sign reversal) of zero field cooled magnetization (M$_{ZFC}$) and exchange bias (EB) as a result of competing spin interaction at low temperature. This feature can be applied in non-volatile memories, where, simply by changing the magnitude of the H$_{ext}$ and T, the polarity of the magnetization can be switched between negative and positive. The observed T dependent sign reversal in the EB was closely associated with the sign reversal of M$_{ZFC}$. The training cycle further confirmed that the H$_{EB}$ value decreased to ~ 2 % of the initial value of observed EB which was very small compared to the observed H$_{EB}$ in YCO, indicated stable spin configuration at the locally formed ferromagnetic (FM)/ antiferromagnetic (AFM) interface.

_____

## 4.5.1 Negative magnetization:

**Figure 1(a)** shows the zero-field cooled and field-cooled magnetization ($M_{ZFC}$, $M_{FC}$) vs. T curves of YCO at $H_{ext}$ = 100 Oe in a temperature (T) range 3–300 K. At RT, the YCO shows paramagnetic (PM) behavior and $Cr^{3+}$ spins order antiferromagnetically (AFM) below $T_N$ ~ 119 K which is close to the Néel transition value reported for YCO single crystal but more than the reported sub-micrometer sized YCO nanoparticles.[21,60]
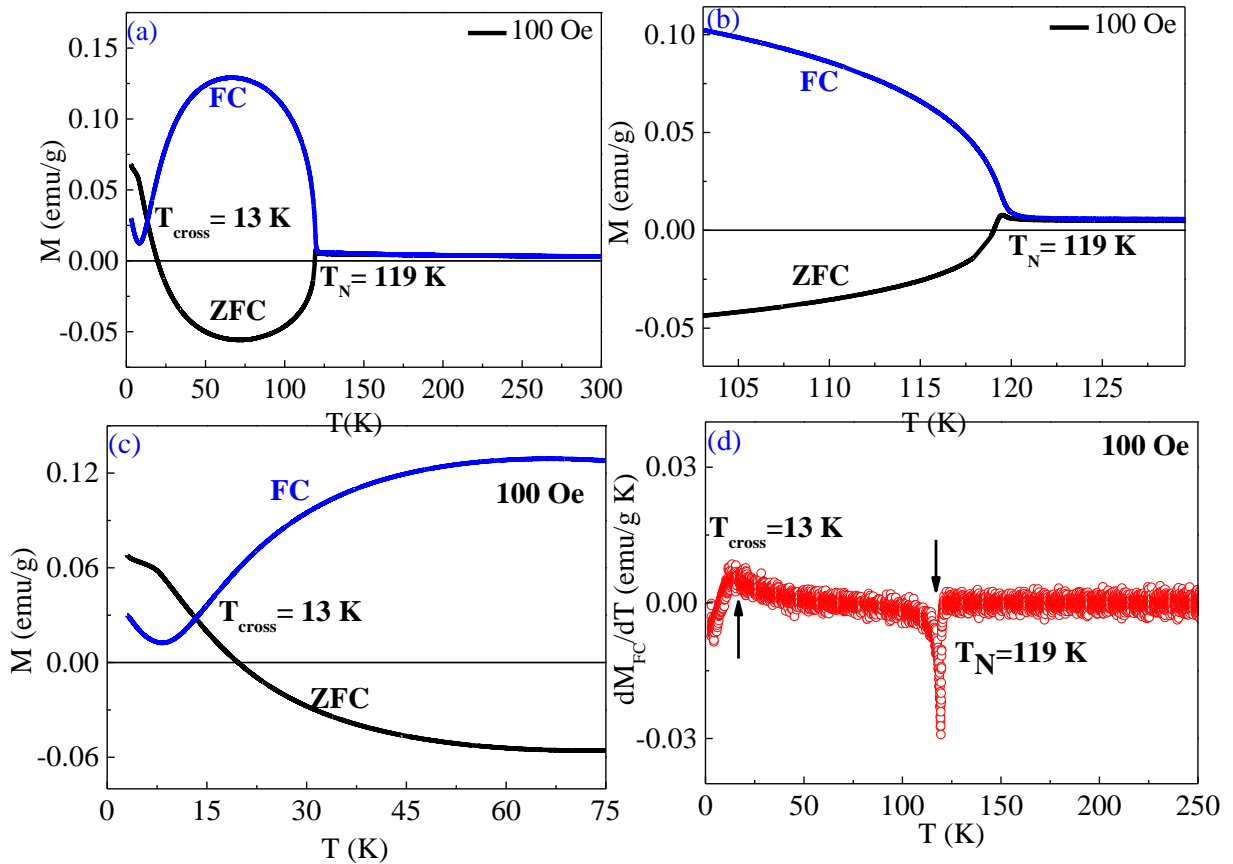


*Figure 1. (a) The $M_{ZFC}$ (T) - $M_{FC}$ (T) curves at $H_{ext}$ ~100 Oe showing zero field cooled negative magnetization below $T_N$ (b, c) showing zoomed view at $T_N$ and $T_{cross}$ and (d) $dM_{FC}$/dT plot of YCO nanocrystallites.*

It was observed that, just below the $T_N$, the $M_{ZFC}$ shows a positive value and shows a shoulder, before decreasing at further lower temperatures as shown in the **Figure 1(b)**. This is characteristic feature of AFM transitions. With further decrease in T,

$M_{ZFC}$ cross $M_{ZFC}$ =0 line at $T_{comp(1)}$ ~ 117 K   (compensation temperature where magnetization is zero) and turns negative. The NM observed in YCO can be attributed to the increase in the induced field ($H_i$) on *$Yb^{3+}$* spins due to the canted *$Cr^{3+}$* spins with respect to $H_{ext}$ = 100 Oe. The $M_{ZFC}$ decreases further to reach a minimum value of ~ − 0.055 emu/g at 60 K and become positive at $T_{comp(2)}$ ~ 19 K. On the other hand, below $T_N$, the value $M_{FC}$ increases due to the fact that *$Yb^{3+}$* and *$Cr^{3+}$* spins were coupled together contributing to the net $M_{FC}$ value, reaching a maximum of ~ 0.129 emu/g at ~ 60 K (in the proximity to the point where $M_{ZFC}$ shows a minimum). Below 60 K, $M_{FC}$ decreased, reaching a minimum value of ~ 0.012 emu/g at ~ 9 K. We also observed $T_{cross}$ ~ 13 K (crossover temperature at which $M_{ZFC}$ and $M_{FC}$ crosses ) which further passes through zero at the compensation temperature $T_{comp(2)}$ ~ 19 K .The observed crossover temperature  agrees well with the reported values of quasi hollow YCO nanostructures ($T_{cross}$ ~ 12 K) with particle size ~ 50-100 nm.[61] As seen from **Figure 1(c)**, the observed $T_{comp(2)}$ ~ 19 K was close to YCO nanoparticles but slightly higher than the bulk YCO reported values $T_{comp(2)}$ ~ 18.3 K and ~ 16.5 K. [50,60,61] This slight variation in the $T_{comp(2)}$ can be accounted to the particle size of the compound. **Figure 1(d)** shows the temperature dependence on derivative of $M_{FC}$. From the $dM_{FC}/dT$ vs. T curve, we observe prominent peaks situated at ~ 119 K and ~ 13 K, respectively. These peaks are consistent with the magnetic transitions observed in $M_{FC}$ vs. T. The magnetic anomalies observed in YCO nanocrystals was found close to single crystal values and also consistent with the reported nanocrystalline phase of YCO.[50,60,61]

## 4.5.2  Temperature and field dependence negative magnetization:

Detailed external magnetic field dependent $M_{FC}$ (T) and $M_{ZFC}$ (T) studies were done to understand the NM behavior in YCO. **Figure 2(a)** shows the field dependent $M_{ZFC}$, $M_{FC}$ -T curves. The zoomed view around $T_N$ and $T_{cross}$ is depicted in **Figure 2(b, c)**.
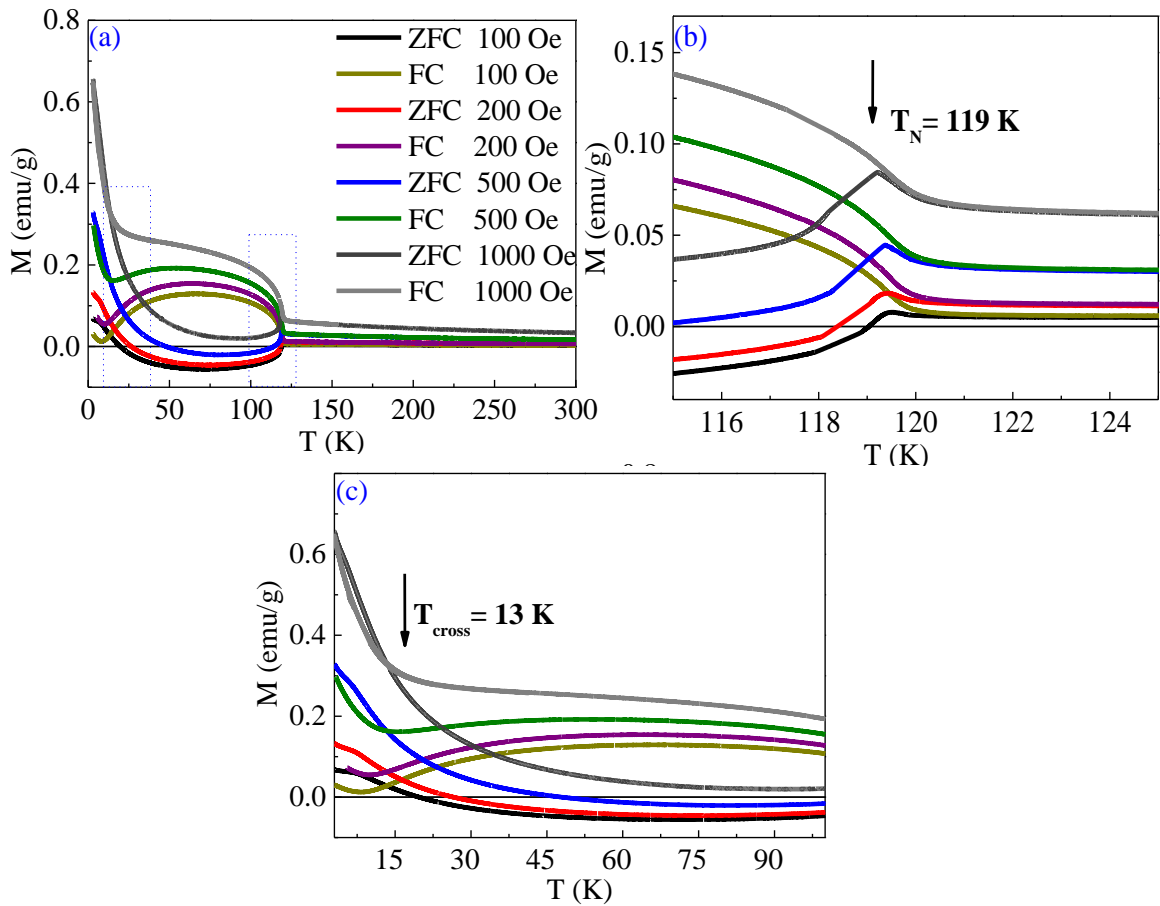
***Figure 2. (a) It shows the external magnetic field dependence of  $M_{ZFC}(T)$-$M_{FC}(T)$ curves. The $M_{ZFC}(T)$ curves clearly indicate a cross-over from negative to positive magnetization at larger $H_{ext}$, (b) The magnified view around the dotted box at higher temperatures show the field dependence of $M_{ZFC}(T)$-$M_{FC}(T)$ curves near $T_N$ and (c) Magnified view around the dotted box at lower temperature which shows the field dependence around $T_{cross}$.***

The $T_{comp(1)}$ was found to be field dependent which monotonically decreases from ~ 117 K to ~ 113 K as we increased the $H_{ext}$ from 100 to 500 Oe. At $H_{ext} \leq 500$ Oe, the NM observed was due to the fact that the canting of $Cr^{3+}$ spins induces local magnetic field on $Yb^{3+}$ spins which results into an antiparallel alignment of $Cr^{3+}$ and $Yb^{3+}$ spins.[4,22] At 1000 Oe, the $H_{ext}$ overcame the induced magnetic field giving positive magnetization in YCO.

The quantitative measure of NM in YCO was given by the ratio of negative to positive magnetization (M$_{-ive}$/M$_{+ive}$ =M$_{ZFC}$/M$_{FC}$) *i.e.* the minimum and maximum values of M$_{ZFC}$ (T) and M$_{FC}$(T) curves, which was found to be – 0.4 for H$_{ext}$ =100 Oe. In some of the polycrystalline rare earth chromites such as GdCrO$_3$, La$_{0.5}$Pr$_{0.5}$CrO$_3$ and LaCr$_{0.85}$Mn$_{0.15}$O$_3$ , these values are reported to be 30, 40, and 2 for 100 Oe applied magnetic field.[62–64] However, after increasing the H$_{ext}$, this ratio decreased down to – 0.25 at 200 Oe and to –0.09 at 500 Oe. Similarly, the relative irreversible magnetization calculated using $\frac{\Delta M}{M_{ZFC}} = \frac{M_{FC} - M_{ZFC}}{M_{ZFC}}$, for YCO, was found to be - 1.4 which is comparable to GdCrO$_3$, La$_{0.5}$Pr$_{0.5}$CrO$_3$ and LaCr$_{0.85}$Mn$_{0.15}$O$_3$ polycrystallites having values in the range from –2 to –9. [62–64]

### 4.5.3  AC-magnetization studies:

The ac-magnetization measurement is an extremely sensitive technique to detect magnetic anomalies such as Nèel transition, reversible rotation of magnetic moments, spin glass transition or small impurities in a single phase multiferroic.[56] The ac-magnetic measurements were done at a 10 Oe excitation field without any applied dc bias in a range of frequencies (between 501-9999 Hz).

**Figure 3(a, b)** represents the real part of ac-magnetization (M′) curves in a temperature range 10-25 K and 115-125 K, respectively At low temperature (**Figure 3(a)**, we didn't detect any anomaly in real part of magnetization (M′) curve. However, the measurements in the vicinity of T$_N$ (**Figure 3(b)**) showed a weak anomaly at T$_N$ ~ 119 K in real part of magnetization (M′) curve which agrees well with the dc-magnetic measurements (inset shows the zoomed view at T$_N$).
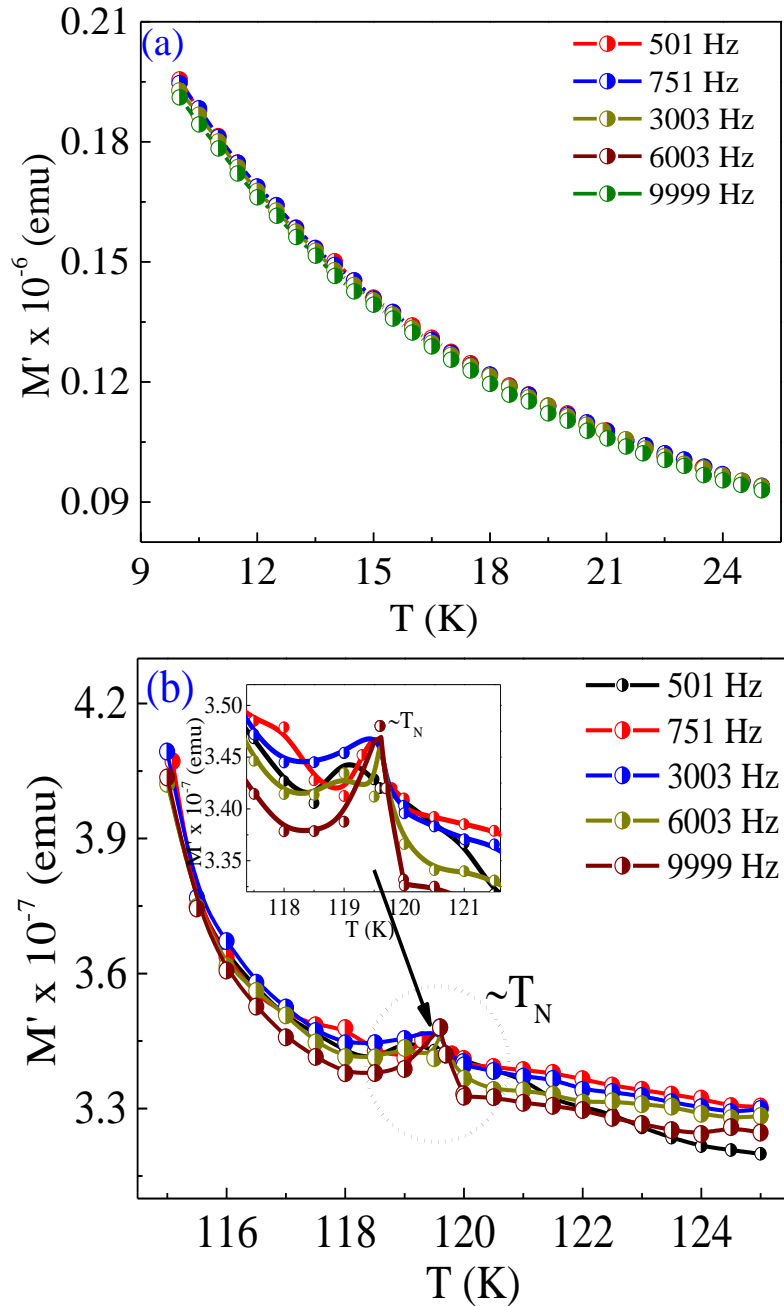
*Figure 3. Temperature and frequency dependence of the real part of the ac magnetization measured at a 10 Oe ac field (a) 10-25 K and (b) 115-125 K for YCO. Inset of panel (b) shows the zoom views of the real component of the ac magnetization around $T_N$ ~119 K.*

We cannot ignore the fact that, surface effects play an important role in determining the magnetic properties of the nanoscale materials. As ac-magnetic measurements are highly sensitive and efficient tool to detect any spin-glass type of

behavior often associated with the superparamagnetic state of the nanoparticles. We have not found any frequency dependence of magnetization in ac-magnetization curve or any such behavior in the dc-magnetization which could be linked to blocking transition in YCO.

### 4.5.4   Study of temperature dependent exchange bias and its origin:

As discussed previously for DCO and SCO nanoparticles, the NM is known to be associated with the EB. Therefore, the observation of NM below $T_N$ ~ 119 K prompted us to explore the possibility of EB behavior in YCO nanocrystallites. The M - H loops were measured in a broad temperature range (5 – 100 K) in ZFC condition and shown in **Figure 8**.  As seen from the **Figure 4(a)**, the linear behavior at RT indicated the paramagnetic nature of YCO. Below $T_N$, we observed an opening of M - H loop and lack of saturation, attributed to the AFM ordering of canted $Cr^{3+}$ spins.[4,22,23]

However, we noticed an asymmetry in the hysteresis loops, as the sample was cooled from 100 K to 20 K (**Figure 4(b-f)**). The $H_{EB}$ was found to switch from positive to negative at ~ 13 K. The sign-reversal temperature of HEB from positive to negative, while cooling, was also found to be consistent with the sign reversal of $M_{ZFC}$ (disappearance of NM). Below 10 K, as shown in **Figure 4(g, h)**, the system shows negative exchange bias (NEB). In general, the competition between weak FM and strong AFM results into the shift of hysteresis toward the negative side of origin.
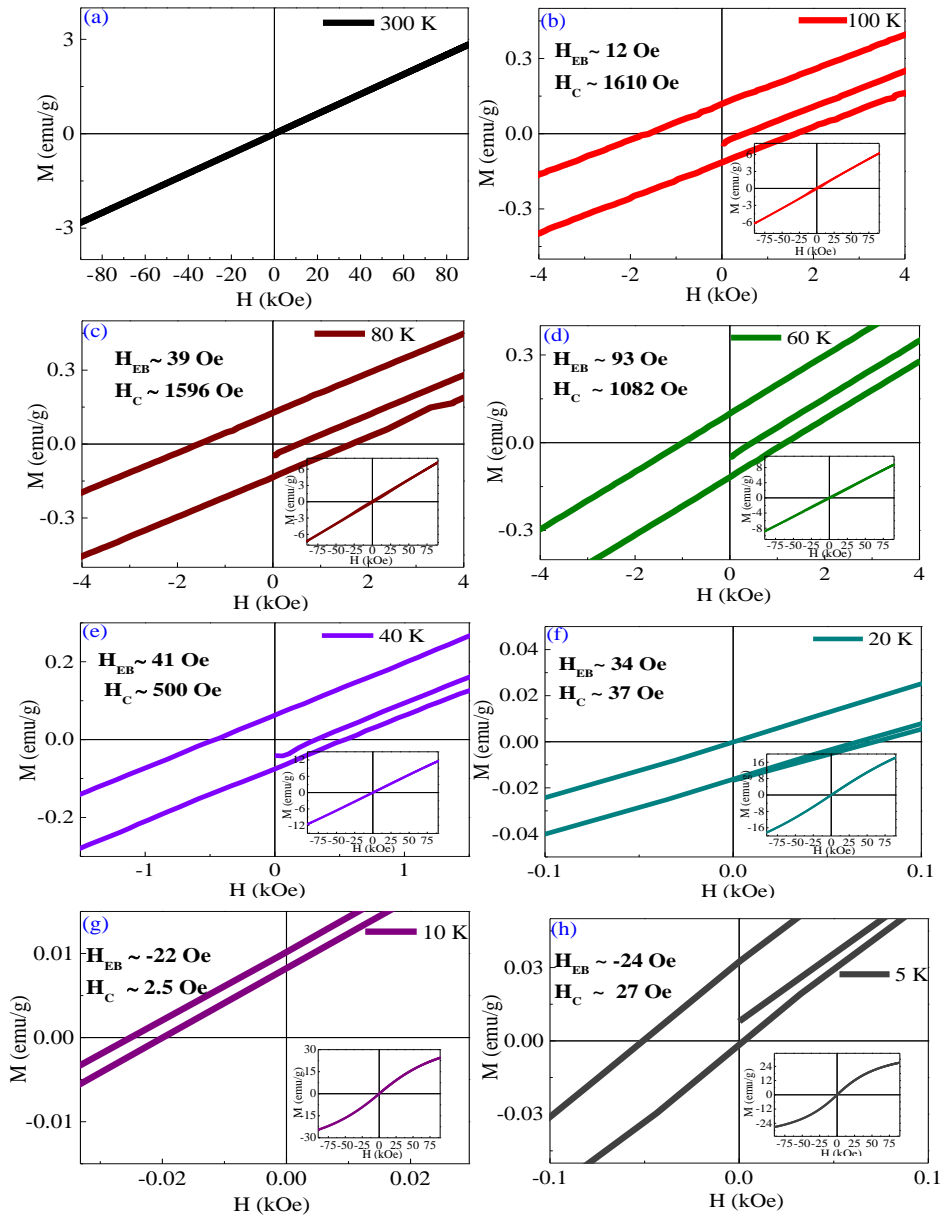
*Figure 4. Zoomed view of M-H curves of YCO nanocrystallites at varying temperature showing switching of exchange bias($H_{EB}$) from positive to negative as indicated in the panels. The respective insets show the full M-H loops in –90 k Oe to +90 k Oe field-sweep.*

As seen from the **Figure 5(a)**, the $H_{EB}$ at 100 K was found to be ~ 12 Oe which reached to maximum of ~ 93 Oe at 60 K. This initial increase in $H_{EB}$ was mainly due to the increase in the AFM ordering of $Yb^{3+}$ spins towards the canted $Cr^{3+}$ spins giving weak FM component with the decrease in T. After cooling below 60 K, we

observed $H_{EB}$ ~ 41 Oe at 40 K and ~ 34 Oe at 20 K. This decrease in $H_{EB}$ can be related with the change in the slope of $M_{ZFC}$ below 60 K where, after reaching $NM_{max}$, the $M_{ZFC}$ values start increasing and cross $M_{ZFC} = 0$ at around 13 K. After reducing temperature further, $H_{EB}$ turns negative and decreased from ~ − 4 Oe at 14 K ($T_{cross}$) to ~ − 24 Oe at 5 K due to the increasing strength of $Yb^{3+}$–$Yb^{3+}$ AFM superexchange interaction which normally appears at very low temperature.
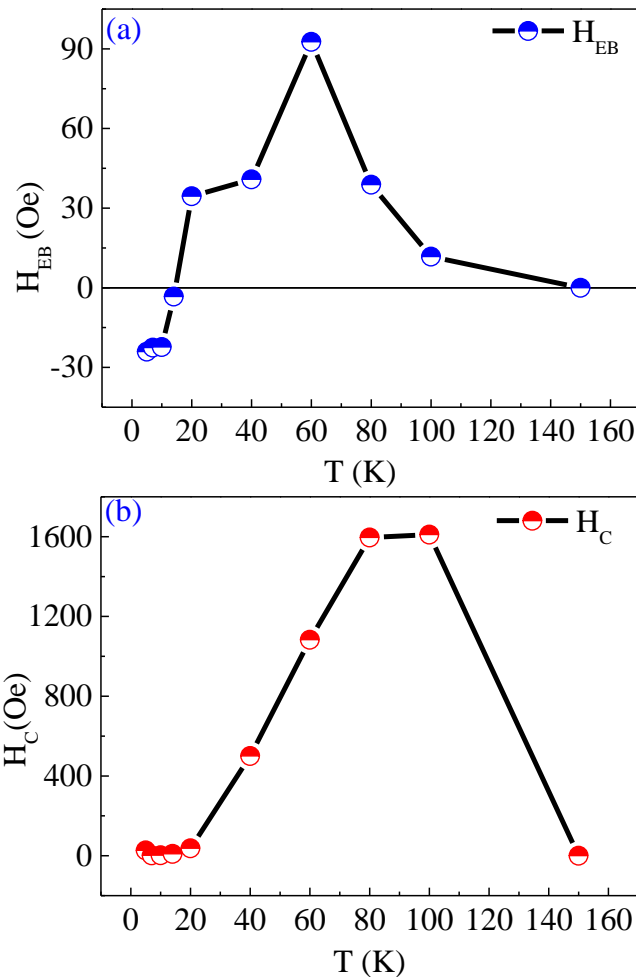


*Figure 5. Temperature variation of (a) exchange bias $H_{EB}$ and (b) coercive field $H_C$ of YCO nanocrystallites in ZFC condition. Switching of $H_{EB}$ from positive to negative can be seen with the decrease in temperature which is consistent with the magnetic transitions seen in the $M_{ZFC}(T)$ -$M_{FC}(T)$ curves.*

Initially, core- shell model were used to explain the observed EB in nanoparticles which was associated with the uncompensated spin at the interface.[5] Here, the ac-magnetic measurements also ruled out the presence of any blocking transition due to the nanocrystalline nature of our samples. This further confirms that the observed EB cannot be explained by core-shell model or finite size effects. Recently, more appropriate model for EB has come up indicating the formation of FM clusters in the canted-AFM matrix and locally formed FM/AFM sublattices at the interface results in observed EB in YCO.[46,58] So we can say that these features are not due to the nanosize of the grain but it is the intrinsic property of the material.

The temperature dependent EB reversal can be explained by considering the NM behavior in YCO. The anisotropic exchange interaction between canted $Cr^{3+}$ and $Yb^{3+}$ spins under the influence of $H_i$ leads to EB in YCO. Below $T_N$ (~ 119 K), the $H_{EB}$ increased till 60 K, mainly owing to the increase in magnitude of AFM component of paramagnetic $Yb^{3+}$ spins due to the canted $Cr^{3+}$ spins until the induced field is negative. Hence, large positive field was required to bring the magnetization to positive value and cross zero giving positive EB (PEB). As soon as the moment became positive and reached compensation temperature ($T_{comp(2)}$ ~ 19 K) the magnitude of $H_{EB}$ became negative. The sign reversal of $H_{EB}$ can be explained by relationship of $H_{EB}$ ~ –M.[27,36,65] At low T, the long range AFM ordering of $Yb^{3+}$-$Yb^{3+}$ spins dominates and results in the decrease in the strength of $Yb^{3+}$–$Cr^{3+}$ magnetic interaction. Moreover, because of the NM, downward shift in M-H curve results in PEB and vice-versa. [36][57] **Figure 5(b)** showed the decrease in $H_C$ from ~ 1610 Oe to ~ 2 Oe with the decrease in T from 100 K to 7 K. The weak FM ordering give rise to a noticeable coercivity in a temperature range 100 – 20 K suggesting the presence of large FM component of canted $Cr^{3+}$ spins. The decrease in $H_C$ can be accounted to the strong AFM interaction of $Yb^{3+}$– $Yb^{3+}$ spins at low T.

## 4.5.5  Effect of field cooling on exchange bias:

The conventional exchange bias (CEB) at 60 K was measured by cooling under various external fields $H_{FC}$ (–2 kOe, –5 kOe and –10 kOe), respectively and shown in **Figure 6**.
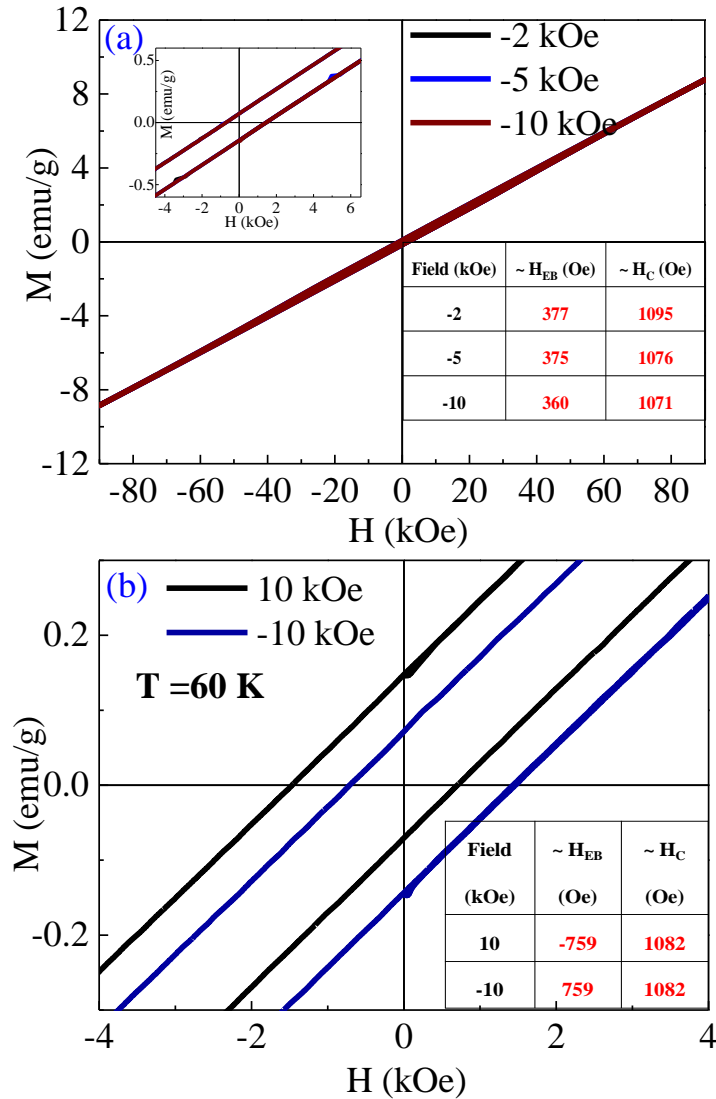


*Figure 6. (a) Effect of field-cooling on the EB of YCO nanocrystallites at different $H_{ext}$. Top left inset shows the zoom-view of shift of hysteresis curve with field cooling and (bottom right) showing the change in coercivity ($H_C$) and exchange bias field ($H_{EB}$) with the change in $H_{FC}$ (b) representing the effect of applied magnetic field ± 10 kOe on M-H curve of YCO.*

The results are compared in **Figure 6(a)** with an inset (**top left**) showing the zoomed view. The M - H loops were found to be elliptical indicating the predominant AFM interaction with weak FM arising due to the canted $Cr^{3+}$ spins. As shown in bottom right of **Figure 6(a)**, the $H_{EB}$ was found to be ~ − 377 Oe at –2 kOe and with the increase in $H_{FC}$ from –5 kOe to –10 kOe, the $H_{EB}$ ~ –375 Oe decreased to ~ –360 Oe, respectively. This NEB effect became further weaker with the increase in $H_{FC}$ (–10 kOe).

The effect of change in polarity of applied magnetic field while field cooling ($H_{FC}$) on the M - H loop parameter of YCO was measured at $H_{FC}$ ±10 kOe. The $H_{EB}$ changed from ~ 385 Oe to ~ 759 Oe and $H_C$ decreased marginally from ~ 1095 Oe to ~ 1082 Oe after increasing the $H_{FC}$ from ± 5 kOe to ±10 kOe (**Figure 6(b)**), respectively. The $H_{EB}$ values remain same but their sign also reverses with the sign reversal in ±$H_{FC}$ as shown in the **Table** (**inset of Fig. 6 (b)**). The applied $H_{FC}$ was comparatively more than the observed $H_C$ of YCO at 60 K. Thus, at this field $H_{FC}$, $Yb^{3+}$ and $Cr^{3+}$ spins follow the direction of $H_{FC}$ and orient itself in such a fashion so as to give FM coupling resulting in NEB. However, by changing the polarity of $H_{FC}$, the $H_{EB}$ changes accordingly. The M - H loops shifted towards the left side of the origin at − 5 and − 10 kOe but symmetrically opposite to what were observed for + 5 and + 10 kOe. This symmetric shift also confirmed that the EB observed is not due to the unsaturated minor loop but due to the uncompensated spins at the locally formed FM/AFM interface.[25,58]

## 4.5.6  Training effect on exchange bias:

As we noticed in the $M_{ZFC}$, $M_{FC}$ vs. T curves (**Figure 1(a)**), for $H_{ext}$ ~ 1 kOe, the $M_{ZFC}$ remains positive at all the measured T-range (*i.e.* it does not show NM). At $H_{FC}$ = 10 kOe, the canted AFM spins align in field direction and drag the $Yb^{3+}$ spins along the $Cr^{3+}$ spins making the interaction at the interface ferromagnetic.
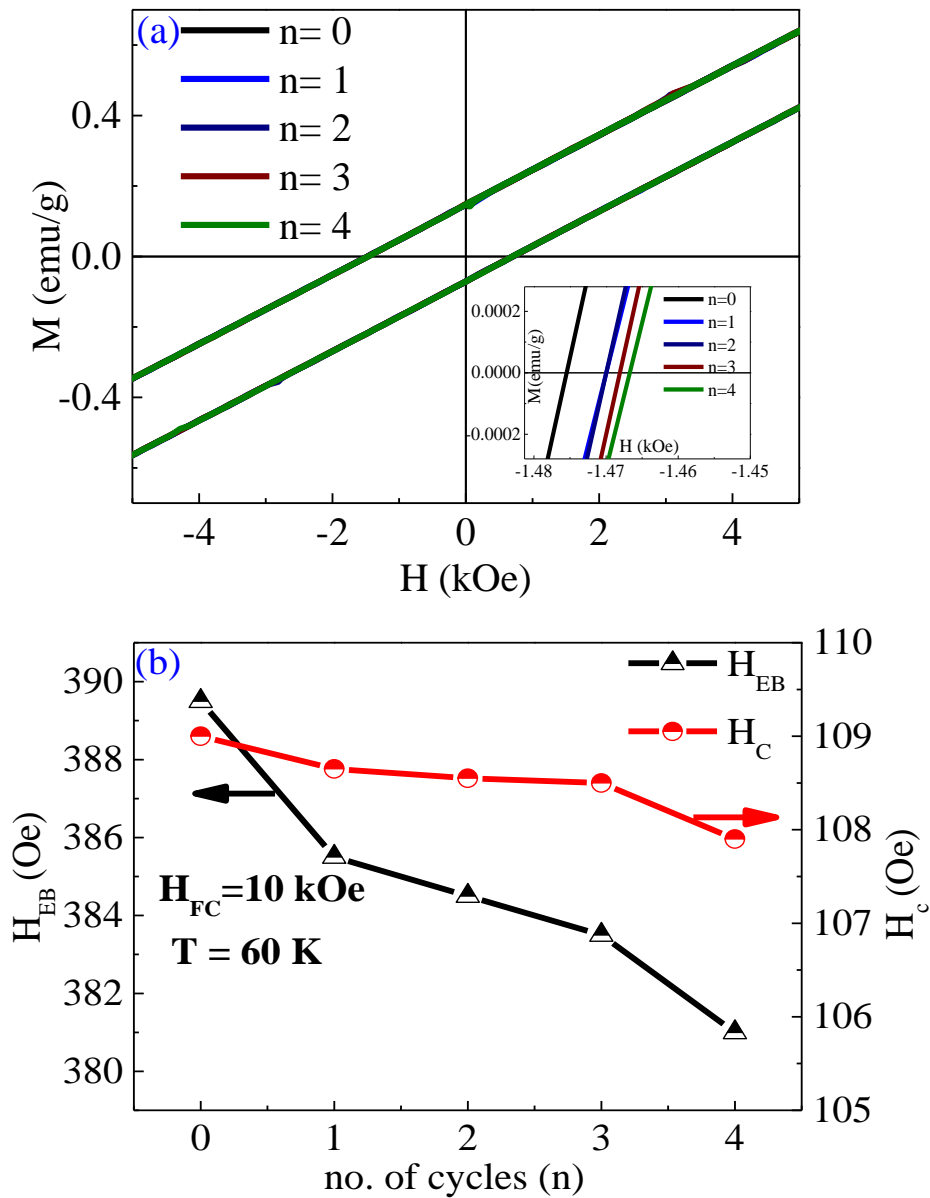
*Figure 7. (a) Effect of training cycle on $H_{EB}$ with an inset at bottom right showing the zoomed view of (a). (b) The figure shows the decrease in $H_{EB}$ and $H_C$ with an increase in  number of measurement cycle (n).*

In conventional systems, the training effect is considered to be one of the best methods to study the EB. Repeating the hysteresis loop a number of times leads to the relaxation of uncompensated spins at the interface making M - H loop increasingly symmetric.[25,3666] The training effect in YCO was measured after applying $H_{FC}$ +10 kOe as shown in **Figure 7(a, b)**. With the increasing number of cycles (n), $H_{EB}$ value

decreased to 2 % from n = 0 to n = 4 at 60 K  which is very small compared to the observed EB in YCO nanocrystallites. This indicates that the spin configuration was quite stable at the interface even against the applied magnetic field and after each cycle, the AFM spins tries to find an energetically favorable condition.[25,57,58] Similarly, $H_C$ also follows the $H_{EB}$ (**Figure 7(b)**) and decreases with the increase in the loop cycle.

### 4.5.7  Temperature and field assisted memory-switching application:

The sign reversal of EB, as seen by us, holds promising towards applications in thermal assisted memory switching.[33,54] As we discussed earlier, the temperature dependence of NM was in agreement with the observed temperature dependent EB. To demonstrate the switching effect for possible applications, magnetization switching was performed by varying T and $H_{ext}$. **Figure 8(a)** showed the switching of $M_{ZFC}$ between negative to positive by switching T from 60 K to 14 K at 100 Oe applied external magnetic field.
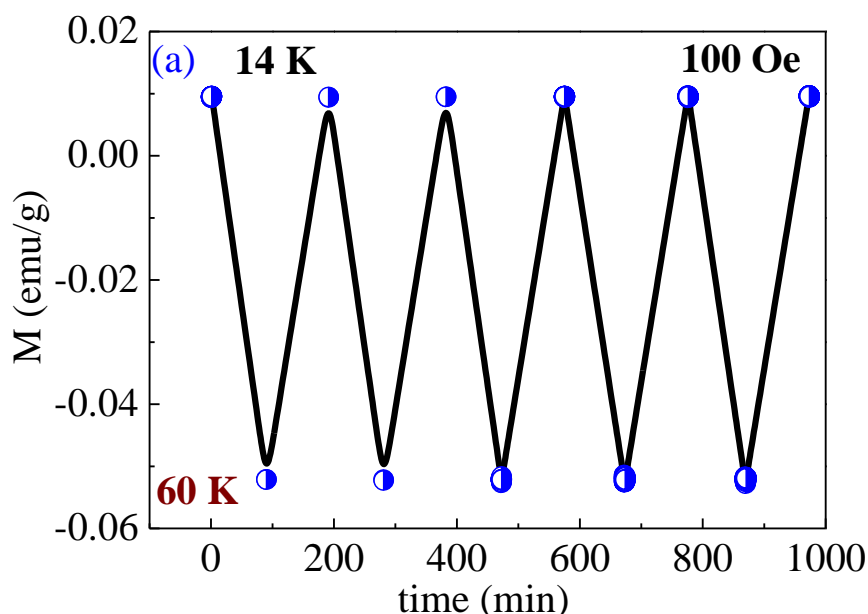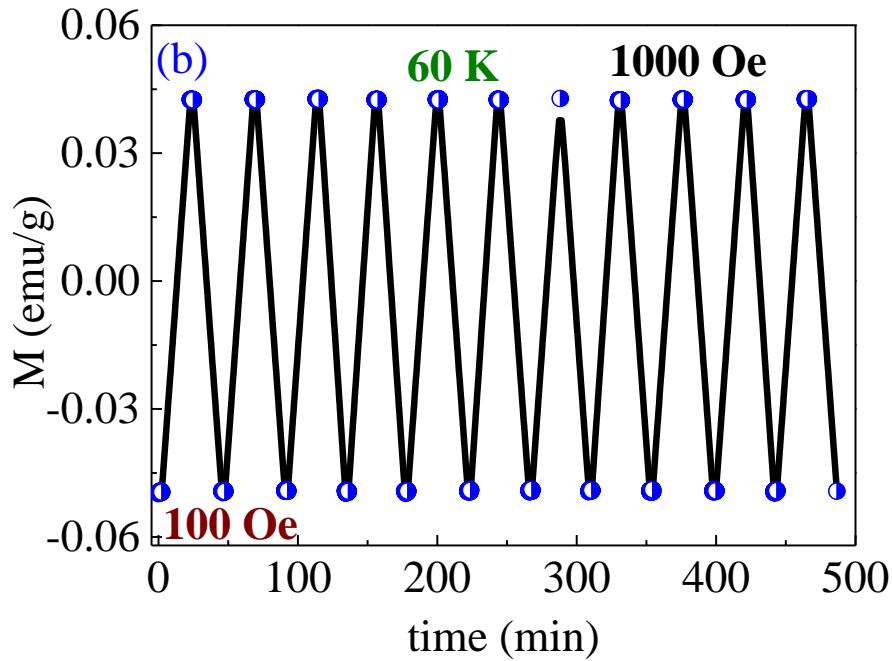
*Figure 8. (a) The figure shows magnetization switching from negative to positive values with the switching in T from 60 K to 14 K in ZFC condition at 100 Oe external magnetic field (b) The figure shows switching of magnetization while changing $H_{ext}$ from 100 to 1000 Oe at 60 K.*

Similarly, the NM observed in ZFC magnetization curve at 100 Oe can be flipped to positive by applying $H_{ext} = 1000$ Oe, as shown in **Figure 8(b)**. The characteristic feature of magnetization flipping from negative to positive by simply changing the T in YCO nanocrystallites is different from conventional magnetic materials where, $H_{ext}$ is required to change the polarity. The change in the polarity of magnetization by varying T and $H_{ext}$, cycled several times showed good reproducibility and no noticeable decay in magnetization was observed. Thus, the magnetization can be tuned in a predictable way and this behavior is favorable for a subtle application in non-volatile magnetic memories, thermomagnetic switches *etc*[33] Similar feature was also observed in other chromites exhibiting NM such as $YFe_{0.5}Cr_{0.5}O_3$,[33] $SmCr_{1-x}Fe_xO_3$[54] and $TmCrO_3$[36]. Thus, by simply changing the magnitude of the $H_{ext}$ and T, the polarity of the magnetization can be switched between negative and positive.

## 4.5.8 Conclusions

In this work, we studied YCO nanocrystals to explore the negative magnetization, exchange bias and magnetization switching behavior by detailed magnetic studies. YCO showed NM below $T_N$ and with the decrease in T, sign reverses and magnetization becomes positive just below $T_{comp(2)}$. The switching of PEB to NEB can be related to the sign reversal of magnetization with the decrease in T. The effect of field cooling and training cycle demonstrated that the EB observed was not due to unsaturated minor loop and thus, confirms the EB behavior of YCO. The YCO also possess the switching characteristic merely by changing the magnitude of the applied magnetic field and temperature. The existence of simultaneous negative and positive magnetization offers thermal assisted switching of magnetization in YCO. Thus, coexistence of sign reversal of NM and EB makes YCO a model system for spintronics and memory based devices and at the same time, seeking materials with enhanced effect and operating temperatures is needed.

## 4.5.9  References:

[1] R. Das, A. Jaiswal, S. Adyanthaya, and P. Poddar, J. Appl. Phys. **109**, 0 (2011).

[2] A. Jaiswal, R. Das, S. Adyanthaya, and P. Poddar, J. Nanoparticle Res. **13**, 1019 (2011).

[3] A. Jaiswal, R. Das, K. Vivekanand, P.M. Abraham, S. Adyanthaya, P. Poddar, and P. Mary Abraham, J. Phys. Chem. C **114**, 2108 (2010).

[4] A. Jaiswal, R. Das, K. Vivekanand, T. Maity, P.M. Abraham, S. Adyanthaya, and P. Poddar, J. Appl. Phys. **107**, 013912 (2010).

[5] A. Jaiswal, R. Das, S. Adyanthaya, and P. Poddar, J. Phys. Chem. C **115**, 2954 (2011).

[6] A. Jaiswal, R. Das, T. Maity, and P. Poddar, J. Appl. Phys. **110**, 124301 (2011).

[7] W. Eerenstein, N.D. Mathur, and J.F. Scott, Nature **442**, 759 (2006).

[8] S.-W. Cheong and M. Mostovoy, Nat. Mater. **6**, 13 (2007).

[9] C. Binek and B. Doudin, J. Phys. Condens. Matter **17**, L39 (2005).

[10] E.. Bertaut and J. Mareschal, Solid State Commun. **5**, 93 (1967).

[11] C. Veyret, J.B. Ayasse, J. Chaussy, J. Mareschal, and J. Sivardière, J. Phys. **31**, 607 (1970).

[12] M. Eibschütz, R.L. Cohen, and K.W. West, Phys. Rev. **178**, 572 (1969).

[13] L. Holmes, J. Appl. Phys. **41**, 1184 (1970).

[14] R.M. and Y.. K. A. Hasson, Hornreich, Phys. Rev. B **12**, 11 (1975).

[15] G.V.S. Rao, B.M. Wanklyn, and C.N.R. Rao, J. Phys. Chem. Solids **32**, 345 (1971).

[16] E.F. Bertaut, J. Appl. Phys. **37**, 1038 (1966).

[17] R.M. Hornreich, Y. Komet, R. Nolan, B.M. Wanklyn, and I. Yaeger, Phys. Rev. B **12**, 5094 (1975).

[18] A. H. Cooke, D.M. Martin, and M.R. Wells, J. Phys. C Solid State Phys. **7**, 3133 (1974).

[19] T. Yamaguchi and K. Tsushima, Phys. Rev. B **8**, 5187 (1973).

[20] G. Gorodetsky, R.M. Hornreich, S. Shaft, B. Sharon, a. Shaulov, and B.M. Wanklyn, Phys. Rev. B **16**, 515 (1977).

[21] K. Sardar, M.R. Lees, R.J. Kashtiban, J. Sloan, and R.I. Walton, Chem. Mater. **23**, 48 (2011).

[22] P. Gupta, R. Bhargava, R. Das, and P. Poddar, RSC Adv. **3**, 26427 (2013).

[23] P. Gupta, R. Bhargava, and P. Poddar, J. Phys. D. Appl. Phys. **48**, 025004 (2015).

[24] P. Gupta and P. Poddar, Inorg. Chem. 150921124621008 (2015).

[25] J. Nogués and I.K. Schuller, J. Magn. Magn. Mater. **192**, 203 (1999).

[26] I.L. Prejbeanu, M. Kerekes, R.C. Sousa, H. Sibuet, O. Redon, B. Dieny, and J.P. Nozières, J. Phys. Condens. Matter **19**, 165218 (2007).

[27] R.P. Singh, C. V. Tomy, and a. K. Grover, Appl. Phys. Lett. **97**, 182505 (2010).

[28] Y. Ren, T.T.M. Palstra, D.I. Khomskii, E. Pellegrin, a. a. Nugroho, a. a. Menovsky, and G. a. Sawatzky, Nature **396**, 441 (1998).

[29] L. Néel, *Propriétées Magnétiques Des Ferrites; Férrimagnétisme et Antiferromagnétisme* (Annales de Physique (Paris), 1948).

[30] M. Hase, V.Y. Pomjakushin, V. Sikolenko, L. Keller, H. Luetkens, A. Dönni, and H. Kitazawa, Phys. Rev. B **84**, 104402 (2011).

[31] H.C. Nguyen and J.B. Goodenough, Phys. Rev. B **52**, 324 (1995).

[32] J. Hemberger, S. Lobina, H. a. Krug Von Nidda, N. Tristan, V.Y. Ivanov, a. a. Mukhin, a. M. Balbashov, and a. Loidl, Phys. Rev. B - Condens. Matter Mater. Phys. **70**, 1 (2004).

[33] J. Mao, Y. Sui, X. Zhang, Y. Su, X. Wang, Z. Liu, Y. Wang, R. Zhu, Y. Wang, W. Liu, and J. Tang, Appl. Phys. Lett. **98**, 3 (2011).

[34] V. a. Khomchenko, I.O. Troyanchuk, R. Szymczak, and H. Szymczak, J. Mater. Sci. **43**, 5662 (2008).

[35] T. Bora and S. Ravi, J. Magn. Magn. Mater. **358-359**, 208 (2014).

[36] K. Yoshii, Mater. Res. Bull. **47**, 3243 (2012).

[37] Y. Cao, S. Cao, W. Ren, Z. Feng, S. Yuan, B. Kang, B. Lu, and J. Zhang, Appl. Phys. Lett. **104**, 14 (2014).

[38] A. Berger, D.T. Margulies, and H. Do, J. Appl. Phys. **95**, 6660 (2004).

[39] C. Won, Y.Z. Wu, E. Arenholz, J. Choi, J. Wu, and Z.Q. Qiu, Phys. Rev. Lett. **99**, 1 (2007).

[40] B.S. and K.Baberschke, Phys. Rev. B **50**, 13467 (1994).

[41] T.M. Hong, Phys. Rev. B **58**, 10 (1998).

[42] J. Krishna Murthy and a. Venimadhav, Appl. Phys. Lett. **103**, 0 (2013).

[43] J. Saha and R.H. Victora, Phys. Rev. B - Condens. Matter Mater. Phys. **76**, 1 (2007).

[44] F. Hong, Z. Cheng, J. Wang, X. Wang, and S. Dou, Appl. Phys. Lett. **101**, 102411 (2012).

[45] P. Mandal, a. Sundaresan, C. Rao, a. Iyo, P. Shirage, Y. Tanaka, C. Simon, V. Pralong, O. Lebedev, V. Caignaert, and B. Raveau, Phys. Rev. B **82**, 1 (2010).

[46] A. Kumar and S.M. Yusuf, Phys. Rep. **556**, 1 (2015).

[47] A. Kumar, S.M. Yusuf, L. Keller, and J. V. Yakhmi, Phys. Rev. Lett. **101**, 1 (2008).

[48] S. Geller, Acta Crystallogr. **10**, 243 (1957).

[49] T. Yamaguchi, J. Phys. Soc. Japan **38**, 1270 (1975).

[50] Y. Su, J. Zhang, Z. Feng, L. Li, B. Li, Y. Zhou, Z. Chen, and S. Cao, J. Appl. Phys. **108**, 013905 (2010).

[51] I.B. Krynetskii and V.M. Matveev, Phys. Solid State **39**, 584 (1997).

[52] K. Tsushima, K. Aoyagi, and S. Sugano, J. Appl. Phys. **41**, 1238 (1970).

[53] Y. Long, Q. Liu, Y. Lv, R. Yu, and C. Jin, Phys. Rev. B - Condens. Matter Mater. Phys. **83**, 4 (2011).

[54] L.H. Yin, Y. Liu, S.G. Tan, B.C. Zhao, J.M. Dai, W.H. Song, and Y.P. Sun, Mater. Res. Bull. **48**, 4016 (2013).

[55] B. Rajeswaran, D.I. Khomskii, a. K. Zvezdin, C.N.R. Rao, and a. Sundaresan, Phys. Rev. B - Condens. Matter Mater. Phys. **86**, 1 (2012).

[56] S. Pütter, H. Ding, Y. Millev, H. Oepen, and J. Kirschner, Phys. Rev. B **64**, 10 (2001).

[57] K. Yoshii, Appl. Phys. Lett. **99**, 142501 (2011).

[58] P.K. Manna and S.M. Yusuf, Phys. Rep. **535**, 61 (2014).

[59] W. H. Meiklejohn and C. P. Bean, Phys. Rev. Lett. **105**, 904 (1957).

[60] and I.Y. S.Shtrikman, B. M. Wanklyn, Int. J. Magn. **1**, 327 (1971).

[61] S. Lei, L. Liu, C. Wang, C. Wang, D. Guo, S. Zeng, B. Cheng, Y. Xiao, and L. Zhou, J. Mater. Chem. A **1**, 11982 (2013).

[62] K. Yoshii, J. Solid State Chem. **159**, 204 (2001).

[63] N. Sharma, B.K. Srivastava, A. Krishnamurthy, and a. K. Nigam, Solid State Sci. **12**, 1464 (2010).

[64] T. Bora and S. Ravi, J. Appl. Phys. **114**, 0 (2013).

[65] P.K. Manna, S.M. Yusuf, R. Shukla, and a. K. Tyagi, Appl. Phys. Lett. **96**, 2 (2010).

[66] C. Binek, Phys. Rev. B - Condens. Matter Mater. Phys. **70**, 1 (2004).

# Chapter 5

## Thermal properties of rare earth chromites

In this chapter, we concentrate on the investigation of thermal properties of rare earth chromites by heat capacity and magnetic measurements. In this work, we also attempt to determine and quantify the electronic, lattice and magnetic contribution to the total heat capacity of the system. The structural and magnetic ordering in these orthochromites suggestive of the probable magnetocaloric effect which is also presented in detail. The large adiabatic temperature change with the change in external magnetic field in DCO is noteworthy. This opens up a possibility for another viable technological application for rare earth chromites, namely, in magnetic cooling at cryogenic temperatures.

## 5.1    Introduction

There has been an increased interest in exploring new multifunctional materials for energy applications in order to deal with the technological and environmental requirements. Current global requirement towards the power efficient, clean, and miniaturized devices has increased the curiosity for the materials having multifunctional properties such as multiferroics, magnetoelectric and magneto/electrocalorics.[1] Recently, the magnetocaloric refrigeration took over the interest of researchers due to its impending advantages of being environmental friendly and efficient over the conventional refrigeration systems.[2–5] The magnetocaloric refrigeration is based on the magnetocaloric effect (MCE). In this effect, when the magnetic material is placed in a magnetic field, it heats up due to the reduction in the entropy and cools down when the field is removed. The change in entropy is reversible with the application/removal of magnetic field.[2,6] The MCE in a system is broadly defined as the adiabatic change in temperature ($\Delta T_{ad}$) or isothermal entropy change ($\Delta S_M$ (T)) with the change in the magnetic field.[3] The MCE was first used to achieve sub-Kelvin temperature by adiabatic demagnetization of paramagnetic salts.[5,6] The discovery of room temperature (RT) magnetocaloric materials such as Gd (10.2 J/kg K at 294 K ), $Gd_5Si_2Ge_2$ (18.4 J/kg K at 276 K) led to the intensive research for  ambient magnetocaloric refrigeration to partly replace the current gas compression-expansion technology.[4,5] Apart from Gd based compounds, intermetallic materials having first order magnetic transitions such as $LaFe_{13-x}Si_x$, $MnAs_{1-x}Sb_x$, $MnFeAs_{1-x}P_x$ also show MCE.[1,7,8] But, large magnetic hysteresis, low resistance to corrosion and oxidation poses a challenge for its use in magnetocaloric refrigeration which was conquer by manganite perovskites compensating in terms of entropy and adiabatic temperature change.[1,7,8] An enormous number of materials are reported with large MCE around paramagnetic (PM) to ferromagnetic (FM) / PM to antiferromagnetic (AFM) transition near RT and at cryogenic temperature.[9–13] Recently, material with AFM-FM transition, spin reorientation transition, ferrimagnetic-FM transition have shown inverse MCE ($\Delta S_M > 0$).[14–20]

There is a need to explore new materials with giant MCE having large entropy change ($\Delta S_M$) and tunable operating temperature. The materials, with MCE at

cryogenic temperature (< 30 K) are advantageous for applications such as space science, liquefaction of hydrogen in fuel industry *etc.*[5] For selecting the material for magnetocaloric refrigeration, large $\Delta S_M$ (T) & $\Delta T_{ad}$, smaller specific heat ($C_P$) & thermal hysteresis, and high chemical stability is required.[21] Initially, manganites were mostly studied for its multiferroic properties in past. Recently, the large entropy change in perovskites manganites, such as $RMnO_3$ crystals (R= Dy, Tb, Ho and Yb) and Dy doped $TbMnO_3$ near the magnetic transition, suggested the possibility for their application in magnetocaloric refrigeration technology at cryogenic temperature.[10,22,23] However, larger heat capacity ($C_P$) values of manganites such as in case of $Ce_{0.67}Sr_{0.33}MnO_3$ (550 J/kg K) limits its use.[24] As large $C_P$ value increases the thermal load therefore, additional energy is required to heat the sample itself, causing a loss of entropy. As $C_P$ is inversely proportional to the $\Delta T_{ad}$, larger $C_P$ will give smaller $\Delta T_{ad}$ and vice versa.[25] Thus, material with smaller $C_P$ value is desirable.

Rare earth chromites ($RCrO_3$: where R: rare earth cations) have attracted much attention recently due to their rich magnetic and ferroelectric properties and possible coupling of both.[26–29] In addition, the unique behavior, such as negative magnetization, exchange bias and magnetization switching which were observed recently in orthochromites, have continued to draw the interest of researchers.[27,30–32] Apart from being studied for their multiferroic properties *i.e.* coexistence of magnetic and electric property, they were also studied for catalytic properties.[33–35] Recently, $RCrO_3$ family of compounds have emerged as a potential MCE materials as smaller $C_P$ values (~ 95-109 J/mol/K) observed in these materials favor larger $\Delta T_{ad}$. The ordering of $R^{3+}$ moments at low temperature makes them advantageous for cryogenic magnetocaloric refrigeration applications.[36] Recently, magnetocaloric properties of bulk $DyCrO_3$ were reported by McDannald *et al.* with a large $\Delta S_M$ ~ 8.1 J/kg K at ~ 12 K, and relative cooling power (RCP) ~ 196 J/kg at 3 T.[12] Also, giant MCE was observed in a single crystal $GdCrO_3$, with the maximum $\Delta S_M$ ~ 31.6 J/kg K for a field change of 44 kOe at 3 K.[37] In multiferroic materials, the ME coupling significantly enhances the magnetization, FE polarization, and thus, isothermal entropy change in an FE–FM coupled multiferroic system gets enhanced. The ME coupling introduces additional contribution to $\Delta T$ thus, large MCE is observed in a

material with strong ME coupling.[38] The large entropy change ~ 11.3 J/kg K at 4.5 T in $DyFe_{0.5}Cr_{0.5}O_3$ was enhanced by ME coupling due to the magnetic field and temperature induced magnetic transition.[13] The current adiabatic demagnetization refrigerators (ADR) make use of PM salts which exhibit large MCE below 1 K.[39,40] Hence forth, it is equally important to explore the materials with larger MCE at the cryogenic temperatures.

In addition, there is an important class of materials which exhibits normal ($\Delta S_M < 0$) and inverse ($\Delta S_M > 0$) MCE, simultaneously. The materials possessing inverse MCE opens up the way for 'adiabatic magnetization process' by allowing the sample to cool rather than heat as it happens in the conventional materials showing 'adiabatic demagnetization process'. Thus, materials with inverse MCE are suggested to be used as a heat sinks with the conventional MCE material *i.e.* $\Delta S_M < 0$, in order to increase the refrigeration efficiency making the device more efficient. The materials such as $Co(FeRu)_2$, $SmMn_2Ge_2$, $NaBaMn_2O_6$ were reported to show simultaneous normal and inverse MCE enhancing the refrigeration efficiency, but materials covering broader working temperature regime are quite limited.[18,41,42] Thus, there is a search for the materials with two or more working temperature ranges in order to further improve the efficiency of magnetic refrigeration.

In an effort towards increasing the $\Delta S_M$, it was realized that the inclusions of superparamagnetic nanoparticles inside the host matrix might enhance the MCE. In the superparamagnetic nanoparticles, it is easy to tune the operating temperature by tuning the blocking transition which is usually determined by the particle size. In addition, large surface area in nanomaterials provide better heat exchange with the surrounding materials. Also, the particle size distribution and interparticle interactions in a magnetic nanoparticles lead to the broadening of the entropy change vs. T curve ($\Delta S_M$ vs. T) over a wide T-range, thus, enhancing the refrigeration capacity (RC). [43–45] Thus, for efficient magnetocaloric refrigeration, the magnetic nanoparticles are considered advantageous than their bulk counterparts.[43,45]

As mentioned earlier, the $\Delta T_{ad}$ is an important MCE parameter and strongly associated with the heat capacity of the material. In late 60's, the thermodynamic properties of $RCrO_3$ were studied by differential scanning calorimeter (DSC) and

thermal anomalies were observed at the magnetic transitions temperature.[36] Therefore, there is a need to study the H-dependence of specific heat of DCO, SCO and YCO nanoplatelets and correlate with the MCE which is connected with the complex spin interaction of $Cr^{3+}$ and $Dy^{3+}$ in these orthochromites.

With this motivation, in this chapter, we investigate thermal properties of DCO, SCO and YCO to realize MCE at cryogenic and Néel transition $\sim T_N$ temperature. We also study the temperature and magnetic field dependent heat capacity of these orthochromites and its association with the magnetic anomalies is also discussed in detail.

## 5.2 Experimental and Characterization Details

### 5.2.1 Synthesis of rare earth chromites:

Polycrystalline rare earth chromites (DCO, SCO and YCO) were synthesized by the hydrolytic sol-gel method. The as-obtained powder was calcined at 800 °C and was used for further characterization. Preliminary results pertinent to structural and morphological analysis along with optical and magnetic characterization have already been discussed in chapter 2, 3 and 4.[19,30] We have used the same batch of samples for the our MCE and heat capacity measurements.

### 5.2.2 Magnetic measurements:

The magnetic measurements of DCO, SCO and YCO nanoplatelets were performed using a Physical Property Measurement System (PPMS) (Quantum Design Inc., San Diego, California equipped with a 9 Tesla superconducting magnet). The powder samples were precisely weighed and packed inside a plastic sample holder which fits into a brass sample holder provided by Quantum Design Inc. with negligible contribution in overall magnetic signal. We collected M − H loops (1st quadrant) at a rate of 50 Oe/s in a field sweep from 0 to 90 kOe at the vibrating frequency of 40 Hz. The M-T was derived from M-H curves and further used to calculate the entropy change in DCO.

### 5.2.3 Heat capacity measurements:

Thermal relaxation method was used to carry out the heat capacity measurement of rare earth chromites (DCO, SCO and YCO) using heat capacity option in PPMS (Quantum Design Inc., San Diego, California equipped with a 9 Tesla superconducting magnet). and the change in adiabatic temperature ($\Delta T_{ad}$) was also determined. For heat capacity measurements, the powder sample was pressed to form a pellet. To ensure a proper thermal contact between the sample and sample platform, and for spanning the temperature from 3-300 K, Apiezon N grease was used. We measured the addenda (only grease) contribution at the zero field so that the heat capacity software can perform an accurate addenda subtraction during sample heat capacity measurements.

## **Section 5.3**

## **Giant magnetocaloric effect and large adiabatic temperature change in DyCrO$_3$ nanoplatelets at low temperature**

_____

In this section, we present the giant magnetocaloric effect (GMCE) in sol-gel derived DyCrO$_3$ (DCO) nanoplatelets across a low temperature ($<$ 10 K) and Néel transition (T$_N$) regime by a detailed temperature and magnetic field (H) dependent magnetization (M) and heat capacity (C$_P$) measurements. At T $\sim$ 9 K, a large change in the magnetic entropy (-$\Delta S_M$ $\sim$ 16.95 J/kg K) and refrigeration capacity (RC) ($\sim$ 66.38 J/kg) is reported for a field change ($\Delta H$) of 5 T. The adiabatic temperature change ($\Delta T_{ad}$) from heat capacity measurements was found to be $\sim$ 15 K (cooling effect) for a $\Delta H$ of 3 T field change. Arrott plots (M$^2$ vs. H/M plot) around $\sim$ T$_N$ show positive slopes which indicate that the observed magnetic transition are of second order. The observed GMCE and large $\Delta T_{ad}$ in DCO nanoplatelets hint that it could be a potential candidate for low-T magnetocaloric refrigeration. The heat capacity of DCO nanoplatelets measured from 3-300 K reveals λ-shape peak which is associated with a conventional second-order paramagnetic to AFM phase transition and a Schottky anomaly at low-T ($<$ 10 K).

_____

### 5.3.1 Arrott plot:

In our previous study on the DCO nanoplatelets, we found the Néel transition temperature ($T_N$) around ~ 143 K  (where $Cr^{3+}$ spins order antiferromagnetically (AFM)) and $Dy^{3+}$ spins starts ordering below 10 K.[27] The Arrott plot can be used to estimate the $T_C$ or $T_N$ in a weak FM or AFM system.[46–48] Based on Arrott-Noakes equation of state, modified Arrott plot method was used to analyze the critical behavior of the magnetic phase transition.[49]

$$(H/M)^{1/\gamma} = a \left(\frac{T-Tc}{Tc}\right) + bM^{1/\beta} \text{...................................(1)}$$

Here, $\gamma$ & $\beta$ are critical exponents and a & b are constants. Generally, for $\gamma = 1$ and $\beta = 0.5$, the $M^{1/\beta}$ vs $(H/M)^{1/\gamma}$ plot forms a set of straight lines and the isotherm which passes through the origin gives ($T=T_N$).[48,50,51]

The **Figure 1(a)** displays the first quadrant M-H curves taken in various temperature ranges *i.e.* 3-10 K ($\Delta T=1$ K), 10-50 K ($\Delta T=2$ K), and 130-150 K ($\Delta T=2$ K), where $\Delta T$ is a temperature step. The field was ramped up to 90 kOe. After each measurement, the sample was heated above its ~ $T_N$ to avoid any remanence from previous measurement history. In **Figure 1(a)** the magnetization isotherms of DCO nanoplatelets reveal that the difference in the magnetization between two temperatures (9 & 10 K) is very large, which reflects a large magnetic entropy change near the ordering temperature. The **Figure 1(b)** shows Arrott plots in T-ranges 3-50 K and 130-150 K, respectively. The curves are non-linear and show positive slope indicating the second order magnetic phase transition.
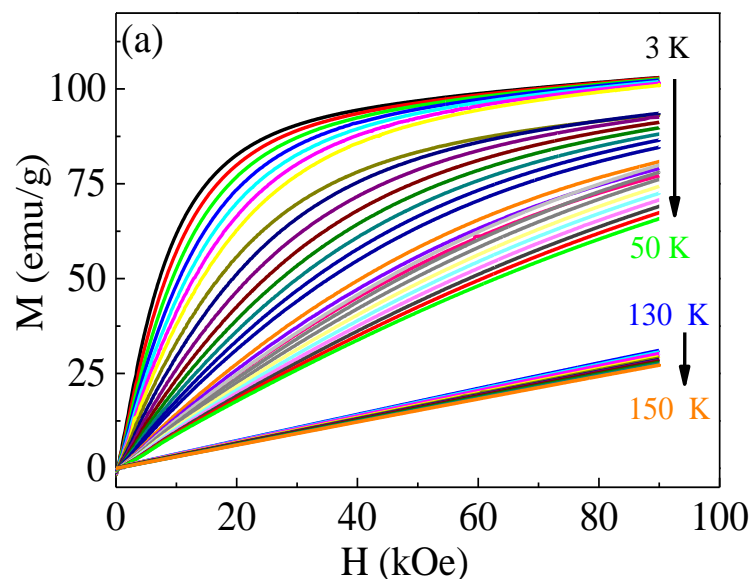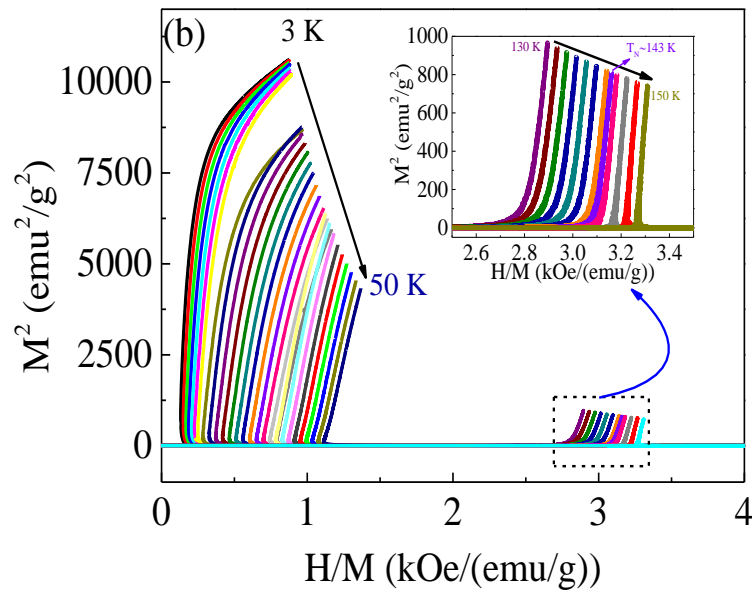
*Figure 1. (a) Initial magnetization isotherms of DCO nanoplatelets. Three sets of isotherms were measured in different temperature regimes: 3 - 10 K (ΔT = 1 K), 10 - 50 K (ΔT = 2 K) and 130 - 150 K (ΔT = 2 K), respectively. (b) Arrott plots in the respective temperature regions calculated from initial magnetization isotherms. The slope is always positive at any measured temperature, indicating the second-order transition.*

## 5.3.2  Magnetocaloric effect:

As we discussed earlier, the nanoparticles are expected to have large MCE when compared to their bulk counterparts. We estimated the magnetic field induced entropy change near the ~ $T_N$ and at low T in DCO nanoplatelets.[21] It is well known that the magnetic entropy change ($\Delta S_M$) can be derived either directly by measuring the adiabatic temperature change ($\Delta T_{ad}$) with the change in magnetic field ($\Delta H$) or indirectly from the $1^{st}$ quadrant M − H isotherms taken at different temperatures. **Figure 2(a)** and **(b)** show the M − T curves calculated from these M - H curves in the two temperature ranges as mentioned earlier. From these curves, the $\Delta S_M$ values were calculated using the Maxwell relation:[5,23,52]

$$\Delta S_M \ (T, H) \ = \int_0^H \left(\frac{\partial M}{\partial T}\right)_H dH \ ................................................ \ (2)$$

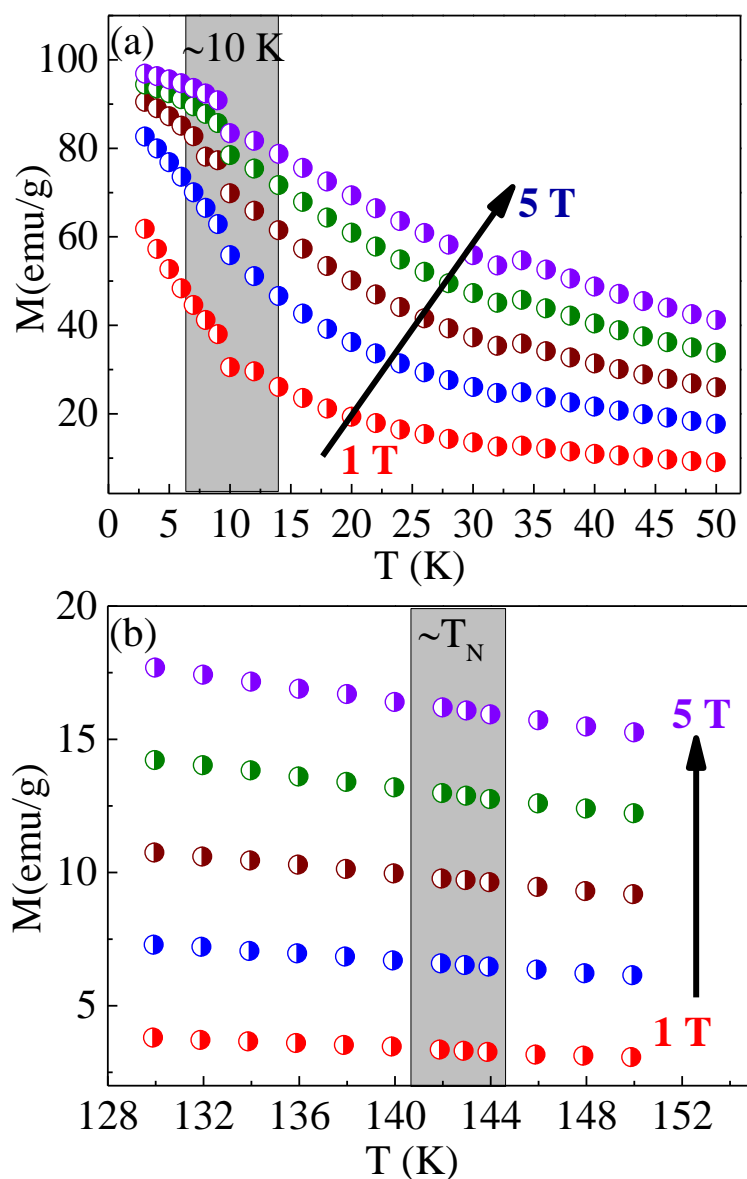The Eq. 2 indicates that, for a larger $\Delta S_M$ value, $\frac{\partial M}{\partial T}$ should be large.



*Figure 2. Magnetization vs. temperature (M-T) curves for different magnetic fields, extracted from magnetization vs. magnetic field isotherms ($1^{st}$ quadrant plotted in Figure. 1(a, b) for DCO nanoplatelets). Panels (a) and (b) show the M-T curves in temperature ranges 3-20 K and 130-150 K, respectively. The grey shaded portion in (a) and (b) indicate the ordering transition region.*

The T-dependence of $\frac{\partial M}{\partial T}$ in two selected T-ranges is shown in **Figure 3(a, b)** which show the largest value of $\frac{\partial M}{\partial T}$ around 9 K.
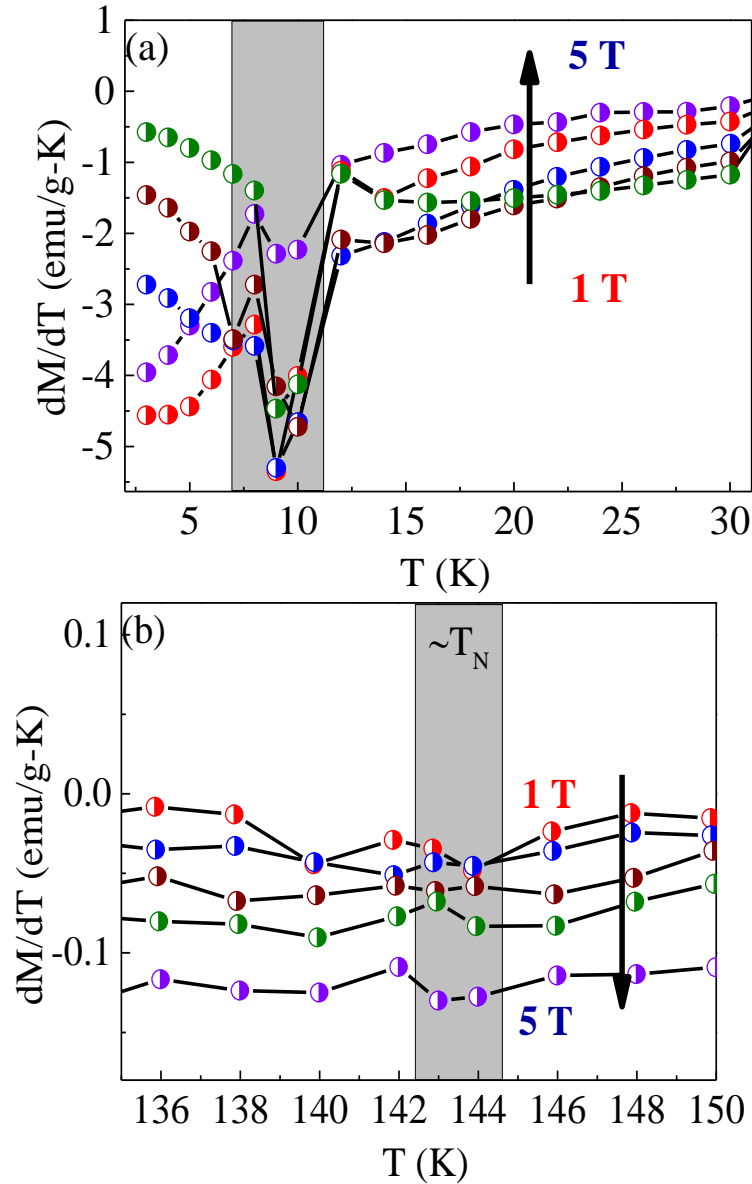


***Figure 3. Derivative of magnetization with respect of temperature plotted as a function of temperature (dM/dT vs. T) in various temperature ranges (Panels (a) and (b)). The data was derived from M-T values for various applied magnetic field (Shown in Figure. 2). The grey shaded portion in (a) and (b) indicates the ordering transition region which also coincide with the maximum entropy change region.***

Next, we calculated the entropy change in the two T-ranges by Eq. 2. The $-\Delta S_M$ vs. T curves in a temperature range 3-50 K calculated for various $\Delta H$ (upto 5 T) are shown in **Figure 4(a)**.
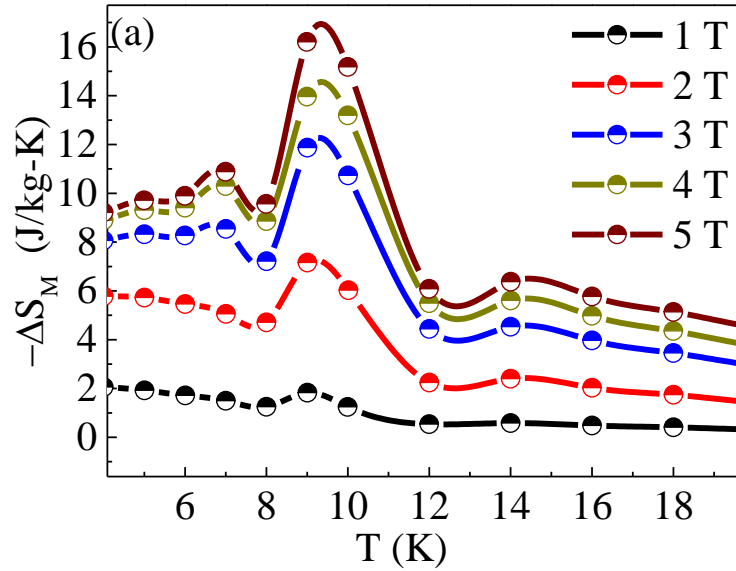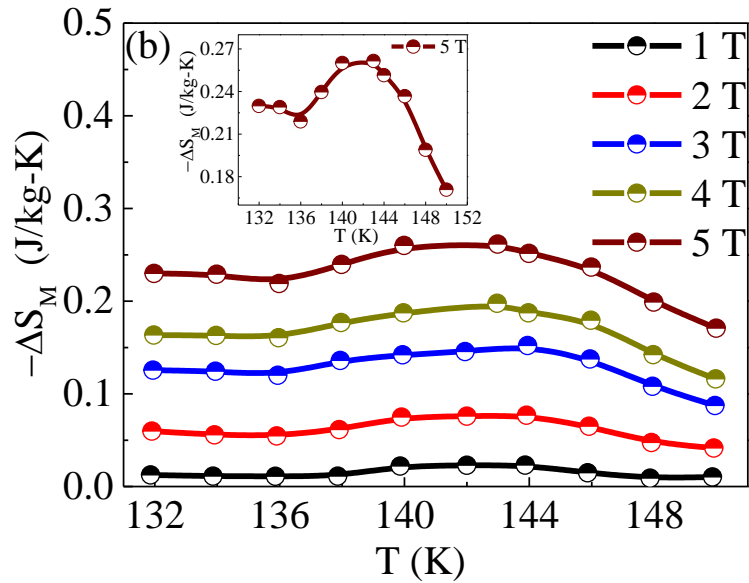


*Figure 4. Isothermal entropy change plotted ($-\Delta S_M$ vs. T) as a function of temperature at various H for DCO nanoplatelets in temperature range (a) 3–20 K. The $-\Delta S_M$ values were calculated from the M-H curves using Maxwell relation and it shows maximum value of 16.95 J/kg K around 9 K at 5 T applied magnetic field.*

At ~ 9 K, the $-\Delta S_M$ reaches maximum values of 16.95 J/kg K and 14.5 J/kg K for $\Delta H$ values of 5 T & 4 T, respectively. These values are larger in comparison to the bulk DCO where, $-\Delta S_M$ attains a maximum of 8.1 J/kg K at 12 K and 3 T and 8.4 J/kg K at 15 K and 4 T, respectively.[12] Thus, in DCO nanoplatelets, the $\Delta S_M^{max}$ is almost double when compared with bulk DCO and $DyFe_{0.5}Cr_{0.5}O_3$.[12,52] For $DyMnO_3$, at 10 K, $-\Delta S_M$ value of 6.8 J/kg K was reported for 7 T which is comparatively less than the bulk DCO and almost half of the values reported in this paper on the DCO nanoplatelets.[23] **Figure 4(b)** shows $-\Delta S_M$ vs. T curves for various $\Delta H$ around $\sim T_N$ regime of DCO. Inset shows the $-\Delta S_M$ vs. T curves for 0-5 T applied field with a maximum $\sim 0.28$ J/kg K at $\sim 143$ K, respectively.

*Figure 4. Isothermal entropy change plotted (-ΔS_M vs. T) as a function of temperature at various H for DCO nanoplatelets in temperature range (b) 130–150 K. The -ΔS_M values were calculated from the M-H curves using Maxwell relation and it shows maximum value of 0.28 J/kg K around 143 K at 5 T applied magnetic field.*

The figure of merit for MCE is determined by the relative cooling power (RCP) using the relation:[21]

$$RCP = \delta T_{FWHM} \ X \ |\Delta S_M^{max}|……………………..(3)$$

Where, $\delta T_{FWHM}$ is full width at half maximum of the peak in $\Delta S_M$ vs. T curve and $|\Delta S_M^{max}|$ is the maximum entropy change. The $-S_M^{max}$ vs. $\Delta H$ and RCP vs. $\Delta H$ curves are shown in **Figure 5(a, c)** and **(b, d)**, respectively for $\Delta S_M^{max}$ ~ 9 K & ~ 143 K ($T_N$).
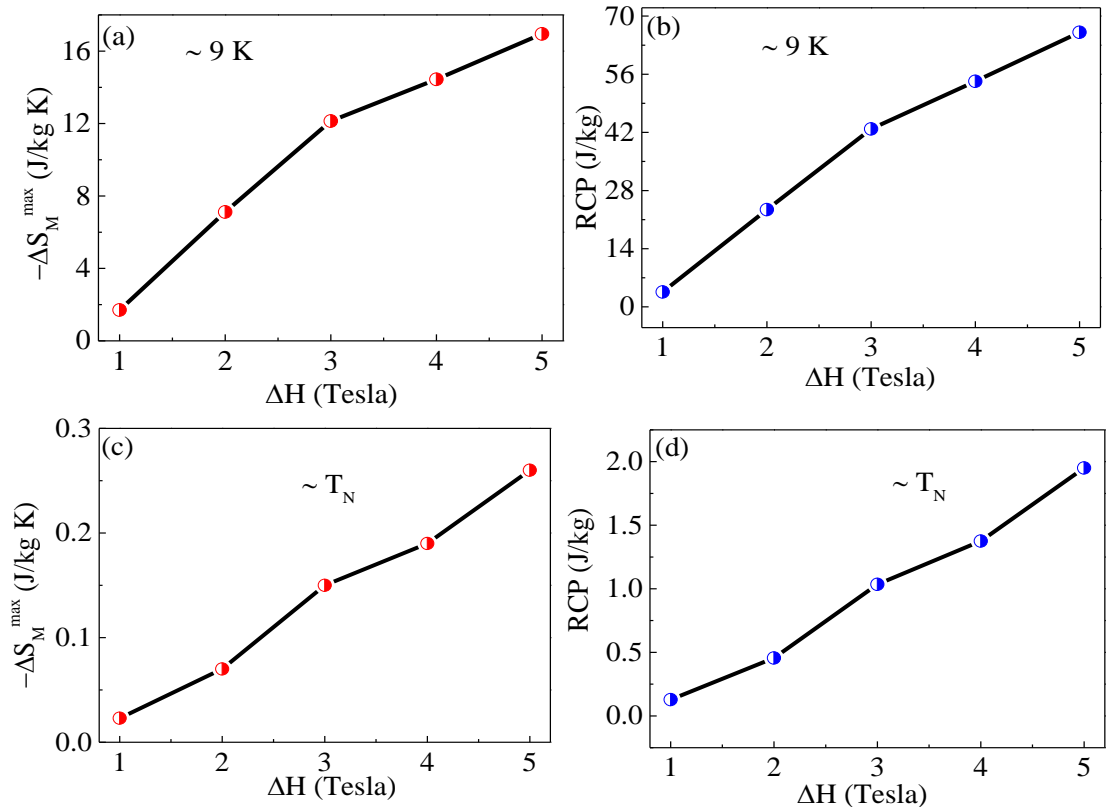
*Figure 5. The curves in various panels show (a, c) maximum entropy change (-$\Delta S_M^{max}$ vs. $\Delta H$) and (b, d) relative cooling power (RCP vs. $\Delta H$) as a function of change in the external magnetic field at 9 K and ~ $T_N$, respectively. The -$\Delta S_M^{max}$ and RCP value at 9 K was found to be 16. 95 J/kg K & 66.38 J/kg, respectively at 5 T applied magnetic field.*

The -$\Delta S_M^{max}$ and RCP value increases monotonically with H. For DCO nanoplatelets, as shown in **Figure** 5(**b, d**), the RCP value was found to be 66.38 J/kg and 1.95 J/kg for 5 T at 9 K and ~ $T_N$, respectively. The RCP was determined using $\delta T_{FWHM}$ obtained by Gaussian peak fitting for respective H. The obtained RCP value of DCO nanoplatelets was found to be less in comparison to the bulk DCO *i.e.* 196 J/kg and 217 J/kg for 3 T and 4 T, respectively as its FWHM was relatively small. The MCE parameters of DCO are compared with few other relevant materials in the similar operating temperature range and shown in **Table 1**. It is noteworthy that the $\Delta S_M$ in DCO nanoplatelets is large as compared to the other oxide perovskite material. The

large $\Delta S_M$ arises due to the paramagnetic response of $Dy^{3+}$ moments, which orient readily parallel to H giving a large magnetization.[27]

Next, we explored the universal behavior of the $\Delta S$ in DCO nanoplatelets by rescaling the axes appropriately. All the $\Delta S_M$ curves were normalized with their maximum entropy change ($\Delta S_M^{max}$), respectively. The temperature axis was also rescaled by parameter $\theta$, defined by the expression: [53–55]

$$\theta = \begin{cases} -\frac{(T-T_C)}{(T_{R1}-T_C)}, T \leq T_C \\ \frac{(T-T_C)}{(T_{R2}-T_C)}, T > T_C \end{cases} \dots\dots\dots\dots\dots\dots\dots\dots(4)$$

where $T_{R1}$ and $T_{R2}$ are the reference temperatures where $\Delta S$ equals $\Delta S_M^{max}/2$, where $T_{R1} < T_C$ and $T_{R2} > T_C$ and $T_C$ is the ordering temperature. Here, $T_C$ is taken in two temperature regime 3-50 K and 130-150 K where $\Delta S_M^{max}$ is observed at ~ 9 K and ~ 143 K, respectively. The transformed curves of DCO under various $\Delta H$ are plotted in **Figure 6(a, b)**. The **Figure** shows that around the peak, all the data points collapse into a single master curve, revealing it's universal behavior around 9 K and 143 K, where $\Delta S_M^{max}$ was obtained.
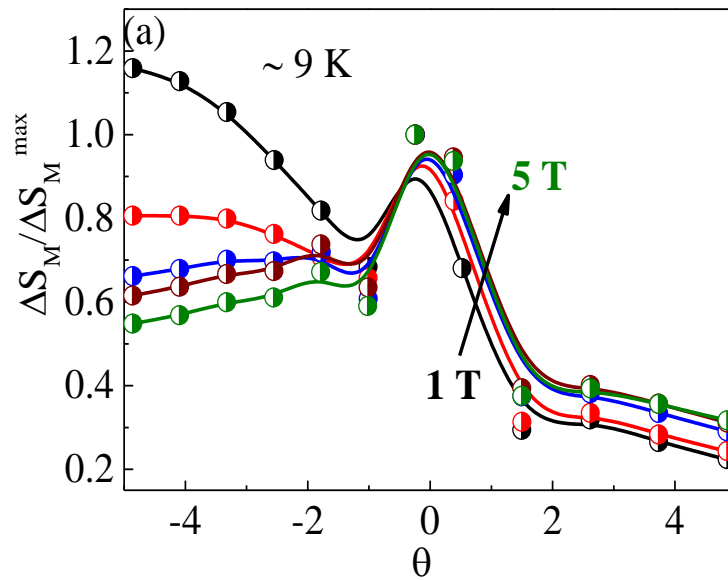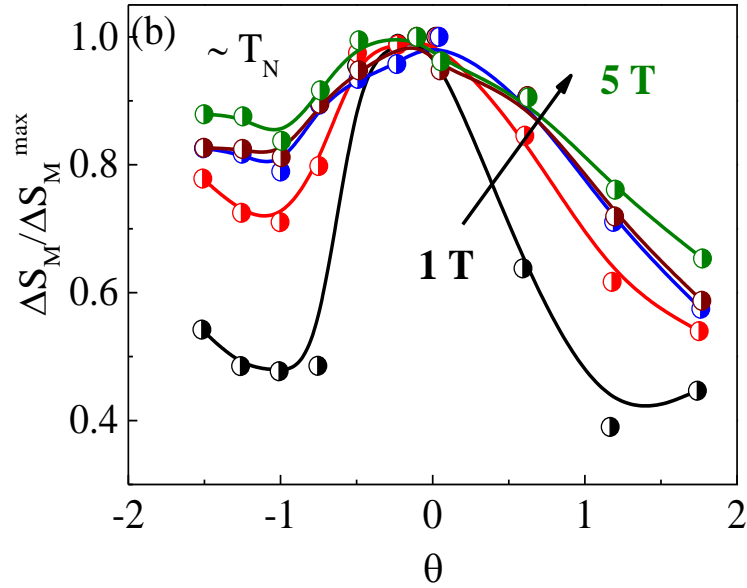
*Figure 6. The curves showing normalized entropy change as a function of the rescaled temperatures (for various ΔH values for DCO nanoplatelets) at $\Delta S_M^{max}$ (a) ~ 9 K and (b) ~ 143 K (~ $T_N$) collapse into a single universal curve.*

However, as we move away from the ordering temperature, where $\Delta S_M^{max}$ is observed, a deviation from the universal behavior can be observed in the curves. The deviation is acceptable as scaling laws need not hold far away from $T_C$.

### 5.3.3 Heat capacity:

The zero-field temperature dependent specific heat ($C_P$ -T) curves for DCO, in a broad temperature range of 2-300 K, are shown in **Figure** 7**(a-c)**. The overall shape of the $C_P$ -T curve was found to be consistent with the other rare earth orthochromites.[56,57] In the high T-region, the DCO follows the Dulong-petit law, as $C_P$ approaches to the classical value of 3nR (R= molar gas constant) per atomic site in formula unit. The $C_p$ approaches its highest value of 106 J/mol/K at 300 K, which is similar to what bulk DCO (105.7 J/mol/K).[36]
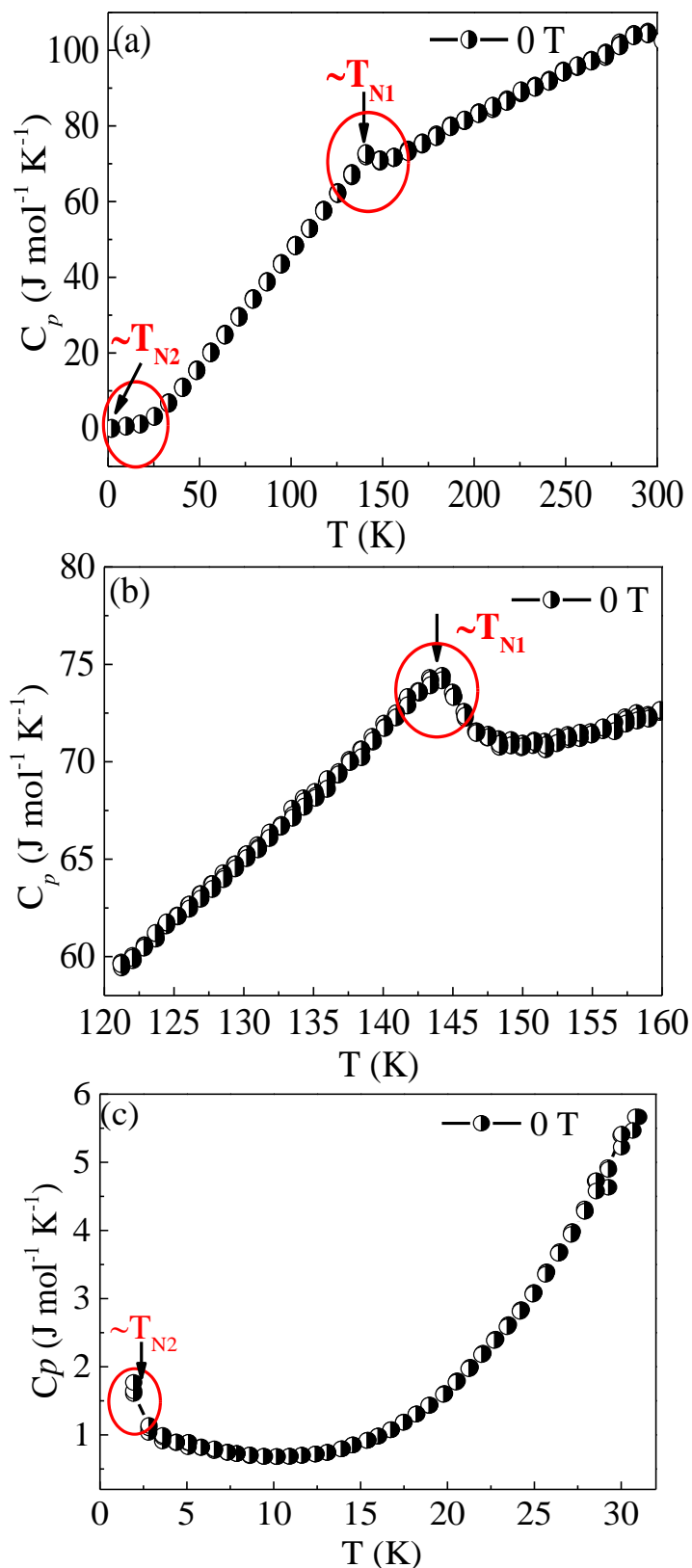
*Figure 7. (a) Thermal evolution of heat capacity of DCO nanoplatelets at H = 0. The panels (b) and (c) show the zoom view of the thermal anomalies observed in*

*panel (a). The curve in panel (b) shows the λ shape, which is associated with the*
*second order paramagnetic to antiferromagnetic phase transition.*

As seen from the **Figure 7(a)**, a clear λ shape anomaly associated with the second order PM to antiferromagnetic (AFM) phase transition was observed at Néel transition $T_{N1}$ ~ 143 K. The $C_p$ decreases with decreasing T and low temperature Schottky anomaly appears below 10 K. The observation of a Schottky anomaly indicates that there are small number of discrete energy levels dominating the behavior of the system. When thermal excitation energy is comparable to the energy spacing, the probability of populating the upper level via. thermal excitations depends on the temperature, and thus, we observe a peak or small hump in the $C_P$ - T plot termed as Schottky anomaly. The **Figure 7(b)** and **(c)** show the magnified view of around $T_{N1}$ and low temperature $T_{N2}$, respectively. The well-defined transitions in $C_P$ - T curves are consistent with our previous magnetization studies on DCO.[27]

To determine and quantify the electronic, lattice and magnetic contributions to the total $C_P$ of the system (DCO), the $C_P$ values are fitted with the equation:[57]

$$C_P = \gamma T + \beta T^3 + \delta T^{3/2} \quad ................................(5)$$

where the $\gamma T$ term gives the electronic contribution, $\beta T^3$ describes the contribution from the lattice and, $\delta T^{3/2}$ gives the spin wave contribution.
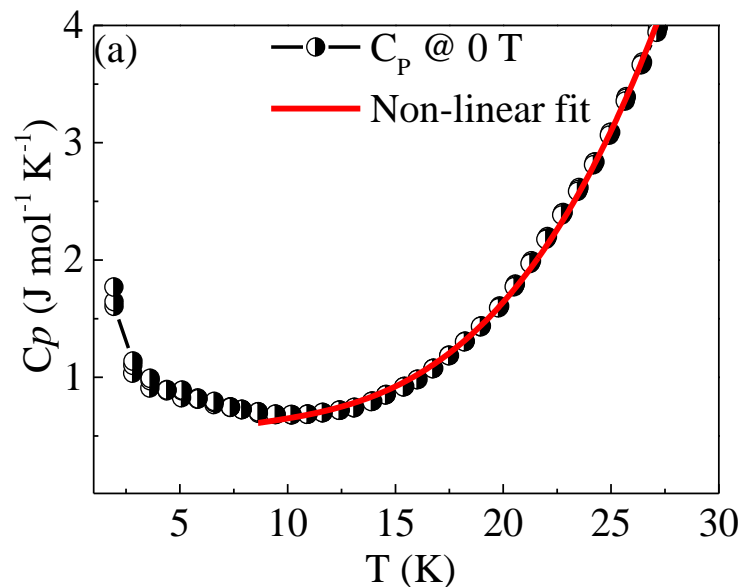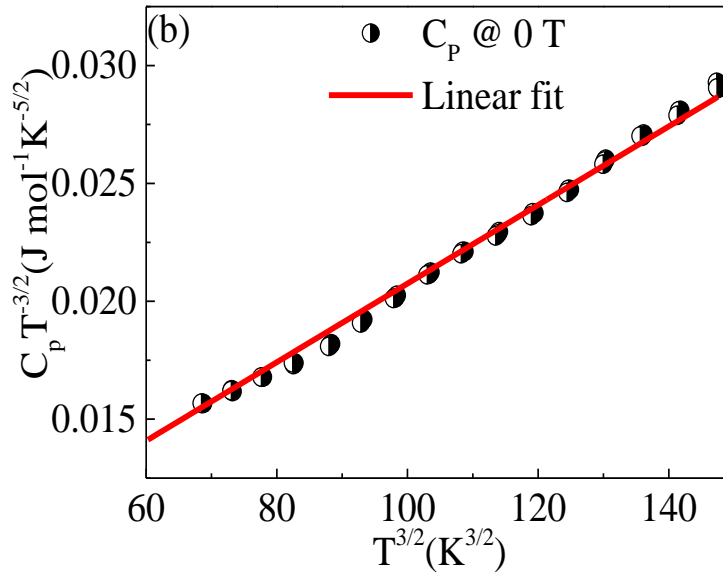
*Figure 8. (a) Experimental $C_p$ data (H = 0) is fitted according to the equation $C_p = \gamma T + \beta T^3 + \delta T^{3/2}$ in low temperature regime. (b) Plot of $C_p T^{-3/2}$ versus $T^{3/2}$ at low temperature range in zero field gives a straight line showing the presence of magnetic $T^{3/2}$ term in heat capacity data.*

At low T, the experimental $C_P$ data (including electronic and lattice contributions) is fitted (2 K< T< 30 K) excluding the Schottky anomaly region and a good fit was observed (**Figure 8(a)**) similar to the other chromites such as $Nd_{1-x}La_xCrO_3$.[57] The plot of $CpT^{-3/2}$ versus $T^{3/2}$ (**Figure 8(b)**) at low T range in zero field gives a straight line which is well in agreement with the experimental data obtained for DCO.

The magnetic field dependent $C_P$ - T curves are shown in **Figure 9(a)** and expanded views in **Figure**s **9(b)** and **9(c)**. No change in $C_P$ was observed with and without applied magnetic field. As seen from the **Figure 9(a)**, no anomaly was observed in a T range 10 - 140 K, where $Dy^{3+}$ and the canted $Cr^{3+}$ moments interact AFM along with weak FM interaction. This further indicates that the overall structure of DCO is AFM.
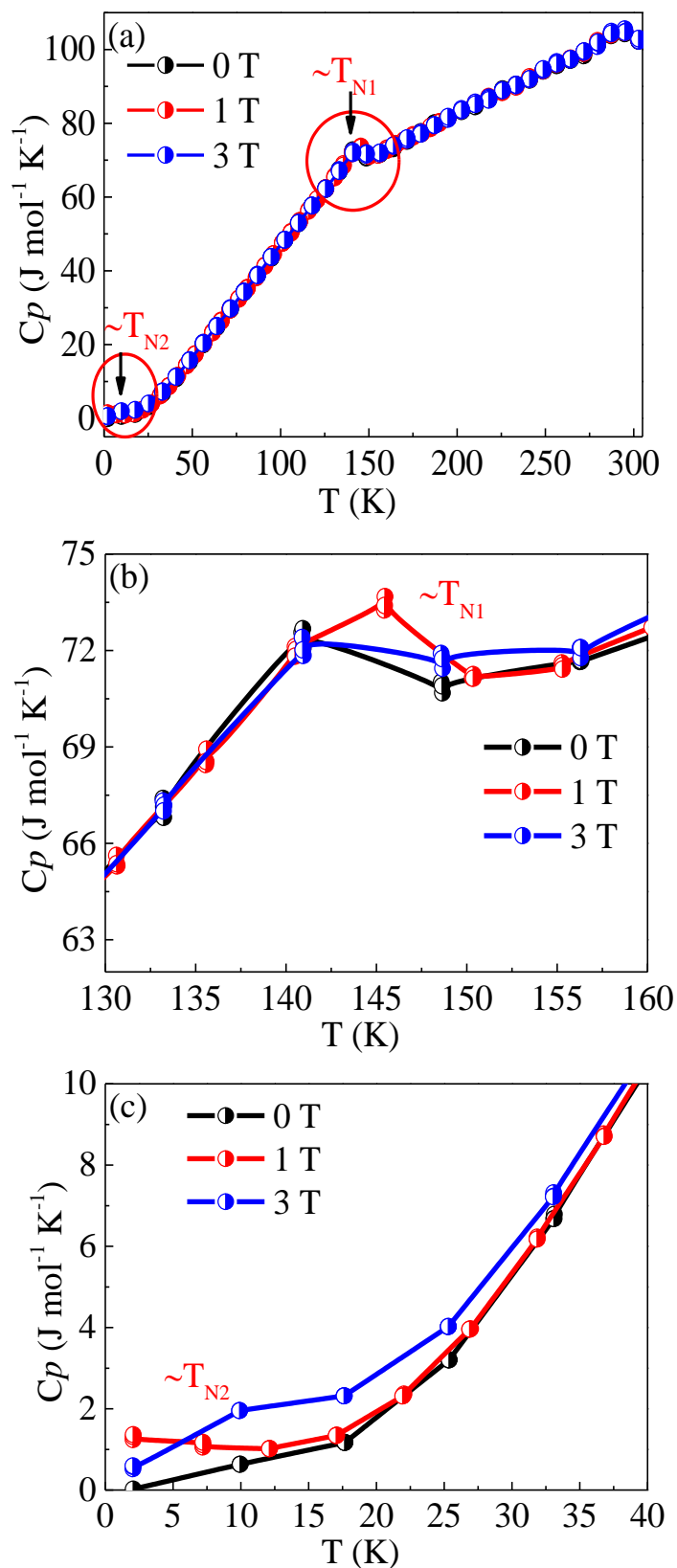
*Figure 9. (a) The curves show temperature evolution of heat capacity of DCO nanoplatelets for various applied fields. The panels (b) and (c) show the zoom view*

*around thermal anomalies at $T_{N1}$ and $T_{N2}$. For higher H, the peak at $T_{N1}$ gets depressed and get broadened with a low temperature Schottky anomaly ($T_{N2}$).*

Moreover, we also note that there is a shoulder below 10 K in the $C_p$-T curves (**Figure 9(c)**) which we can identify as a Schottky anomaly arising from a combination of crystal field effects and the $Dy^{3+}$ spins.[56]

## 5.3.4  Calculation of adiabatic change ($\Delta T_{ad}$) with magnetic field:

Next, we calculated the adiabatic temperature change ($\Delta T_{ad}$) as a function of applied magnetic field using the relation:

$$\Delta T_{ad} = -\int_0^H \frac{T}{C_{P,H}} \left(\frac{\partial M}{\partial H}\right)_H dH ....................................(6)$$

The T-dependent $\Delta T_{ad}$ behavior are shown in **Figure 10(a, b)** with a maximum of 15.1 K and 0.08 K at 3 T around 9 & 143 K, respectively.
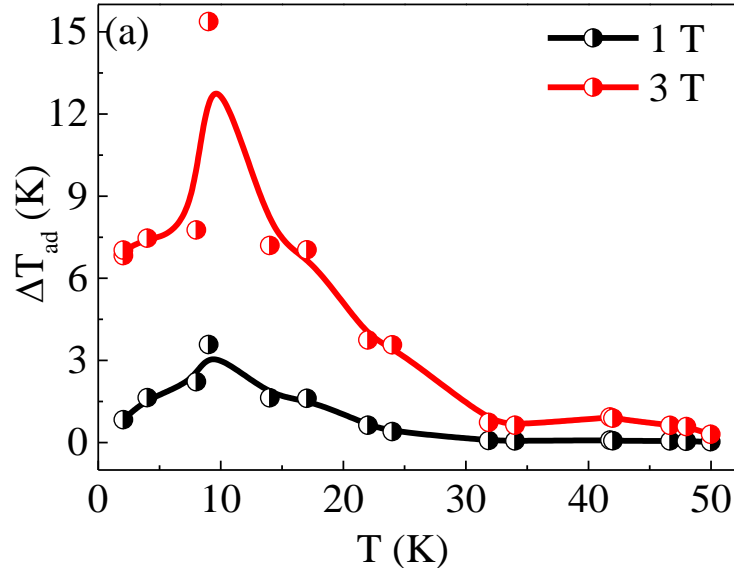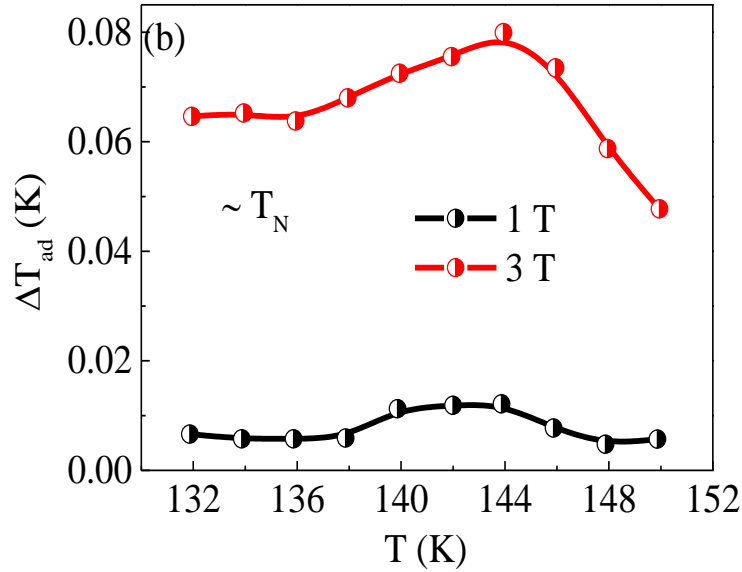
*Figure 10. The curves show adiabatic temperature change ($\Delta T_{ad}$) in a temperature regime (a) 3 - 50 K and (b) 130 - 150 K, calculated from magnetization and heat capacity measurements for a field change $\Delta H$ of 1 T and 3 T. The $\Delta T_{ad}$ vs. T curves peak at ~ 9 K and ~ 143 K with a large value of $\Delta T_{ad}$ around 9 K (15 K for $\Delta H = 3$ T) is indicative of its potential use in low temperature application.*

## 5.3.5  Conclusions

In summary, thermal properties of DCO nanoplatelets was studied by magnetic and heat capacity measurements. We observe that DCO exhibits GMCE with $-\Delta S_M =$ 16.95 J/kg K at 9 K and 5 T applied magnetic field. The $\Delta T_{ad}$, as determined from the heat capacity and magnetic measurements, is also noteworthy with $\Delta T_{ad} = 15$ K at $\Delta H = 3$ T, which is much larger for the perovskites. The temperature dependent heat capacity ($C_P$ - T) measurements show a pronounced anomaly at $T_N \sim 143$ K followed by a small hump in the $C_P$ - T curve below 10 K. In presence of magnetic field, the heat capacity anomaly at $T_N$ get depressed and shifted to higher T, whereas, the low T Schottky anomaly becomes more prominent with an increase in H. Thus, our studies open-up a possibility for another viable technological application for multiferroic chromites, namely, in magnetic cooling at low T.

## Section 5.4

## Coexistence of inverse and normal magnetocaloric effects in SmCrO$_3$ polycrystallites covering wide range working temperature

_____

In the broad area of magnetism, the search for new giant magnetocaloric materials covering a wide working temperature range is of an immense interest since last several decades. The underlying physics behind this effect is quite challenging. However, there are only few materials, which exhibit both normal and inverse MCE. In this section, we investigate detailed magnetocaloric studies on samarium chromite (SCO) which is an exceptional material as it possesses both inverse (positive) and normal (negative) MCE at and above the spin reorientation transition ($T_{SR}$) with -$\Delta S_M^{max}$ values ~ - 0.24 & 0.13 J/kg K, respectively. The SCO also shows another normal (negative) MCE peak around its Néel transition ($T_N$) with -$\Delta S_M^{max}$ ~ 0.11 J/kg K. The presence of two successive MCE peaks in the SCO in a temperature range 3 - 50 K, lead to a ~ 47 K operating temperature with one thermodynamic cycle. In addition, the low temperature heat capacity ($C_P$) measurements of SCO nanoplatelets reveals a λ-shape peak at $T_N$ and a weak anomaly around the ~ $T_{SR}$ along with a Schottky anomaly below 10 K. The results indicate that material with spin reorientation and magnetic ordering transitions may constitute an important class of magnetocaloric material.

_____

## 5.4.1 Arrott plot:

To determine the nature of phase transition in SCO, whether, it is a first order or a second order transition, $1^{st}$ quadrant isothermal M - H hysteresis measurements are performed to plot H/M vs. $M^2$ (Arrott plot) in the region of interest. Below the second order phase transition temperature, these curves show positive slope, while, below the first order transition, curves with negative slope along with small kinks are observed in the Arrott plot.[50] Apart from the ordering transition, nature of slope either negative or positive also, depends on the grain size of the sample.[48–50] The detailed magnetization behavior is already discussed in the case of DCO and similar explanation holds for SCO.[27,30]

   The **Figure 1** represents the isothermal magnetization hysteresis (M−H) curve ($1^{st}$ quadrant) measured in various temperature ranges of **(a)** 3 - 200 K ($\Delta T = 2$ K), **(b)** 10 - 50 K ($\Delta T = 2$ K), and **(c)**130 - 200 K ($\Delta T = 2$ K) with an applied field ramped up to 9 T. The values in parenthesis give temperature step-size.
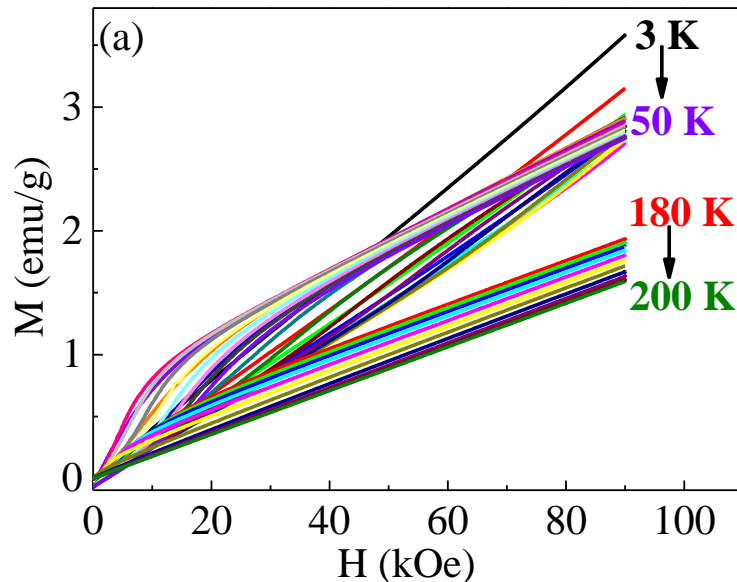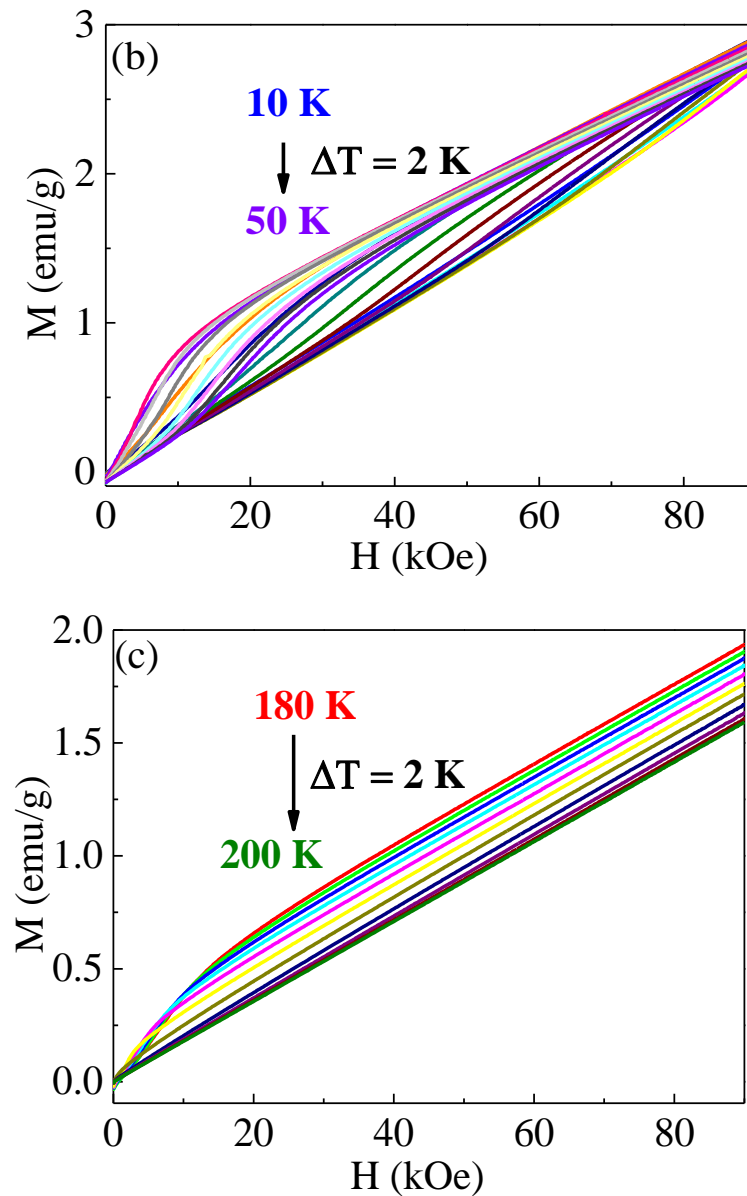
*Figure 1. The M - H isotherms (1ˢᵗ quadrant) of SCO polycrystallites measured in temperature ranges of 3 - 200 K (ΔT = 2 K). The panel (b)10 - 50 K (ΔT = 2 K), and (c) 130 - 200 K (ΔT = 2 K) shows the M-H isotherms with an applied field ramped up to 9 T.*

The H/M vs. $M^2$ curves (**Figure 2(a)**) show the change in slope near $20 - 30$ kOe indicating weak FM interaction in SCO. This behavior is similar and consistent with

other orthochromites and manganites.[6,10–12,21,52,58] The slope of Arrott plot was found to be positive confirming the overall second order phase transition in SCO.



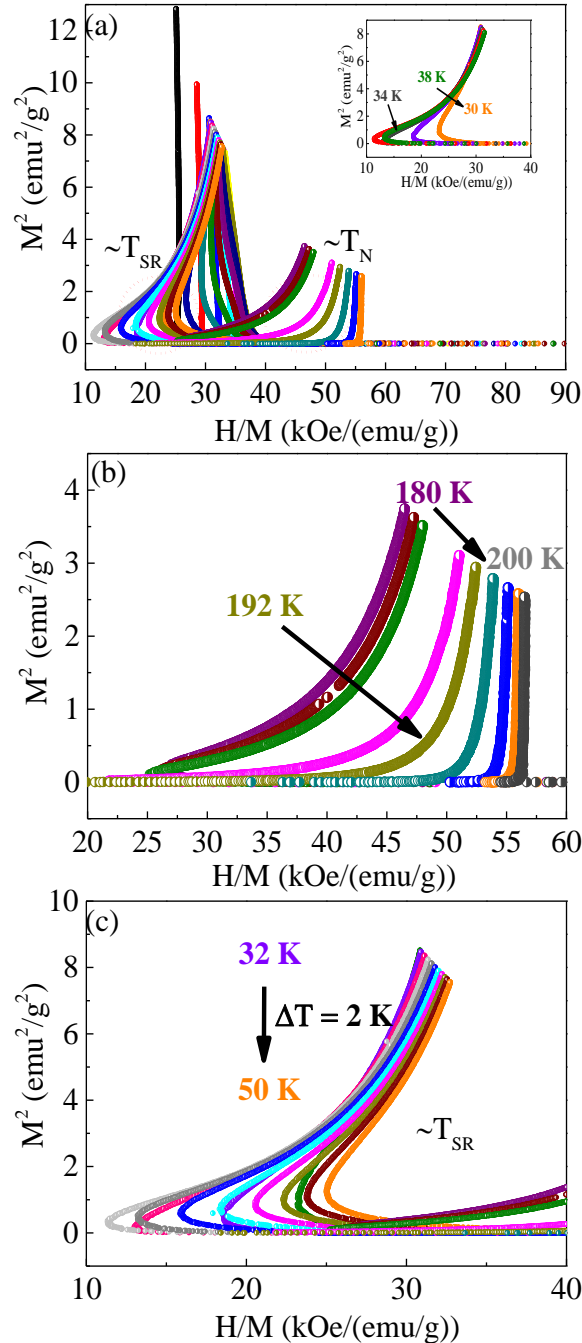*Figure 2.   (a) Arrott plots (H/M vs. M²) of isothermal magnetization. The inset shows the isotherms in a temperature range 30 - 38 K. (b) The curves show the zoomed view in a temperature range 180 - 200 K  and (c) 32 - 50 K, respectively.*

The comparison between isotherm curves (inset of **Figure 2(a)**) taken at 32 K and 34 K shows a large difference. This is due to the presence of SR transition at 34 K (34 K) and usually the magnetic entropy change shows a maximum in the critical region. The **Figure 2(b, c)** shows the zoom view of Arrott plot at ~ $T_N$ and ~ $T_{SR}$, respectively, which is the region of interest for exploring the magnetocaloric behavior in SCO.

### 5.4.2  Magnetocaloric effect:

Next, we investigated the MCE behavior in SCO nanoplatelets. The change in entropy is directly proportional to the change in the magnetization as a function of temperature $(\frac{\partial M}{\partial T})$, as seen from equation (1).[5,13,23]

$$\Delta S_M \,(T, H) \; = \int_0^H \left(\frac{\partial M}{\partial T}\right)_H \, dH \; \ldots\ldots\ldots\ldots\ldots\ldots..(1)$$
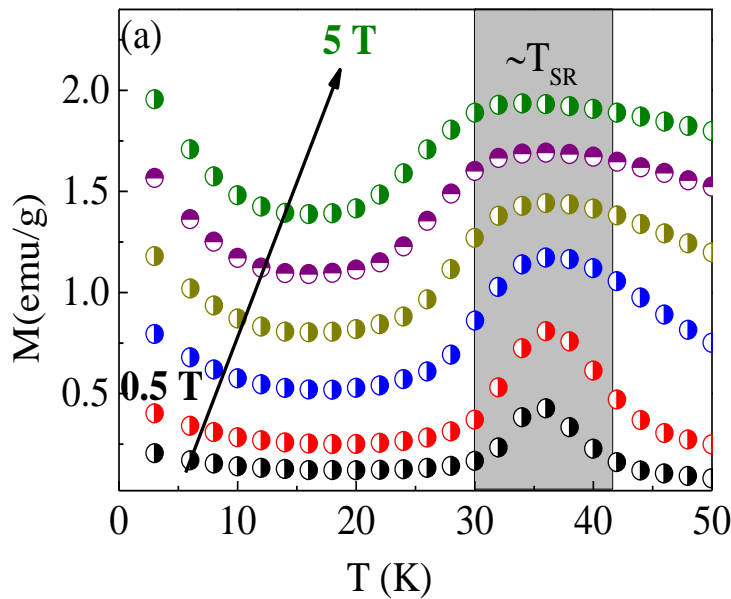


It can be inferred from the Eq. 1 that larger $(\frac{\partial M}{\partial T})$ is a key for larger $\Delta S_M$. The M-T curves are extracted from the $1^{st}$ quadrant isothermal hysteresis curves and represented in **Figure 3(a) & (b)** with a prominent peak at ~ $T_{SR}$ and ~ $T_N$ which is consistent the magnetic transitions of SCO reported by us earlier.[30]
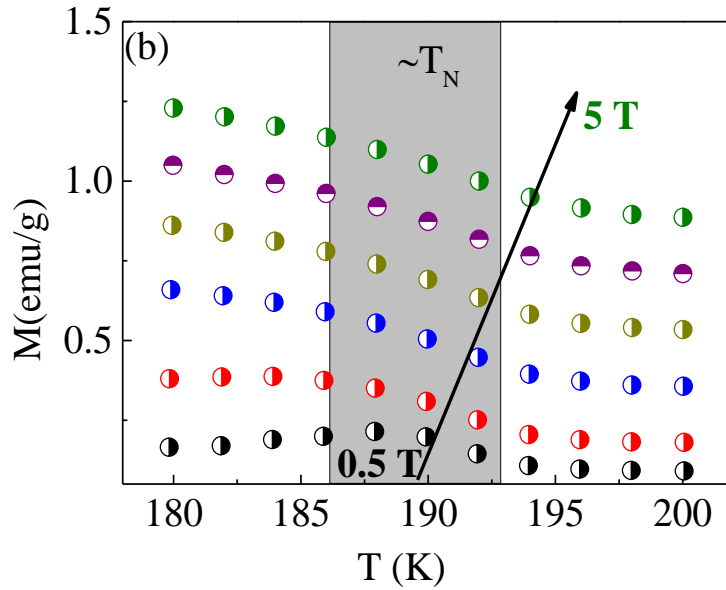
*Figure 3. Field dependent M - T curves derived from 1ˢᵗ quadrant isothermal M - H curves shown in the temperature ranges (a) 3-50 K and (b) 180-200 K, respectively. The grey shaded portion indicates the spin reorientation transition (~ $T_{SR}$) and Néel transition temperature (~ $T_N$) of SCO.*

After integrating $(\frac{\partial M}{\partial T})$ with respect to the field, we obtained $\Delta S_M$ values. In **Figure 4 (a)** and **(b)** the $\Delta S_M$ vs. T curves are plotted in the regions of interest (~ $T_{SR}$ and ~ $T_N$ ). As evident from **Figure 4(a)**, the $\Delta S_M$ is positive at ~ $T_{SR}$ and becomes negative above and below the $T_{SR}$.
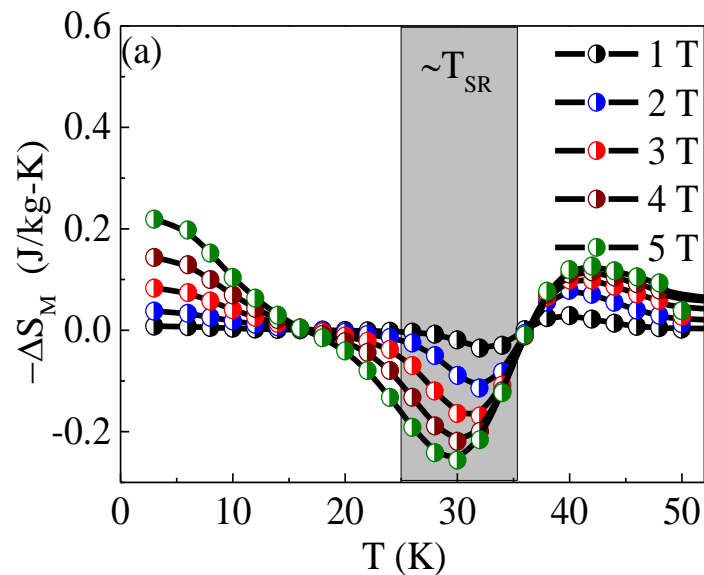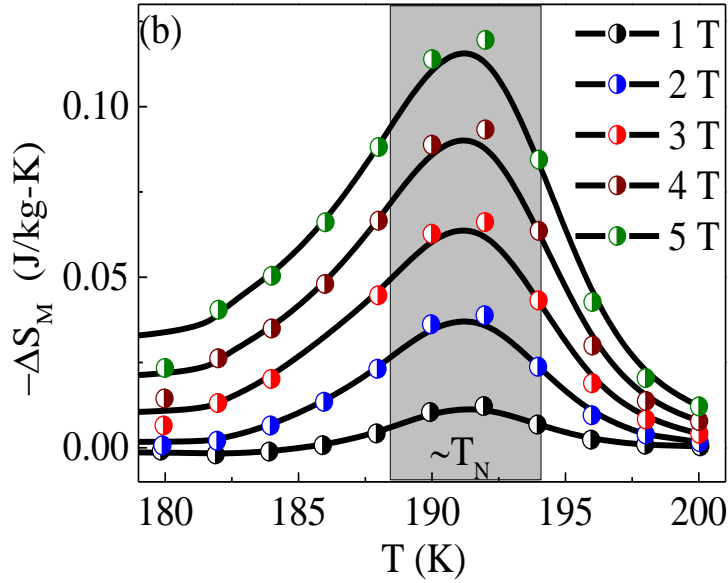
***Figure 4. The ΔS$_M$ vs. T curves for various magnetic fields for SCO around (a) T$_{SR}$
and (b) T$_N$ (shown as shaded regions). In the panel (a), the SCO shows successive
normal and inverse MCE along with broad range of operating temperature. In the
panel (b), the SCO shows a normal MCE around T$_N$.***

The coexistence of the normal ($\Delta S_M < 0$) and inverse MCE ($\Delta S_M > 0$) (IMCE) at ~ T$_{SR}$
in SCO covering almost ~ 47 K working temperature regime, in addition to the
existence of a normal MCE at ~ T$_N$, makes it an interesting model system for the
further studies. As expected, the maximum entropy change is seen at 32 K (T$_{SR}$) and
192 K (T$_N$). The SCO exhibits positive $\Delta S_M$ peak (inverse MCE) around T$_{SR}$ (32 K)
corresponding to the spin reorientation of Sm$^{3+}$ moments with respect to the canted
Cr$^{3+}$ moments. It was also observed that with the increasing magnetic field, $\Delta S_M$ peak
around T$_{SR}$ broadens asymmetrically towards the high temperatures. At 32 K, the -
$\Delta S_M$ attains a maximum value of  - 0.16 J/kg K and - 0.24 J/kg-K  at 3 T & 5 T,
respectively. In addition,  we also observed negative peak ($\Delta S < 0$) above and below
T$_{SR}$ covering broad temperature range. However, $\Delta S_M$ was found to be negative, at ~
T$_N$, corresponding to the PM-AFM transition with -$\Delta S_M^{max}$  0.12 J/kg K at 5 T as
shown in **Figure 4(b)**.

Another important parameter, useful in determining the good magnetocaloric
properties, is the relative cooling power (RCP) which strongly depends on the -

$\Delta S_M{}^{max}$ and full width of half maxima (FWHM) of $-\Delta S_M$ peak which is given by Eq 2.

$$RCP = \delta T_{FWHM} \ X \ |\Delta S_M^{max}|\ldots\ldots\ldots\ldots\ldots..(2)$$

Where, $\delta T_{FWHM}$ is full width at half maximum of the peak and $|\Delta S_M^{max}|$ is the maximum entropy change at and above $\sim T_{SR}$ for varying field. As shown in **Figure 5(a)**, the $-\Delta S_M{}^{max}$ at $\sim T_{SR}$ (inverse MCE) and above $\sim T_{SR}$ (normal) was found to be strongly H dependent with $-\Delta S_M{}^{max}$ - 0.24 & 0.13 J/kg K at 5 T applied magnetic field. This interesting MCE behavior in a temperature range 3 - 50 K, gives wide ($\sim$ 47 K) working temperature range with one thermodynamic cycle ($\Delta T_{cycl} = T_{hot} - T_{cold}$) where, $T_{hot}$ and $T_{cold}$ are hot and cold ends of the cycle. The RCP of SCO at and above $\sim T_{SR}$ was found to be 2.5 and 1.75 J/kg at 5 T, respectively, as shown in **Figure 5(b)**.
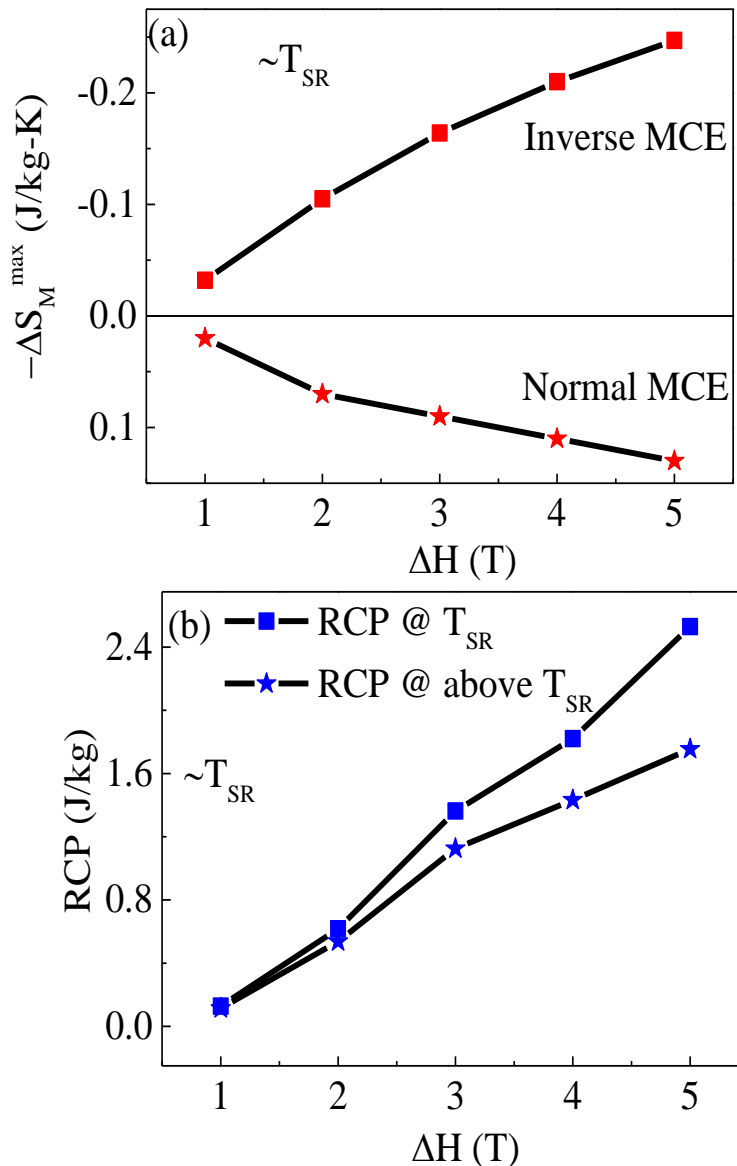
*Figure 5. (a) The change in the magnetic entropy and (b) the relative cooling power (RCP) plotted against the change in field (ΔH) around $T_{SR}$ for both inverse and normal MCE.*

Next, we investigated the MCE behavior at ~ $T_N$. The **Figure 6(a, b)** shows the H dependent $\Delta S_M$ and RCP plot at ~ $T_N$, respectively. As seen from **Figure**, -$\Delta S_M$ and RCP at ~ $T_N$ was found to be strongly field dependent with a maximum value 0.11 J/kg K and 1.18 J/kg, at 5 T. Although, the $\Delta S_M$ and RCP value was found to be less as compared to other chromites such as $DyCrO_3$ and $GdCrO_3$, the existence of conventional MCE and IMCE is an added advantage.[11,12]
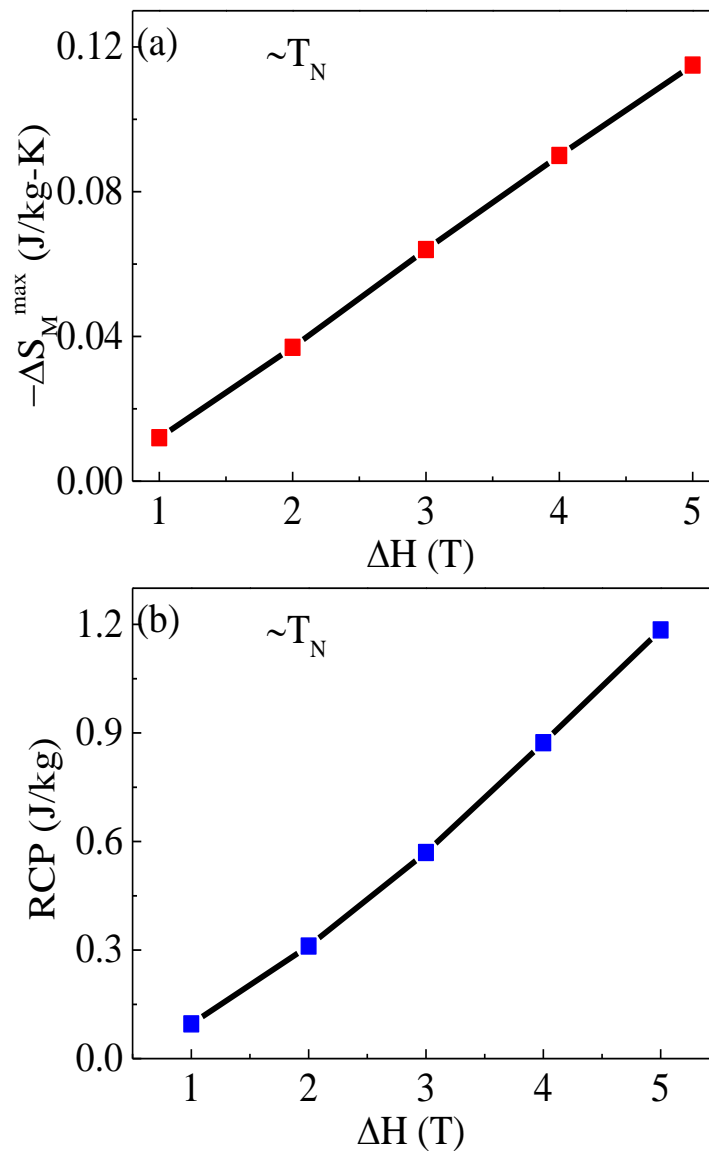
*Figure 6. (a) The change in the magnetic entropy plotted against the change in field (ΔH) at $T_N$. (b) The relative cooling power RCP is plotted against the change in field (ΔH) at $T_N$ for SCO.*

The IMCE is generally observed in a material whose magnetization decreases with decreasing temperature. In manganites such as $NdBaMn_2O_6$, the IMCE is related to the PM/FM to AFM transitions.[18] Due to the SR transition, compounds such as $NdCo_5$ and $Nd_2Co_7$ also show IMCE.[59,60] However, IMCE in our SCO is due to the SR transition. The successive positive and negative entropy change at ~ $T_{SR}$ strongly suggest that both the magnetizing and demagnetizing processes can be employed for cooling, thus, increasing the refrigeration efficiency. This unique feature in SCO is due to the fact that SR transition is often accompanied by the IMCE.[9] The SCO could be utilized to stabilize the temperature of a magnetic refrigerator to ~ 35 K due to the change in sign of $-\Delta S_M$ around the critical temperature (~ 35 K), which most other materials with only normal MCE cannot satisfy.[61]

Then, we explore the universal behavior for the entropy change in SCO with second order phase transition (SOPT) which can be established by scaling the axes appropriately. The universal behavior of SCO nanoplatelets was investigated by rescaling the axes for a universal curve, *i.e.* all the $\Delta S_M$ curves are normalized with their maximum entropy change ($\Delta S_M{}^{max}$), respectively by equation 3:[53,55,62]

$$\theta = \begin{cases} -\frac{(T-T_C)}{(T_{R1}-T_C)}, T \le T_C \\ \frac{(T-T_C)}{(T_{R2}-T_C)}, T > T_C \end{cases} \dots\dots\dots\dots\dots(3)$$

where $T_{R1}$ and $T_{R2}$ are the reference temperatures where, $\Delta S$ equals $\Delta S_M{}^{max}/2$. The two reference temperatures $T_{R1}$ and $T_{R2}$, are needed to characterize the entropy change, where $T_{R1} < T_C$ and $T_{R2} > T_C$ and $T_C$ is the ordering temperature, here, $T_C = \sim T_{SR}$ and ~ $T_N$ corresponding to $\Delta S_M{}^{max}$. The transformed curves of SCO under various H at ~ $T_{SR}$ and ~ $T_N$ are plotted in . 7(a, b) which shows that all the data points collapse onto a single master curve, revealing it's universal behavior.
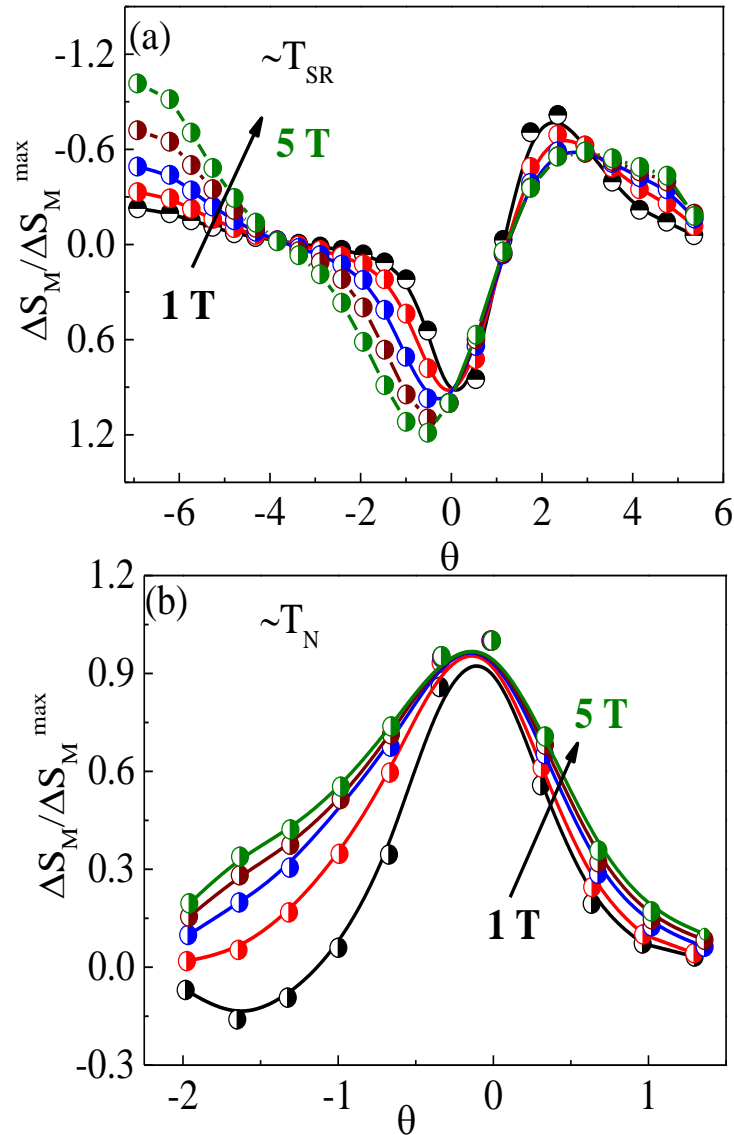
*Figure 7. Normalized entropy change for different applied magnetic fields (1-5 T) for SCO nanoplatelets at $T_{SR}$ and $T_N$ as a function of the rescaled temperatures collapse into a single universal curve.*

All the curves collapse into a single curve in temperature regions near to ordering temperature ($\theta = 0$) further validating our treatment of data according to SOPT in SCO. However, as we move away from the ordering temperature, where, $\Delta S_M^{max}$ is observed, breakdown can be observed in the curve which is acceptable as scaling laws need not hold far away from T ~ 32 and ~ 192 K.

### 5.4.3  Heat capacity:

The zero field temperature dependent of heat capacity for SCO is shown in **Figure 8**. The overall shape of $C_P$ -T plot was found to be similar to other chromites such as YbCrO$_3$, NdCrO$_3$ *etc.* [56,57]
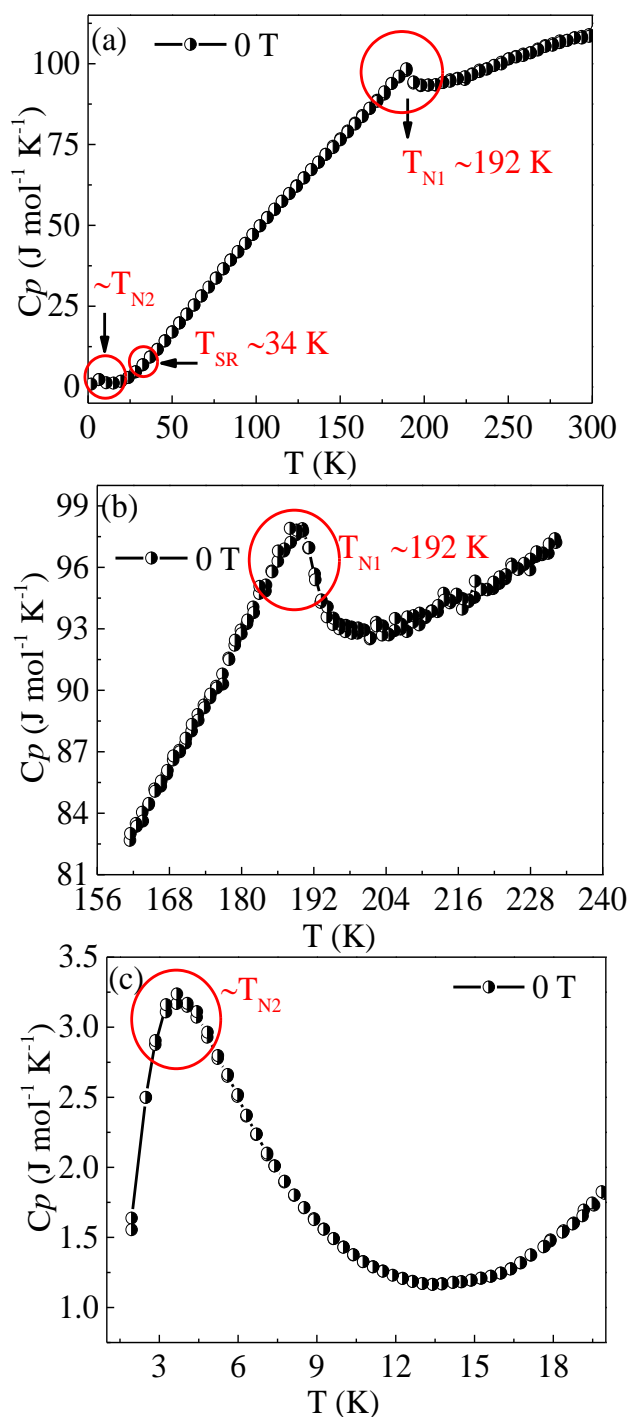


*Figure 8.(a) Thermal evolution of  heat capacity of SCO nanoplatelets at zero field*

*condition (b and c) shows the zoom view of the thermal anomalies observed (a) at $T_N$ and low T. The λ shape peak is associated with the second order paramagnetic to antiferromagnetic phase transition.*

**Figure 8(a)** shows the clear λ shape anomaly at ~ 192 K with a weak signature of $T_{SR}$ at ~ 32 K. The $C_P$ of SCO at 300 K was found to be 101.2 J/mol/K and agreed well with the reported value of bulk SCO.[36] The $C_P$ was found to be temperature dependent which decreased with the temperature and a small hump *i.e.* Schottky anomaly was observed at ~ 4 K. **Figure 8(b, c)** shows the zoom view of $C_P$-T at ~ $T_N$ and low temperature clearly indicating the well defined transition as observed from our previous magnetic studies on SCO.[30]

The total $C_P$ of a system is a combined electronic, lattice and magnetic contribution. The $C_P$ data at low temperature are fitted with the equation:[57]

$$C_P = \gamma T + \beta T^3 + \delta T^{3/2} \dots\dots\dots\dots\dots\dots\dots (3)$$

Where the γT term gives the electronic contribution, $\beta T^3$ describes the contribution from the lattice and, $\delta T^{3/2}$ gives the spin wave contribution. We clearly see a hump *i.e.* termed as Schottky anomaly below 10 K similar to the other chromites.[56,57] When thermal excitation energy is comparable to the energy spacing, the probability of populating the upper level via. thermal excitations depends more sensitively on temperature, and thus, we observe a peak in the $C_P$-T plot termed as a Schottky anomaly.
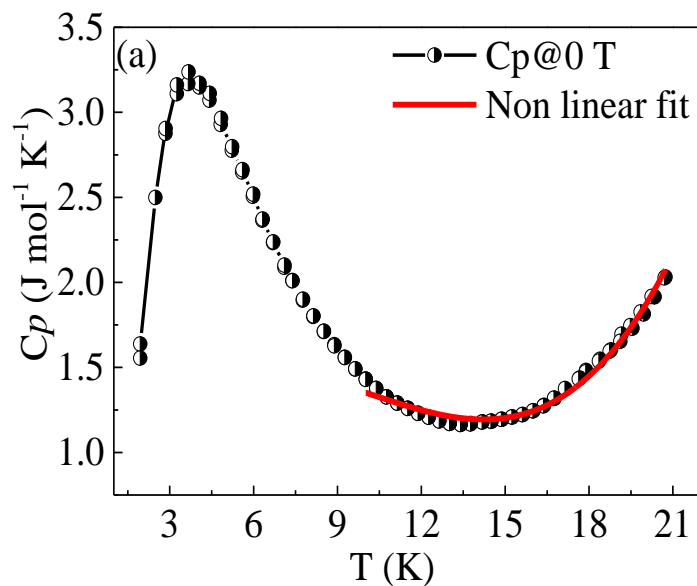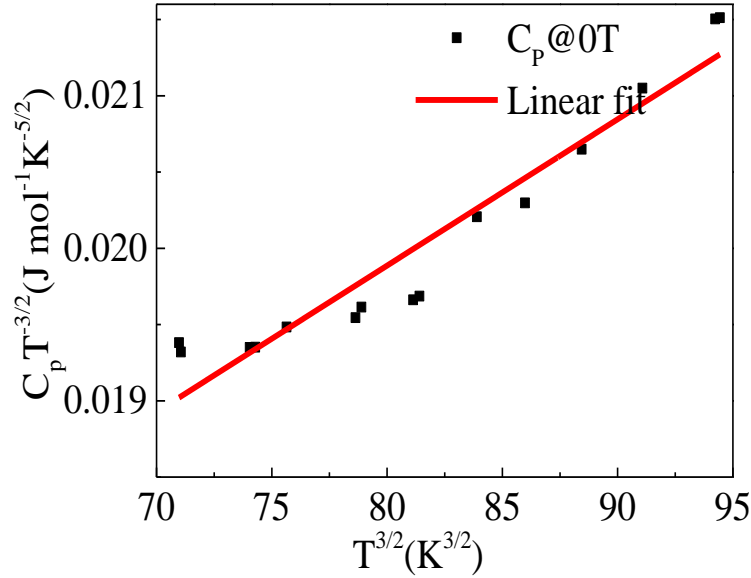
*Figure 9. (a) Experimental $C_p$ data is fitted according to the equation $C_p = \gamma T + \beta T^3 + \delta T^{3/2}$ below 20 K in zero field condition. (b) plot of $C_p T^{3/2}$ versus $T^{3/2}$ at low temperature regime(< 20 K) in zero field gives a straight line showing the presence of magnetic $T^{3/2}$ term in heat capacity data.*

As shown in **Figure 9(a)**, the $C_P$ data is fitted below 20 K, with the above eq. 3 excluding the Schottky anomaly region and good fit was observed. The zero field $C_P T^{-3/2}$ - $T^{3/2}$ plot (**Figure 9(b)**) at low T range gives a straight line well in agreement with the experimental data obtained for SCO.

Next, we also studied the H dependent $C_P$ - T as shown in **Figure 10**. As evident from **Figure 10(a),** no significant change in $C_P$ - T with and without applied magnetic field was observed. The expanded view at $T_N$ and below 30 K is shown in **Figure 10(b & C)**. However, the peak at ~ $T_N$ in SCO (**Figure 10(b)**) was suppressed and broaden with the increase in applied field. Below 10 K, we observe a Schottky anomaly which was found to be shifted towards higher T with increasing field from 0-3 T (**Figure 10(c)**). The field dependent $C_P T$ curves is further used to calculate the adiabatic temperature change.
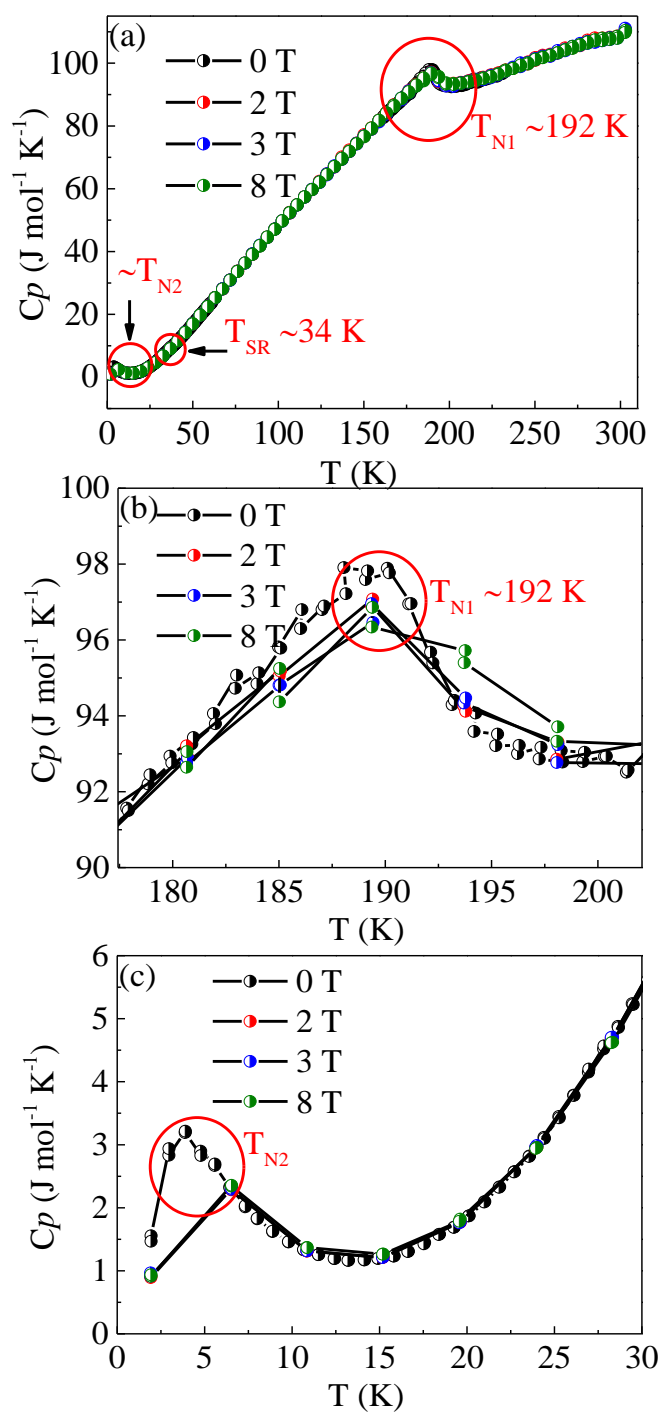
*Figure 10. (a) Field dependency of thermal evolution of heat capacity of SCO nanoplatelets (b and c) shows the zoom view of the thermal anomalies at $T_{N1}$ and $T_{N2}$. For higher applied magnetic field, the peak at $T_{N1}$ gets depressed and becomes broaden.*

### 5.4.4 Calculation of adiabatic change ($\Delta T_{ad}$) with magnetic field:

It is well known that MCE has a figure of merit which include parameters such as $\Delta S_M$, RCP and $\Delta T_{ad}$, respectively. Thus, it is essential to determine the $\Delta T_{ad}$ which strongly depends on the $C_P$ value and change in magnetization with the field $\left(\frac{\partial M}{\partial H}\right)$. It is given by the equation:

$$\Delta T_{ad} = - \int_0^H \frac{T}{C_{P,H}} \left(\frac{\partial M}{\partial H}\right)_H dH \ldots\ldots\ldots\ldots(4)$$

For a larger $\Delta T_{ad}$, large $\left(\frac{\partial M}{\partial H}\right)$ and smaller $C_P$ is essential.
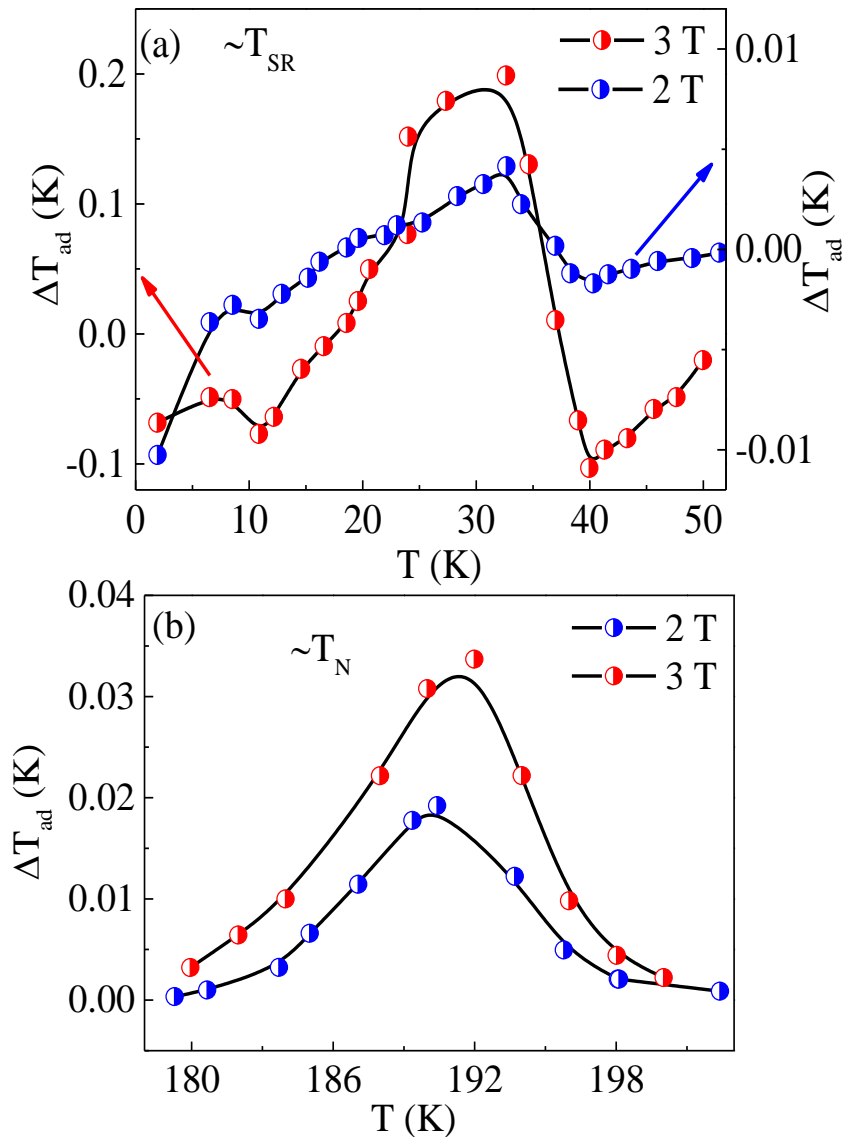
*Figure 11. The plot of adiabatic temperature change ($\Delta T_{ad}$) with temperature calculated indirectly from magnetization and heat capacity measurements in a temperature range (a) 3-50 K and (b)180-200 K for 2 T and 3 T, respectively. The maximum value of $\Delta T_{ad}$ at ~ $T_{SR}$ and ~$T_N$ was found to be 0.2 K and 0.03 K /3T applied field.*

The $\Delta T_{ad}$ was found to be maximum 0.2 K and 0.03 K ~ $T_{SR}$ and ~ $T_N$, respectively for 3 T field change. The T and H dependency of $\Delta T_{ad}$ at ~ $T_{SR}$ and ~ $T_N$ is shown in **Figure 11(a, b)**. Thus, all the MCE parameters *i.e.* $\Delta S_M$, RC and $\Delta T_{ad}$ derived for SCO polycrystallites and coexistence of inverse and normal MCE suggest another novel aspect of these material.

## 5.4.5  Conclusions

We have studied the thermal and magnetic properties of SCO polycrystallite focusing on the possible magnetocaloric effect. It is interesting to note, successive inverse and normal MCE with $\Delta S_M$ peak at and above ~ $T_{SR}$ and ~ $T_N$ are 0.24 and 0.13 J/kg K for a field change of 5 T, respectively. We also observe normal MCE at $T_N$. Also, this double peak MCE behavior in SCO in a temperature range 3-50 K, leads to a ~ 47 K broader working temperature range. The thermal anomaly was found to be consistent with the magnetic transition in SCO and smaller $C_P$ value at ~ $T_{SR}$ favor $\Delta T_{ad}$ ~ 0.2 K/3 T field change. Though, SCO is suitable for low temperature application but it might be possible to shift the ordering temperature towards the room temperature by tuning the particle size, chemical substitution *etc.* which is subjected to future study. This important result in SCO may be a stimulus to the search for suitable refrigerant materials that exhibit two or more successive magnetic transition, specially spin reorientation.

# Section 5.5

# Magnetocaloric effect in YbCrO$_3$ polycrystallites

_____

In this section, we present the study on thermal and magnetic properties of YbCrO$_3$ polycrystallites. The MCE parameters $\Delta S_M$, RCP and $\Delta T_{ad}$ was found to be strongly dependent on the applied magnetic field. The maximum change in the entropy at $T_{N2}$ and $T_{N1}$ was found to be 2.6 J/kg K, for 5 T applied magnetic field.

_____

## 5.5.1 Arrott plot:

The Arrott plot can be used to estimate the $T_C$ or $T_N$ in weak ferromagnetic or antiferromagnetic system.[46–48] Based on the Arrott-Noakes equation of state, modified Arrott plot method was used to analyze the critical behavior of the magnetic phase transition.[49]

$$(H/M)^{1/\gamma} = a \left(\frac{T-Tc}{Tc}\right) + bM^{1/\beta} \dots\dots\dots\dots\dots\dots\dots\dots\dots(1)$$

Here, $\gamma$ & $\beta$ are critical exponents and a & b are constants. Generally, for $\gamma = 1$ and $\beta = 0.5$, the $M^{1/\beta}$ vs $(H/M)^{1/\gamma}$ plot forms a set of straight lines and the isotherm which passes through the origin gives $(T=T_N)$.[48,50,51] Isothermal magnetization (M - H) curves were measured with increasing the field 0-9 T in a temperature interval of 2 K. The **Figure 1** shows the 1$^{st}$ quadrant M - H curves at different temperature from **(a)** 3 - 50 K and **(b)** 110 - 130 K with $\Delta T$= 2 K.
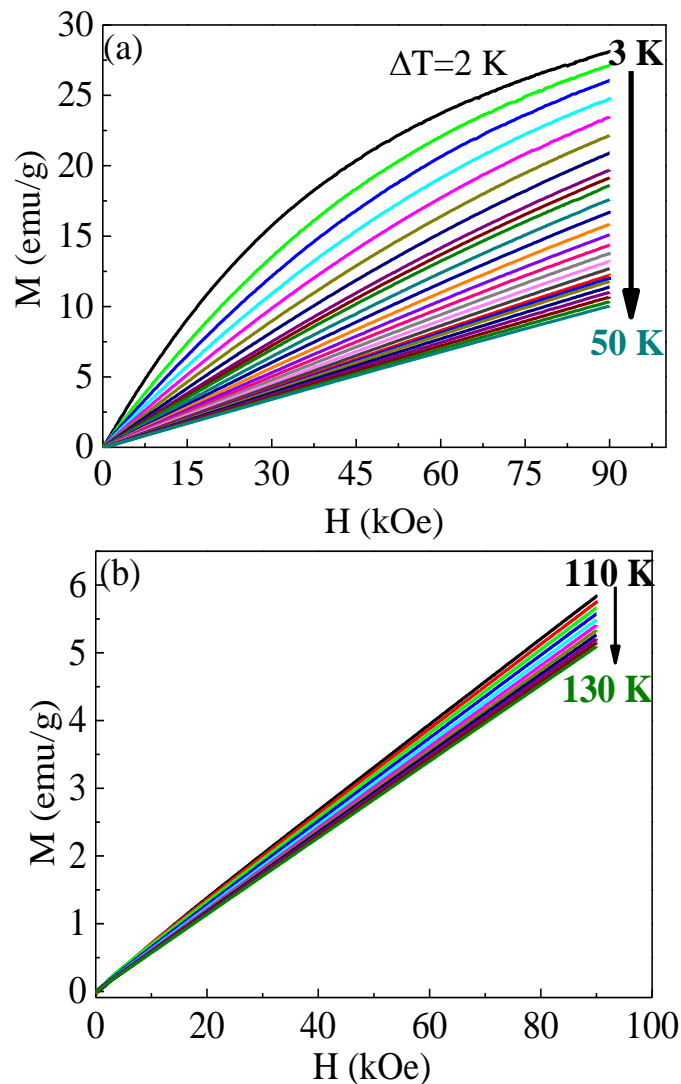
*Figure 1. M-H ($1^{st}$ quadrant) curves at different temperature from (a) 3 - 50 K and (b)110 -130 K with $\Delta T = 2$ K.*

In **Figure 1(a)** the magnetization isotherms of YCO nanoplatelets reveal that the difference in the magnetization between 3 and 5 K is large. This temperature is close to the Yb ordering transition which reflects a large magnetic entropy change can be expected. The sample was heated above its Neel transition (~ $T_N$) temperature to avoid any remanence from the history of previous measurement.However, even after 9 T applied magnetic field it doesn't saturate indicating strong AFM behavior which is consistent with the AFM ordering of $Yb^{3+}$ spins.[56]

From the $1^{st}$ quadrant M-H curves presented in the **Figure 1**, we derived Arrott plots of YCO nanoplatelets and elucidated in **Figure 2**. Arrott plot is generally used to determine the nature of phase transition. According to Banerjee criteria, negative slope of plot is associated with the first order transition and positive slope with the second order phase transition.[47,50] In YCO, positive slope is observed at low T(3-50 K) and around $T_N$ (**Figure 2(a, b)**) suggesting the possible second order magnetic transition.
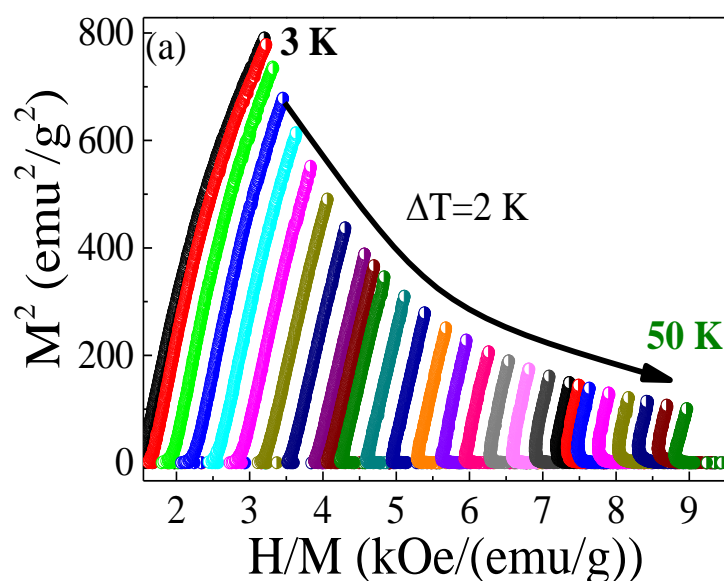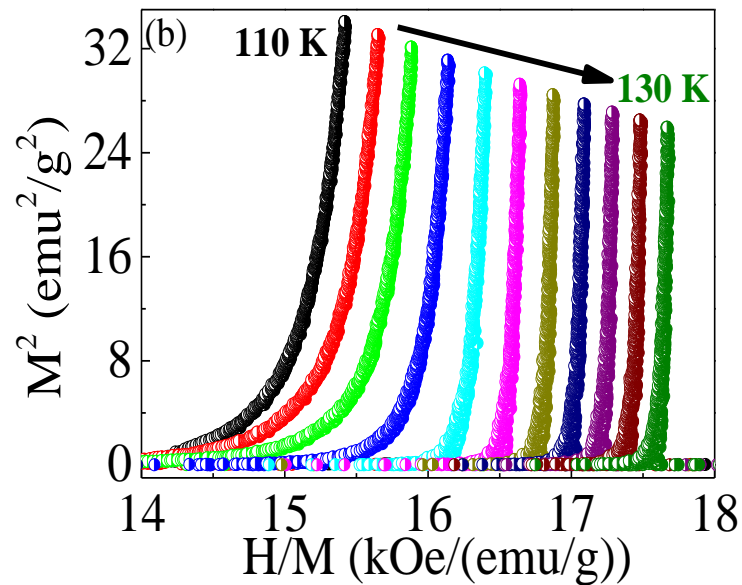
**Figure 2.** *Arrott plots (H/M vs M$^2$) of isothermal magnetization in a temperature range (a) 3-50 K (b) 110- 130 K  with ΔT=2 K, respectively.*

The Néel transition temperature derived from the Arrott plot is around~ 119 K.

M - T magnetization curves as shown in **Figure 3**. were extracted from 1st quadrant isothermal M - H curves in the temperature range from **(a)** 3-50 K and  **(b)** 110-130 K, respectively with ΔT = 2 K.
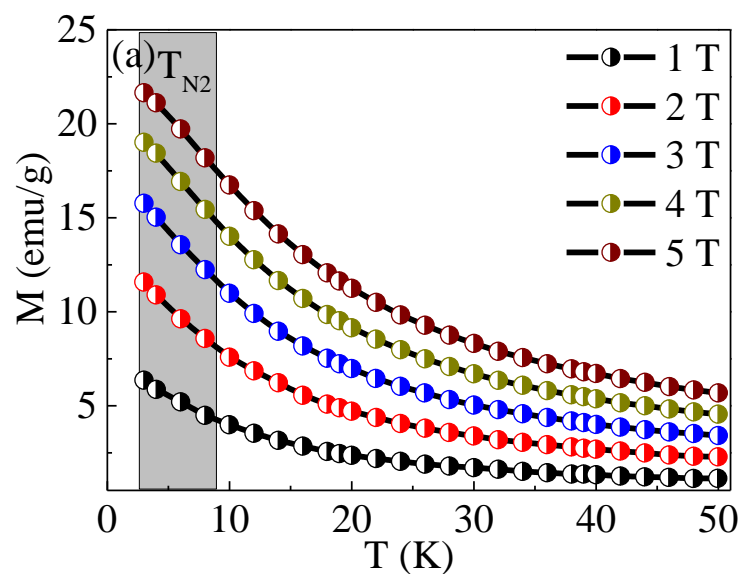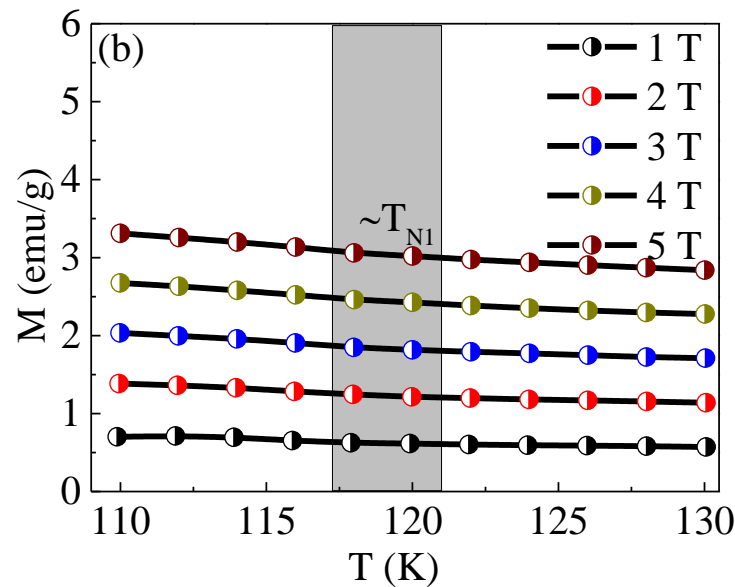
*Figure 2. Field dependent M - T derived from 1$^{st}$ quadrant isothermal M - H curves in a temperature range (a) 3-50 K and (b)110-180 K, respectively. The grey shaded portion indicates the Neel transition temperature (~ $T_{N1}$ and ~ $T_{N2}$) of YCO.*

We can see from the **Figure**, that M - T curves show an anomalies at $T_{N1}$ and $T_{N2}$ corresponding to Néel transition observed in YCO by dc-magnetic measurements.[56] Thus, it is expected to have a large entropy change near the transition temperature. The grey shaded region represent the *Cr$^{3+}$* and *Yb$^{3+}$* ordering transition in YCO polycrystallites at $T_{N1}$ and $T_{N2}$.

## 5.5.2  Magnetocaloric effect:

The magnetic entropy changes rapidly in the vicinity of phase transition as the magnetization changes rapidly. The change in magnetization is expected to be large near $T_{N1}$ and $T_{N2}$, respectively.  The magnetic entropy change $\Delta S_M$  as a function of temperature  for a different magnetic field change up to 5 T is evaluated using the Maxwell relation:[5,23,52] and shown in **Figure 4**.

$$\Delta S_M (T, H) = \int_0^H \left(\frac{\partial M}{\partial T}\right)_H dH$$

It is well known that, $\Delta S_M$ is directly proportional to the change in magnetization with temperature .Thus, if $\left(\frac{\partial M}{\partial H}\right)$, is large, $\Delta S_M$ will be larger. The $\Delta S_M^{max}$ was found to be strongly field dependent and increases with the applied magnetic field. The $\Delta S_M^{max}$ at $T_{N2}$ (2.6 J/kg K) and $T_{N1}$ (0.12 J/kg K) was found to be around 5 T applied magnetic field, as shown in **Figure 4(a, b)**. The $\Delta S_M$ value was found to be negative around $T_{N1}$ & $T_{N2}$ and such an effect is known as normal magnetocaloric effect.
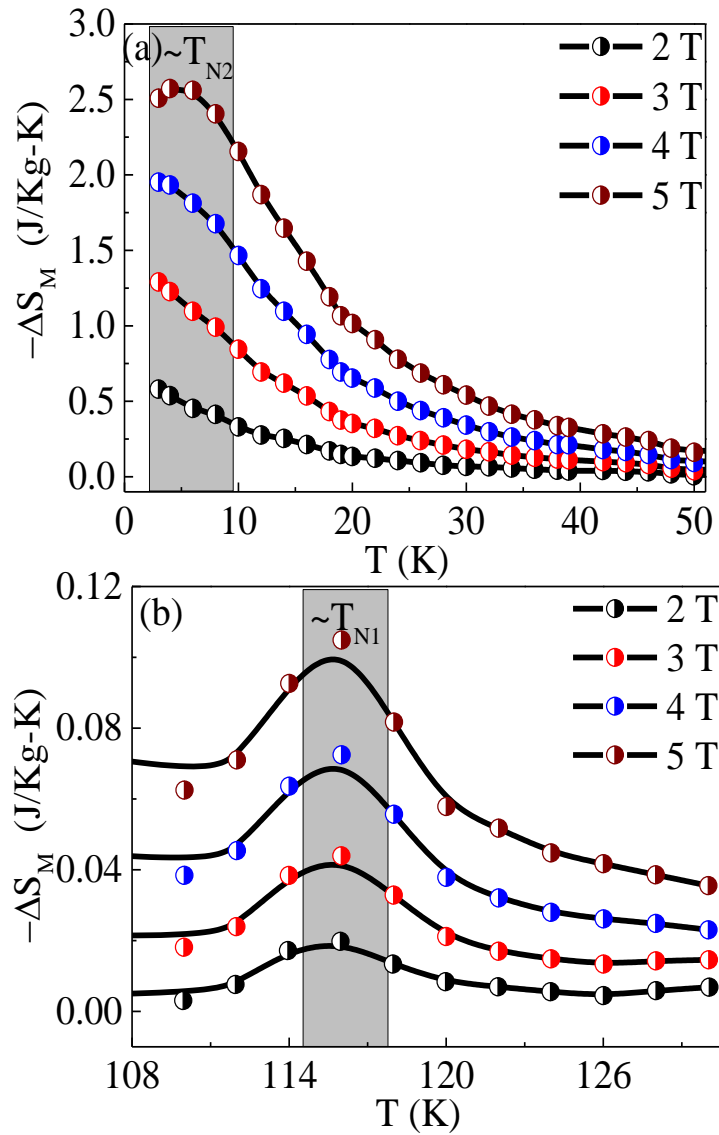
*Figure 4. Temperature dependence of magnetic entropy change $\Delta S_M$ for YCO at (a) ~ $T_{N2}$ and (b) ~$T_{N1}$ under different field changes up to 5 T.*

The most important MCE parameter *i.e.* RCP which determines the cooling efficiency of magnetic refrigerant and given by:[21]

$$RCP = -\Delta S_M(T, H) \times \delta T_{FWHM}$$

The H-dependent $\Delta S_M^{max}$ at $T_{N1}$ and $T_{N2}$ and RCP at $T_{N1}$, obtained are plotted in **Figure 5(a-c)**.
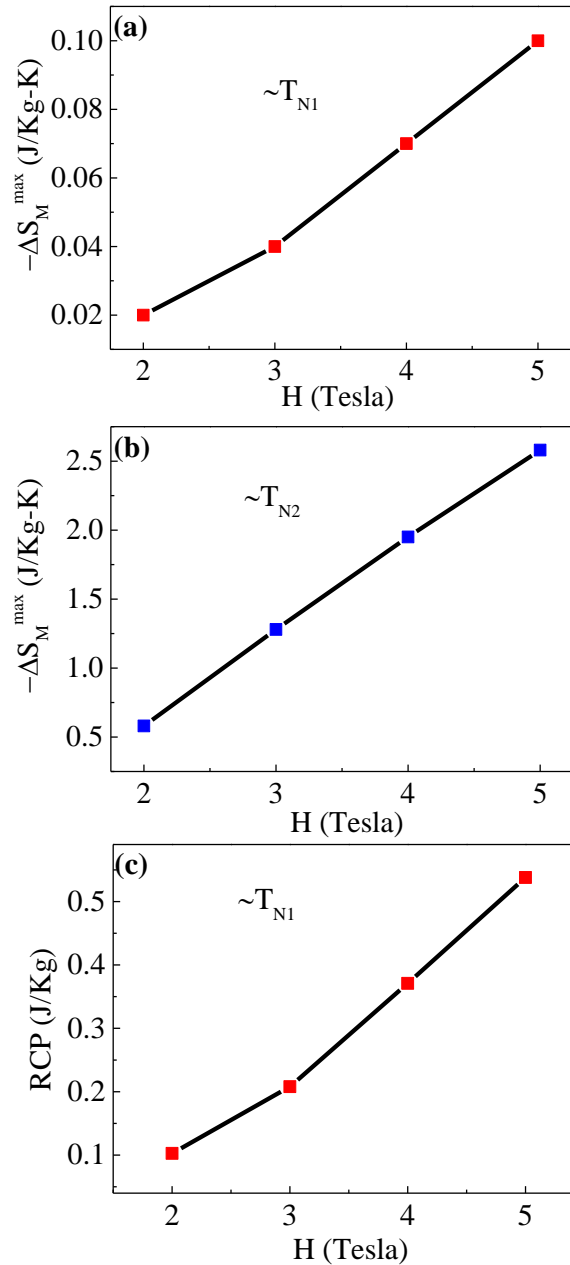
*Figure 5. H dependent (a, b) magnetic entropy change at $T_{N1}$ and $T_{N2}$  (c) relative cooling power  for YCO, respectively. Both the MCE parameters were found to be strongly dependent on H.*

As evident from the **Figure**, $\Delta S_M^{max}$  at $T_{N1}$ and $T_{N2}$ increases monotonically with H and reaches 0.1 J/Kg K. and 2.6 J/Kg K, at 5 T respectively. The RCP of YCO nanoplatelets was found to evolve linearly with the increasing H at $T_{N1}$, as shown in **Figure 5(c)**. The RCP at $T_{N1}$ value was found to be 0.53 J/Kg for 5 T applied field which was determined using $\delta T_{FWHM}$ obtained by Gaussian peak fitting for respective H.

It is suggested that the magnetic entropy change in a material under varying applied magnetic field for second order phase transition (SOPT) collapses into a single master curve which can be established by scaling the axes appropriately. Thus, universal behavior of YCO nanoplatelets was investigated by rescaling the axes. [53,63]



*Figure 6. Normalized entropy change for different applied magnetic fields (2-5 T) for YCO nanoplatelets at $T_{N1}$ as a function of the rescaled temperatures collapse into a single universal curve.*

We plotted the normalized $\Delta S_M$ curves (*i.e.* $\Delta S_M / \Delta S_M{}^{max}$) at $T_{N1}$, against the rescaled temperature axis defined by the parameter $\theta$: [41]
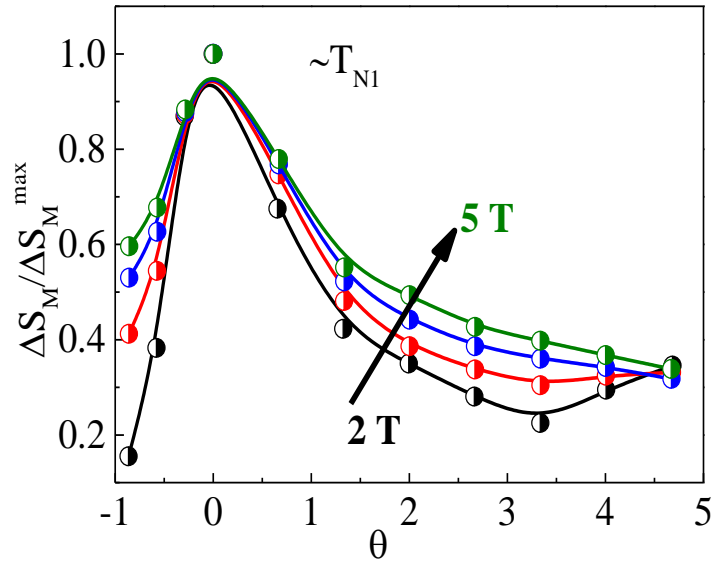
$$\theta = \begin{cases} -\frac{(T-T_C)}{(T_{R1}-T_C)}, T \leq T_C \\ \frac{(T-T_C)}{(T_{R2}-T_C)}, T > T_C \end{cases} \text{.................................(10)}$$

where $T_{R1}$ and $T_{R2}$ are the reference temperatures where $\Delta S$ equals $\Delta S_M{}^{max}/2$. The two reference temperatures $T_{R1}$ and $T_{R2}$, are needed to characterize the entropy change, where $T_{R1} < T_C$ and $T_{R2} > T_C$ and $T_C$ is the ordering temperature. Here, $T_C = T_{N1}$ (~ 119 K) where the entropy change is maximum. The transformed curves of YCO under various H are plotted in **Figure 6**. As seen from the **Figure**, all the curves collapse onto a single master curve, revealing it's universal behavior in a temperature regime close to $T_{N1} \sim 119$ K where, $\Delta S_M{}^{max}$ was obtained. However, as we move away from the ordering temperature, breakdown can be observed in the curve which is acceptable as scaling laws need not hold far away from T~ 119 K.

## 5.5.3  Heat capacity:

The zero field temperature dependent heat capacity of YCO is shown in **Figure 7**. The overall shape of $C_P$ -T plot was found to be similar to other chromites such as DCO, YCO, $NdCrO_3$ with a clear $\lambda$ shape anomaly at $T_N$ ~119 K. At high T region, similar to $DyCrO_3$, $SmCrO_3$, the YCO also follows Dulong-petit law, as $C_P$ approaches to classical value of 3nR (R= molar gas constant) per atomic site in formula unit. With the decrease in temperature, $C_P$ of YCO also decreases with a small hump observed below 10 K where, rare earth starts ordering. At 300 K, the $C_P$ was found to be 102.2 J/mol/K. The thermal anomalies observed in $C_P$-T curves was found to be consistent with the magnetic transitions and peak at $T_N$ in $C_P$-T plot is associated with the PM to AFM phase transition.[56]
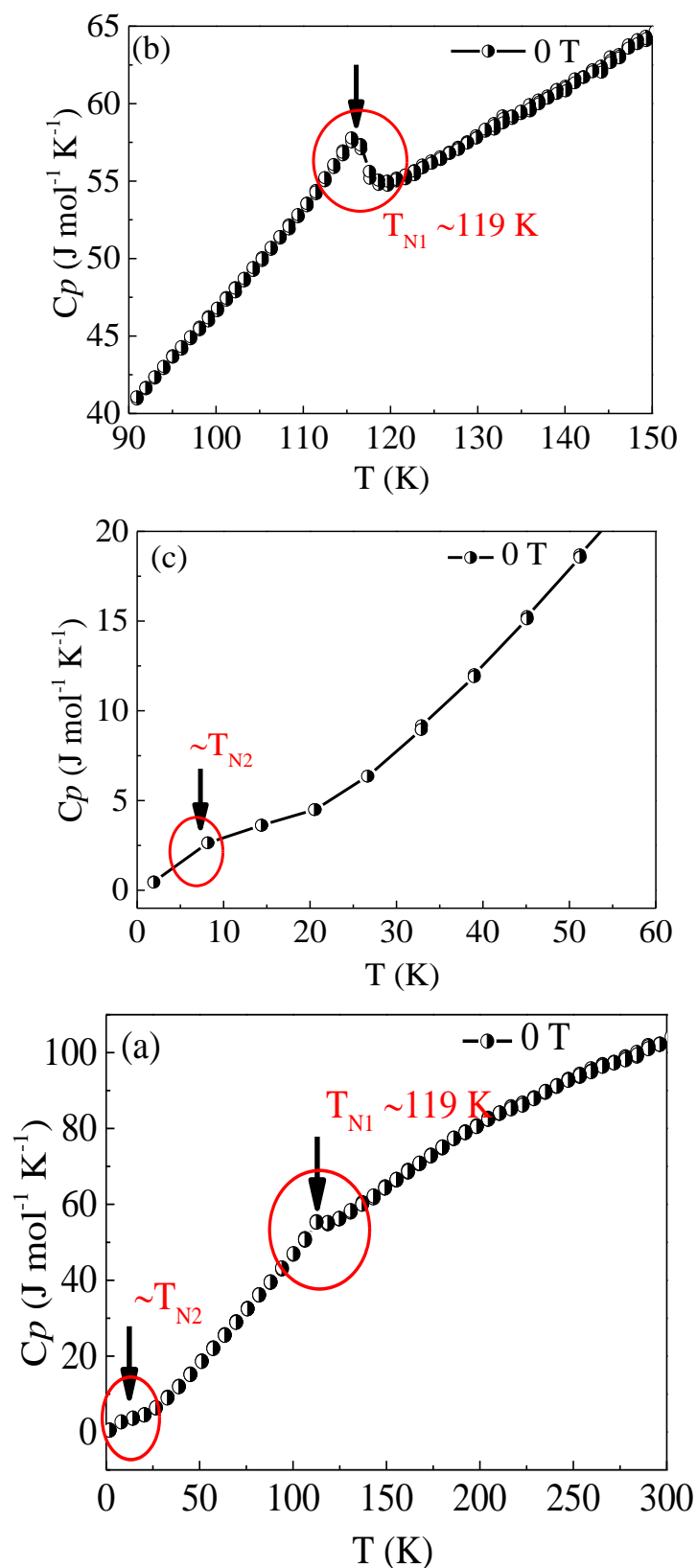
*Figure 7. (a) Thermal evolution of heat capacity of YCO nanoplatelets at zero field condition (b and c) shows the zoom view of the thermal anomalies observed in (a) at*

$T_N$ *and low T. The λ shape peak is associated with the second order paramagnetic to antiferromagnetic phase transition.*

**Figure 7( b & c)** shows the zoom view of $C_P$-T around $T_N$ and low temperature (< 60 K), clearly indicative of the well defined transition as observed from our previous magnetic studies on YCO.[64]

As total heat capacity $C_P$ of a system is given by equation:[57]

$$C_P = \gamma T + \beta T^3 + \delta T^{3/2} \dots\dots\dots\dots\dots\dots\dots\dots(11)$$

where the $\gamma T$ term gives the electronic contribution, $\beta T^3$ describes the contribution from the lattice and, $\delta T^{3/2}$ gives the spin wave contribution.

The Schottky anomaly in the low temperature regime below 10 K is mainly due to the crystal field effects and $Yb^{3+}$ spins.[56] The $C_P$-T data is fitted with the above equation in the temperature regime 3-60 K ,excluding the Schottky anomaly region and good fit was observed as showing **Figure 8(a)**. **Figure 8(b)** shows the zero field $C_P T^{-3/2}$- $T^{3/2}$ plot at low T, and data was fitted using linear equation. The fit gives a straight line well in agreement with the experimental data obtained for YCO.
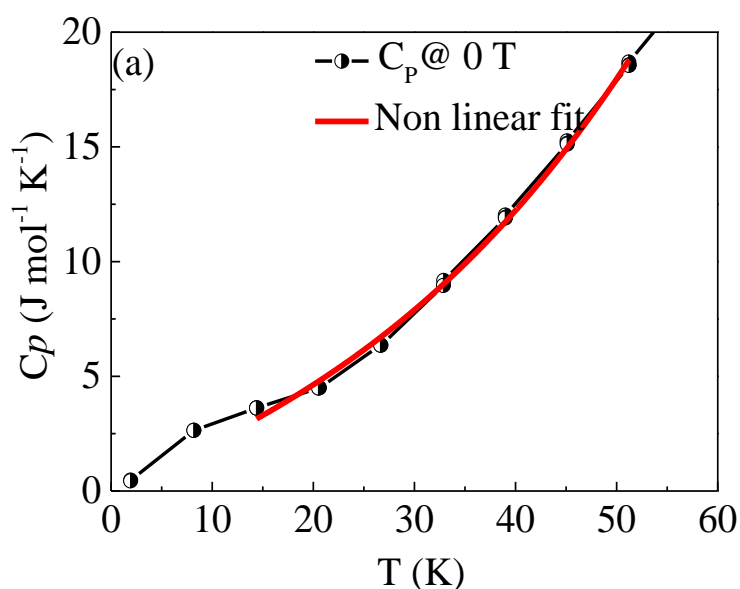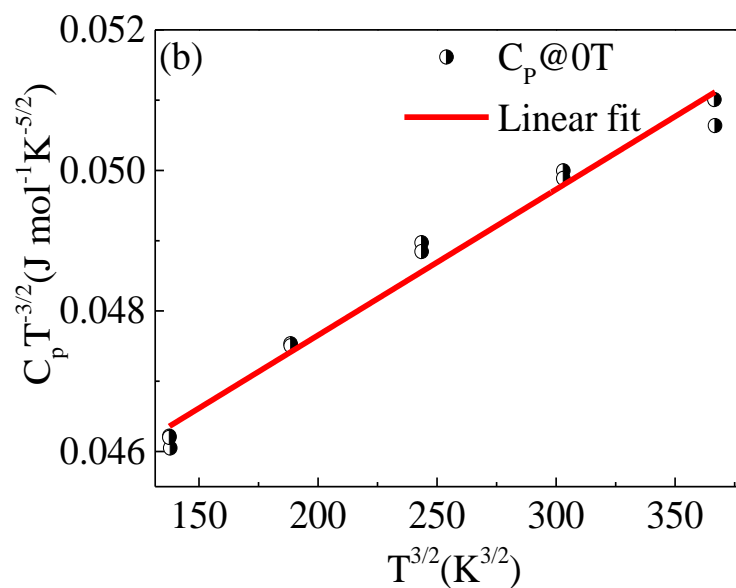
*Figure 8. (a) Experimental $C_p$ data is fitted according to the equation $C_p = \gamma T + \beta T^3 + \delta T^{3/2}$ at low temperature region in zero field condition. (b) plot of $C_p T^{-3/2}$ versus $T^{3/2}$ at low temperature range in zero field gives a straight line showing the presence of magnetic $T^{3/2}$ term in heat capacity data.*

We also studied the H dependent $C_P$-T and no change in $C_P$-T (**Figure 9(a-c)**) was observed with increasing the applied magnetic field 0-8 T, respectively.
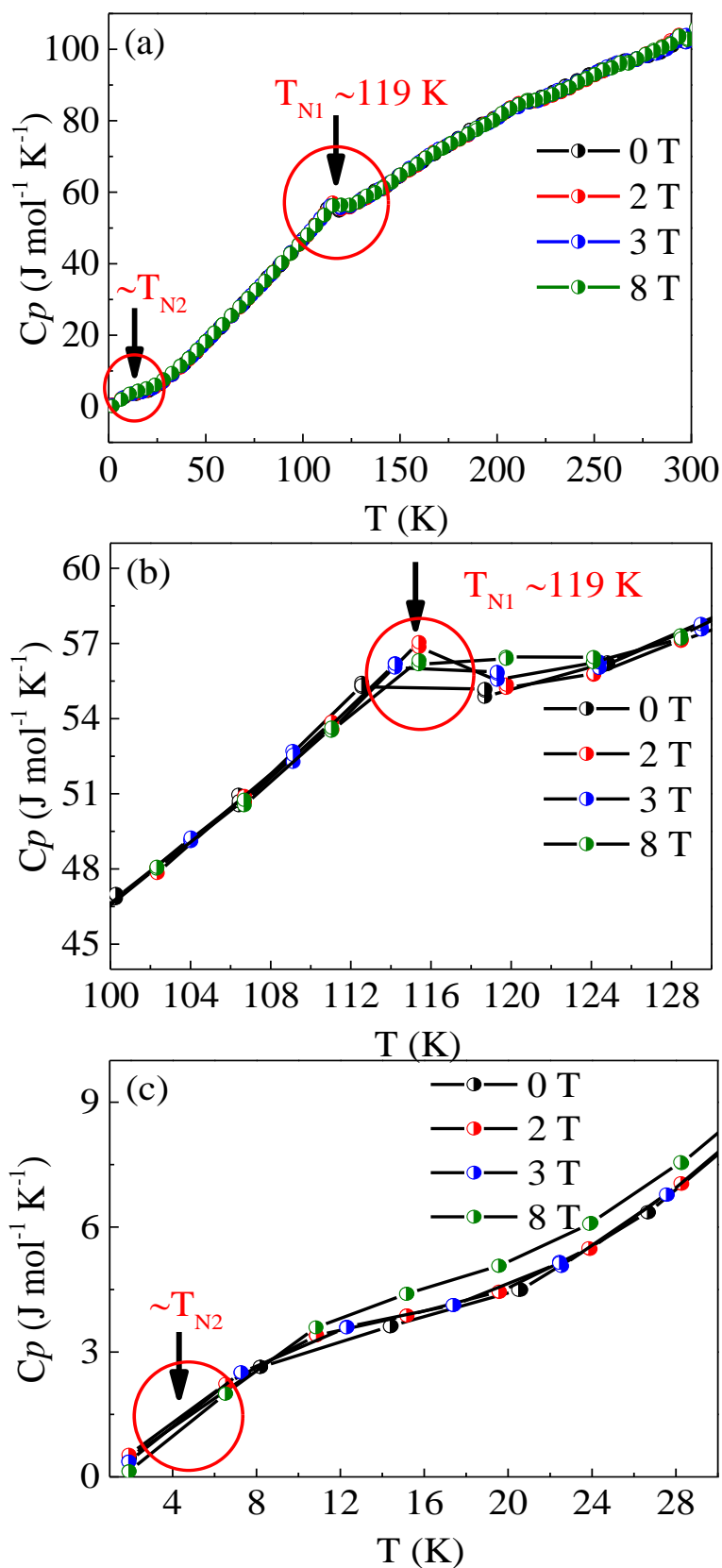
*Figure.9 (a) Field dependency of thermal evolution of heat capacity of YCO*

*nanoplatelets (b and c) shows the zoom view of the thermal anomalies at $T_{N1}$ and $T_{N2}$. For higher applied magnetic field the peak at $T_{N1}$ gets depressed and becomes broaden and low temperature anomaly as a Schottky anomaly ($T_{N2}$) arising from a combination of crystal field effects and the $Yb^{3+}$ spins.*

As evident from the **Figure 9(b)**, the peak at $T_N$ suppressed and broaden with the increase in H from 0-8 T. The overall structure of YCO is AFM and no additional anomaly was observed in 10-120 K temperature regime. However, low T anomaly *i.e.* Schottky anomaly was found to be strongly dependent on the magnitude of the applied field which was found to be shifted towards higher T with the increasing field from 0-8 T.[57]

## 5.5.4  Calculation of adiabatic change ($\Delta T_{ad}$) with magnetic field:

The adiabatic temperature change ($\Delta T_{ad}$), strongly depends on the $C_P$ value and change in magnetization $\left(\frac{\partial M}{\partial H}\right)$. For a larger $\Delta T_{ad}$, large $\left(\frac{\partial M}{\partial H}\right)$ and smaller $C_P$ is essential as given by the equation below:

$$\Delta T_{ad} = - \int_0^H \frac{T}{C_{P,H}} \left(\frac{\partial M}{\partial H}\right)_H dH$$

The T and H dependency of $\Delta T_{ad}$, in temperature range 3-50 K, is shown in **Figure 10**.
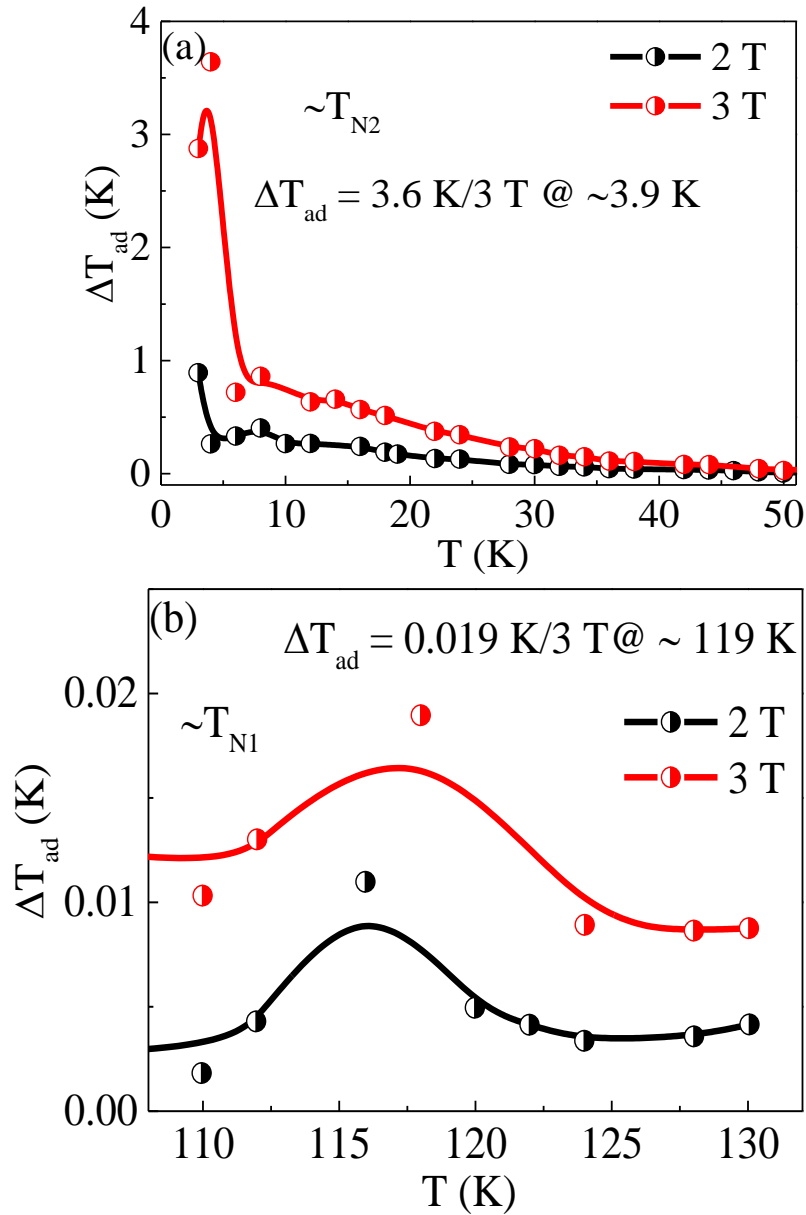
*Figure 10. The plot of adiabatic temperature change ($\Delta T_{ad}$) with temperature calculated indirectly from magnetization and heat capacity measurements in a temperature range (a) 3-50 K and (b)110-130 K for two different field value 2 T and 3 T, respectively.*

The $\Delta T_{ad}$ for YCO was found to be ~ 3.6 and ~ 0.02 K for 3 T field change at $T_{N2}$ ~ 3.9 and $T_{N1}$ ~ 119 K, respectively, where $\Delta S_M^{max}$ was obtained.

### 5.5.5  Conclusions

In summary, we have investigated the thermal and magnetic properties of YCO polycrystallite. The MCE parameters $\Delta S_M$, RCP and $\Delta T_{ad}$ was found to be strongly dependent on the applied magnetic field. The maximum change in the entropy at $T_{N2}$ and $T_{N1}$ was found to be 2.6 J/kg K and 0.1 J/kg K, respectively, for 5 T applied magnetic field. We also address the important MCE parameter $\Delta T_{ad}$, which strongly depends on the temperature and applied field. The peak at $T_{N1}$ in $C_P$-T plot was found to be suppressed and broaden with the increase in H from 0 - 8 T. Our results also present that the overall structure of YCO is AFM and no additional anomaly was observed in 10 - 120 K temperature regime and smaller $C_P$ value favors larger $\Delta T_{ad}$ 3.6 K/3T field change.

### 5.5.6 References:

[1] M. Balli, P. Fournier, S. Jandl, and M.M. Gospodinov, J. Appl. Phys. **115**, 173904 (2014).

[2] N.P. Kumar and P.V. Reddy, Mater. Lett. **122**, 292 (2014).

[3] K. Das, T. Paramanik, and I. Das, J. Magn. Magn. Mater. **374**, 707 (2015).

[4] V.K. Pecharsky and K. a Gschneidner, Phys. Rev. Lett. **78**, 3 (1997).

[5] K. a GschneidnerJr, V.K. Pecharsky, and a O. Tsokol, Reports Prog. Phys. **68**, 1479 (2005).

[6] N. Pavan Kumar and P. Venugopal Reddy, Mater. Lett. **132**, 82 (2014).

[7] H. Wada, T. Takahara, K. Katagiri, T. Ohnishi, K. Soejima, and K. Yamashita, J. Appl. Phys. **117**, 172606 (2015).

[8] O. Tegus, E. Brück, K.H.J. Buschow, and F.R. de Boer, Nature **415**, 150 (2002).

[9] X. Zhang, B. Zhang, S. Yu, Z. Liu, W. Xu, G. Liu, J. Chen, Z. Cao, and G. Wu, Phys. Rev. B - Condens. Matter Mater. Phys. **76**, 2 (2007).

[10] a. Midya, S.N. Das, P. Mandal, S. Pandya, and V. Ganesan, Phys. Rev. B - Condens. Matter Mater. Phys. **84**, 1 (2011).

[11] L.H. Yin, J. Yang, X.C. Kan, W.H. Song, J.M. Dai, and Y.P. Sun, J. Appl. Phys. **117**, 133901 (2015).

[12] A. McDannald, L. Kuna, and M. Jain, J. Appl. Phys. **114**, 0 (2013).

[13] L.H. Yin, J. Yang, R.R. Zhang, J.M. Dai, W.H. Song, and Y.P. Sun, Appl. Phys. Lett. **104**, 10 (2014).

[14] Q. Zhang, J.H. Cho, B. Li, W.J. Hu, and Z.D. Zhang, Appl. Phys. Lett. **94**, 182501 (2009).

[15] S. Chandra, A. Biswas, S. Datta, B. Ghosh, V. Siruguri, A.K. Raychaudhuri, M.H. Phan, and H. Srikanth, (n.d.).

[16] P. Lemoine, a. Vernière, T. Mazet, and B. Malaman, J. Magn. Magn. Mater. **323**, 2690 (2011).

[17] P. Alvarez-Alonso, P. Gorria, J. a. Blanco, J. Sánchez-Marcos, G.J. Cuello, I. Puente-Orench, J.A. Rodríguez-Velamazán, G. Garbarino, I. De Pedro, J.R. Fernández, and J.L. Sánchez Llamazares, Phys. Rev. B - Condens. Matter Mater. Phys. **86**, 1 (2012).

[18] Q. Zhang, F. Guillou, a. Wahl, Y. Bŕard, and V. Hardy, Appl. Phys. Lett. **96**, 2013 (2010).

[19] P. Mandal, C.R. Serrao, E. Suard, V. Caignaert, B. Raveau, a. Sundaresan, and C.N.R. Rao, J. Solid State Chem. **197**, 408 (2013).

[20] P.J. von Ranke, T.S.T. Alvarenga, B.P. Alho, E.P. Nóbrega, P.O. Ribeiro, a. M.G. Carvalho, V.S.R. de Sousa, a. Caldas, and N. a. de Oliveira, J. Appl. Phys. **111**, 113916 (2012).

[21] M.H. Phan and S.C. Yu, J. Magn. Magn. Mater. **308**, 325 (2007).

[22] J.-L. Jin, X.-Q. Zhang, G.-K. Li, Z.-H. Cheng, L. Zheng, and Y. Lu, Phys. Rev. B **83**, 1 (2011).

[23] M. Shao, S. Cao, S. Yuan, J. Shang, B. Kang, B. Lu, and J. Zhang, Appl. Phys. Lett. **100**, 222404 (2012).

[24] M.A. Hamad, J. Supercond. Nov. Magn. **26**, 2981 (2013).

[25] M.M. Vopson, J. Phys. D. Appl. Phys. **46**, 345304 (2013).

[26] A. Jaiswal, R. Das, K. Vivekanand, T. Maity, P.M. Abraham, S. Adyanthaya, and P. Poddar, J. Appl. Phys. **107**, 013912 (2010).

[27] P. Gupta, R. Bhargava, R. Das, and P. Poddar, RSC Adv. **3**, 26427 (2013).

[28] J.R. Sahu, C.R. Serrao, N. Ray, U. V. Waghmare, and C.N.R. Rao, J. Mater. Chem. **17**, 42 (2007).

[29] R. Schmidt, J. Romero, A. David, U. Amador, and E. Mora, (2013).

[30] P. Gupta, R. Bhargava, and P. Poddar, J. Phys. D. Appl. Phys. **48**, 025004 (2015).

[31] P.K. Manna and S.M. Yusuf, Phys. Rep. **535**, 61 (2014).

[32] A. Kumar and S.M. Yusuf, Phys. Rep. **556**, 1 (2015).

[33] K. Sardar, M.R. Lees, R.J. Kashtiban, J. Sloan, and R.I. Walton, Chem. Mater. **23**, 48 (2011).

[34] V. Srinu Bhadram, B. Rajeswaran, a. Sundaresan, and C. Narayana, EPL (Europhysics Lett. **101**, 17008 (2013).

[35] P. Gupta and P. Poddar, RSC Adv. **5**, 10094 (2015).

[36] N.K. Hirohisa Satoh, Shin-ichi Koseki, Masaki Takagi, won Yang Chung, Journal of Alloys and Compounds, **259**, 176 (1997).

[37] L.H. Yin, J. Yang, X.C. Kan, W.H. Song, J.M. Dai, and Y.P. Sun, J. Appl. Phys. **117**, 133901 (2015).

[38] M.M. Vopson, Solid State Commun. **152**, 2067 (2012).

[39] M. Aparnadevi and R. Mahendiran, J. Appl. Phys. **113**, 0 (2013).

[40] C. Krishnamoorthi, S.K. Barik, Z. Siu, and R. Mahendiran, Solid State Commun. **150**, 1670 (2010).

[41] M.K. Chattopadhyay, M. a Manekar, and S.B. Roy, J. Phys. D. Appl. Phys. **39**, 1006 (2006).

[42] Z. Han, H. Wu, D. Wang, Z. Hua, C. Zhang, B. Gu, and Y. Du, J. Appl. Phys. **100**, (2006).

[43] P. Poddar, J. Gass, D.J. Rebar, S. Srinath, H. Srikanth, S. a. Morrison, and E.E. Carpenter, J. Magn. Magn. Mater. **307**, 227 (2006).

[44] S. Srinath, P. Poddar, R. Das, D. Sidhaye, B.L.V. Prasad, J. Gass, and H. Srikanth, ChemPhysChem **15**, 1619 (2014).

[45] P. Poddar, S. Srinath, J. Gass, B.L. V Prasad, and H. Srikanth, J. Phys. Chem. C **111**, 14060 (2007).

[46] R. Singh, S.K. Srivastava, A.K. Nigam, V. V. Khovaylo, L.K. Varga, and R. Chatterjee, J. Appl. Phys. **114**, (2013).

[47] S.K. Banerjee, (1964).

[48] A.K. Pramanik and A. Banerjee, (2010).

[49] A. Arrott and J.E. Noakes, Phys. Rev. Lett. **19**, 786 (1967).

[50] A. Arrott, Phys. Rev. **108**, 1394 (1957).

[51] J. Mira, J. Rivas, M. Vázquez, J. García-Beneytez, J. Arcas, R. Sánchez, and M. Señarís-Rodríguez, Phys. Rev. B **59**, 123 (1999).

[52] L.H. Yin, J. Yang, R.R. Zhang, J.M. Dai, W.H. Song, and Y.P. Sun, Appl. Phys. Lett. **104**, 1 (2014).

[53] C.M. Bonilla, J. Herrero-Albillos, F. Bartolomé, L.M. García, M. Parra-Borderías, and V. Franco, Phys. Rev. B - Condens. Matter Mater. Phys. **81**, 1 (2010).

[54] V. Franco, K.R. Pirota, V.M. Prida, A.M.J.C. Neto, A. Conde, M. Knobel, B. Hernando, and M. Vazquez, Phys. Rev. B - Condens. Matter Mater. Phys. **77**, 1 (2008).

[55] V. Franco, J.S. Blázquez, B. Ingale, and a. Conde, Annu. Rev. Mater. Res. **42**, 305 (2012).

[56] Y. Su, J. Zhang, Z. Feng, L. Li, B. Li, Y. Zhou, Z. Chen, and S. Cao, J. Appl. Phys. **108**, 013905 (2010).

[57] Y. Du, Z.X. Cheng, X.-L. Wang, and S.X. Dou, J. Appl. Phys. **108**, 093914 (2010).

[58] B. Tiwari, M.K. Surendra, and M.S.R. Rao, **25**, (2013).

[59] S. a. Nikitin, K.P. Skokov, Y.S. Koshkid'Ko, Y.G. Pastushenkov, and T.I. Ivanova, Phys. Rev. Lett. **105**, 1 (2010).

[60] M. Ilyn, M.I. Bartashevich, a. V. Andreev, E. a. Tereshina, V. Zhukova, a. Zhukov, and J. Gonzalez, J. Appl. Phys. **109**, (2011).

[61] H. Zhang, Y.J. Sun, L.H. Yang, E. Niu, H.S. Wang, F.X. Hu, J.R. Sun, and B.G. Shen, J. Appl. Phys. **115**, 063901 (2014).

[62] Q.Y. Dong, H.W. Zhang, J.R. Sun, B.G. Shen, and V. Franco, J. Appl. Phys. **103**, 101 (2008).

[63] V. Franco, a. Conde, D. Sidhaye, B.L. V Prasad, P. Poddar, S. Srinath, M.H. Phan, and H. Srikanth, J. Appl. Phys. **107**, 1 (2010).

[64] P. Gupta and P. Poddar, Inorg. Chem. 150921124621008 (2015).

# Chapter 6

## Summary and future scope

**This chapter presents a summary of the research work described in this thesis with the concluding remarks and then lays out the scope of future work in this field.**

## 6.1    Summary:

There has been an augmented trend in the research for discovering new multifunctional materials and exploring the existing materials to deal with the technological and environmental requirements. Also, there is a renewed interest among physicists and chemists in evolving new routes to synthesize complex oxides due to their potential use in the magnetoelectric, magnetocaloric and optoelectronic devices as well as in catalysis.

The **chapter 1** provides the background of the research work and also addresses the motivation behind studying the rare earth chromites (section 1). It also discusses the stimulating features such as negative magnetization, exchange-bias and magnetization-switching which make rare earth chromites so interesting to study. The chapter also introduces the origin of magnetocaloric effect (MCE) in some of the orthochromites. It also addresses the possible grounds for MCE to exist in the chromites, which are subjected to our study. The section 2 discusses the scope of present investigation in the thesis work. The chapter 2 - 5 is divided into three sections addressing the physical properties of $DyCrO_3$ (DCO), $SmCrO_3$ (SCO) and $YbCrO_3$ (YCO) polycrystallites.

The **chapter 2** deals with the synthesis and structural properties of the rare earth chromites ($RCrO_3$, R = Dy, Sm and Yb). In this chapter, we have reported the successful synthesis of single-phase DCO, SCO and YCO. The structural characterization techniques such as X-ray diffraction, and X-ray photoelectron spectroscopy further confirmed the single phase formation and stoichiometry of the compound. The chapter also discusses the role of different chelating agents in the phase formation. The morphology, crystallinity and particle size of the rare earth chromite particles were studied by transmission electron microscopy. It also highlights the possible role of nitrate and citrate ions and their molar ratio in the formation of 2D nanoplate-like morphology. In addition, a scheme was developed to elucidate the mechanism for the formation of nanoplatlets morphology in these orthochromites.

Followed by the synthesis and structural studies, we explored the optical properties of these rare earth chromites ($RCrO_3$, R = Dy, Sm and Yb). The **chapter 3** addresses the optical properties of these orthochromites by using experimental

techniques including Raman and UV-vis-NIR spectroscopy. To further elucidate the spin-phonon and magnetoelectric coupling in these rare earth chromites, DCO was used as a representative material. The temperature dependent Raman studies on $DyCrO_3$ indicated the shift in the phonon frequency of the most intense modes. The observed change in the Raman line-width is correlated with the spin-phonon coupling. The impedance spectroscopy reveals the dielectric anomaly in the vicinity of the magnetic transition. These results hint towards the possible weak magnetoelectric coupling in $DyCrO_3$ nanoplatelets. The interest in this family of compounds has largely remained confined to study the multiferroic properties. But, they can be classified as semiconductors rather than insulators based on their band edge information.  The band-edge information of the DCO, SCO and YCO nanoplatelets raised a probability of exploring its catalytic behavior. The photocatalytic activity was also studied for DCO, as a representative. The DCO nanoplatelets were found to be an efficient photocatalyst, which degraded the methyl orange to 65 % after 8 h UV illumination. In summary, rare earth chromites were found to be an improvement over conventional photocatalytic materials such as titania, as their rich optical nature provides the absorption bands in the visible region also (in contrast to pure titania).

The **chapter 4** is divided into three sections. Each section addresses the unique features such as negative magnetization (NM), exchange bias (EB) and magnetization switching in DCO, SCO and YCO polycrystallites, respectively. The negative magnetization has practical implications such as exchange bias, magnetization switching and magnetocaloric effect (MCE) in a magnetic system. An understanding was developed about the origin of EB phenomenon. The model discussed in this thesis to understand the EB for the polycrystallites, is different then the conventional core-shell model proposed earlier in literature for the nanoparticles. The observed field assisted magnetization switching in DCO, SCO and YCO hints towards its plausible use in the spintronics application. The presence of two compensation temperature regions in YCO, were utilized to study the temperature-assisted magnetization-switching which is useful for application in thermomagnetic switches.

The thermal properties of DCO, SCO and YCO were studied in the **chapter 5** by employing heat capacity and magnetic measurements. There is a need for the new materials with large entropy change ($\Delta S_M$) and tunable operating temperature. The

possible MCE in these orthochromites was studied and discussed in chapter 5. The $Dy^{3+}$ has a large magnetic moment (10.6 $\mu_B$), hence, giant MCE is expected near the Dy ordering transition temperature. Thus, MCE was explored in DCO nanoplatelets. The giant MCE at 9 K was observed in DCO with large change in magnetic entropy and  temperature ~ 16.95 J/kg K and 15 K, respectively.  However, $Sm^{3+}$ with small magnetic moment (0.84 $\mu_B$) is not expected for giant MCE in SCO. The spin reorientation transition in SCO polycrystallites is anticipated to give inverse MCE leading to the enhance refrigeration efficiency. The SCO nanoplatlets, where, the spin reorientation transition ( ~ $T_{SR}$) and Néel transition (~ $T_N$ ) are the key features, were further explored to study the coexistence of inverse and normal MCE in a single material.  The SCO nanoplatelets hold tremendous advantage over conventional MCE materials which provides ~ 47 K broader working temperature regime. The MCE parameters *i.e.* $\Delta S_M$, RCP and $\Delta T_{ad}$ in YCO with $Yb^{3+}$ magnetic moment (4.5 $\mu_B$) were found to be strongly field dependent. The smaller $C_P$ value in YCO favors larger $\Delta T_{ad}$ 3.6 K/3T field change.

## 6.2    Scope for future work:

While the research presented in this thesis was being performed, several advances have been occurring on the international front in the field of multiferroics, addressing the rare earth chromites. The most debatable topic is the origin of ferroelectricity in the rare earth chromites and a significant work was done to understand the origin by engaging theoretical and experimental tools. Theoretically, the key reason for ferroelectricity in the orthochromites was attributed to the local structural distortion. To prove it experimentally, EXAFS study on the orthochromites is required, as it is an expedient tool to study the local structural distortion in a system. The temperature dependent EXAFS study will further reveal the local information in more detail.

However, during my ongoing thesis work, synthesis of these orthochromites was also studied explicitly on an international front mainly in bulk form using different wet-chemical techniques. Since, the particle size and morphology play an important role in determining the physical properties of the material, there is an open problem to be addressed in the future. These orthochromites are well studied for its multiferroic properties and are generally considered to be insulators. But, our studies on the band edge information revealed that it could be used for catalytic studies. In this context, this is yet another aspect of the rare earth chromites, which needs to be explored in the near future. Till date, optical properties of the rare earth chromites are not explored much in the literature. Thus, it is necessary to investigate the optical properties, band gap *etc.* and study their catalytic activity. In addition, their applications in hydrogen generation using water splitting remain unexplored.

Our group observed negative magnetization in $GdCrO_3$ nanoparticles, which sparked the interest in this field. The question arises as why orthochromites exhibit negative magnetization unlike similar family of compounds namely, ferrites and manganites. This led us to explore the orthochromites for these strange behaviors. My thesis work revealed that DCO, SCO and YCO polycrystallites possess interesting and unique behavior, negative magnetization and practical implication of NM *i.e.* exchange bias and magnetization switching. The thesis work discussed the possible reason and proposed a model for NM and EB in these orthochromites. Still, the origin of negative magnetization and exchange bias in this class of materials, in polycrystalline form, is not understood completely. To explore the plausible reason

behind these unique behaviors in orthochromites, a lot of work is required. We believe that the locally formed ferromagnetic (FM) /antiferromagnetic (AFM) interface is responsible for the observed exchange bias in these compounds. Neutron depolarization is known to be an effective tool to study the phase transformation kinetics, formation of FM or AFM clusters, spatial magnetic inhomogeneity *etc*. In an unsaturated ferromagnet or ferrimagnet, the magnetic domains exert a dipolar field on the neutron polarization and depolarize the neutrons and similarly, no depolarization is expected in the paramagnetic state because the temporal spin fluctuation is too fast for the neutron polarization to follow the variation in the magnetic field acting on the moving thermal neutrons. As there is no restriction on the domain size, this technique is advantageous in obtaining the domain size information over the entire sample. Thus, in addition to the DCO, SCO and YCO polycrystallites, it is essential to probe the other orthochromites also by Neutron depolarization studies. The complex magnetic interactions in the orthochromites are temperature dependent. Thus, temperature and external magnetic field dependent experiments are essential to get the complete picture of NM and EB in these compounds.

These rare earth chromites show magnetic transitions at low temperature which hinders its vast use in room temperature commercial applications. To solve this issue, it is important to tune the Néel transition so that it can be used for room temperature application. Thus, by substituting with suitable dopant such as Fe in $DyCrO_3$, $SmCrO_3$ and $YbCrO_3$ we can tune the transition temperature and underlying physics can be addressed in the future.

Another important aspect of the work is magnetocaloric effect in orthochromites, which was observed at low temperature. The goal of the current research in MCE is to search of new material with large entropy change ($\Delta S_M$) and tunable operating temperature so that, systems showing larger MCE at RT would be useful for ambient condition technological applications. While, large MCE at low T regime down to sub-Kelvin are advantageous for applications such as space science, liquefaction of hydrogen in fuel industry. Thus, these concerns can be addressed in future by tuning the transition temperature and particle size, which will enhance the MCE in orthochromites. As MCE parameters strongly depend on the nature of

transition, particle size, and heat capacity of the compound, it is essential to tune these parameters in order to improve the MCE. Also, to increase the entropy change, it is essential to dope with large magnetic moment elements. Since, we observe large entropy change in DCO, we believe that by doping with gadolinium, enhancement in MCE will be observed. This problem is also left open to study and to be addressed in the near future. The nanomaterials provide better heat exchanger than bulk due to the large surface area. Thus, the refrigeration capacity can be improved further by reducing the particle size.

# List of publications:

1. Temperature and magnetic field assisted switching of magnetization and exchange bias in $YbCrO_3$ nanocrystals.
   ***Preeti Gupta*** and *Pankaj Poddar*,(Accepted, Inorganic Chemistry, 2015)
   DOI:10.1021/acs.inorgchem.5b01448

2. Using Raman and dielectric spectroscopy to elucidate the spin phonon and magnetoelectric coupling in $DyCrO_3$ nanoplatelets.
   ***Preeti Gupta*** and *Pankaj Poddar*, *RSC Advances* 5 (14), 10094-10101, 2015

3. Colossal increase in negative magnetization, exchange bias and coercivity in samarium chromite due to a strong coupling between $Sm^{3+}$–$Cr^{3+}$ spins sublattices.
   ***Preeti Gupta,*** *Richa Bhargava, Pankaj Poddar*, *Journal of Physics D: Applied Physics*, 48, 2015

4. Synthesis, Characterization and In Vitro Study of Biocompatible Cinnamaldehyde Functionalized Magnetite Nanoparticles (CPGF Nps) For Hyperthermia and Drug Delivery Applications in Breast Cancer.
   *Kirtee D Wani, Brijesh S Kadu, P Mansara,* ***Preeti Gupta***, *AV Deore, RC Chikate*, *PloS one* 9 (9), e107315, 2014

5. Static and dynamic magnetic properties and effect of surface chemistry on the morphology and crystallinity of $DyCrO_3$ nanoplatelets.
   ***Preeti Gupta***, *Richa Bhargava, Raja Das and Pankaj Poddar, RSC Advances*., 3, 26427-26432, 2013

6. Giant magnetocaloric effect and large adiabatic temperature change in $DyCrO_3$ nanoplatelets at low temperature.
   ***Preeti Gupta*** and *Pankaj Poddar* (Communicated).

7. Coexistence of inverse and normal magnetocaloric effect in $SmCrO_3$ polycrystallites covering ~ 47 K wide working temperature range.
   ***Preeti Gupta*** and *Pankaj Poddar* (Communicated).